University of California
Santa Barbara

Getting in shape: physical principles underlying order generation and shape change in the morphogenesis of thin tissues

A dissertation submitted in partial satisfaction
of the requirements for the degree

Doctor of Philosophy
in
Physics

by

Dillon Jeffrey Cislo

Committee in charge:

Professor Boris Shraiman, Co-Chair
Professor Sebastian Streichan, Co-Chair
Professor Zvonomir Dogic

September 2022

The Dissertation of Dillon Jeffrey Cislo is approved.

Professor Zvonomir Dogic

Professor Sebastian Streichan, Committee Co-Chair

Professor Boris Shraiman, Committee Co-Chair

August 2022

Getting in shape: physical principles underlying order generation and shape change in the morphogenesis of thin tissues

by

Dillon Jeffrey Cislo

For the harmony of the world is made manifest in Form and Number,
and the heart and soul and all the poetry of Natural Philosophy
are embodied in the concept of mathematical beauty.

D'Arcy Wentworth Thompson, *On Growth and Form* (1917) [246]

Acknowledgements

The work contained within this dissertation was made possible by the support and guidance many people over the years. My deepest gratitude goes to:

My first co-advisor, Boris Shraiman, for his support, mentorship, advice, and critical insight. By example, Boris has taught me how to think about physics in a way that balances intuition and rigor. His enthusiasm is infectious and it is impossible not to be excited about science when working with him. I hope I have absorbed a fraction of his skill as a scientist and his patience as a mentor during my time at UCSB.

My second co-advisor, Sebastian Streichan, who has been an invaluable source of support and mentorship. Sebastian's broad mastery of both physics and biology has been an inspiration to me for how a physicist should approach problems in an interdisciplinary field. Sebastian's keen sense for communicating complicated ideas in a simple and direct fashion have helped me immensely.

My dynamic collaborator Noah Mitchell, whose ability to wrest results from dauntingly complicated systems sometimes feels to me like wizardy. Working with Noah has been a highlight of my PhD and I hope to continue our collaborations in the future.

Mark Bowick whose insight and knowledge provided our work on orientational order in *Parhyale* a much needed sense of rigor and clarity.

Zvonomir Dogic for serving on my PhD committee and always asking insightful questions.

Members of the Shraiman/Streichan labs, past and present, with particular thanks to Nick Noll, Farzan Vafa, Hannah Gustafson, Nikolas Claussen, Fridtjof Brauns, Aimel Khankel, Eyal Karzbrun, and Matt Lefebvre. Thank you for the camraderie and stimulating discussions.

My family for their unconditional love and support. My mom for being a shoulder

to lean on, my support system, and my biggest fan. My dad for instilling in me a love of learning and showing me that hard work can build things of quality. My sister, Allie, for always believing in me and always keeping me honest.

I have been unreasonably lucky throughout my life to have been surrounded by the most excellent friends and my time at UCSB has been no exception. Thank you to Eric Jones, my roommate of four years, and the rest of my physics cohort, Brent Roth, my dive buddies, the Abrego crew, and all the rest. Thanks for the hikes, the backpacking trips, the early morning dives, the late night conversations, the bonfires, the paddle boarding sessions, the BBQs, the mountain parties, the nights we spent on State Street and in IV (and the mornings we spent regretting them), the concerts, the festivals, the roadtrips, and the long walks on the beach. You all are the real reason that my time at UCSB has been special.

Curriculum Vitæ

Dillon Jeffrey Cislo

Education

2022	Ph.D. in Physics (Expected), University of California, Santa Barbara.
2018	M.A. in Physics, University of California, Santa Barbara.
2015	B.S. in Engineering Physics, Cornell University

Publications

1. M.C. Harris, **D.J. Cislo**, J.S. Lenz, C. Umbach, M. Lindau (2017) " AFM/TIRF force clamp measurements of neurosecretory vesicle tethers reveal characteristic unfolding steps." *PLoS ONE* 12(3): e017399
2. **D.J. Cislo**, H. Qin, F. Yang, M.J. Bowick, S.J. Streichan (2021) "Active cell divisions generate exotic fourfold orientationally ordered phase in living tissue." *bioRxiv* 2021.07.28.453899; doi: https://doi.org/10.1101/2021.07.28.453899
3. N.P. Mitchell* and **D.J. Cislo*** (2022) "TubULAR: Tracking deformations of dynamic tissues and interfaces in 3D." *bioRxiv* 2022.04.19.488840; doi: https://doi.org/10.1101/2022.04.19.488840. *equal contribution
4. N.P. Mitchell, **D.J. Cislo**, S. Shankar, Y. Lin, B.I. Shraiman, S.J. Streichan (2022) "Visceral organ morphogenesis via calcium-patterned muscle constrictions." *eLife* **11**:e77355.
5. **D.J. Cislo** and B.I. Shraiman (2022) "A morphogenetic action principle for the anisotropic growth of thin tissues." (in preparation).

Abstract

Getting in shape: physical principles underlying order generation and shape change in the morphogenesis of thin tissues

by

Dillon Jeffrey Cislo

In plants and animals, developmental programs transform single-celled zygotes into fully formed and functional organisms. Understanding morphogenesis, the collective set of mechanisms that transduce discrete genetic information into the 3D form of tissues, organs, and appendages, is a foundational problem at the interface of biology and physics. While great progress has been made characterizing the molecular components that determine the initial body plan, the subsequent dynamics of cellular rearrangements and tissue deformations that ultimately shape the organism are far less understood. A thorough description of morphogenesis necessitates an understanding of the intricate interplay among genetics, mechanics, and geometry.

This dissertation presents a body of work aimed at understanding how mechanics and geometry sculpt thin tissues into complex shapes during development. We apply a combination of theoretical, computational, and experimental methods to build quantitative descriptions of a variety of morphogenetic processes, including germband organization, organogenesis, and limb growth. In each setting, careful analysis reveals how physical mechanisms dynamically coordinate the self-organization of shape and form across multiple scales, from the cellular to the organismal. The synthesis of these various results contributes towards building a quantitative and predictive understanding of morphogenesis.

In Chapter 2, we present set of computational methods for the characterization and

analysis of tissue deformation in tubelike surfaces. These methods, contained within our open-source TubULAR package, enable users to extract dynamic surfaces, construct 2D parameterizations optimized for tracking tissue parcels, measure whole-organ tissue deformation, and compute signatures of 3D motion. We showcase the power of these methods by quantifying tissue flow during the development of the *Drosophila* midgut and the zebrafish heart. Decomposition of complicated flow fields in to simple components with straightforward physical interpretations enable novel insights that would be difficult or impossible to find with exisiting methodologies.

In Chapter 3, we demonstrate how actively oriented cell divisions organize the ectodermal germband in *Parhyale hawaiensis*. Live imaging and computer vision reveal that waves of cell proliferation sweep across the embryo in such a way that the initially fluid germband flows towards a fourfold orientationally ordered state. We develop a hydrodynamic model that can predict coarse-grained flow fields from division events, bridging the gap between cell-scale and tissue-scale dynamics. Vertex model simulations demonstrate that oriented cell divisions constitute a robust mechanism for generating orientational order in living tissues far from thermal equilibrium.

In Chapter 4, we study the transformation of the *Drosophila* midgut from a simple tube into a complex, coiling configuration of folds and compartments. We demonstrate that tissue shape is controlled by gene expression via mechanical interactions between heterologous tissue layers. Hox genes mediate calcium signaling that regulates muscle contractions at precise locations along the length of the gut. These muscle contractions induce sharp folds and convergent extenstion in the gut endoderm, which is strongly constrained by tissue incompressibility. We show that the tissue scale flow is mediated by anisotropic cell shape change resulting from the mechanical coupling to muscle contractility. Taken together, these results form a concrete link from genes to cell-scale mechanics to tissue morphodynamics via active forces.

In Chapter 5, we present a theoretical and computational framework for tackling the problem of growth pattern selection in epithelial morphogenesis. We show that developmental programs can be quantified in terms of anistropy and areal growth rates. Arbitrarily complicated growth patterns can be built up by composing simple infinitesimal updates to the system's intrinsic geometry. We proposed an action principle that selects for simple growth patterns that minimize spatiotemporal variation in these quantities. We then applied this formalism to seveal synthetic and experimental systems, including limb morphogenesis in *Parhyale*.

Contents

Curriculum Vitae **vii**

Abstract **viii**

1 Introduction **1**
- 1.1 Growth and shape change in thin tissues 7
- 1.2 Quantiative methods for the live-imaging and analysis of epithelial morphogenesis 12
- 1.3 Segmentation and the developmental body plan 16
- 1.4 Orientational order and tissue organization 18
- 1.5 Bridging cell scale behaviors and tissue scale morphogenesis 21
- 1.6 Emergent simplicity and the search for principles in growth pattern selection 26
- 1.7 Dissertation outline 28
- 1.8 Permissions and Attributions 29

2 TubULAR: *in toto* tissue cartography, material parameterization, and flow field analysis in tube-like surfaces **31**
- 2.1 Introduction 32
- 2.2 Implementation and application to a model organ 36
- 2.3 Decomposing deformations during heart morphogenesis 48
- 2.4 Discussion 51

3 A geometric body plan: active cell divisions organize *Parhyale* embryo into fourfold ordered state **53**
- 3.1 Introduction 54
- 3.2 *In toto* live imaging of *Parhyale* embryo reveals fourfold ordered state . . 55
- 3.3 Ectodermal grid is build by waves of oriented cell divisions 62
- 3.4 Active hydrodynamic model confirms divisions generate tissue scale motion 68
- 3.5 Active vertex model reveals how directed divisions generate orientational order 71
- 3.6 Discussion 76

4 A kinetic mechanism links gene expression to visceral organ morphogenesis in *Drosophila* 78
4.1 Introduction . . . 79
4.2 Live deep tissue imaging reveals bilayer morphogenesis . . . 80
4.3 Endodermal cell shape change underlies tissue shape change . . . 82
4.4 Tissue-scale convergent extension via constriction . . . 84
4.5 Muscle contractions drive cell and tissue shape change . . . 90
4.6 Calcium pulses spatiotemporally pattern muscle contractility . . . 94
4.7 Discussion . . . 98

5 A morphogenetic action principle for thin tissues 100
5.1 Introduction . . . 101
5.2 Quasiconformal parameterizations of anisotropic growth patterns . . . 105
5.3 Growth pattern selection as an optimization problem . . . 113
5.4 Results . . . 119
5.5 Discussion . . . 124

6 Conclusions and Outlook 127

A TubULAR implementation details 132
A.1 Overview of approach by example . . . 132
A.2 Surface extraction using level sets . . . 135
A.3 Constrained mapping to the plane follows tissue motion . . . 136
A.4 Example of inferring intercalation rates ('tissue tectonics') using TubULAR 150
A.5 Analysis of beating zebrafish heart dynamics . . . 152
A.6 A cytoskeletal gel actively deforms liquid droplets . . . 152

B Materials and methods for analysis of germband extension in *Parhyale* 154
B.1 Light sheet microscopy . . . 154
B.2 Data post processing and microscope automation . . . 155
B.3 Extraction of dynamical surfaces of interest . . . 155
B.4 In-plane cell segmentation and pathline reconstruction . . . 159
B.5 Region of interest selection for dynamical quantities . . . 162
B.6 Calculation of discrete curvatures . . . 162
B.7 Construction of correlation functions . . . 165
B.8 Circular statistics for division events . . . 168
B.9 Determination of the average division velocity . . . 168
B.10 Generation of synthetic data sets and comparison with measured data . . . 170
B.11 Timing and orientation of cell divisions is not predicted by local mechanical or geometric signals . . . 173
B.12 Additional figures for Chapter 3 . . . 179

C Derivation of hydrodynamic model for active stress due to cell divisions 182
C.1 Cell divisions and active stresses 185
C.2 Numerical prediction of tissue velocities from cell divisions 192

D Vertex model simulations of orientational order generation 197
D.1 Initial lattice construction 198
D.2 Growth, division, relaxation, and confinement 199

E Materials and methods for analysis of *Drosophila* midgut morphogenesis 202
E.1 Microscopy 202
E.2 Parameterization of organ shape 203
E.3 Endodermal cell segmentation and shape change 204
E.4 Single-cell tracking 207
E.5 Topological cell rearrangements in the endoderm 209
E.6 Quantification of tissue deformation 211
E.7 Minimal ingredients demonstrate geometric interplay between compressibility and shear 213
E.8 Quantification of tissue shear 216
E.9 Relative motion between layers 219
E.10 Optogenetic experiments 221
E.11 Wild-type calcium dynamics 222
E.12 Calcium activity in *Antp* mutants 224
E.13 MLCK RNAi and SERCA mutant analysis 228

F Numerical methods for optimal growth pattern selection 230
F.1 Embedding intrinsic geometries in 3D 230
F.2 Non-Parametric Representations of Discrete Surfaces as Smooth Interpolants 236
F.3 Discretization of the Beltrami holopmorphic flow 239
F.4 Evaluation and minimization of the optimal growth energy 243

Bibliography 245

Chapter 1

Introduction

What does it take to build a body? In plants and animals, the adult organism develops from a single cell, called a zygote. This cell divides repeatedly, its progeny growing exponentially in number, until the embryo eventually adopts a nontrivial multicellular configuration. Initially identical cells differentiate through cascades of cell fate decisions and associate preferentially to form specialized tissue architectures. These tissues stretch, fold, bend, and twist into the complicated and specific shapes of organs and appendages. Order and structure emerge across scales, from the cellular to the organismal, until a final synthesis of morphology and patterning is achieved that ensures the biomechanical functionality of the adult body parts. All the while, from before the first division and continuing after the assembly of the complete adult body, each and every element of this process is informed by spatio-temporal patterns of gene expression. *Morphogenesis*, the collective set of mechanisms by which discrete genetic information is transduced into the 3D form of tissues, organs, and organisms via the coordinated behavior of cells, is arguably the most monumental task of self-assembly in nature. Building a quantitative and predictive understanding of morphogenesis continues to be a fundamental endeavor in the life sciences.

Naively, one might expect that all of the necessary ingredients for morphogenesis are conveniently stored in the genetic code. In fact, this idea has dominated the field of developmental biology since the mid 20th century. At least as far back as the re-discovery of Mendelian inheritance in 1900, it was widely understood that discrete parcels of heredity could segregate during reproduction and be associated with particular phenotypes according to simple statistical laws [268, 52]. Around this time, Boveri and Morgan first promulgated the notion that continuously varying properties or substances that form 'gradients' may dictate the spatial coordination of cell fates in embryos [136, 86]. Advances in biochemistry during the 1920s and 1930s encouraged increasingly concrete thinking about the nature of these molecules and their mechanism of action in pattern formation [90].

The notion of 'chemical embryology' [170] was finally given a firm mathematical foundation by Alan Turing, in his landmark 1952 paper entitled *The Chemical Basis of Morphogenesis* [250]. Setting aside considerations of 'mechanical morphogenesis', i.e. the movement and shape change of cells and tissues, Turing postulated that patterns may spontaneously arise in the embryo as a result of simple chemical reactions among diffusing molecules, called *morphogens*. In Turing's model, and its conceptual descendants, fast-diffusing, long-range inhibitors couple to and react with slow-diffusing, short-range activators to spontaneously generate tunable, spatially periodic concentration landscapes from an initially homogeneous state[250, 84]. These morphogens could then instruct the spatial coordination of cell fate based on their concentration profiles. In the late 1960s and early 1970s, Lewis Wolpert introduced the idea of positional information to explain a complementary problem. Rather than asking how patterns can arise from nothing, Wolpert sought to understand how increasingly complex patterns could be built from prior asymmetries in the tissue [266, 267]. By introducing an 'interpretation' step, Wolpert showed how smooth monotonic morphogen concentration gradients can gener-

ate arbitrary patterns, including not only the periodic spots and stripes typical of Turing patterns, but also non-period arrangements like the sequence of red, white, and blue in the French flag.

There was now a solid theoretical basis for viewing morphogenesis as the result of chemical patterning, but the precise nature of these theoretical morphogens and their connection to heredity remained ambiguous. A major breakthrough came less than a year after the publication of *The Chemical Basis of Morphogenesis*, when Watson and Crick discovered the molecular structure of DNA [258]. This discovery was followed by a flurry of work over the next decade elucidating the central dogma of molecular biology, which details how sequential information in the genetic code is transferred residue-by-residue into the structure of proteins [56]. The first bona fide morphogens were identified in the late 1970s, when Christiane Nüsslein-Volhard and Eric Wieschaus performed large-scale mutagenesis screenings for the genes required during early development in *Drosophila* [179]. For example, Nüsslein-Volhard and Wieschaus discerned that gradients in the concentration of the diffusible transcription factor *bicoid*, which is maternally deposited at the anterior pole of the embryo, provided the necessary positional information to distinguish the head of the animal from its tail [178]. This initial anterior-posterior symmetry breaking lies upstream of cascade of pattering genes that subdivide the embryo into discrete regions which each undergo bespoke morphogenetic programs that generate specific domains of the body [268].

The synthesis of these many theoretical and experimental breakthroughs yielded a tidy picture of how genes might instruct morphogenesis. Genetic codes are unpacked according to specific expression patterns into concentration landscapes of morphogens (nucleic acids, proteins, etc.). Multiple species of morphogens may react with each other to generate patterns *de novo* from initially homogeneous states (à la Turing) or simple asymmetries may build upon each other to generate progressively more complex patterns

(à la Wolpert). These morphogens then orchestrate embryonic development through concentration dependent induction of cell fate. Heavily influenced by the success of this synthesis, developmental biologists set about producing prodigious lists of molecules and documenting their corresponding regulation of specific embryonic phenotypes [13].

Simple narratives, however, rarely tell the whole story. The techniques used to probe the genetic orchestration of morphogenesis were essentially discrete in nature. Experimenters could either disable the effects of a particular gene, for instance, through the use of genetic knockout mutants, or, alternatively, induce that gene's ectopic expression. The primarily qualitative results of such investigations were sufficient to describe dramatic phenotypes, such as, in the case of *Drosophila*, the loss of entire body segments [261] or the growth of legs where antennae normally should be [218]. Constructing descriptions of more subtle phenotypes proved to be challenging. The most glaring gap, however, was that subsequent molecular characterization in *Drosophila* and other systems revealed that patterning genes do not, in general, directly control cell and tissue shape [86]. Despite the fruitful investigations into how patterning genes dictate long-range tissue patterning and coordinate cell fate, it remains unclear how these patterns actually sculpt tissues into the complex shapes produced during morphogenesis.

In this context, physics offers a natural route toward resolving these gaps in our understanding. Cells and tissues can only move and rearrange when they are subject to a net force. Surely then, an accounting for the forces that shape living systems can help to build a more complete description of morphogenesis. Contextualizing morphogenesis as resulting from the spatio-temporal coordination of mechanical forces across scales is not a new school of thought. In the late 19th and early 20th century, embryologists of the *Entwicklungsmechnik* (developmental mechanics) movement sought to understand morphogenesis as the result of physical forces produced by cells [86, 122]. These included the forced generated by oriented cell division, cell growth, directed cell crawling, and

cell shape change [101]. Seminal contributions from Holtfreter, Steinberg, and others elucidated this viewpoint by analyzing how selective cell affinities and integrated cell motile behaviors coordinate to drive morphogenesis [122].

Perhaps the most enduring early contribution to this school of thought was given by D'Arcy Wentworth Thompson in his monumental opus *On Growth and Form* (1917) [246]. Applying mathematical principles to a broad range of examples, Thompson's book establishes a compelling and exhaustive case that morphogenesis is the result of physical processes and mechanical forces. Thompson achieved a variety of fresh insights, including the notion that diverse biological shapes could be related through simple deformations of a coordinate system. At the scale of the entire organism, shape and form could be understood as resulting from a spatio-temporal field of growth rates and directions. As summarized by Thompson, "It is obvious that the form of an organism is determined by its rate of growth in various directions; hence rate of growth needs to be studied as a preliminary to the theoretical study of form".

In recent years, new experimental techniques and computational methodologies have revolutionized our ability to probe and monitor morphogenesis [224]. High-resolution 3D time-lapse imaging [88], precise genetic manipulations [97], optogenetics [63], and a slew of other techniques have provided unprecedented insight into developmental dynamics, from the scale of individual molecules within cells to individual cells to the collective behavior of cells in tissues. The result has been a rich and beautiful synthesis of the chemical and mechanical viewpoints of morphogenesis. Morphogen expression patterns and force generating motor protein distributions actively depend on dynamical stresses and tissue geometry [177, 236, 142]. In some situations, mechanical interactions can organize tissues prior to the expression of associated genes [184] or generate complex long-range patterning over length and time scales that are inaccessible by the diffusion of molecular morphogens [208, 37].

From Thompson through to the present day, interpretations of the dynamics of in-vivo development have been primarily qualitative in nature [180, 60]. Moreover, what progress has been made towards codifying quantifications of morphogenesis has largely been constrained to piecemeal descriptions of distinct developmental processes. The recent explosion of live-imaging data and the advent of powerful computational techniques have positioned the field at an exciting precipice. Now, more than ever, is the opportune time to synthesize quantitative descriptions of mechanistic behaviors of cells and tissues and relate them to biochemical patterning, thereby initiating a transition to a predictive understanding of developmental biology.

This dissertation presents a body of work comprised of disparate projects, all of which are are connected by the following goal: to construct quantitative, predictive models of morphogenesis and to extract, to whatever extent is possible, the unifying principles underlying development. If the reader makes it all the way to the end, they should not be surprised to find that this goal is far from having been achieved. Accomplishing this task will take the collective effort of a diverse community of scientists, including physicists, biologists, mathematicians, computer scientists, and engineers, combining their skill sets and expertise to generate novel insights and discoveries in the coming years. I would like to think, however, that the work contained herein is at least a step in the right direction.

Since this dissertation is essentially an anthology, the goal of each chapter is to tell an interesting and self-contained story. A great amount of work and care was invested to ensure that the statements and conclusions in each project are based on rigorous and honest analysis. Including these substantiating details and methods in the main text would render each chapter virtually unreadable, but I feel that the text would be incomplete if I were to omit them entirely. Instead, they have been compiled into the unusually long appendices at the end of the dissertation. As a theoretically minded physicist working on problems in biology, I have found that a great deal of hard work

usually gets consigned to the supplementary text. It is somewhat fitting, therefore, that my dissertation is no exception.

The projects presented in this dissertation focus specifically on the morphogenesis of thin sheets of cells. In the next section, I clarify the important role these tissue architectures play in development. Next, I briefly review a set of relevant experimental and computational technologies used to extract the dynamics of development in living systems. The following sections contain a discussion of the ways in which complex morphogenetic programs are modularized into simpler, local processes thanks to the construction of segmented body plans and a framework for quantifying geometric order in certain relevant body plan architectures. After that, I examine how coarse-grained modeling can offer important insights by framing descriptions of morphogenesis in terms of a small set of crucial dynamical variables and parameters. Finally, I discuss the prospect of unearthing unifying principles constraining growth pattern selection.

1.1 Growth and shape change in thin tissues

Epithelial tissues are the primary building blocks of multicellular systems [86, 92]. They are composed of cohesive sheets of cells joined together by cell-cell contacts such as adherens junctions [89]. This direct coupling enables the output of intracellular machines to be coordinated across muitlple cells and facilitates the emergence of tissue-scale organization. Another important feature of epithlia is the presence of apicobasal polarity. This polarity, maintained by polarity protein complexes, distinguish the apical and basolateral surfaces of the cell, allowing them to adopt distinct behaviors during development [86]. In the early embryo, epithelia are typically organized into monolayers, but can form multi-layered arrangements, such as the skin. During morphogenesis, these sheets of cells undergo dramatic changes in shape in order to support the structure of embryos

and organs and also to serve as effective barriers against pathogens [92].

The adhesive contacts linking epithelial cells to each other are mainly supported by E-cadherin molecules. E-cadherin forms complexes that connect the cytoskeletal elements of neighboring cells via molecules such as β-catenin, α-catenin, and vinculin.[89, 271]. Additional adhesive complexes, primarily integrins, also couple epithelial cells to the extracellular matrix (ECM). The ECM is a rigid network of secreted proteins that provides support and structure to the embedded cells [79]. This zoo of adhesive interactions joins epithelial cells and their external environment into a unified trans-cellular mechanical network that integrates and coordinates forces throughout the tissue [101]. Cellular force generation is typically mediated by the activity of motor proteins, such as myosin, that interact with cytoskeletal structures, such as actin fibers (F-actin), to change their organization [106, 211]. These changes are then transmitted to neighboring cells and the extracellular environment through cell-cell and cell-matrix contacts, respectively. The global mechanical network can also transmit tissue wide forces originating from extrinsic sources in the extracellular environment [64]. The structure of this mechanical network at the cell and molecular scales is illustrated in Figure 1.1.

Changes in tissue shape and geometry resulting from cellular behavior can generically be decomposed into contributions from a small set of cell scale motifs [74, 93]. In particular, cells can change their size [174], change their shape [199, 165], or rearrange in a way that modifies the topological connectivity of the tissue [169, 36]. The elemental topological rearrangements are local neighbor exchanges (T1 transitions), cell death/delamination (T2 transitions), and cell divisions (T3 transitions). These various cell scale motifs are illustrated in Figure 1.2. Epithelial folding frequently involves polarized cell shape change that transforms columnar cells into a wedge-like or bottle shape [192]. The shrinking or expanding of one side of the tissue relative to the other generates curvature. This type of shape change is typically due either to polarized constriction

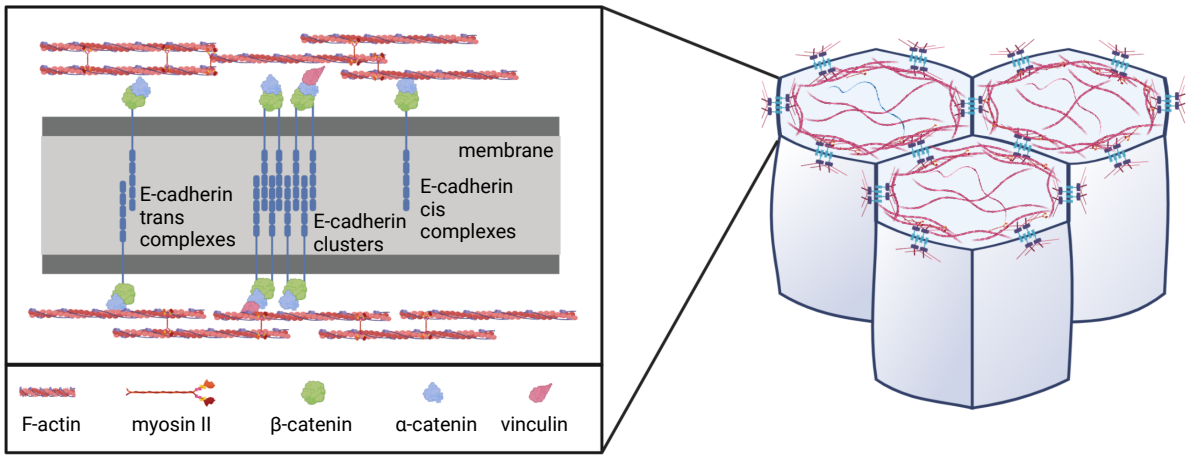

Figure 1.1: **Structure of epithelial junctions during tissue stretching and remodeling**. In epithelial tissues, adhesive contacts and the actomyosin network are organized in belt-like structures around the apical cortex of the cell. The arrangement of the epithelial cells is determined by competition between actomyosin contractility and cell-cell adhesion. Inset shows a close up of the structure of a single epithelial junction between two neighboring cells. E-cadherin forms cis and trans clusters stabilized by interaction between the extracellular domains and the actin filaments (F-actin) comprising the cytoskeletial structure of the cell. Contacts are constructed via β-catenin, α-catenin, and vinculin. Myosin II utilizes ATP to actively contract the network by sliding filaments relative to each other.

[216], which can occur on either side of the epithelium, or to to the relaxation and expansion of one of the tissue surfaces [216, 238]. The lateral sides and height of cells in epithelia can also play a crucial role in tissue shape changes. For instance, the stereotypic dorsal folds appearing during *Drosophila* gastrulation are initiated by the dramatic shortening of cells within the fold, leading to an apical indentation within the tissue [257]. Interestingly, the same mechanism of cell shortening can also cause highly curved tissues to flatten out and extend, as seen during the eversion of the *Drosophila* leg during limb morphogenesis [67].

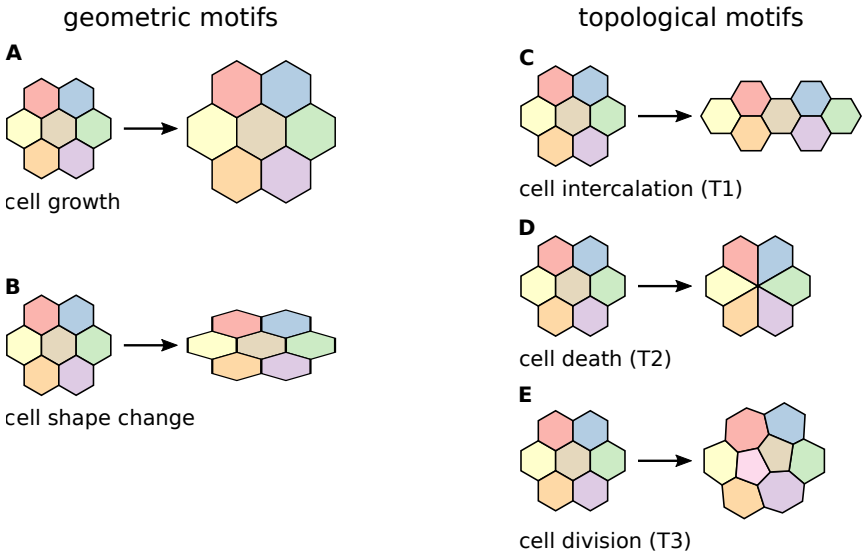

Figure 1.2: **Cell-scale motifs underlying tissue-scale morphogenesis**. (A to B) Geometric motifs do not change cell connectivity. (A) Cell growth. (B) Area-preserving cell shape change. (C to D) Topological motifs change cell connectivity. (C) Cell neighbor exchange. (D) Cell death or delamination. (E) Cell division.

Since cells in epithelia are mechanically coupled, the forces generated both by these autonomous cell-scale motifs and from external sources can be propagated across the tissue to determine how it folds. The pressure and movement of many cells towards high density regions can promote bending [64]. In some scenarios, folds can be shaped and oriented through tension generated by anisotropic supracellular actomyosin networks that stiffen the tissue preferentially along a particular axis [43]. The constriction of actomyosin

cables or the differential motility of cells crawling along the ECM may lead to apicobasally polarized pressures and tensions that initiate tissue buckling [64]. Folds can also be shaped by forces normal to the plane of the epithelium, such as differential fluid pressure on either side of the tissue [135]. Tissues may also change their configuration without any remodeling of cell shape at all. Differential growth due to oriented cell division may change the intrinsic geometry of the tissue in such a way that induces curvature. For example, differential growth was demonstrated to be crucial for generating a precise pattern of fold in the *Drosophila* wing [247].

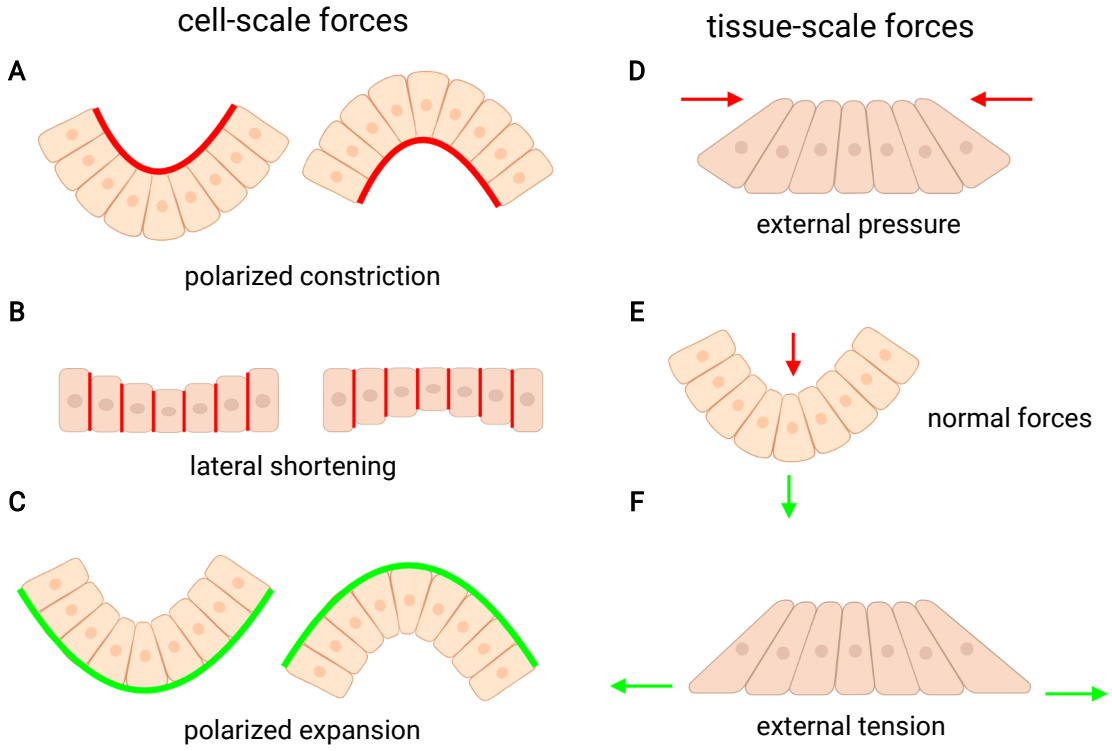

Figure 1.3: **Force generating mechanisms underlying epithelial folding.**. (A to C) Cell-autonomous forces leading to tissue folding. (A) Polarized constriction. (B) Lateral shortening. (C) Polarized expansion. (D to F) Tissue-scale forces leading to tissue folding. (D) External pressure. (E) External force normal to the plane. (F) External tension. Figure inspired by the presentation in [64].

While epithelia may be the main building block of multi-cellular systems, they are not the only way that cells organize themselves into thin sheets. The other principal architec-

ture of cells during embryonic development is the mesenchyme. In contrast to epithelia, mesenchymal cells exhibit only limited adhesion to their neighbors and therefore form a loose aggregate of cells capable of rapid migration along the ECM. Cell migration is one of the key drivers of morphogenesis and the process through which epithelia adopt mesenchymal properties, termed an epithelial mesenchymal transition, has been extensively studied [244]. Muscle tissue may also be organized into thin sheets during organogenesis, such as during the development of the beating structure of the heart [228]. These disparate types of cellular sheet architectures may also combine to form more complex multi-layered structures. As we will discuss in Chapter 4, the complicated pattern of folds in the *Drosophila* midgut is controlled by the mechanical interaction between an epithelial layer and two ensheathing layers of orthogonally oriented muscle fibers [165].

Determining how biochemical signalling couples to cell-scale and tissue-wide forces to sculpt thin tissues is a crucial step towards improving our understanding of morphogenesis. Despite the wealth of live-imaging data and previous research on the topic, there remains a dearth of quantitative modeling that synthesizes the many behaviors governing shape change. Towards this goal, this dissertation presents multiple projects wherein geometry and mechanics are exploited to generate testable predictions for the developmental dynamics of thin tissues.

1.2 Quantiative methods for the live-imaging and analysis of epithelial morphogenesis

Extracting quantitative measurements of developmental dynamics in-vivo presents a considerable experimental challenge. In this section, we briefly review the cutting-edge microscopy methods driving the current revolution in the live-imaging of morphogenesis.

We also discuss the computational techniques scientists employ to analyze and interpret the immense quantities of data produced by these microscopy platforms. We first note that the recent explosion of quantitative data has been spurred by the creation of genetically encoded fluorescence markers such as the green fluorescent protein (GFP) [249] and its derivatives. Upon transgenic implantation in to a targeted gene, these markers enable researchers to optically measure the expressed concentration of particular proteins within live cells using a fluorescent microscope [40]. This technology, in addition to non-genetic fluorescent labels, allows for the dynamic mapping of gene expression patterns and also the identification and tracking of particular organs, organelles, and macrocmolecules.

The traditional method for obtaining 3D data sets in biology is through the use of a confocal microscope [190]. Confocal microscopes can provide excellent optical sectioning and produce high resolution images of fluorescent samples. By construction, however, confocal systems rely on scanning and are therefore limited in the number of optical slices they can produce per second (generally $\sim 10 - 100$ Hz) [88]. As a result, volumetric imaging can be relatively slow, possibly missing rapid dynamic effects. Additionally, the excitation light produced by a confocal microscope illuminates not only the volume of interest, but also a cone of the sample above and below the focal volume. These factors increase the risk of phototoxic events and photobleaching of the fluorophore.

Light-sheet fluorescence microscopy (LSFM) is an exciting alternative that addresses many of the shortcomings of confocal microscopy [235, 204, 88]. The basic concept behind LSFM is that a sheet of light is produced by an excitation arm that illuminates a single plane of the sample. A second detection arm, oriented at 90 to the excitation arm, then collects the emitted light from the entire optical section. Generally, the sample is then moved through the light sheet to collect the next optical plane. This construction means that only the fluorophores in a thin cuboid centered on the illumination plane are excited, greatly decreasing the risk of photobleaching and phototoxic events. Samples

may be exposed to up to 5000 times less energy than from a confocal microscope when recording stacks of similar quality, greatly increasing the viability of the sample [235]. LSFM also offers drastic improvements in imaging speed, allowing one to record millions of pixels in parallel. Further customization of LSFM platforms, such as the multiview selective-plane illumination microscopy (MuVi-SPIM) [127], allow for rapid imaging of large fluorescent specimens from multiple directions over biologically relevant timescales. The views of the sample collected from multiple angles can then be computationally fused in to a common frame [195], producing high quality, in toto recordings of developmental dynamics. An schematic of the light-sheet microscopy set up used in Chapter 4 is shown in Fig. 1.4.

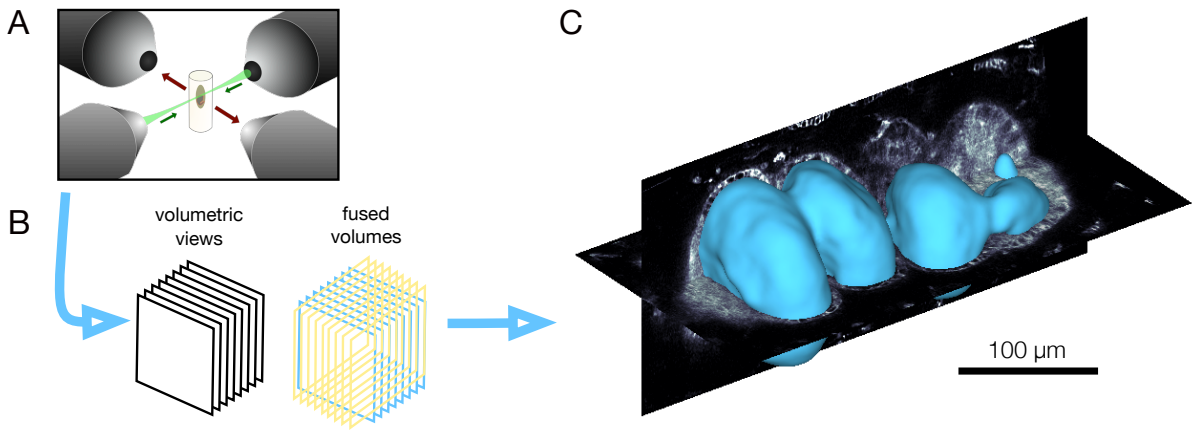

Figure 1.4: **Multi-view light sheet microscopy enables volumetric imaging.** (*A*) We illuminate embryos embedded in an agarose column via a laser beam emerging from two illumination objectives (green). The laser sweeps along the long axis of the column to raster a sheet of light. Two detection objectives capture fluorescence in the orthogonal axis (red arrows). (*B*) By translating, rotating, and repeating, we build volumetric views from a series of angles. (*C*) Through fusion and deconvolution, multiple volumetric views build data volumes with nearly isotropic resolution for analysis.

No matter which fluorescence microscopy platform is employed, the output is strucuturally identical: a time series of voxelized sample volumes, with an associated intensity for each voxel corresponding to the number of channels used during the recording. These

data sets can be massive. A SPIM platform equipped with an sCMOS camera can record as much as 90 Tb in a 24 hour period [204]. Storing, processing, and transferring data sets of this size can be challenging. Recordings of thin sheets pose additional conceptual challenges. In such samples, the surface of interest occupies only a small fraction of the sample volume. Even when it is computationally feasible to process such data in 3D, interpreting the results via orthographic projects or cross-sections can be difficult.

Tissue cartography is a computational technique developed to address these challenges in the investigation of 4D recordings of shape-shifting sheets [217, 99, 102, 164]. In this approach, curved tissue surfaces are extracted from data volumes and endowed with a planar representation that preserves the integrity of the geometric properties of the surface. This process reduces the data from 3D to 2D, greatly decreasing the computational complexity of common analysis steps such as cell segmentation and cell tracking. A typical tissue cartography pipeline begins with the detection of the surface of interest. This can be accomplished, for instance, through the use of derivative-based edge detection methods [187] or level-set segmentation methods [168]. Next, the detected surface is endowed with an atlas of coordinate charts. For simple surfaces, like the fly embryo, it is generally sufficient to approximate the true shape of the tissue with an idealized surface, like a cylinder [99]. Arbitrarily complicated surfaces can be fit with more flexible discrete approximations, such as a mesh triangulation, through a surface reconstruction step [164]. Typically, the surface is then partitioned into disk-like patches, each of which is computationally mapped into the plane. Properly constructing and maintaining this correspondence between the 3D surface and its 2D representations enables the accurate measurement of quantities such as size, shape, direction, and velocity without suffering from geometric distortion.

Tissue cartography has facilitated insights in a wide variety of biological systems [99, 236, 46, 164]. In some form or another, the tissue cartography approach is utilized

in every chapter of this dissertation. Despite having fuelled so many tremendous results, existing packages for tissue cartography suffer from several shortcomings. One major limitation is the difficulty constructing consistent global representations of topologically non-trivial surfaces, such as tubes. For instance, while it is possible, using the ImSAnE package [99], to generate representations of arbitrary surfaces, constructing planar parameterizations of topologically non-trivial surfaces requires chopping them up into separate disk-like patches. This means that analysis pipelines must be run separately for each patch and subsequently fused together, increasing complexity and decreasing the transparency of data visualization. Another caveat is the difficulty generating robust analysis of dynamical data in a consistent material frame. Understanding the dynamic mechanisms by which the thin tissues change shape requires not only capturing instantaneous motion in 3D, but following the material as it deforms. In Chapter 2, we present a TubULAR, a tissue cartography suite extending the functionality of the ImSAnE package, to efficiently construct robust parameterizations of tube-like surfaces and generate dynamical parameterizations that follow material parcels of the surface as it grows and deforms.

1.3 Segmentation and the developmental body plan

Whenever confronted with a daunting task, it always helps to have a plan. A common feature of animal development conserved in a broad variety of creatures is the presence of a *segmented* body plan. Simply put, segmentation is the organization of the body into a series of repeated units arranged along the anterior-posterior axis of the organism. The construction of segements modularizes development and enables complicated body plans to be built through bespoke, local morphogenetic programs. While serial morphological repitition is widespread in the animal kingdom [163], discussion of segmented body

plans is typically limited to three phyla: Annelida, Arthopoda, and Chordata [44]. In arthropods and chordates in particular, segmentation plays the important role of helping to organize and orient external limbs and appendages in a manner than ensures proper biomechanical functionality.

Despite serving a convergent organizing role, the methods through which different types of organisms construct their segments vary wildly. Perhaps the most celebrated example of segmentation is found in *Drosophila*. As previously mentioned, the diffusible transcription factor *bicoid* is maternally deposited at the anterior pole of the embryo and provides the positional information for patterning the anterior-posterior axis. The gradient of *bicoid* is sequentially processed by a through a hierarchy of genes, beginning with the so-called 'gap genes', such as *hunchback* [268]. Broad expression of these gap genes is refined into the sharp expression of 14 segment forming 'pair-rule' genes that further subdivide into 'segment polarity' genes. Adult appendages such as wings, halteres, and legs can be associated to the segments that are created during this process. Misexpression of any gene in this hierarchy will lead to the loss of the corresponding segments in the larvae. For instance, the deletion of *even-skipped* will lead to the loss of every other larval denticle band [179].

Another important example of segmentation is the process of somitogenesis in vertebrates, which has been studied extensively in a wide variety of systems including zebrafish, chickens, and mice [268]. Somites are epithelial structures that contain precursors of vertebrae, ribs, and skeletal muscles [17]. Somites are formed from a pool of tissue at the posterior pole of the embryo called the presomitic mesoderm (PSM). New somites pinch off from the anterior tip of the PSM in pairs, on either side of the neural tube, rythmically so that the segmented body structure is formed sequentially in an anterior-to-posterior fashion. The delineation of somites is determined by the displacement of an oscillator at the posterior end of the animal, which has been described theoretically in the 'clock and

wavefront' model [51]. A wavefront, defined by morphogen gradients produced by a pulsing source at the extending tip of the tail, freeze oscillating genetic expression patterns of cells in the PSM [181]. In this way, the clock and wavefrom mechanism translates the temporal information of the genetic oscillations into a fixed periodic pattern in space.

In Chapter 3, we employ cutting edge experimental methods and theoretical modeling to describe the formation of the segmented body plan of the crustacean *Parhyale hawaiensis*. *Parhyale* presents a unique solution to the problem of tissue organization. In contrast to *Drosophila*, the pattering process in *Parhyale* does not appear to require complicated biochemical cascades. Additionally, unlike the segments of the *Drosophila* and vertebrate body plans, which consist of thousands of disordered cells, the organization of the segmented body plan in *Parhyale* is evident all the way down to the cellular scale. Cells in the *Parhyale* germband arrange themselves into a rectangular grid, constituting a pattern akin to a coordinate system spanning the entire embryo. This cellular grid subsequently acts as a template for the patterning of limbs on the adult body [263]. The biological organization of *Parhyale* is therefore best described using the physical and geometric concept of *order*.

1.4 Orientational order and tissue organization

One of the most fundamental challenges of condensed matter physics, i.e. the physics of everyday length and energy scales, is to understand and characterize the various possible phases of matter. Distinct phases of matter are typically identified by the presence or absence of particular symmetries [132]. Order, in this context, refers to a broken symmetry. For example, a translationally ordered system is one in which translational invariance has been broken. Symmetry broken phases can be quantitatively distinguished from symmetry preserving phases using an 'order parameter', an idea originally intro-

duced by Landau [131]. Landau subsequently exploited this framework to develop powerful effective field theories capable of describing phases and phase transitions in terms of a small number of phenomenological parameters. Since the inception of this formalism and Landau's groundbreaking application to the theory of superconductivity [87], it has since been generalized to describe an incredibly broad variety of physical phenomena, including ferromagnetism, superfluidity, liquid crystals, and gauge theories in high-energy physics [222, 61, 50].

Defects in ordered media have been shown to play an essential role in many aspects of condensed matter physics. Vacancies and interstitials mediate particle diffusion in solids, dislocations determine the strength of crystalline materials, and vortex motion controls the resistance of superconductors [173]. Mathematically, defects are identified as singularities in the order parameter field mediating topologically non-trivial configurations [159]. An exciting result of investigations into defect mediated phase transitions, was the discovery of orientationally ordered phases [173]. Orientationally ordered phases are intermediate between the rigid order of a crystalline solid. Orientationally ordered phases, in particular the sixfold ordered 'hexatic' phase, were predicted theoretically in the celebrated Kosterlitz-Thouless-Halperin-Nelson-Young (KTHNY) model of two-dimensional melting [126, 94, 273]. They have since been observed in multiple non-living systems, including magnetic bubble lattices [221], colloidal crystals [167], and liquid crystal films [45]. More recently, it has also been observed in the living systems in the late stages of development in the absence of cell proliferation, for instance in zebrafish retina [210] and the organization of hair cells in the mammalian ear [49].

Briefly, crystalline solids are distinguished from liquids by two separate broken symmetries. The regular rows of atoms in a crystal reflect a breakdown in the translational invariance characteristic of a liquid. In a 2D crystal at finite temperature, the translational correlations $G_{\mathcal{T}}(\mathbf{r}) = \langle \hat{\rho}_G(\mathbf{r})\, \hat{\rho}_G(\mathbf{0}) \rangle$, where $\hat{\rho}_G(\mathbf{r})$ is the number density of a crystal

at a reciprocal lattice vector $\mathbf{G}$, will decay algebraically to zero, i.e. $G_{\mathcal{T}}(r) \sim r^{-\eta(T)}$ for some materially and temperature dependent exponent $\eta(T)$. In contrast, the *directions* of the crystallographic axes represent a different, broken orientational symmetry. The n-fold orientational order at a lattice site $\mathbf{r}_j$ is characterized by a complex order parameter $\psi_n(\mathbf{r}_j)$ defined in terms of the 'bonds' between neighboring sites

$$\psi_n(\mathbf{r}_j) = \frac{1}{N} \sum_{k \in \mathcal{N}(j)} e^{n\, i\, \theta_{kj}}, \tag{1.1}$$

where n is an integer ($n = 6$ for a hexatic phase and $n = 4$ for a fourfold ordered tetratic phase), N is the number of sites contained in the neighborhood of $\mathcal{N}(j)$ of site $\mathbf{r}_j$, and θ_{kj} denotes the angle of the bond between sites $\mathbf{r}_j$ and $\mathbf{r}_k$ relative to a fixed axis. The connectivity of the medium may be inferred, for instance, through the use of a Voronoi construction. The construction of the n-fold orientational order parameter is illustrated in Figure 1.5. The presence of a broken translational symmetry implies the existence of long-range orientational order. In such a situation, one would expect that the orientational correlations, defined as $G_n(\mathbf{r}) = \langle \psi_n(\mathbf{r})\, \psi_n^*(\mathbf{0}) \rangle$, decay to a non-zero constant at long distances, i.e $\lim_{r\to\infty} G_n(r) = \text{constant} \neq 0$. In a fluid, both the translational and orientational correlations decay exponentially. In contrast, an orientationally ordered phase is characterized by short-range translational correlations, $G_{\mathcal{T}} \sim e^{-r/\xi(T)}$, but spatially extended orientational correlations, $G_n(r) \sim r^{-\eta_n(T)}$.

As previously mentioned, the transition between these states is mediated by the dynamics of defects. A crystalline lattice transitions into an orientationally ordered phase in the presence of freely roaming dislocations [173]. These gas of dislocations destroys translational order, but preserves orientation order [54]. As the medium becomes increasingly agitated, dislocations can unbind into disclinations, which completely destroy the orientational order and facilitate the transition into a fluid state. In Chapter 3,

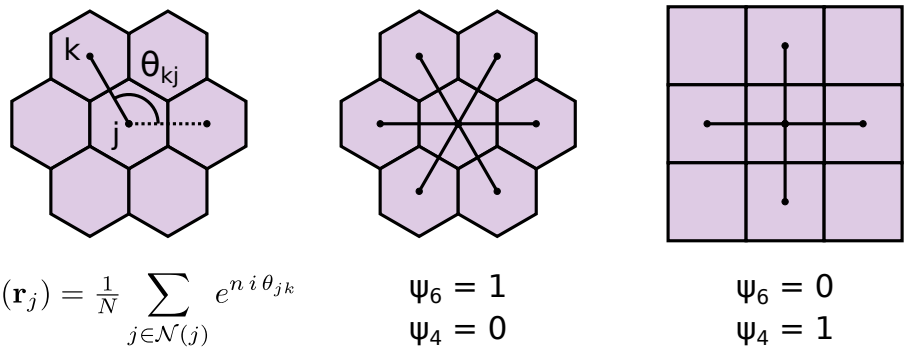

Figure 1.5: **Orientational order parameter.** A graphical illustration of the n-fold orientational order parameter. Middle image shows a perfectly ordered sixfold lattice. Right image shows a perfectly ordered fourfold lattice.

we demonstrate the the segmented structure of the developing *Parhyale* germband is, in fact, a fourfold orientationally ordered phase. This constitutes an exciting example of how physical principles such as order and symmetry can help us understand how morphogenetic programs organize developing embryos.

1.5 Bridging cell scale behaviors and tissue scale morphogenesis

Morphogenesis proceeds through the coordination of biological and physical mechanisms across every relevant scale in the embryo, from the molecular to the cellular to the organismal. Shape change at the tissue scale results, in a proximal sense, from the collective mechanics of thousands of interacting cells. Each of the many cellular processes mediating these behavior are in turn controled by gene regulatory networks, which frequently consist of numerous elements and interactions of dizzying complexity [144]. At present, constructing a comprehensive, predictive understanding of morphogenesis *ab initio* from the regulatory function of genes is impossible. Similar to the way in which high-energy physics has become effectively decoupled from physics at ångström unit scales

[173], the most promising path to answering the "fundamental" questions surrounding development almost certainly not a naively reductionist approach. Instead, coarse grained theories, which seek to describe morphogenesis using a limited set of releveant physical or mechanical parameters, offer a a promising route towards the construction of a predictive developmenal biology.

Continuum mechanics is an effective method for capturing how force balance is associated with local deformation and flow [133]. In the simplest models, the forcing that generates flow can be neatly decomposed into a set of separate passive and active contributions. The tendency of cells to resist deformation and the viscous coupling between cells translate local forces into long range flows. Interactions among these various contributions, both locally and over large scales, can be then be built up with increasing degrees of complexity to create more accurate descriptions of biological realities. This framework has proved effective in numerous biological applications elucidating how active forces generate non-trivial flow fields [74, 236, 208].

In the continuum approach, a thin tissue is represented by a continuous curved surface $S \subset \mathbb{R}^3$. We assign to each material parcel in the tissue a set of curvilinear coordinates $\vec{\mathbf{x}} = (x^1, x^2) \in \mathcal{B}$ defined over a planar domain of parameterization $\mathcal{B} \subset \mathbb{R}^2$. We define the embedding of the surface by a map $\vec{\mathbf{R}} : \mathcal{B} \to \mathbb{R}^3$. Each point $\vec{\mathbf{R}}(x^1, x^2)$ on the surface is characterized by its tangent vectors $\vec{\mathbf{e}}_1 = \partial\vec{\mathbf{R}}/\partial x^1$, $\vec{\mathbf{e}}_2 = \partial\vec{\mathbf{R}}/\partial x^2$ and its unit normal vector $\hat{\mathbf{n}} = \vec{\mathbf{e}}_1 \times \vec{\mathbf{e}}_2/||\vec{\mathbf{e}}_1 \times \vec{\mathbf{e}}_2||$. In what follows, Greek indices vary in the set $\{1, 2\}$. The covariant geometry of the surface is captured by two objects. The first fundamental form or induced metric tensor

$$g_{\alpha\beta} = \frac{\partial\vec{\mathbf{R}}}{\partial x^\alpha} \cdot \frac{\partial\vec{\mathbf{R}}}{\partial x^\beta} \tag{1.2}$$

quantifies lengths and angles between points on the surface. The inverse metric tensor $g^{\alpha\beta}$ is defined by $g^{\alpha\sigma}g_{\sigma\beta} = \delta^\alpha_\beta$, so that indices of tensorial quantities are raised and lowered

with respect to the first fundamental form. The second fundamental form

$$b_{\alpha\beta} = \hat{\mathbf{n}} \cdot \frac{\partial^2 \vec{\mathbf{R}}}{\partial x^\alpha \partial x^\beta} = -\frac{\partial \vec{\mathbf{R}}}{\partial x^\alpha} \cdot \frac{\partial \hat{\mathbf{n}}}{\partial x^\beta} \tag{1.3}$$

characterizes the intrinsic and extrinsic curvature of the surface via the change in the surface unit normal vector. In particular, the mean and Gaussian curvatures of the surface are given by

$$H = (g^{\alpha\beta} b_{\alpha\beta})/2, \qquad K = \det\left[g^{\alpha\sigma} b_{\sigma\beta}\right], \tag{1.4}$$

respectively. If we take the coordinates (x^1, x^2) to constitute a time independent, Lagrangian parameterization, the changing shape of the surface is simply captured in the time dependence of the embedding $\vec{\mathbf{R}}(t)$.

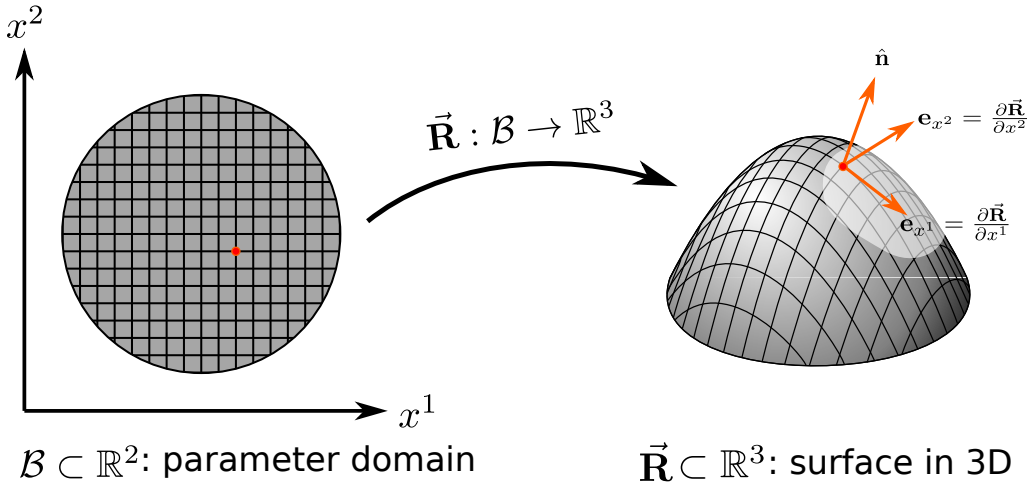

Figure 1.6: **Surface geometry.** The surface $\mathcal{S}$ is defined as an embedding $\vec{\mathbf{R}}$ of an arbitrary region of the plane $\mathcal{B} \subset \mathbb{R}^2$ into $\mathbb{R}^3$.

The geometry of the system is coupled to its mechanics through the choice of a constitutive relation. It is well known that tissues can adopt both elastic and fluidlike behaviors, depending on the situation and the relevant timescales. In general, at short

time scales, tissues behave elastically [75, 220]. Incremental increases in strain, defined relative to some intrinsic geometry, generate corresponding increases in stress. Overtime, however, stresses created in this fashion can then be relaxed either locally, via internal rearrangement of the cytoskeletal cortex [120, 269], or at the tissue scale, via cell rearrangements [74]. The result is an exotic type of viscoelasticity, wherein the tissue responds elastically to active stresses over short timescales and then reverts to a fluidlike flow at longer timescales as the tissue adaptively relaxes stress. The choice of model therefore depends on the scenario under consideration. For instance, some models have been constructed that represent growing tissues purely as active fluids [212]. Such models frequently include phenomenological features, such as the inclusion of of an active nematic term to describe the influence of actomyosin contractility on the growth and regeneration of tentacles in *Hydra* [104].

Of particular relevance to this dissertation is the formalism of incompatible elasticity [71, 223]. An incompatible elastic shell is assumed to be governed by the following energy functional

$$E = \frac{h}{8} \int_{\mathcal{B}} d^2\vec{\mathbf{x}} \sqrt{\bar{g}} \left\{ \mathcal{A}^{\alpha\beta\gamma\delta} \left(g_{\alpha\beta} - \bar{g}_{\alpha\beta}\right) \left(g_{\gamma\delta} - \bar{g}_{\gamma\delta}\right) + \frac{h^2}{3} \mathcal{A}^{\alpha\beta\gamma\delta} \left(b_{\alpha\beta} - \bar{b}_{\alpha\beta}\right) \left(b_{\gamma\delta} - \bar{b}_{\gamma\delta}\right) \right\}, \tag{1.5}$$

where h is the thickness of the tissue,

$$\mathcal{A}^{\alpha\beta\gamma\delta} = \frac{Y}{1+\nu} \left(\frac{\nu}{1-\nu} \bar{g}^{\alpha\beta} \bar{g}^{\gamma\delta} + \bar{g}^{\alpha\gamma} \bar{g}^{\beta\delta} \right) \tag{1.6}$$

is the isotropic elastic tensor, Y is Young's modulus, ν is the Poisson ratio, and $\bar{g}$ and $\bar{b}$ are a pair of tensors specifying the instrisic target geometry of the system. The target geometry is presumed to be set by internal biological processes. Essentially, the system will adopt an equilibrium configuration that balances the comptition between the stretching

contribution and the bending contribution. Importantly, it is not assumed that $\bar{g}$ and $\bar{b}$ satisfy the Gauss-Codazzi-Mainardi-Peterson (GCMP) compatibility conditions [78]. If this is the case, then there is no attainable 3D configuration for which the energy vanishes identically and the equilibrium configuration will harbor residual stresses. Such residual stresses have been shown to exist in biological systems, for instance, in the Bauhinia plant, where they facilitate the dispersal of seeds from residually stressed pods [223]. When the timescale of growth in the system (i.e. rate of cell division, etc.) is long compared to the timescale of mechanical relaxation, the tissue will always effectively remain in mechanical equilibrium. In this quasistatic regime, active growth dynamics can be characterized by assigning a time dependence to the target geometry, $\bar{g}(t)$ and $\bar{b}(t)$, and determining the resulting equilibrium configurations as a function of time.

In some form or another, all of the chapters in this dissertation exploit coarse grained modeling and continuum approaches to extract novel insights from developing systems. In Chapter 2, discretizations of continuous surface geometries enable the construction of a suite of methods for analyzing complex tissue flow fields. In Chaptar 3, a simple 2D hydrodynamic model is employed to characterize the role that actively oriented cell divisions play in mediating the fourfold order of the *Parhyale* germband. In Chapter 4, nontrivial coupling between cell shape and curvature illuminate a novel mechanism for tissue folding. Finally, in Chapter 5, mathematical properties of continuous deformations are exploited to build a quantitative formalism to understand the problem of growth pattern selection.

1.6 Emergent simplicity and the search for principles in growth pattern selection

According to Albert Einstein, "A theory is the more impressive the greater the simplicity of its premises, the more different kinds of things it relates, and the more extended its area of applicability" (quoted in [28]). The beautiful and broadly applicable quantitiave theories of physics are possible because macroscale phenomena are often independent of microscopic details. Diffusive behvaior, such as the type observed in the formation of Turing patterns, is largely independent of the underlying random collision processes [222]. The Navier-Stokes equations provide an accurate description of fluid mechanics since macroscopic fluid motions do not depend in great detail on the shapes and interactions of the constituent molecules [130]. Elementary quantum mechanics relies on the fact that the behavior of elections, nuclei, and photons is is largely independent of the way in which the nucleus is assembled - non-relativistic quantum mechanics emerges from more complicated unified theories at low energies [209]. In the 1970s, renormalization group methods, exported from particle physics by Kenneth Wilson, revealed that the behavior of systems near critical-points is almost totally insensitve to the physics of matter at microscopic length scales [222, 173]. It is possible to make accurate quantitative predictions about certan universal critical exponents or scaling functions without precise knowledge of the microscopic physics. Instead, what matters is symmetry, conservation laws, the range of interactions, and the dimensionality of space. The task of building up theories of macroscopic phenomena from microscopic physics, the purview of kinetic theory, is worthwhile and has yielded many important results [117]. However, the immense success of these coarse-grained, effective theories suggest that, rather than trying to catalogue each minute aspect of a large and complex system, we should seek to find simple effective laws that emerge at each new level of complexity.

While this goal is beautiful and pleasing to the aesthetic preferences of a physicist, it is not clear a priori that such an enterprise can be accomplished in developmental biology. Are we doomed to be 'stamp collectors', constructing patchwork phenomenological theories of disparate developmental processes? Fortunately there is evidence to suggest otherwise. As we have already mentioned, coarse-grained theories of tissue mechanics have yielded exciting insights into a broad set of applications in morphogenesis. Develepmental processes, genetic regulatory complexes, stages of embryonic morphology, and even entire body plans are strongly conserved among species [207, 111]. There are also numerous cases of convergent evolution of organismal form, despite massively divergent evolutionary paths [231]. Taken together, these observations tenuously suggest that physical laws and common selective pressures constrain the types of growth patterns we can expect to find in developing systems.

Of particular relevance to this disseration is the problem of growth pattern selection. From a purely geometric perspective, thare exists an infinite famility of tissue scale growth patterns that can transform the same initial configurtation of cells into a specified target shape. Despite this degeneracy, all typical individauls of the same species follow virtually the same stereotypic growth trajectories to grow their organs and appendages. Understanding how these stereotypic growth patterns are selected will require a set of tools to simplify and navigate the enormous 'morpho-genetic' spaces [140] of potential shapes that living forms can assume and the evolutionary trajectories from which these shapes arise. Chapter 5 details both the construction of such a mathematical toolkit and a formalism for generating quantitative predictions for growth pattern selection.

1.7 Dissertation outline

This dissertation presents a series of projects investigating the morphogenesis of thin tissues. The subject matter is varied. We showcase results in multiple model organisms, including *Drosophila*, *Parhyale hawaiensis*, and zebrafish (*Danio rerio*). All projects contain a sythesis of experimental observation, data analysis through numerical methods, and theoretical modeling. While the topics covered may appear disparate, they are connected by the common goal of building a predictive machinery for understanding tissue growth and the principles underlying morphogenesis.

In Chapter 2, we present the Tube-like sUrface Lagragian Analysis Resource (TubULAR) software package. TubULAR combines cutting edge computational geometry and computer vision methods to provide a single, comprehensive tissue cartography package for the analysis of growth and deformation in tube-like surfaces. In addition to its topology handling, the major contribution of TubULAR is the ability to easily construct deformation maps that follow tissue parcels in the material frame of reference. TubULAR also contains a variety of analysis tools that enable users to decompose complex deformation maps into simple elementary contributions. We demonstrate the power of the TubULAR package by analyzing the growth of the midgut in the *Drosophila* embryo and the beating of the embryonic zebrafish heart.

In Chapter 3, we demonstrate how actively oriented cell divisions coordinate the organization of the ectodermal germband in the developing *Parhyale* embryo. Using *in toto* live-imaging and conformal tissue cartography, we show that tightly choreographed waves of oriented cell proliferation sweep across the embryo is such a way that the initially fluid germband flows towards a fourfold orientationally ordered state. The role of cell divisions in producing the tissue scale flow fields are elucidated through the use of an active hydrodynamic model. Finally, we implement simple vertex model simulations

to directly investigate the conditions underwhich oriented divisions constitute a robust ordering mechanism in living tissues far from thermal equilibrium.

In Chapter 4, we investigate the transformation of the D̂rosophila midgut from a simple tube into a complex, coiling configuration of folds and compartments. A combination of *in toto* light-sheet microscopy and computational techniques reveal that Hox genes control spatiotemporally patterned calcium pulses that trigger muscle contractions in the developing gut. These muscle contractions induce cell shape change in the the adjacent tissue, driving a convergent extension pattern. In-plane shape change is linked to out-of-plane organ folding by tissue incompressibility. Taken together, these results describe a novel mechanism for gene expression to generate shape change in visceral organs.

In Chapter 5, we use the mathematical formalism of quasiconformal maps [1] to build a machinery to describe arbitrary deformations of growing thin tissues are compositions of elementary infinitesimal updates. We use this framework to construct a simple action principal that allows us to quantiatively compare different growth patterns. We propose that stereotypic growth patterns are the 'simplest' growth patterns, in the sense that the minimize spatiotemporal variation in growth rates and anistropy. We demonstrate the power of this framework by generating a prediction for the growth patterns of limbs in *Parhyale hawaiensis*.

Finally, Chapter 6 is a brief conclusion, summarizing the work presented in each chapter and detailing possible future directions.

1.8 Permissions and Attributions

1. The content of chapter 2 is the result of a collaboration with Noah Mitchell [164].

2. The content of chapter 3 is the result of a collaboration with Fengshuo Yang,

Haodong Qin, Anastasios Pavlopoulos, Mark Bowick, and Sebastian Streichan [46].

3. The content of chapter 4 is the result of a collaboration of Noah Mitchell, Suraj Shankar, Yuzheng Lin, Boris Shraiman, and Sebastian Streichan, which has previously appeared in the journal *eLife* [165].

4. The content of chapter 5 is the result of a collaboration with Boris Shraiman [47].

Chapter 2

TubULAR: *in toto* tissue cartography, material parameterization, and flow field analysis in tube-like surfaces

A common motif in biology is the arrangement of cells into tube-like sheets, which further transform into more complex morphologies. Traditionally, analysis of the dynamic surfaces of growing tissues has relied on inspecting static snapshots, live imaging of cross-sections, or tracking isolated cells in 3D. However, capturing the interplay between in-plane and out-of-plane behaviors requires following the full surface as it deforms and integrating cell-scale motions into collective, tissue-scale deformations. The advent of methods for whole-organ live imaging accentuates the need for *in toto* analysis methods to understand these collective tissue dynamics. Here, we introduce an approach to build *in toto* maps of surface deformation that follow tissue parcels in the material frame of reference. The Tube-like sUrface Lagrangian Analysis Resource (TubULAR)

provides an open-source MATLAB implementation whose functionality is accessible either as a standalone toolkit or as an extension of the ImSAnE package used in the developmental biology community. TubULAR provides a framework for linking in-plane and out-of-plane behaviors and decomposing complex deformation maps into elementary contributions defining physically meaningful signatures of motion. We underscore the power of our approach by analyzing shape change in the embryonic Drosophila midgut and beating zebrafish heart. Following deformations in the tissue/material frame reveals the signatures of tissue flow and a reduced-dimensional mode decomposition of the dynamics. The method naturally generalizes to *in vitro* and synthetic systems, including a stem cell model of neural tube morphogenesis and deforming condensates in a reconstituted cytoskeletal system. This work was produced in collaboration with Noah Mitchell [164].

2.1 Introduction

In biological and synthetic settings alike, the morphogenesis of tube-like sheets and films is driven by a dynamic interplay between in-plane and out-of-plane behaviors [150, 118, 113, 138, 30, 252, 125, 223]. Tissue morphogenesis is a particularly rich example of this interaction, in which the dynamics of shape generation are intertwined with mechanical forces, cellular fates, and organ function. In epithelia [95, 96], visceral organs [9, 165], vasculature [206], elastic shells [72], and whole organisms [154], quasi-2D surfaces deform in 3D space, contracting and dilating in-plane and bending out-of-plane in a coupled fashion. Understanding the dynamic mechanisms by which the systems change shape requires not only capturing instantaneous motion in 3D, but following the material as it deforms to build so-called 'Lagrangian' measures of deformation [219, 208, 142]. Furthermore, decomposing that motion into in-plane and out-of-plane components enables

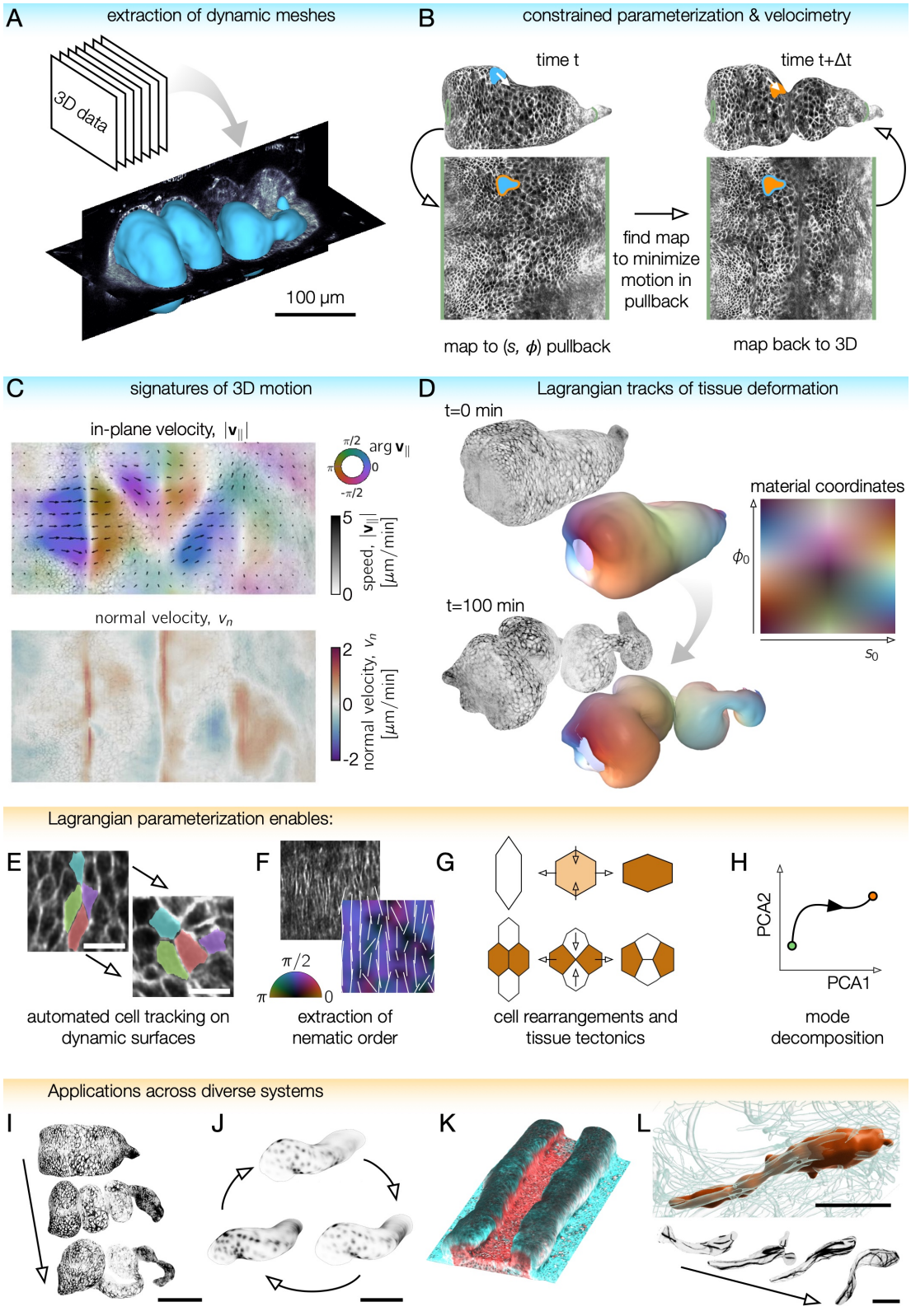
A
extraction of dynamic meshes
3D data
100 μm
B
constrained parameterization & velocimetry
time t
time t+Δt
find map to minimize motion in pullback
map to (s, ϕ) pullback
map back to 3D
C
signatures of 3D motion
in-plane velocity, |v||
arg v||
speed, |v||
[μm/min]
normal velocity, vn
normal velocity, vn
[μm/min]
D
Lagrangian tracks of tissue deformation
t=0 min
t=100 min
material coordinates
Lagrangian parameterization enables:
E
automated cell tracking on dynamic surfaces
F
extraction of nematic order
G
cell rearrangements and tissue tectonics
H
PCA2
PCA1
mode decomposition
Applications across diverse systems
I
J
K
L

Figure 2.1: **TubULAR is a toolkit for following the dynamics of evolving tube-like surfaces, such as visceral organs and *in vitro* biological surfaces.** *(A)* TubULAR first extracts dynamic surfaces of interest from volumetric datasets. *(B)* Whole-surface parameterization using a generalized cylindrical coordinate system facilitates tracking tissue deformations. Since pullback images of adjacent timepoints are optimized to be nearly stationary in the parameterization space, 3D tissue velocities are obtained by linking the pre-image of the pullback coordinates across timepoints. *(C)* By extracting in-plane and out-of-plane tissue motion, TubULAR decomposes the underlying motion, here shown by a 2D pullback representation of the in-plane tissue velocity $\mathbf{v}_{\parallel}$ (colored quiverplot) and the normal motion, v_n (red for inward velocity, blue for outward). *(D)* Finally, the toolkit tracks tissue deformations over time in the tissue's frame of reference (the Lagrangian frame). Here, a whole organ is colored by the location of each tissue parcel in its intrinsic material coordinate system (s_0, ϕ_0). Patches retain their original color as they move, stretch, and bend. *(E)* Computational microscopy enables dynamic tissue surface extraction and cell tracking. After selectively imaging the endodermal layer in a *w;48Y GAL4 / UAS-CAAX::mCh;klar* embryo, we track and highlight the motion of four cells that exhibit intercalations. Scale bars are 10 μm. *(F)* Performing a radon transform on a patch of circular visceral muscle cells – which form a 'palisade' structure ensheathing the midgut endoderm – returns a measure of tissue anisotropy aligned with the circumferential direction ($\phi = \pi/2$, violet). *(G)* Constructing material-frame pullback images facilitates measurements of tissue shape change, cell shape change, and cell intercalation rates. *(H)* Following the tissue's deformation enables mode decomposition of the dynamics, offering descriptions with reduced complexity, shown schematically as a path of the system through mode space after performing principal component analysis (PCA). *(I-L)* This method tracks deformations for organs and *in vitro* systems alike, including the Drosophila midgut, the beating zebrafish heart, a stem-cell-based neural tube, and a phase-separated droplet deforming in a cytoskeletal gel. Scale bars are 100 μm for all panels. *(K)* Characterizing the tissue surface offers a route to study neural tube development [118]. *(L)* We follow a DNA-nanostar-based droplet (red) deforming in an active fluid. Here, mechanical coupling between the interface of a liquid-liquid phase separated DNA droplet and a surrounding active microtubule fluid (cyan rods) generates continuous deformation towards droplet breakup. In the time series, microtubule fluorescence within 10 μm of the interface is projected onto the deforming droplet surface.

insights into the (bio)material's constitutive behavior, the processes generating its shape, and its physiological function [139, 162, 165, 77].

Much of of our understanding of morphogenesis built during the last century has relied on qualitative analysis of 2D live imaging and static snapshots of dynamic growth processes in 3D [13, 143, 179]. Emerging computational approaches in the life sciences have enabled quantitative characterizations that often challenge traditional assumptions and clarify the complex relationship between gene expression patterns, physical forces, and tissue geometry [215, 11, 74, 138, 236, 263, 123, 142]. In a particularly fruitful methodological advance, the community has applied 'tissue cartography' methods that map curved tissues to a planar representation, dramatically reducing the computational power required to store and analyze 3D data [217, 99, 102, 166]. This framework has facilitated insights in a wide variety of systems including fly wings [277], eyes [81], egg chambers [57], ascidian vasculature [153], zebrafish endoderm [217], and mouse intestines [39].

While these methods are sufficient to track cells rearranging within static geometries and in local patches of complex shapes [99], *in toto* measurements of tissue deformation in more complex, dynamic geometries have remained elusive. Here we propose automated methods for registering dynamic tube-like surfaces across time – with arbitrarily complex geometry – and classifying the signatures of tissue deformation underlying organ-scale shape change. As shown in Fig. 2.1, this provides a framework for tracing the dynamics of complex shapes. This method then naturally decomposes tissue-frame measurements for interpretation, handling all computational subtleties that arise from the surface's curvature and motion.

By applying this approach to the developing embryonic digestive tract in the fly *Drosophila melanogaster* [109, 22, 21, 165] and the beating heart of the embryonic zebrafish *Danio rerio* [9, 20, 77, 232, 20, 41], we extract the signatures of in-plane and out-of-plane tissue deformation. Despite the complexity of their motion, we obtain sim-

ple geometric descriptions underlying shape change.

2.2 Implementation and application to a model organ

Contemporary microscopy methods generate volumetric data, wherein each voxel carries a (potentially multi-channel) intensity measured at a specific location in the sample [127]. At the same time, many biological processes harness quasi-2D, thin tissues or interfaces to sculpt complex 3D forms. To probe the interplay between in-plane interactions and out-of-plane dynamics in such systems, we must extract the tissue surface, track motion within the surface as it deforms, and decompose the resulting motion into signatures of deformation.

We package this functionality in the Tube-like sUrface Lagrangian Analysis Resource (TubULAR). TubULAR is publically available on GitHub, with documentation and example scripts at `https://npmitchell.github.io/tubular/`. The package includes (and uses) independent toolkits for surface visualization (`TexturePatch`), conformal mapping (`RicciFlow`), and discrete exterior calculus (`DECLab`). A typical workflow passes through (1) level sets segmentation for surface detection, (2) generation of a pullback representation for surface parameterization and visualization, (3) flow analysis using TubULAR's discrete exterior calculus implementation, and, if appropriate, (4) mode decomposition of the dynamics. In addition to the standalone toolkit, we have incorporated the core functionality of TubULAR within the ImSAnE environment [99], with updates available at `https://github.com/npmitchell/imsane`.

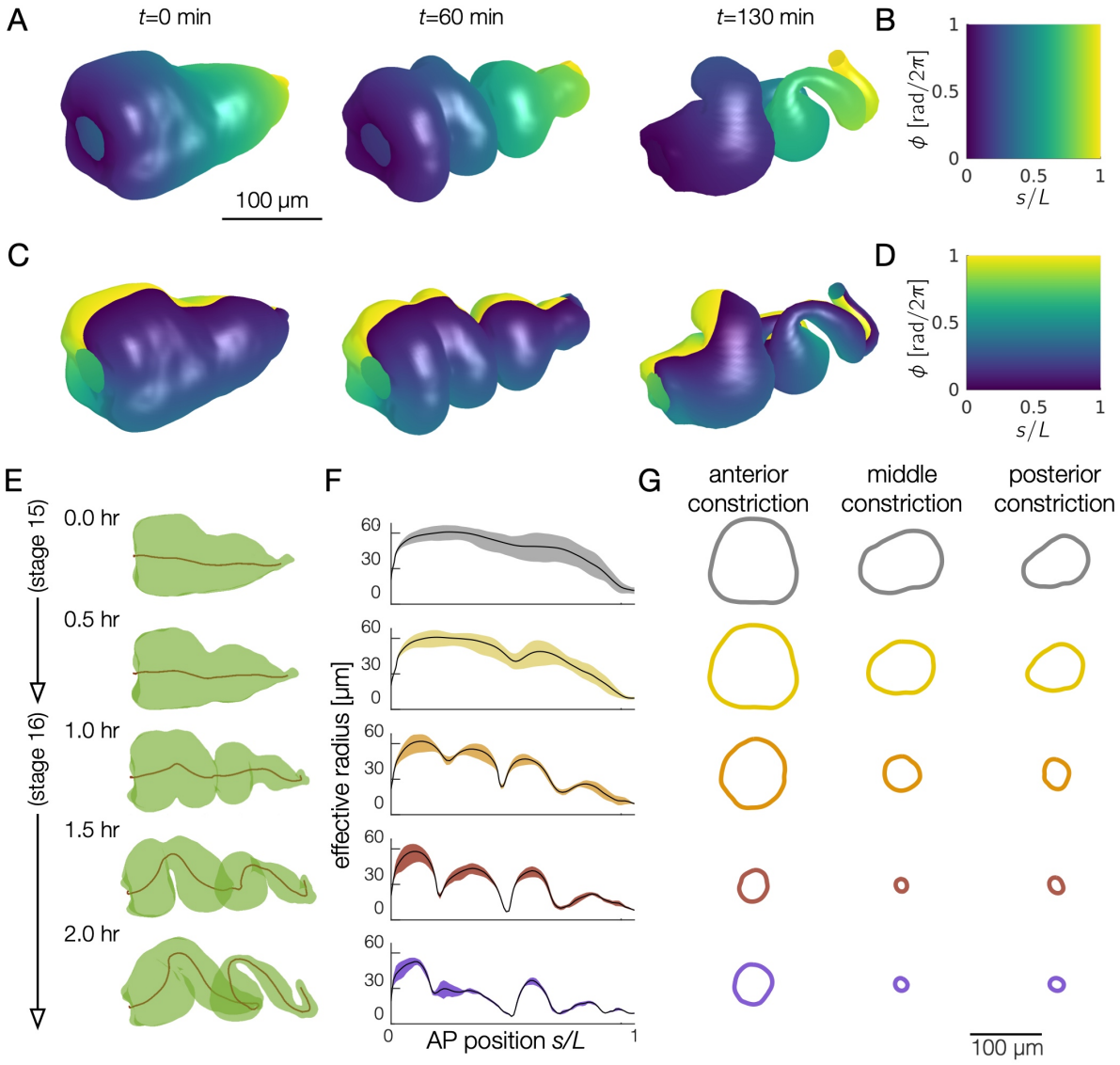
A
t=0 min
t=60 min
t=130 min
100 μm
B
ϕ [rad/2π]
s/L
C
D
E
(stage 15)
(stage 16)
0.0 hr
0.5 hr
1.0 hr
1.5 hr
2.0 hr
F
effective radius [μm]
AP position s/L
G
anterior constriction
middle constriction
posterior constriction
100 μm

Figure 2.2: **Coordinate parameterization follows 3D deformations of the evolving surface, enabling quantification of geometric dynamics, shown here for the fly midgut as it folds into a coil of compartments.** *(A)* Constructing a dynamic map to fixed material coordinates, we label the midgut's intrinsic longitudinal axis as the surface deforms into a convoluted shape. *(B)* A 2D pullback representation of the material frame reflects the longitudinal coordinates colored in (A). *(C)* Dynamic mapping to fixed material coordinates tracks circumferential motion of the tissue. *(D)* Colors correspond to the surfaces shown in (C). *(E-F)* After computing centerlines of the surface directly from the parameterization (brown curves), we then measure a cross-sectional width of the organ (effective radius) as a function of longitudinal position. In (F), as before, s is a measure of proper distance along the organ surface in the material frame. The shaded band represents the minimum and maximum effective radii along each circumference (each defined by s =constant). The narrowing shaded band near each constriction reflects the increasingly circular cross–sectional shape of each constriction. *(G)* Computational sectioning of the midgut shows that constrictions adopt circular shapes in the intrinsic material cross-sections. When viewed in their intrinsic, dynamically tilting cross-sectional planes, midgut constrictions are shown to adopt circular shapes as they tighten. Note that these intrinsic cross-sectional planes stray far from the Eulerian anterior-posterior axis, making this a difficult measurement if not for our material parameterization.

2.2.1 From volumetric data to dynamic textured surfaces

We first set out to identify and extract 2D surfaces of interest from 3D data. For the tube-like shape of the systems we address here, TubULAR segments the data space into an 'inside' (i.e. everything within the tube) and an 'outside' (i.e. everything outside the tube), modulo the potentially necessary inclusion of virtual 'end caps' to close off the interior of an open tube [182]. As illustrated in Fig. 2.1A, level set methods are a robust and powerful tool used to dynamically segment data volumes into complex watertight geometries whose boundaries are defined as the null contours of a signed distance function $u(\mathbf{x})$. The signed distance function is taken to be positive, $u(\mathbf{x}) > 0$, on the interior of the test surface and $u(\mathbf{x}) < 0$ on the exterior. The problem of surface detection is thereby reduced to optimizing the signed distance function so that $u(\mathbf{x}) = 0$ matches the tissue surface.

Once a level set partitions the data volume for a given time point, we the point cloud

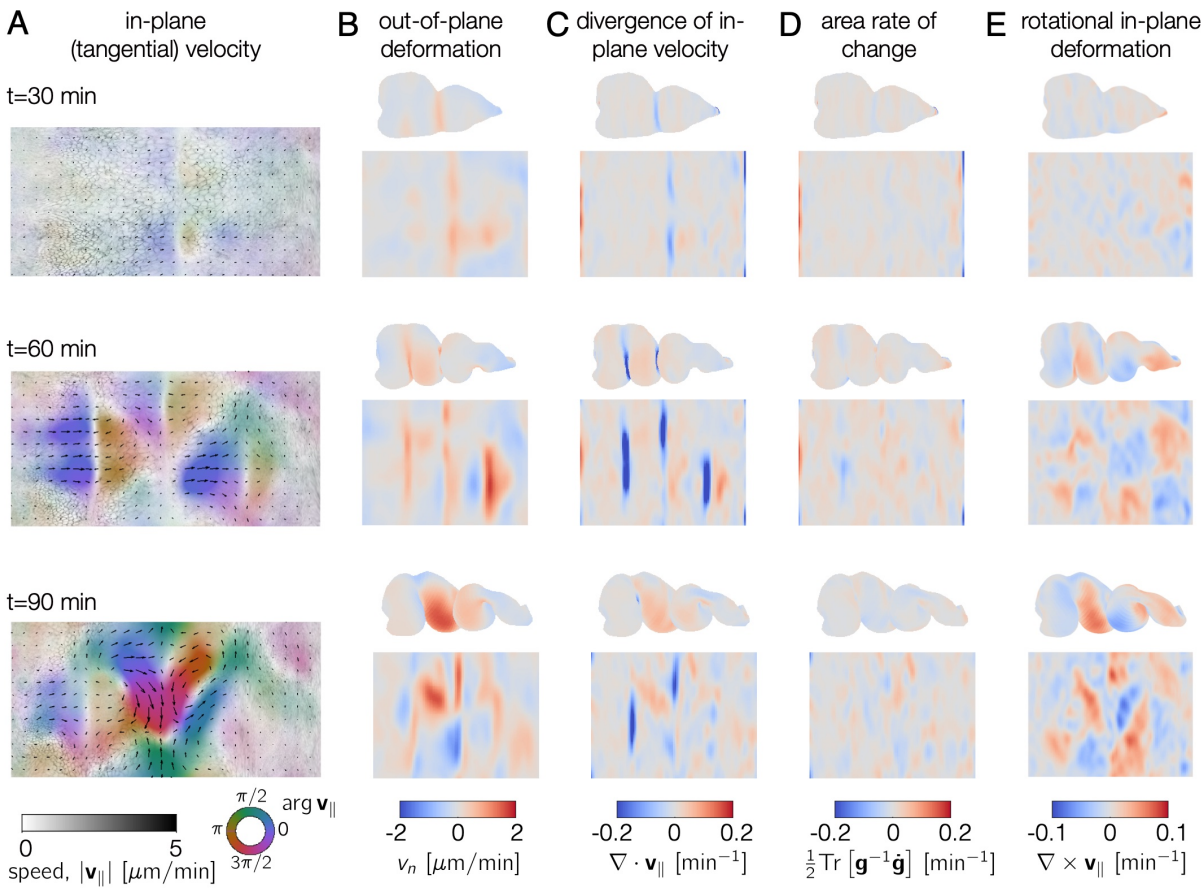

Figure 2.3: **Discrete exterior calculus measurements of tissue velocity return signatures of motion.** *(A)* 2D pullback representation of in-plane (tangential) tissue motion shows a line defect near the middle constriction, then defects at the anterior and posterior constrictions, followed by increasingly complex in-plane flows. The orientation of flow relative to the longitudinal axis $\hat{s}$ is denoted by color and the magnitude of the motion reflected by opacity and arrow length. *(B)* The underlying out-of-plane velocity v_n is positive (inwards) near constrictions. *(C)* DEC computation of the divergence of the in-plane velocity $\nabla \cdot \mathbf{v}_\parallel$ shows patterns of sinks in the constrictions and sources in the chambers' lobes, in synchrony with the out-of-plane deformation. *(D)* As a result of the match between in-plane and out-of-plane, the areal growth rate – defined as Tr $\left[\mathbf{g}^{-1}\dot{\mathbf{g}}\right]/2$ – remains relatively quiescent. Here $\mathbf{g}$ is the first fundamental form of the tissue surface. *(D)* DEC computation of the rotational component of motion reveals vortices of alternating sign along the longitudinal axis. For this sign convention, positive rotational flow corresponds to a curl aligned with the inward surface normal.

defined by the voxels on the boundary of the segmented region to generate a smooth mesh triangulation. The surface triangulation is the mathematical workhorse we use to measure material motion. The result is a dynamic set of surfaces tracing the tube-like surface over time, as illustrated in Fig. 2.1B-D. Users may alternately generate surfaces via other software (such as Imaris), then use TubULAR for subsequent analysis. A toolkit for rendering the data onto the surface (`TexturePatch`) is included and implemented within TubULAR – and is also functional as a standalone tool.

2.2.2 Constrained surface parameterization enables tracking surface dynamics in the material frame

Understanding the ways in which shape dynamics couple to biological processes such as cell shape change, intercalation, intracellular patterning, and gene expression requires the ability to identify and follow patches of tissue as they move and deform. On its own, the previous surface extraction step provides an instantaneous description of the surface geometry, but does not identify how particular patches of cells move and deform from time point to time point. Generating a consistent, time-dependent coordinate system taking into account tissue flow and deformation presents a considerable technical challenge, particularly in the presence of dramatic shape change. In the language of continuum mechanics, we must advance from an *Eulerian* description, wherein dynamical observables are measured at particular locations in space, to a *Lagrangian* description, wherein the dynamics – whether of deformation, anisotropy, morphogen concentration, or any another observable – are queried by following material parcels along the surface as morphogenesis proceeds [130].

As illustrated in Fig. 2.1B and Fig. 2.2A-D, we build a parameterization scheme such that the motion of the cells (or other objects) in the pullback representation move as

little as possible. This enables us to easily follow a virtual representation of in-plane deformations in pullback space, which we can then project into 3D to follow the true motion. To this end, TubULAR first cartographically maps the surface to the plane – defining a material frame of reference – then stabilizes virtual motion of the material in the pullback plane. The end result is a dynamic map $\varphi(t)$ mapping the dynamic surface to a fixed material frame of reference, with no movement of the tissue over time in the material frame.

We first map the mesh at a single reference timepoint into the plane to define the material frame. To do so, we cut small 'endcaps' at the poles and create a virtual seam along the long axis so that the now-cylindrical mesh topology can be 'unrolled' into the plane. To facilitate the analysis of anisotropic tissue deformations later in the pipeline, this mapping into the plane is *conformal* – i.e. a totally isotropic, angle-preserving map. This conformal map is constructed either by discrete Ricci flow [276] (included as a custom package within TubULAR, also a fully independent, standalone package) or can be approximated quickly via minimizing the Dirichlet 'energy' of the mapping [194]. We ensure that the choice of virtual seam along the mesh's long axis does not affect the resulting mapping by placing periodic boundary conditions in the ϕ direction, with an implementation inspired by recent work on orbifold mappings of spherical surfaces [2].

Finally, we advance from this initial map to follow the tissue motion. We do so by adjusting the mapping to the plane at other timepoints $\varphi(t)$ so that any virtual tissue motions are subtracted off in the pullback image. As detailed in the Appendix A, we found that a four-step approach to constructing this map aided in numerical stability for the systems we have considered: $\varphi(t) = J \circ \Phi \circ Z \circ f$, where f is a conformal map, Z adjusts the longitudinal axis, Φ minimizes motion along the circumferential axis, and J accounts for residual motion through optical correlation of adjacent pullback images. We are then able to follow extreme deformations of the tissue in 3D space simply by reading

off the dynamic inverse map $\varphi^{-1}(t)$ as sketched in Fig. 2.1D.

2.2.3 Following surface geometry in the material frame enables insights into midgut formation

Before analyzing tissue *dynamics* on deforming curved surfaces, we first underscore the insights afforded from following the surface geometry alone, without reference to velocity fields. Our approach to material parameterization naturally returns geometric descriptors which otherwise can be challenging to obtain. In particular, we show here that Drosophila midgut constrictions become increasingly circular as they deepen, despite their initially anisotropic shape.

During embryonic development in Drosophila, the midgut closes into a tube and takes on a rectangular shape in its anterior and tapers to an irregular shape towards the posterior [38, 124, 203, 21, 203, 265]. Subsequently, the midgut forms a constriction midway along its length, then two more constrictions subdividing the organ into four chambers [109, 165].

Using the computational sectioning offered by TubULAR's surface parameterization, we can quantify the degree of azimuthal symmetry about the organ's centerline. A useful byproduct of the surface parameterization is a time-dependent centerline curve spanning the full length of the surface (Fig. 2.2E). Despite being desirable for medical and scientific purposes alike [272], constructing such a centerline via traditional methods raises numerous technical hurdles [53] (see Appendix A). With a material coordinate parameterization, however, we need only link the centroids of each circumferential 'ring' (s = constant) to return an organ-spanning curve with association between each point along the curve and points in the tissue surface.

As shown in Fig. 2.2F-G, we find that though the gut tube initially has irregular

cross sections, the constrictions rapidly adopt circular cross sections. This tightening of the cross-sectional geometry suggests that the tension is uniform throughout the DV direction, consistent with a model in which the highly elongated circular visceral muscles drive force generation during this process (c.f. [165, 203]). We note that these measurements would be challenging without a consistent method for constructing a single, organ-spanning centerline with associations between the surface and each point along the curve. Nonetheless, these features all follow trivially from our approach.

2.2.4 Covariant measures of motion access signatures of deformation

By constructing material pathlines, we have already obtained velocity vectors of the tissue defined over the surface and over time. In order to *interpret* these tissue flows, we now decompose the velocity fields into their underlying components. A given parcel can move both along the surface and normal to the surface, and separating these motions is needed to parse whether tissue is rotating or shearing, contracting or dilating, and protruding or ingressing – and to find the spatiotemporal pattern in which these motifs occur. After computing a Lagrangian reference frame for the tissue, the default implementation in a TubULAR pipeline therefore (1) extracts the in-plane divergence and the local rotation rate of the tissue velocity, (2) relates the in-plane divergence to the out-of-plane motion v_n to determine the rate of areal growth across the surface, and (3) measure area-preserving shear deformations in the tissue.

Dealing with velocity fields on curved surfaces requires certain computational care: parallel lines cross and diverge, and the orientation of a cell may change by simply traveling along 'straight' lines (geodesics). In TubULAR, our calculations therefore rest on an implementation of the discrete exterior calculus (DEC) formalism [65, 55]. Signals

are represented as discrete differential forms on the simplicial structure of the triangulated mesh which yield natural definitions for linear differential operators. These basic operations can be combined together to form covariant representations of more complicated differential operators, including the divergence, curl, and Laplacian operators that are a part of TubULAR's default workflow. These operators can be directly applied to geometric data (e.g. surface curvature), kinematic data (e.g. surface velocities), and beyond (e.g. surface data intensity, surface data anisotropy fields etc.) to understand the ways in which spatiotemporal variation in observable fields generate 3D shape change. Advanced users can use these operators to construct soluble, discrete representations of physical models (e.g. diffusion of morphogens or the Navier-Stokes equations [6, 175]) and directly test their predictions on evolving non-trivial geometries.

In order to make these methods accessible to the broadest possible audience, we have packaged all of this functionality within `DECLab`, a simple and flexible framework for discrete geometry processing. It is included with TubULAR and also functions as a standalone toolkit. No deep knowledge of differential geometry or exterior calculus is necessary to use our implementation. Appendix A and online documentation describe the DEC methods.

Fig. 2.3 displays examples of these calculations applied to the developing Drosophila midgut. Whole-organ measurements of the tangential velocity are represented in the 2D pullback coordinates for snapshots of a representative embryo in Fig. 2.3A, with normal velocities shown in Fig. 2.3B. Further processing via DEC of the in-plane velocity fields shows localized sinks in the flow ($\nabla \cdot \mathbf{v}_{\parallel} < 0$) near constrictions, as shown in Fig. 2.3C. The strong divergence in the tissue velocities is compensated by the out-of-plane deformation, such that the rate of area change is relatively small Fig. 2.3D. The rotational component of the flow, meanwhile, adopts a pattern of vorticity in each chamber, with alternating sign (Fig. 2.3E).

2.2.5 Lagrangian measures of time-integrated tissue strain

Endowing the evolving surface with a set of Lagrangian coordinates enables the construction of a *material metric*. The metric tensor, $\mathbf{g}(t)$, is a geometric object enabling the measurement of distances and angles between nearby points on the surface. The rate-of-deformation tensor describes how lengths and angles change locally as the surface deforms in time:

$$\frac{dg_{ij}(t)}{dt} = \nabla_i v_j + \nabla_j v_i - 2\, v_n\, b_{ij}, \tag{2.1}$$

where v_i, $i \in \{1, 2\}$, and v_n denote the tangential and normal components, respectively, of the Lagrangian surface velocity, ∇_i denotes the covariant derivative with respect to the i^{th} tangential coordinate, and b_{ij} denote the components of the second fundamental form – another geometric tensor object that contains all information about both intrinsic and extrinsic measurements of surface curvature. Essentially, Eq. (2.1) tells us that lengths and angles deform under the surface motion when there are gradients in the tangential velocity *and/or* when there is normal motion in curved regions of the tissue. We can then integrate the rate-of-deformation tensor along pathlines to construct a Lagrangian measurement of cumulative tissue strain, i.e.

$$\varepsilon(t) = \frac{1}{2} \int_{\tau=0}^{\tau=t} d\tau\, \frac{d\mathbf{g}(\tau)}{d\tau} = \frac{1}{2}\,(\mathbf{g}(t) - \mathbf{g}(0)). \tag{2.2}$$

In the language of geometric elasticity, this is equivalent to the Green-St. Venant strain tensor [71], defined relative to the 'undeformed' reference configuration at time $t = 0$.

2.2.6 Field decomposition simplifies complicated deformations

Frequently, seemingly complicated patterns of motion can be decomposed into a sum of contributions from simpler components. This strategy has been successfully adopted in various contexts within morphogenesis, including analysis of the complicated tissue motions observed in zebrafish gastrulation [205] and in reconstructing the 4D growth patterns generating vertebrate limbs [58]. The TubULAR package deconstructs complex observable fields into elementary components at multiple stages of analysis.

We include the capability to decompose surface vector fields (e.g. material tissue velocities) into their geometric components. Our implementation generates a Helmholtz-Hodge decomposition of tangential vector fields [55], i.e. a decomposition into dilatational, rotational, and harmonic parts. This procedure determines the relative contribution of the geometric signatures of the in-plane flow to the out-of-plane deformation.

TubULAR also constructs mode decompositions of arbitrary tensor fields on the surface. This functionality comes in two forms. First, our DEC implementation decomposes signals onto a basis of the eigenfunctions of the discrete Laplace-Beltrami operator [145]. More simply, this compares the relative importance of long-wavelength modes (with smooth spatial variation) and short-wavelength modes (with rapid spatial variation) in generating the observed signals. Second, we include functions to decompose signals using principal component analysis (PCA) [115], as demonstrated in the next section. This type of analysis lets users extract more general patterns of motion that contribute most strongly to the variance observed across time or across datasets.

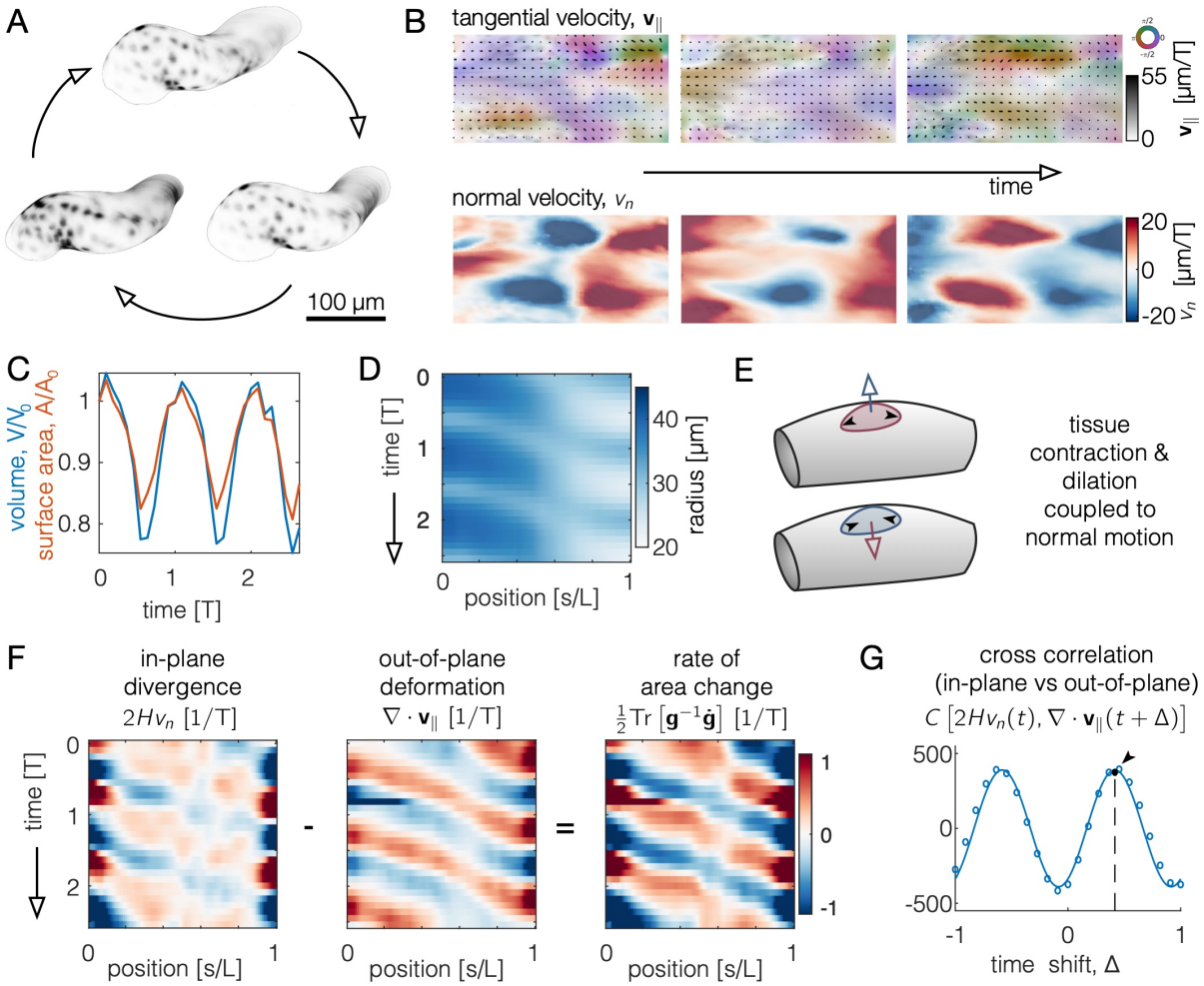
A
100 µm
B
tangential velocity, $\mathbf{v}_\parallel$
55
0
$\mathbf{v}_\parallel$ [µm/T]
time
normal velocity, v_n
20
0
-20
v_n [µm/T]
C
volume, V/V_0
surface area, A/A_0
1
0.9
0.8
0
1
2
time [T]
D
time [T]
0
1
2
40
30
20
radius [µm]
0
position [s/L]
1
E
tissue
contraction &
dilation
coupled to
normal motion
F
in-plane
divergence
$2Hv_n$ [1/T]
out-of-plane
deformation
$\nabla \cdot \mathbf{v}_\parallel$ [1/T]
rate of
area change
$\frac{1}{2}\mathrm{Tr}\left[\mathbf{g}^{-1}\dot{\mathbf{g}}\right]$ [1/T]
time [T]
position [s/L]
-
=
1
0
-1
G
cross correlation
(in-plane vs out-of-plane)
$C\left[2Hv_n(t), \nabla \cdot \mathbf{v}_\parallel(t+\Delta)\right]$
500
0
-500
-1
0
1
time shift, Δ

Figure 2.4: **Tracing the in-plane and out-of-plane dynamics of a beating heart reveals the phased coupling between dilatational and transverse deformations.** *(A)* Segmentation of a beating zebrafish heart shows cyclic deformations in 3D, shown at three equally spaced timepoints within a beat period, T. *(B)* Decomposing tissue motion into in-plane and out-of-plane demonstrates how pulsed deformation travels along the long axis of the tube. The tangential velocity is represented as a color denoting its direction along the long axis (purple or orange) or along the circumferential axis (green or pink), with magnitude denoted by opacity. Inward motion corresponds to $v_n > 0$. *(C)* Both the total enclosed volume and the surface area oscillate over time. *(D)* A kymograph of the radius of the tube measured along the long axis shows cyclic beating. We average the radius around the circumferential axis for each axial position s in this plot. *(E)* During each cycle, tissue undergoes both out-of-plane motion and in-plane deformation. These two are coupled, such that the rate of area change depends on both the normal motion and the divergence of the in-plane velocity. *F)* Kymographs of in-plane and out-of-plane motion averaged along the circumferential axis highlights waves of contraction. During each cycle, the in-plane and out-of-plane deformations are nearly out of phase, so that the rate of local tissue area change is large. *(L)* Because of the phase difference between in-plane motion and out-of-plane deformation, cross correlation of the two motions indicates an offset phase relationship. The curve shown is a fit to the data by an offset sinusoidal wave, with a peak at $\Delta = 0.416 \pm 0.006\ T$.

2.3 Decomposing deformations during heart morphogenesis

To demonstrate the generality of the method, we analyzed a beating zebrafish heart during during the second day of development post fertilization. *In toto* imaging of the heart relied on light-sheet illumination of a transgenic Tg(*cmlc2:eGFP*) embryo expressing GFP in cardiomyocytes [107]. These data were taken using a temporal superresolution approach [41], in which acquisition was synchronized with the beating of the developing heart to build volumetric data at 11 equally-spaced phases of the heart beat cycle. The 3D shape of the beating heart is shown for a set of illustrative time points in Fig. 2.4A. Passing the volumetric data through TubULAR returns covariant measures of in-plane and out-of-plane deformation.

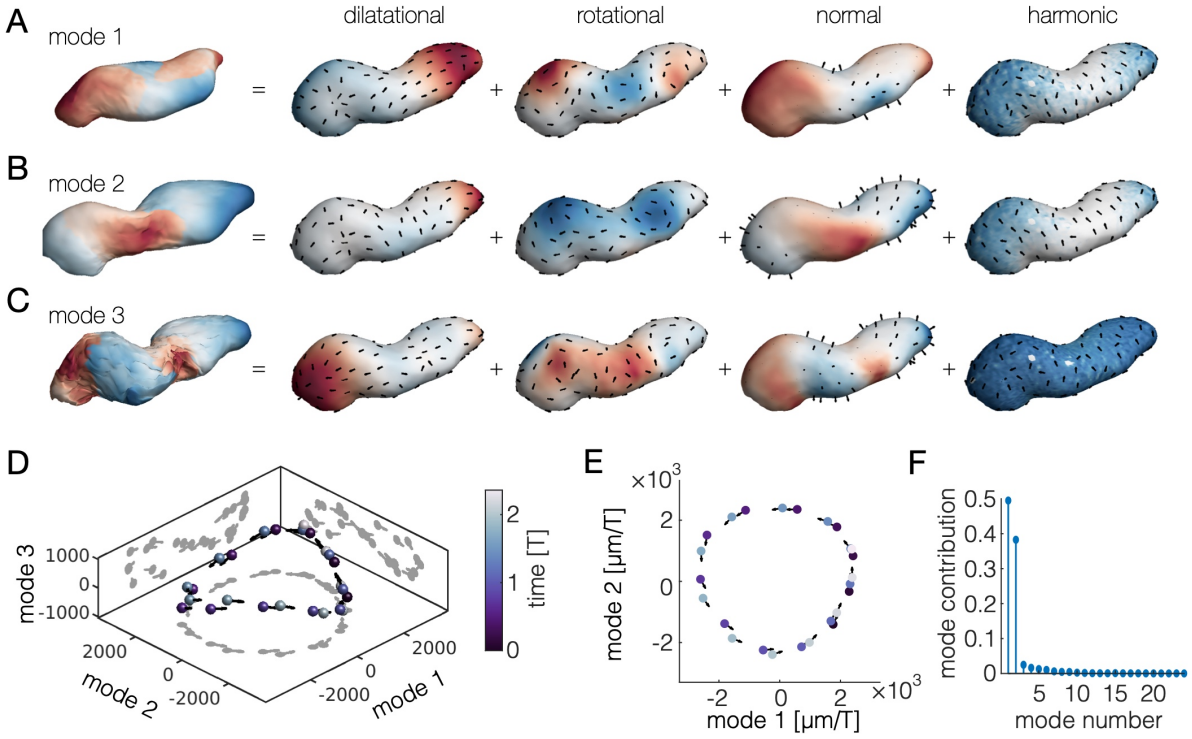

Figure 2.5: **Decomposition of tissue motion in the beating heart reveals two principal components with non-reciprocal dynamics.** *(A-C)* Visualization of the principal components of Lagrangian tissue velocities. The first image in each panel shows the deformation induced by moving along the associated component axis, colored by the alignment of the component axis with the surface normal direction. Subsequent images illustrate the Helmholtz-Hodge decomposition of the tangent part of the mode and also the normal part of the mode. Color in the dilatational part, rotational part, and harmonic part are given by the scalar potential, vector potential, and norm of the harmonic mode respectively. Color in the normal part is given by the norm of the normal component of the mode. *(D-E)* Principal component analysis on the time course of deformations returns two dominant modes of deformation with a phase relationship of nearly $\pi/2$, such that the system winds in state space along a nearly planar, circular pattern. *(F)* A comparison of the relative contribution of the first 24 modes. Mode contribution is defined as the time averaged ratio of the squared length of the projection of the velocity along each mode normalized by the total squared length of each velocity vector in state space.

2.3.1 Beating heart exhibits a phase delay between in-plane motion and out-of-plane deformation

Cyclic deformations of the heart result in in-plane velocities $\mathbf{v}_{\parallel}$, colored by their orientation in Fig. 2.4B-D and out-of-plane motion v_n that constricts or dilates the tube Fig. 2.4E-G. The extracted heart shape changes both surface area and volume as it beats, shown in Fig. 2.4H. We highlight the waveform of the beat by plotting a kymograph of the radius as a function of time and position along the long axis of the tube in Fig. 2.4I. In this measurement, we average along the circumferential axis of the tube, given that the developing heart is reasonably symmetric along its circumference at this stage.

Unlike in midgut morphogenesis, the beating heart's in-plane velocities are not directly correlated with the out-of-plane deformation so as to produce incompressible motion. While both the in-plane divergence and out-of-plane motion display directional waves in their kymographs, the two fields are out of phase. As shown in Fig. 2.4L, we measure a phase offset between the two fields of $0.42\,T$, where T is the period of heart beating. In other words, as the tube constricts in the normal direction, the tangential velocities are compressive, such that the tissue locally changes area in an oscillating manner. This feature contrasts sharply with the irreversible constrictions of the fly midgut during embryonic stages 15-16, in which nearly incompressible kinematics lead to a 97% correlation between the two fields [165].

2.3.2 Mode decomposition of the heart reveals two out-of-phase characteristic deformations.

Finally, we applied TubULAR's mode decomposition tools to extract the extent to which the complex cyclic beating of the embryonic zebrafish heart can be explained by

simpler constituent motions. In order to do so, the 3D tissue velocities defined along material pathlines were first lifted to reside in a high-dimensional space where each point was defined by the set of all velocities on the surface at a given time point. We then performed principal component analysis (PCA) to determine the axes in this high-dimensional space that explained the majority of the variance in the data over time. The three most important modes are displayed in Fig. 2.5A-C. We performed a Helmholtz-Hodge decomposition of the mode velocities using the built-in functionality of the DEC package contained in TubULAR to probe the signatures of motion contributing to each mode.

We find that two modes dominate the dynamics, offering insight into the kinematics driving unidirectional pumping. As shown in Fig. 2.5E, the system oscillates between the first two modes, sweeping out a roughly circular trajectory subtending a nonzero area. Other pairings, in contrast, generate trajectories that subtend balanced virtually zero area (Fig. 2.5D). This phased oscillation between the first two principal components indicate unidirectional pumping of the heart. Computing the contribution of each mode to the total motion validates this 2D state representation: the first two modes capture nearly 90% of the deformation (Fig. 2.5G).

2.4 Discussion

We have developed a computational framework for unravelling the complex, dynamic shapes of tube-like surfaces into their principal signatures of deformation, providing a documented, open-source MATLAB implementation to the community. Our implementation unifies the core elements of this toolkit with the existing ImSAnE package [99]. This framework computes Lagrangian measures of strain and strain rate, decomposing dilatational and rotational signatures and mapping them onto the a reference mate-

rial configuration. Using this approach, we characterized the geometry of constrictions during midgut morphogenesis, revealing symmetric constrictions in the moving material reference frame and linking in-plane tissue flows to organ shape. We then characterized the cyclic deformations of the beating zebrafish heart – highlighting a phase difference between in-plane motion and out-of-plane deformation – and captured the heart's directional pumping motion with a two-dimensional principal component analysis.

As sketched in Fig. 2.1K-L, an efficient method for tracing surface dynamics in the Lagrangian frame of reference offers new opportunities for understanding not only organ dynamics during morphogenesis, but also organoid systems and sub-cellular structures. To illustrate this, we captured a surface representation of a developing neural tube derived from human stem-cells [118] and tracked a deforming phase-separated droplet in a microtubule gel [240].

A remaining challenge is to extend methods of tracking deformation through changes in topology of the surface. While here we address the challenges of complex and dynamic geometries, we focus our efforts to follow tubes with a single opening on each end. Extending to higher-order networks of tubes [160] and shapes which fuse or separate [118] poses additional challenges.

Chapter 3

A geometric body plan: active cell divisions organize *Parhyale* embryo into fourfold ordered state

Morphogenesis, the process through which genes generate form, establishes tissue scale order as a template for constructing the complex shapes of the body plan. The extensive growth required to build these ordered substrates is fuelled by cell proliferation, which, naively, should destroy order. Understanding how active morphogenetic mechanisms couple cellular and mechanical processes to generate order, rather than annihilate it, remains a crucial outstanding question in animal development. Using live imaging and tissue cartography, we quantitatively analyze the dynamics of fourfold tissue ordering in the trunk segmental ectoderm of the crustacean *Parhyale hawaiensis* beginning 72 hours after egg lay (AEL). We show that cell divisions are the primary drivers of tissue flow leading to a fourfold orientationally ordered phase. Waves of anisotropic cell proliferation propagate across the embryo with precise choreography. Defects introduced into the nascent lattice by cell divisions are ferried out of the tissue bulk towards the boundary

by subsequent divisions. Orchestrating cell proliferation rates and orientations enables cell divisions to organize, rather than fluidize, the tissue. The result is a robust, active mechanism for generating global orientational order in a non-equilibrium system that sets the stage for the subsequent development of shape and form. This work was the result of a collaboration with Fengshuo Yang, Haodong Qin, Anastasios Pavlopoulos, Mark Bowick, and Sebastian Streichan

3.1 Introduction

Ordered cellular geometries in developing tissues serve as patterned substrates from which complex arrangements of body parts can be built. The crucial organizing role that order plays in morphogenesis is particularly apparent in direct developers. These animals assemble a complete, miniature version of the adult body during embryogenesis [13]. The limbs and organs comprising the adult form are arranged according to specific body plans that ensure proper biomechanical functionality [146, 268]. Body parts develop with ordered placements and are aligned and oriented relative to distinct principal body axes [268]. In order to reliably generate the correct arrangements of limbs and organs, direct developers create organizational templates from ordered regions of tissue, akin to a coordinate system spanning the entire body.

Such templates must be ordered to delineate the body plan, but also retain sufficient fluidity to facilitate the large deformations necessary during development. Orientational order, an intermediate state between solid and and liquid matter, has been previously studied in non-living, thermally equilibrated systems [94, 221, 167, 45, 274]. More recently, orientational order has been demonstrated in the late stages of development, where organs use planar polarized signals to arrange cells into an ordered phase in the absence of proliferation [48, 210, 12, 49]. In contrast, the initial structuring of the body plan

during early embryonic stages occurs via the sequential outgrowth of segments and is fuelled by cell proliferation [13]. Generically, cell proliferation should give rise to fluidlike rearrangements that mix cells and prevent the initially fluid tissue from ever achieving an ordered state [198, 201, 129]. Orientationally ordered phases occupy only small fractions of their respective phase spaces in thermally equilibrated systems [19, 5, 148, 69, 188]. Thus, it remains unclear how non-equilibrium mechanisms in living systems can generate the requisite order to specify the body plan in the presence of cell divisions.

Here, we used *Parhyale hawaiensis*, an emerging model system of direct limb morphogenesis [233, 262], to study the interplay of growth and order. *Parhyale* implements its body plan sequentially via extensive cell proliferation [34]. Prior to appendage outgrowth, the ectoderm forms a grid of locally ordered cells [239, 34] (Fig. 3.1, A and C to E), a feature shared among malacostracans [262]. The rows of this grid correspond to segments of the adult body [239, 34]. Limb buds form at specific locations in the grid and give rise to numerous functionally specific appendages [233]. Importantly, limb orientation, in terms of the dorso-ventral (D-V) and antero-posterior axes (A-P), can be traced back to the local arrangement of precursor cells at the grid stage [263, 34].

3.2 *In toto* live imaging of *Parhyale* embryo reveals fourfold ordered state

We performed whole embryo live imaging of *Parhyale* using multiview light sheet microscopy [127]. Transgenic embryos with fluorescently labeled nuclei were imaged for 35 hours beginning three days after egg lay (AEL) (Fig. 3.1A). For the duration of this period, the ectoderm is a monolayer [34] and can be well approximated as a curved 2D surface. Tissue cartography, a computational technique wherein curved tissue

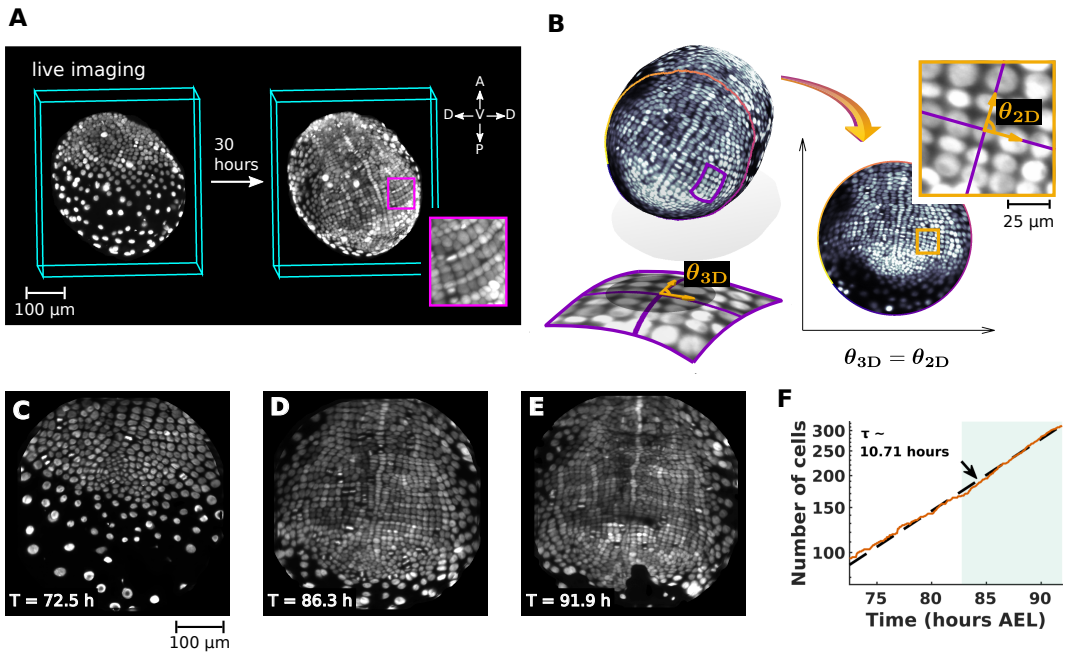

Figure 3.1: **Live imaging reveals the dynamics of a fourfold orientationally ordered phase in living tissue.** (*A*) Multiview light sheet microscopy allows for non-invasive 3D imaging of growing *Parhyale hawaiensis* embryos. (*B*) Conformal tissue cartography faithfully captures relative orientations of cells and streamlines data analysis via dimensional reduction. (*C* to *E*) The trunk ectodermal germband pulled back to the plane by tissue cartography. (*F*) The number of cells in a tracked region within the tissue, shown on a log scale. Dotted line is an exponential fit to the cell doubling time.

surfaces are endowed with 2D parameterizations, could therefore be used to facilitate data analysis by exploiting the inherent low dimensionality of the system [99]. The surface of interest corresponding to the ectoderm was dynamically extracted at each time point via a combination of machine learning [18] and level-set methods [168] (see Appendix B, Fig. B.1). We then used discrete Ricci flow [276] to define conformal charts that mapped the curved surface into the plane in a way that preserved angles (Fig. 3.1, B to E and Fig. B.2). Conformal tissue cartography ensures that the relative cell orientations, and therefore the orientational order, can be faithfully quantified from the planar data.

Working in the 2D conformal parameterization space, we implemented automated image segmentation routines to detect cells (see Appendix B). We found that the number of cells increases exponentially with a typical doubling time of 10 h (Fig. 3.1F). Next, we constructed a complex order parameter to quantify the relative orientations of neighboring cells (Fig. 3.2). Cell positions were taken to be the centers of mass of the nuclei. Instantaneous cell-cell connectivity was approximated by Voronoi tessellation (Fig. B.3). The order parameter assigns to each cell a pair of quantitative measures, magnitude and phase, indicating the extent to which neighboring cells are coherently positioned according to a specific n-fold lattice structure and the local orientation of the ordered neighborhood, respectively. Explicitly, the n-fold order parameter of cell j is given by

$$\psi_n(j) = \frac{1}{\sum_k \ell_{jk}^2} \sum_{k \in \mathcal{N}(j)} \ell_{jk}^2 \, e^{i\, n\, \theta_{jk}}, \tag{3.1}$$

where the sum runs over all the nearest neighbors k of cell j, i.e. $k \in \mathcal{N}(j)$, θ_{jk} is the angle formed by the separation vector between cells j and k and the horizontal axis in 2D, and ℓ_{jk} denotes the length of the Voronoi edge shared by cells j and k. Weighting the sum by the squared Voronoi edge lengths ℓ_{jk}^2 reduces the influence of noise in the centroid positions on the final value of the orientational order parameter. The magnitude of the

order parameter ranges between 0 (no n-fold order) and 1 (maximal n-fold order). For $n = 4$, i.e. the fourfold order parameters, the magnitude of the order parameter peaks when all neighbors of a cell are organized in a rectangular fashion (Fig. 3.2, B and C). Our analysis reveals that the tissue initially exhibits no four fold order (Fig. 3.3, A and B). Gradually, as the number of cells grows, the tissue adopts an increasingly fourfold ordered state, which peaks in magnitude around 82.5 h AEL (Fig. 3.3, A and C).

We also calculated the two point correlation functions of the order parameter, $C_n(r) = \langle \psi_n(r)\, \psi_n^*(0) \rangle$ $(n = 4, 6)$, which measure the agreement of the magnitude and phase of local order between cells as a function of their separation (Fig. 3.3, D and E and Fig. B.13, A and B). At early times, orientational order is short range, restricted to less than a cell length. In contrast, at later times, when the global fourfold order parameter peaks, orientational order is quasi-long range, with correlations that decay algebraically across the entire surface (Fig. 3.3A and Fig. B.13A). Therefore, strongly ordered local cell neighborhoods are coherently ordered, in both magnitude and phase, across the whole embryo. No significant sixfold order was detected at any time during this stage (Fig. 3.3, A and E, and Fig. B.13B). In particular, while the global sixfold order parameter does transiently rise to a modest $|\langle \psi_6 \rangle| \sim 0.3$ (for comparison the sixfold order parameter observed in hexagonally ordered arrangement of hair cells in the mammalian inner ear peaks $\gtrsim 0.7$ [49]), the sixfold order correlations always decay exponentially. Exponentially decaying correlation functions categorically prohibit the possibility of a hexatically ordered phase [19].

Next, we tested if the ectodermal grid exhibits translational order, which would be reflected in a periodic positioning of cells along the D-V or A-P axis (Fig. B.8). Positional order was investigated using the 2D pair correlation function $g(\Delta\mathbf{r})$, i.e. the high-resolution histogram of pair distances, $\Delta\mathbf{r}_{ij} = \mathbf{r}_i - \mathbf{r}_j$, between cells normalized by the number of pairs expected for a Poisson distributed set of cell centers. Integrating this

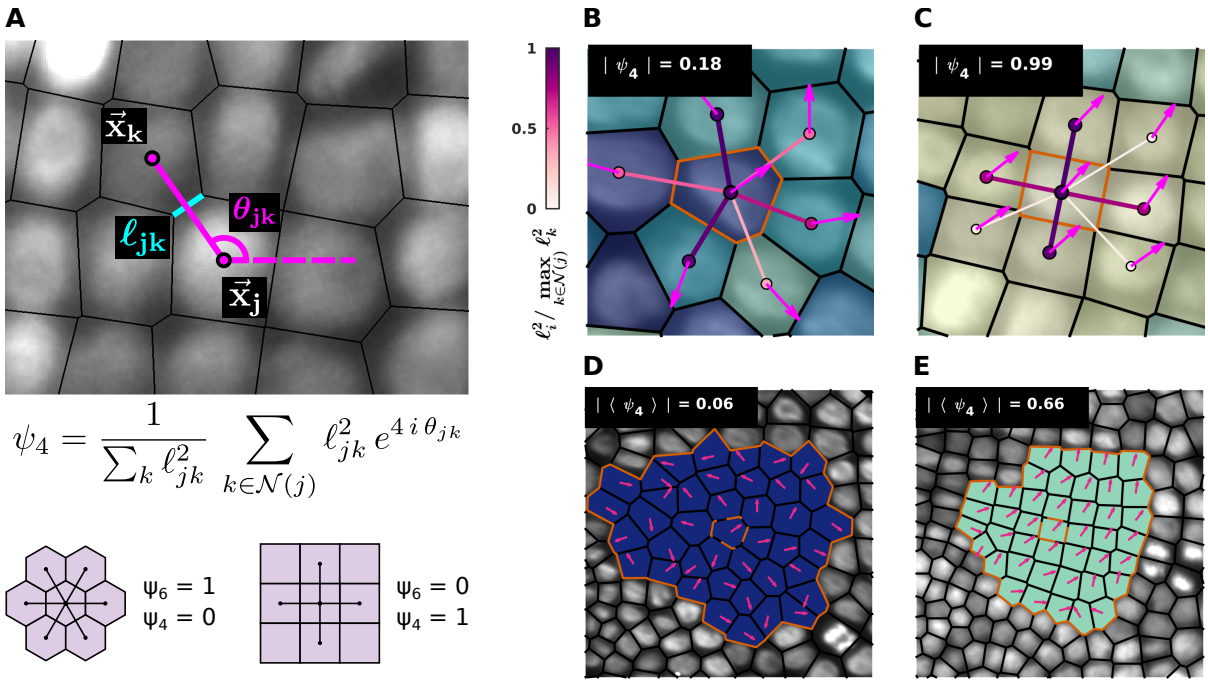

Figure 3.2: **Construction of the orientational order parameter.** (*A*) A schematic of the discrete n-fold complex orientational order parameter. Here, $\vec{\mathbf{x}}_j$ and $\vec{\mathbf{x}}_k$ denote the centroids of cells j and k, respectively, θ_{jk} denotes the angle between the horizontal axis and the separation vector $\vec{\mathbf{x}}_k - \vec{\mathbf{x}}_j$, and ℓ_{jk} denotes the length of the Voronoi edge shared by cells j and k. The sum runs over all cells k in the neighborhood of cell j, i.e. $k \in \mathcal{N}(j)$. The weighting of the sum by the squared Voronoi edge lengths ℓ_{jk}^2 reduces the influence of noise in centroid positions on the final value of the orientational order parameter. Inset at panel bottom shows the order parameter for a schematic pair of perfectly ordered lattices. (*B* and *C*) Specific examples of the construction of the single cell order parameter. Value shown in the inset is the magnitude of the order parameter of the seed cell highlighted by an orange boundary. Cell color and arrows indicate the magnitude and phase of the single cell order parameters, respectively. The color and thickness of the bonds between the seed cell and its neighbors indicate the relative weight with which each bond contributes to the sum defining the order parameter. (*B*) A disordered cell. (*C*) A highly ordered cell. (*D* and *E*) Average fourfold order parameter over the third order natural neighborhood of the single cells shown in (*B*) and (*C*). The dotted orange boundary denotes the seed cell. The solid orange boundary denotes the averaging region. Arrows indicate the orientation of the single cell order parameter for each cell in the averaging region. (*D*) Average order parameter in a disordered region. (*E*) Average order parameter in a highly fourfold ordered region. In general, small differences in orientation will result in significantly lower mean order parameters compared to the magnitude of the single cell order parameters. This effect is especially noticeable in the high order case.

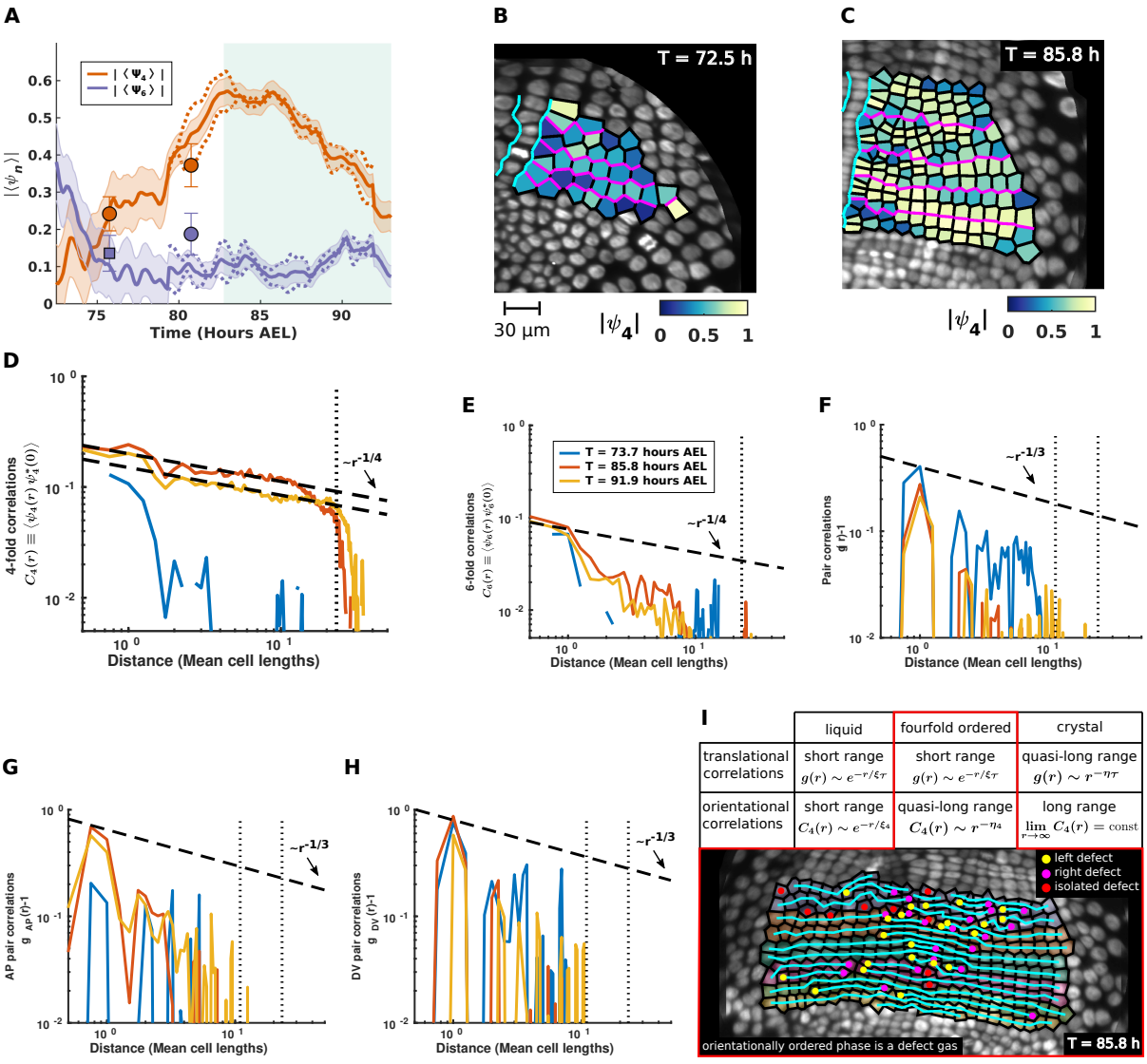
A
B
C
D
E
F
G
H
I
Time (Hours AEL)
T = 72.5 h
T = 85.8 h
30 μm
Distance (Mean cell lengths)
T = 73.7 hours AEL
T = 85.8 hours AEL
T = 91.9 hours AEL
~r^-1/4
~r^-1/3
4-fold correlations
6-fold correlations
Pair correlations
AP pair correlations
DV pair correlations
liquid
fourfold ordered
crystal
translational correlations
orientational correlations
short range
quasi-long range
long range
left defect
right defect
isolated defect
orientationally ordered phase is a defect gas
T = 85.8 h

Figure 3.3: *Parhyale* **germband achieves a fourfold orientationally orderd phase.** (A) The absolute value of the mean fourfold and sixfold orientational order parameters over the whole embryo. Shaded contours show standard errors. (B and C) The absolute value of the single cell fourfold orientational order parameter in the left ectodermal compartment. (D) The two-point correlator of the fourfold orientational order parameter $C_4(r) \equiv \langle \psi_4(r)\, \psi_4^*(0) \rangle$. Vertical line shows the largest lateral dimension of the system. (E) The two-point sixfold orientational correlation functions, $C_6(r) \equiv \langle \psi_6(r)\, \psi_6^*(0) \rangle$, at three representative time points. All time points exhibit exponential decay. Vertical dotted line indicates largest lateral length scale in the system. (F) The isotropic pair correlation function. Vertical dotted lines indicate length scale of the system along the A-P and D-V axes. All time points exhibit exponential decay, implying no isotropic translational order. (G - H) Anisotropic variations of the pair correlation function. All time points for both variations decay exponentially. The lack of anisotropic translational order along any preferred direction preclude the possibility of smectic order in the system. (G) The pair correlation function measured along the D-V axis. (H) The pair correlation function measured along the A-P axis. (I) Table enumerating the types of translational and orientational correlations associated with the different material phases. Translational correlations are measured using the pair correlation function $g(r)$. Note that, unlike a crystal, an orientationally ordered phase is characterized by a gas of defects. Inset image shows edge defects introduced into rows of cells by division during a time when the germband is fourfold ordered.

function over all orientations of the separation vectors yields the isotropic pair correlation function $g(r)$, which gives information about the positional order present in all directions as a function of distance. Anisotropic characteristics of positional order were investigated by analyzing a cut through $g(\Delta \mathbf{r})$ along specific directions [19, 188], i.e. the A-P and D-V axes. More details about the construction of all types of orientation and positional correlation functions, including a discussion of finite size effects (Fig. B.5), can be found in Appendix B. Analysis of the pair correlation functions indicates that the tissue has no isotropic positional order (Fig. 3.3F and Fig. B.13C) and that cell spacing is not periodic along any axis (Fig. 3.3, G and H). Thus, the tissue exhibits neither translational nor smectic order, i.e. positional order along a single spatial direction, despite its seeming regularity. The significance of these measurements was confirmed by extensive validation against synthetic data sets with similar cell densities and system sizes (Fig. B.7 and

Appendix B). The different spatial ranges of translational and orientational correlations associated with the various material phases are summarized in Fig. 3.3I. This lack of periodic cell spacing can be partly explained by the presence of edge defects in rows of cells. Edge defects are locations where a lattice row freely terminates in the interior, i.e. three rows become two. In elasticity theory, such defects are called 'dislocations' and are well-known to disrupt translational order, but preserve orientational order [173]. In the *Parhyale* germband, these defects are disordered, reminiscent of the defect gases characteristic of orientationally ordered phases (Fig. 3.3I). Cell divisions are the primary mechanism mediating both defect generation and subsequent defect dynamics within the tissue. While defects are generally isolated during the time the tissue peaks in orientational order, many defects can be associated with one another by a row of ordered cells with a defect on the left and right sides, respectively (Fig. 3.3I). Together, these results show that the tissue achieves a true orientationally ordered phase extending over the entire trunk ectodermal germband.

3.3 Ectodermal grid is build by waves of oriented cell divisions

We performed single cell tracking to reconstruct the flow fields that organize the ectoderm during the rise of fourfold order. A parasegment pre-cursor row (PSPR) is the fundamental supercellular unit of morphogenesis in the trunk ectodermal germband during this phase of growth [34, 239]. A PSPR is a single row of cells, oriented perpendicularly to the A-P axis, that can be directly associated with particular segments of the adult body. As a unit, PSPRs are appended to the grid sequentially. Cells are recruited from a pool of unorganized ectoderm at the posterior pole of the embryo and assembled

into nascent rows so that each newly constructed PSPR lies immediately posterior to the PSPR that preceded it (Fig. 3.4A). Despite being arranged as a row and in general not containing any edge defects, newly built PSPRs do not yet exhibit fourfold order (Fig. 3.3A and Fig. B.15).

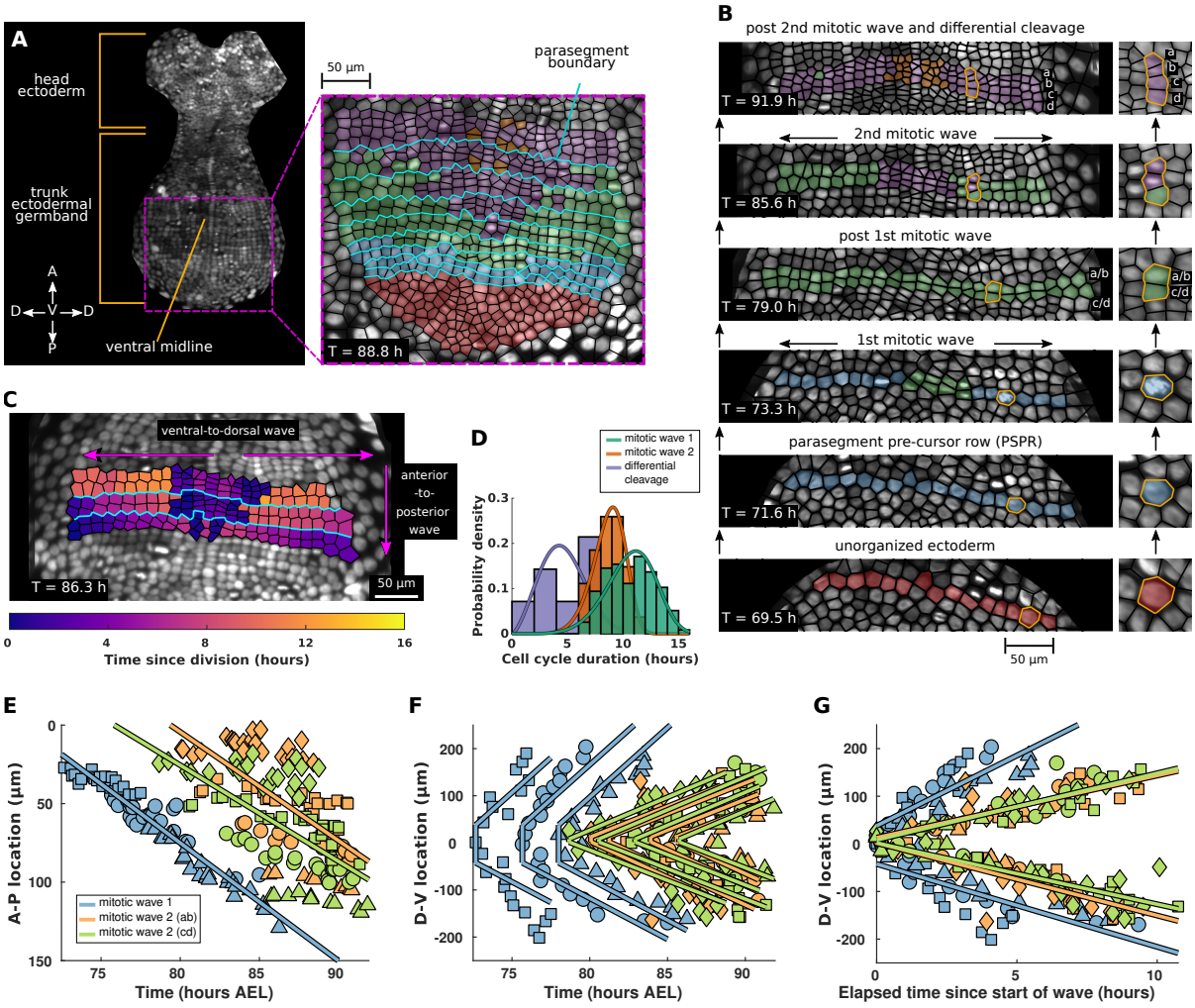

Once a PSPR is assembled, its constituent cells characteristically undergo two rounds of highly choreographed cell divisions. Within each parasegment, mitotic waves are initiated at the ventral midline and spread outward towards the dorsal regions of the embryo (Fig. 3.4B). The timing of these intra-segment waves is stereotypic among all segments (Fig. 3.4G and Fig. B.14C) and, since PSPRs are constructed sequentially,

Figure 3.4: **Waves of actively oriented divisions generate fourfold order.** (A and B) A schematic of parasegment formation and cell proliferation in the trunk ectodermal germband. Inset in (A) shows the spatial distribution of cell populations delineated by number of divisions since parasegment formation once parasegments are assembled from the pool of unorganized ectoderm at the posterior pole. (B) shows the proliferation of a single parasegment. (C) Snapshot of elapsed time since division reveals two orthogonal phase waves within and across parasegments. (D) Distribution of cell cycle durations throughout growth. Solid lines are Weibull distributions fit to the cell cycle duration histograms. Average duration and standard deviation for mitotic wave 1 is 10.7 ± 2.2 hours from $N = 117$ cell cycles. Average duration and standard deviation for mitotic wave 2 is 8.7 ± 1.5 hours from $N = 27$ cell cycles. Average duration and standard deviation for differential cleavage is 4.6 ± 2.0 hours from $N = 7$ cell cycles. (E to G) The location of mitotic wave division events over time. Shapes indicate the parasegment within which a division occurs. Indicated lines are linear fits to all division events associated to a particular mitotic wave. (E) shows the location of each division along the A-P axis. The speed of mitotic wave 1 is 7.5 ± 0.3 μm/hr. The speed of mitotic wave 2 (AB) is 6.9 ± 0.9 μm/hr. The speed of mitotic wave 2 (CD) is 6.1 ± 0.9 μm/hr. (F) and (G) show the location of each division along the D-V axis. Division times in (G) have been normalized to the occurrence of the first division event associated with a particular wave in a specific parasegment. The speed of mitotic wave 1 is 19.2 ± 2.1 μm/hr. The speed of mitotic wave 2 (AB) is 13.9 ± 1.2 μm/hr. The speed of mitotic wave 2 (CD) is 13.1 ± 0.9 μm/hr.

their onset is staggered between adjacent PSPRs (Fig. 3.4, E and F and Fig. B.14, A and B). This choreography leads to two orthogonal phase waves of cell divisions with distinct wave velocities: a fast wave within each PSPR spreading ventral-to-dorsal and a slower one across PSPRs that moves anterior-to-posterior (Fig. 3.4C). After completing these two mitotic waves, each PSPR subsequently undergoes rapid differential cleavage in localized regions adjacent to the ventral midline (Fig. 3.4B). The total duration of the cell cycle differs during these stages, with cells dividing faster during differential cleavage than during the mitotic waves (Fig. 3.4D). Together, these results indicate that PSPRs behave as weakly coupled, independent units running the same modular proliferation program. In other words, cells in different PSPRs begin to divide at different times, but the relative timing of division waves is shared among segments.

The orientations of the divisions comprising the mitotic waves are tightly distributed about the A-P axis (Fig. 3.5A). This coherence of cell division axes appears to be actively maintained. We frequently found that condensed nuclei with the wrong orientation would rapidly rotate to align with the global division axis (Fig. 3.5C). In fact, 7.4% of 770 tracked division events underwent a re-orientation of more than 45 in the 5 minutes prior to dividing. This patterning of oriented and wave-like timed cell divisions ensures that the defects inserted into the lattice by cell division are effectively ferried out of the tissue towards the boundary (Fig. 3.5B). Explicitly, as the mitotic waves gradually insert new rows into the bulk of the grid, the incomplete rows manifest defects at their left and right edges (Fig. 3.3I). As the mitotic waves unfold, these defects are pushed out towards the dorsal regions of the tissue, leaving behind an intact fourfold ordered grid. This type of defect motion is known as ‘defect climb’. It can be contrasted against ‘defect glide’, another familiar type of defect motion, wherein the nascent rows of cells would not extend laterally and defects would instead jump between adjacent PSPRs. In non-living systems, glide generally dominates climb since gliding only requires simple updates to

the connectivity of nearest-neighbors, whereas climb requires the creation of vacancies or interstitial defects [54]. Defect climb in non-living systems typically only becomes the dominant mode of defect motion at extremely high temperatures [245]. Here, the presence of cell divisions excites defect climb at room temperature, such that defects, which would otherwise disorder the lattice, are healed by subsequent divisions. In this way, cell divisions are able to serve as an order generating mechanism.

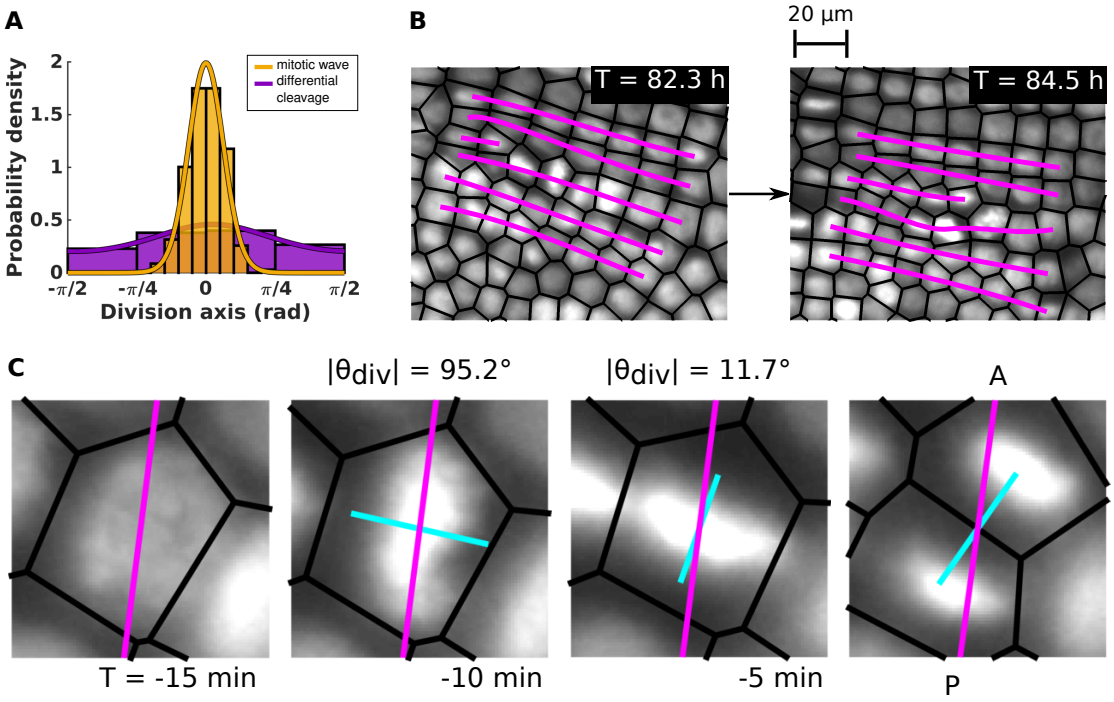

Figure 3.5: **Divsion orientations are actively aligned with the A-P axis.** (A) The orientation of cell division axes relative to the A-P axis. Indicated curves are von Mises distributions fit to histogram counts. The circular mean division angle and angular deviation for the mitotic waves are $\overline{\theta}_{MW} = 0.00$ rad and $s_{MW} = 0.41$. The circular mean division angle and angular deviation for the differential cleavage are $\overline{\theta}_{DC} = 0.15$ rad and $s_{MW} = 1.27$. (B) Schematic of division induced defect climb along parasegments. (C) Example of active re-orientation of a nucleus immediately prior to cell division.

Next, we investigated how the division choreography dynamically shapes the ectoderm at the tissue scale. For the purposes of this analysis, we focused on a subset of six PSPRs. We determined that growth proceeds in two stages (Fig. 3.6A). In the first stage, mitotic

waves extend the germband by inserting new rows without changing the average cell density (Fig. 3.6, B to D). The tissue elongates along the A-P axis and increases in total area, but its width remains approximately constant. In the second stage, the tissue undergoes convergent extension. Its width is sharply pinched, but its length continues to increase in such a way that the total tissue area is held approximately fixed. Since the rate of cell division remains constant throughout both stages (Fig. 3.1F), the average cell density necessarily increases during convergent extension.

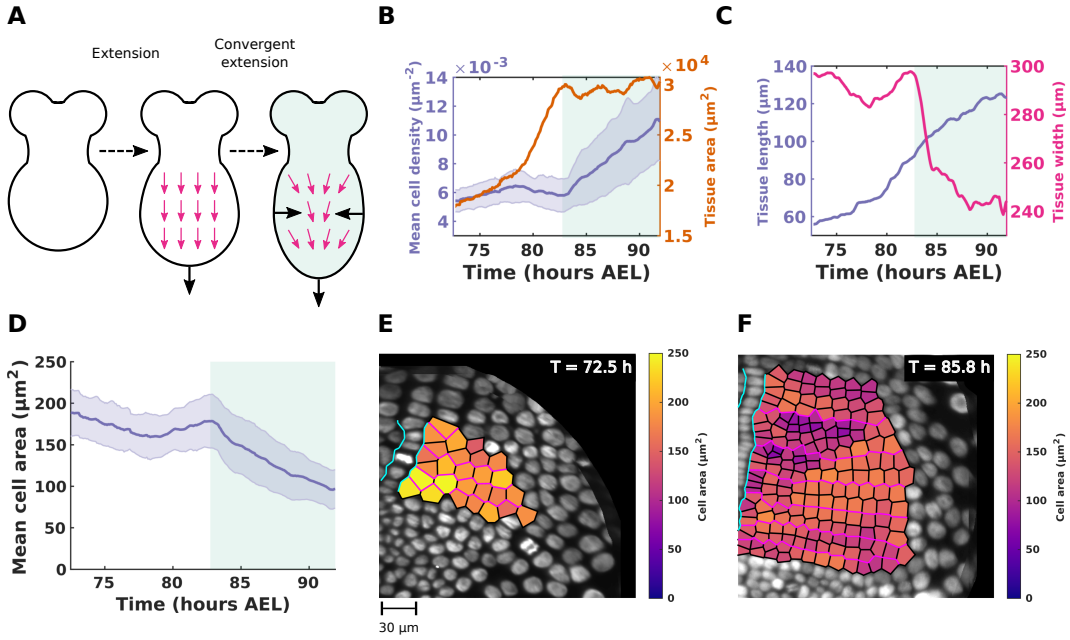

Figure 3.6: **Germband extension proceeds in two stages defined by different modes of tissue scale shape change.** (*A*) Schematic of the two stages of tissue scale growth observed in the germband. (*B* to *C*) Tissue scale observable fields in the germband. Tissue cartography ensures 3D geometry is properly accounted for. Shading corresponds to the two observed stages of growth. (*B*) Mean cell density and total tissue area . Blue shaded region shows standard deviation. (*C*) The tissue length measured along the A-P axis and the tissue width measured along the D-V axis. (*D*) The mean cell area over time. Shaded region shows standard deviation. (*E* and *F*) Cell areas at two representative time points in the left ectodermal compartment. Cell size varies primarily as a function of timing in the cell cycle (recently divided cells are smaller - see Fig. B.10B). However, cell size is essentially uniform in space at each time point for cells in similar points in their respective cell cycles.

These two stages also feature markedly different dynamics of the global order pa-

rameter (Fig. 3.3A). During the first stage, when the large scale motion of the tissue appears to be dominated by the mitotic waves, the global order parameter consistently increases. In the second stage, wherein the tissue experiences a reduction in width that is not explained by the mitotic waves alone, the global order parameter is initially static, but slowly falls off.

3.4 Active hydrodynamic model confirms divisions generate tissue scale motion

Having separately elucidated the kinetics of cell proliferation and the time course of tissue geometry, our next goal was to explicitly connect local cell behaviors with global tissue shape and flow. We adopted a coarse-grained description of the tissue-scale mechanics, similar to recent applications aimed at decoding how active forces generate tissue flow patterns [74, 236, 208, 26, 197]. Motivated by our observation of exponential growth through cell proliferation, we developed a hydrodynamic model, similar to the Stokes equations, that directly links tissue flow to bulk contributions from oriented cell divisions via an active sourcing term:

$$\nu_1 \nabla^2 \mathbf{v} + \nu_2 \nabla (\nabla \cdot \mathbf{v}) = -\nabla \cdot \boldsymbol{\sigma}^a \equiv -\mathbf{F}^a, \tag{3.2}$$

where $\mathbf{v}$ denotes the tissue velocities, $\boldsymbol{\sigma}^a$ are the active stresses, $\mathbf{F}^a$ are the corresponding active forces, $\nu_1 = \tau_R \mu$ is an effective shear viscosity, $\nu_2 = \tau_R(\mu + \lambda)$ is an effective bulk viscosity, τ_R is a time scale corresponding to mechanical relaxation due to growth/tissue remodeling, and μ and λ are the familiar Lamé parameters of continuum elasticity (see Appendix C). For simplicity, we assume in our model that cell divisions are the only source of active stresses. During division, the mitotic spindle within cells generates

extensile forces akin to a force dipole [201, 68]. These division events push on nearby cells, deforming the dividing cell's neighbors and generating local plastic strain. Viscoelastic relaxation of this instantaneous strain leads to flow in the surrounding tissue (Fig. 3.9A). In this way, many division events can combine to create large scale collective motion. We investigated the extent to which the integrated deformations induced by divisions could collectively account for the observed global tissue flow. We first deduced the average plastic deformation induced by a single cell division by rotating all observed cell division events into a common frame (Fig. 3.7 and Fig. 3.8). Informed by the features of this average flow field, individual division events were modeled as circular inclusions, i.e. finite regions within which the tissue undergoes a permanent plastic strain [73], with an orientation chosen to align with each measured division axis. We then solved our model using the finite element method (FEM) with Dirichlet boundary conditions to predict the tissue flow from observed cell divisions (Fig. C.1).

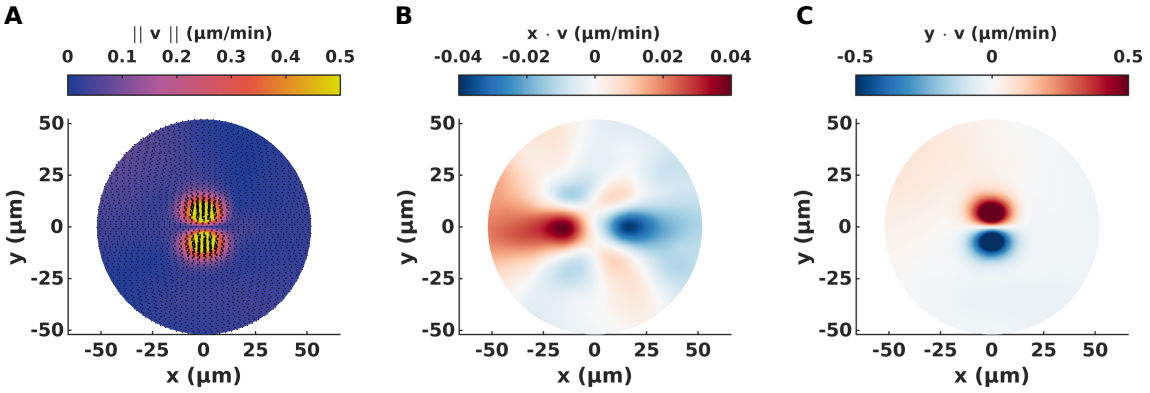

Figure 3.7: **Average velocity induced by division events in the tissue.** (A) The magnitude of the velocity of the mean cell division event. Arrows showing orientation are scaled by the norm of the velocity. (B) The x-component of the velocity of the mean cell division event. (C) The y-component of the velocity of the mean cell division event.

To benchmark accuracy of this model, we compared the predicted tissue flow to velocity fields quantified from individual cell tracking. Measured tissue flow fields were mostly harmonic, irrotational, and divergence-free, except at cell divisions, where the

divergence, curl, and Laplacian of the flow fields all spiked (Fig. 3.9, C to E and Fig. B.6). Visually, the flow fields predicted from our model appear strikingly similar (Fig. 3.9, F to H).

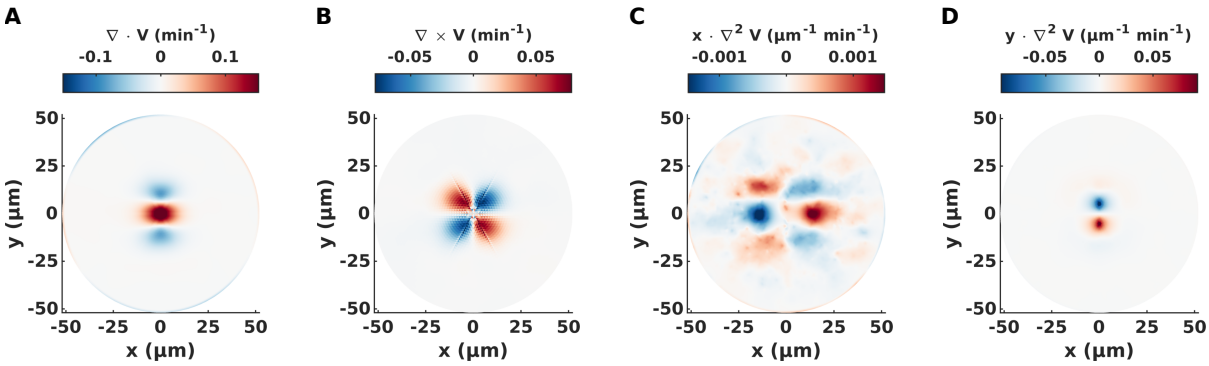

Figure 3.8: **Gradients of the velocity of the mean cell division event.** (**A**) The divergence of the mean cell division velocity. (**B**) The 'curl' of the mean cell division velocity. (**C**) The x-component of the Laplacian of the mean cell division velocity. (**D**) The y-component of the Laplacian of the mean cell division velocity.

To compare the measured flow fields $\mathbf{v}(\mathbf{x})$ to the predicted flow fields $\mathbf{u}(\mathbf{x})$ in a quantitative fashion, we defined a global measure for the spatial velocity residual that was insensitive noise dominated fluctuations in the regions of slow flow. Let

$$< \mathbf{u} > \equiv \sqrt{< \mathbf{u}(\mathbf{x}) \cdot \mathbf{u}(\mathbf{x}) >_{embryo}} \tag{3.3}$$

define an overall magnitude of the field $\mathbf{u}(\mathbf{x})$. Here, $< \mathbf{u}(\mathbf{x}) \cdot \mathbf{u}(\mathbf{x}) >_{embryo}$ denotes an average of the spatially dependent field $\mathbf{u}^2(\mathbf{x}) = \mathbf{u}(\mathbf{x}) \cdot \mathbf{u}(\mathbf{x})$ over the entire embryo and is therefore not space dependent. We define our velocity residual as

$$R = \frac{(< \mathbf{u} >^2 \ \mathbf{v}^2(\mathbf{x}) + \mathbf{u}(\mathbf{x})^2 \ < \mathbf{v} >^2) - 2\sqrt{< \mathbf{u} >^2 < \mathbf{v} >^2}\, \mathbf{v}(\mathbf{x}) \cdot \mathbf{u}(\mathbf{x})}{2 \ < \mathbf{u} >^2 < \mathbf{v} >^2}. \tag{3.4}$$

This residual provides a spatial discrepancy map, indicated the prediction quality as a function of location on the embryo. An identical velocity residual was used in [236].

The velocity residual quantitatively confirms that our simple model accurately predicts both the direction and magnitude of the observed tissue flow (Fig. 3.9, I to K) (see Appendix C). During the first phase of growth, velocity residuals are typically below 10% (Fig. 3.9B and Fig. C.2). This suggests that about 90% of the flow can be accounted for in terms of cell divisions as the dominant bulk contribution. Velocity residuals subsequently increase moderately during convergent extension, reaching a typical level around 20%. This suggests divisions are still the main driver, but other mechanisms, currently not accounted for by the model, provide small but measurable adjustments.

3.5 Active vertex model reveals how directed divisions generate orientational order

Finally, we directly investigated the role of oriented divisions in mediating both cell and tissue scale orientational order by simulating division waves using a simple vertex model defined by the energy

$$E = \frac{1}{2} \sum_c \left[(A_c - A_0)^2 + (P_c - P_0)^2 \right] . \tag{3.5}$$

where c is a label for cells, A_c is the area of cell c, P_c is the perimeter of cell c, A_0 is a target cell area, and P_0 is a target cell perimeter. Both A_0 and P_0 were assumed to be the same for all cells. For all simulations, we set the shape index parameter $p_0 = P_0/\sqrt{A_0} = 4$, i.e. the preferred shape index of a perfect square. This choice was consistent with the observation that actual cells in the tissue obtain $p_0 \approx 4$ throughout the entire process of ectodermal grid formation (Fig. 3.10A). Initial conditions for our simulations consisted of a hexatically, but not translationally, ordered arrangement of cells and a division order constructed so that cells divided in a wave. We chose to use a hexatically ordered initial

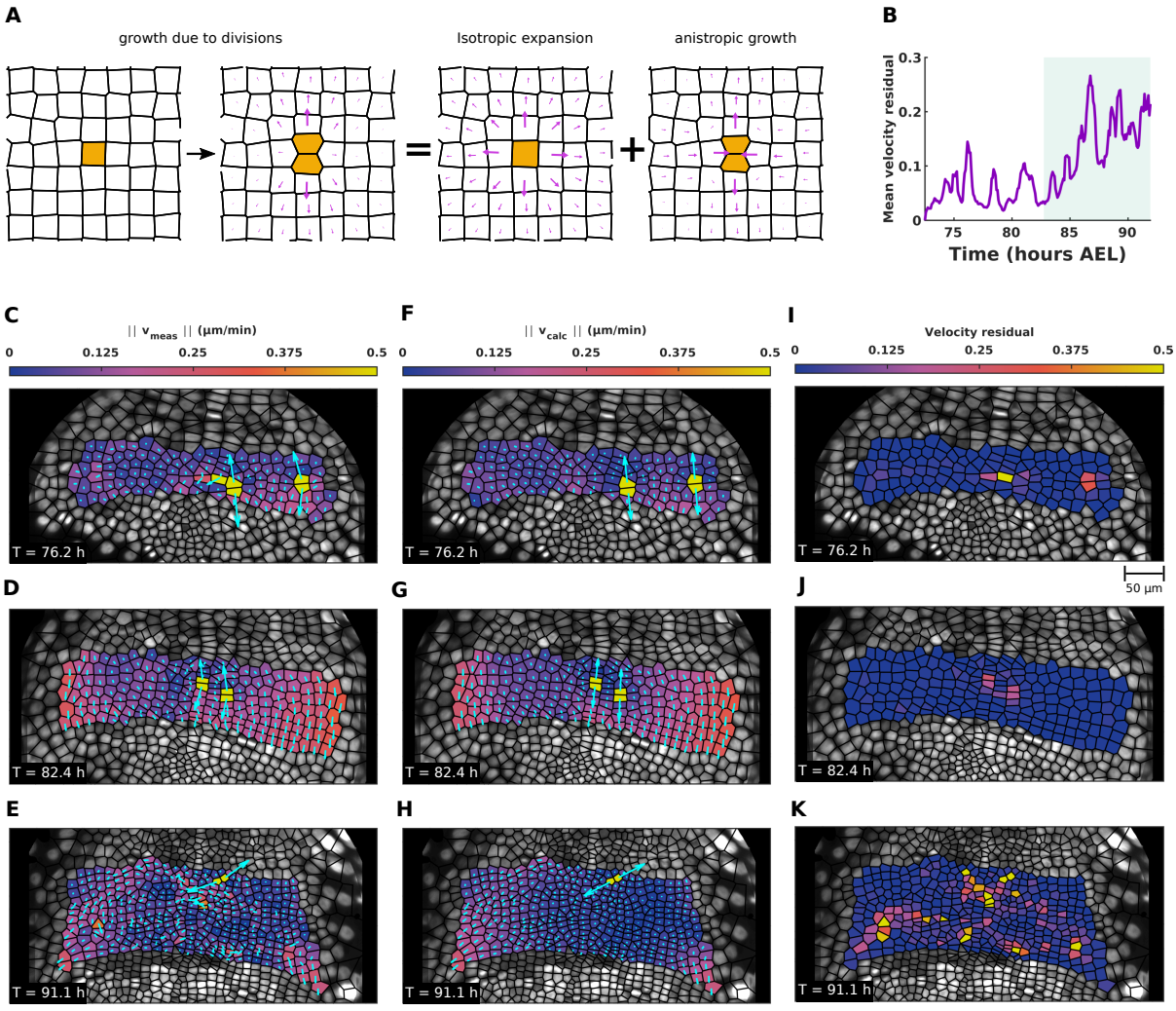

Figure 3.9: **Active cell divisions dictate tissue velocities during germband extension.** (A) Schematic of the flow field induced by a single division event. (B) Mean residual between the measured cell velocities and the cell velocities predicted by the active hydrodynamic model. $(C$ to $E)$ Cell velocities measured by single cell tracking. $(F$ to $H)$ Predicted cell velocities. $(I$ to $K)$ Single cell velocity residuals for the measured and calculated velocity fields shown in $(C$ to $E)$ and $(F$ to $H)$, respectively.

condition in order to ensure that the simulated tissue was comprised of well defined rows with no fourfold order. Simulations then proceeded by growing and dividing a single cell at a time. Each cell was selected to divide along an axis drawn from a circular von Mises distribution with variable concentration k (Fig. 3.10F). The entire tissue was then completely relaxed to an equilibrium configuration at the end of each growth/division step. We also imposed a confinement constraint on the tissue that kept its total width constant throughout the growth process, consistent with the behavior of the germband during the first stage of growth (Fig. 3.6C). More details about our choice of algorithm and parameters can be found in Appendix D. The results of a typical division wave simulation are shown in Fig. 3.10, B and C.

After a single division wave, all simulations with division orientation concentrations of $k \gtrsim 4$ managed to produce global fourfold order parameters of similar magnitude to those observed in the real tissue (Fig. 3.10D) and exhibited algebraically decaying fourfold orientational correlations over the entire simulated domain (Fig. 3.10E). Simulations with sufficiently random division orientations destroyed all order within the system (Fig. 3.10D and Fig. D.1). Interestingly, the simulations also showed that the wave-like spatiotemporal choreography of division timings was not strictly necessary to generate fourfold order. In fact, while the time course of order through the simulations was markedly different, simulations with random division timings produced almost identical fourfold ordering once all of the cells had divided (Fig. 3.10G). This observation reinforces the conclusion that oriented divisions constitute a robust mechanism for fourfold order generation without the need for micromanaged division timings. Our simulations also provided a platform to directly test the extent to which defects introduced into the ectoderm by cell division mediate the loss of order within the tissue (Fig. 3.10H).

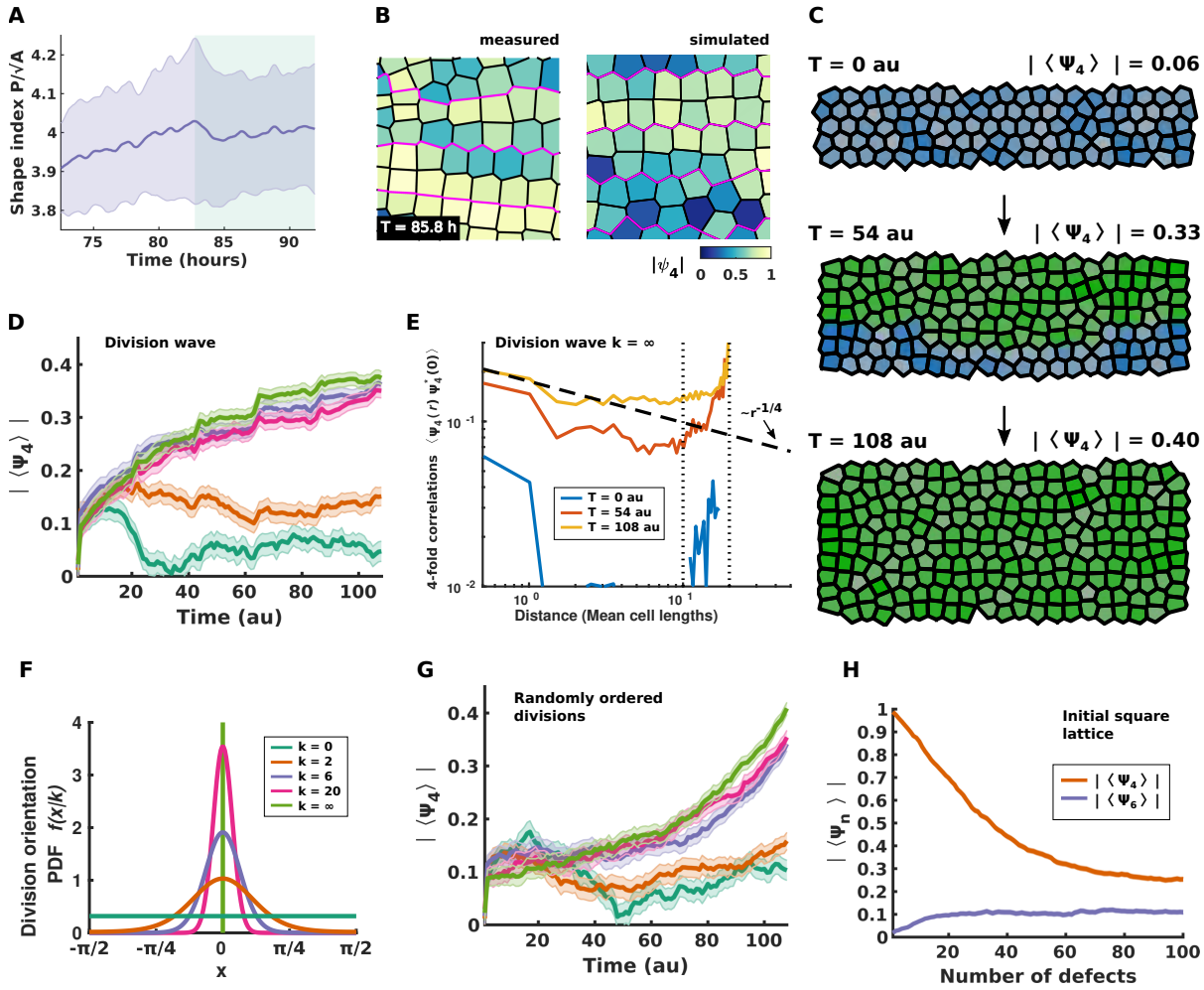
A
Shape index P/√A
4.2
4.1
4
3.9
3.8
75
80
85
90
Time (hours)
B
measured
simulated
T = 85.8 h
|ψ4|
0
0.5
1
C
T = 0 au
| ⟨Ψ4⟩ | = 0.06
T = 54 au
| ⟨Ψ4⟩ | = 0.33
T = 108 au
| ⟨Ψ4⟩ | = 0.40
D
Division wave
| ⟨Ψ4⟩ |
0.4
0.3
0.2
0.1
0
20
40
60
80
100
Time (au)
E
Division wave k = ∞
4-fold correlations ⟨Ψ4(r) Ψ4*(0)⟩
10 -1
10 -2
10 0
10 1
~r-1/4
T = 0 au
T = 54 au
T = 108 au
Distance (Mean cell lengths)
F
Division orientation PDF f(x/k)
4
3
2
1
0
-π/2
-π/4
0
π/4
π/2
x
k = 0
k = 2
k = 6
k = 20
k = ∞
G
Randomly ordered divisions
| ⟨Ψ4⟩ |
0.4
0.3
0.2
0.1
0
20
40
60
80
100
Time (au)
H
Initial square lattice
| ⟨Ψn⟩ |
1
0.9
0.8
0.7
0.6
0.5
0.4
0.3
0.2
0.1
0
| ⟨Ψ4⟩ |
| ⟨Ψ6⟩ |
20
40
60
80
100
Number of defects

Figure 3.10: **Oriented divisions generate fourfold order in vertex model simulations.** (A) The mean cell shape index $p_0 = P/\sqrt{A}$ as a function of time in the trunk segmental ectoderm, where P is the cell perimeter and A is the cell area. Shaded region shows standard deviation. The shape index remains close to 4 (the shape index of a perfect square) for the entirety ectodermal grid formation. (B) A comparison of cell geometry and fourfold order drawn from data (left) and simulation (right). Magenta lines denote boundaries between adjacent parasegments. (C) Illustration of a typical division wave simulation. Hue corresponds to number of cell divisions within a lineage and saturation represents orientational order (disordered regions are less saturated). (D) The absolute value of the mean fourfold order parameter during division wave simulations. Different curves correspond to different concentrations k of distributions from which division orientations were randomly drawn (see panel (F)). Above $k \gtrsim 5$ the division wave reliably generates fourfold order. Shaded regions show standard error. (E) The two-point correlation function of the fourfold orientational order parameter generated by division wave simulations with $k = \infty$. Vertical lines indicate the length and width of the tissue, respectively. Final configurations obtain quasi-long range fourfold order. (F) Illustrations of the von Mises distributions from which division orientations were drawn during simulation. $k = 0$ corresponds to uniformly random divisions and $k = \infty$ correspond to perfectly oriented divisions. (G) The absolute value of the mean fourfold order parameter generated using the same parameters as panel D, but with random division timings rather than a division wave. (H) Illustration of the breakdown of orientational order in an initially square lattice due to the presence of defects inserted by cell divisions.

3.6 Discussion

In this work, we combined mathematical modeling with quantitative flow analysis to show that cell divisions are the primary drivers of global tissue flow during *Parhyale* germband extension. We uncovered a global fourfold bond orientationally ordered phase that emerges via precisely oriented cell divisions. In a scheme we call defect driven morphogenesis, cell proliferation introduces defects into the local tissue structure, which are then mobilized by subsequent cell divisions, ultimately giving rise to a highly ordered cell network (Fig. 3.11). The choreography of these events is arranged in a timed mitotic wave, spreading at distinct wave velocities across the A-P and D-V axes. The anisotropic timing of this wave of cell divisions results in defect climb at room temperature. Many defects migrate out of the ectodermal bulk toward the boundary. The sparse set of defects that remain destroy translational order, but leave the orientational order intact. Defect driven morphogenesis is both an efficient and a highly robust mechanism for establishing global orientational order in presence of cell divisions. Similarly to non-living matter [8], the insertion of new particles is an efficient strategy for exploring regions of configuration space corresponding to orientational order. Provided a preferred axis, order can then be produced by having cells divide according to independent, internal timing mechanisms. This timing does not have to be precise (Fig. 3.4D). Order within a local region is preserved so long as most of the cells within that region divide once before any particular cell divides twice.

We showed that defect driven morphogenesis at the single cell level relies on tightly oriented cell divisions. Our analysis demonstrated that neither the orientation (Fig. B.9) nor the timing of cell divisions (Fig. B.10, Fig. B.11, Fig. B.12) exhibit strong correlations with mechanical or geometric signals. This suggests that cell division timing and orientations are actively instructed by biochemical signals, such as morphogen gradients

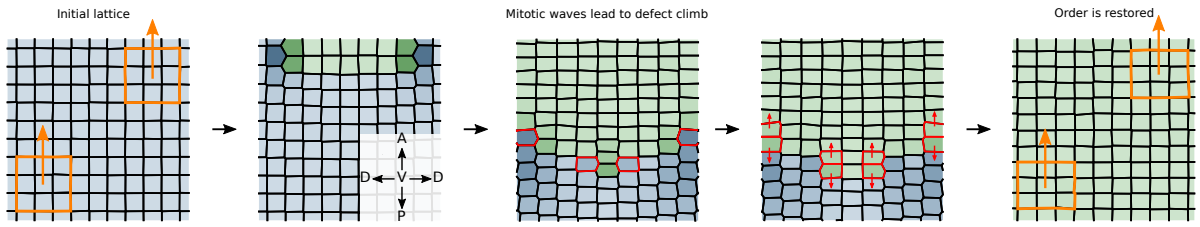

Figure 3.11: **Defect driven morphogenesis generates fourfold order in growing tissue.** A schematic summarizing the role of division choreography in generating and maintaining orientational order. Hue corresponds to number of cell divisions within a lineage and saturation and value represent orientational order (less ordered regions are darker). Order is maintained and the grid is restored so long as the divisions are oriented along a single axis and each cell divides once before any particular cell divides twice. Cells divisions shown in the middle panels are highlighted in red. Orange regions in the first and last panels show the direction of local order is coherent over long distances and preserved by the division choreography.

or planar cell polarity, rather than by mechanical feedback. It would be interesting to investigate the precise nature of these biochemical signals and, in particular, the role of myosin, since heterogeneous distributions of junctional myosin have been shown to be capable of generating similar cobblestone patterns in the absence of cell proliferation [12]. For small direct developers, like *Parhyale*, arranging cells in an ordered grid might be one of very few possibilities to establish a coordinate system in the presence of growth [262]. It is intriguing to speculate whether large embryos, with abundant cell numbers, utilize a similar ordering strategy at the mesoscale when arranging bigger periodic units comprised of many cells, such as the somites in vertebrates [225]. Future work will investigate how defect driven morphogenesis differs in implementation between relatively small embryos and embryos with large cell numbers and the relationship between tissue scale order and shape change (Fig. B.4).

Chapter 4

A kinetic mechanism links gene expression to visceral organ morphogenesis in *Drosophila*

Organ architecture is often composed of multiple laminar tissues arranged in concentric layers. During morphogenesis, the initial geometry of visceral organs undergoes a sequence of folding, adopting a complex shape that is vital for function. Genetic signals are known to impact form, yet the dynamic and mechanical interplay of tissue layers giving rise to organs' complex shapes remains elusive. Here, we trace the dynamics and mechanical interactions of a developing visceral organ across tissue layers, from subcellular to organ scale in vivo. Combining deep tissue light-sheet microscopy for in toto live visualization with a novel computational framework for multilayer analysis of evolving complex shapes, we find a dynamic mechanism for organ folding using the embryonic midgut of Drosophila as a model visceral organ. Hox genes, known regulators of organ shape, control the emergence of high-frequency calcium pulses. Spatiotemporally patterned calcium pulses trigger muscle contractions via myosin light chain kinase. Muscle

contractions, in turn, induce cell shape change in the adjacent tissue layer. This cell shape change collectively drives a convergent extension pattern. Through tissue incompressibility and initial organ geometry, this in-plane shape change is linked to out-of-plane organ folding. Our analysis follows tissue dynamics during organ shape change in vivo, tracing organ-scale folding to a high-frequency molecular mechanism. These findings offer a mechanical route for gene expression to induce organ shape change: genetic patterning in one layer triggers a physical process in the adjacent layer – revealing post-translational mechanisms that govern shape change.

4.1 Introduction

Visceral organ morphogenesis proceeds by the assembly of layered cell sheets into tubes, which develop into complex shapes [172]. Through this process, genetic patterning instructs cellular behaviors, which in turn direct deformations in interacting tissue layers to sculpt organ-scale shape. This motif arises, for instance, in the coiled chambers of the heart, contortions of the gut tube, and branching airways of the lung [215, 138, 160]. Meanwhile, elastic bilayer sheets highlight the potential for mechanical interactions alone to generate nontrivial 3D shape transformations [252]. While studies of monolayer tissue development in planar geometries imaged near the embryo surface or *ex vivo* have uncovered general principles [112, 236, 208, 202], following the dynamics of fully 3D visceral organ shape change has remained out of reach [160, 200]. Physical models inferred from static snapshots of organ morphology have proven useful in this regard, but connecting dynamics at the cellular and sub-cellular level with the dynamics of shape change at the organ scale through live imaging remains a new frontier [253, 215, 226].

Uncovering cell and tissue dynamics in a shape-shifting organ presents several challenges. A conceptual challenge is that visceral organs exhibit both genetic and mechanical

interactions between multiple tissue layers [230, 108]. Technical challenges arise as well, since their complex, dynamic shapes develop deep inside embryos. Capturing dynamics *in vivo* therefore requires imaging methods that overcome image degradation due to scatter [62] and a computational framework for analysis of complex shapes.

The embryonic midgut – composed of muscle cells ensheathing an endodermal layer, linked by extracellular matrix (Fig. 4.1A) – offers a system in which we can overcome these challenges and probe *in toto* organ dynamics across tissue layers at sub-cellular resolution. Its size and the molecular toolkit of the model system render the midgut ideal for light-sheet microscopy [127], tissue cartography [100], and non-neuronal optogenetics [91]. Hox genes expressed in the muscle layer are required for the midgut to form its four chambers, but the mechanism by which genetic expression patterns are translated into tissue deformation, and in turn to organ shape, remains unclear (Fig. 4.1B-C) [21, 105, 265, 22, 109, 203, 186]. Here we connect this genetic patterning to mechanical interactions between layers during development and track the kinematic mechanism linking mechanical action to organ shape transformations. We find that dynamic, high-frequency calcium pulses drive patterned muscle contraction, inducing bending and convergent extension in the endoderm to sculpt stereotyped folds.

4.2 Live deep tissue imaging reveals bilayer morphogenesis

The midgut is a closed tube by stage 15 of embryonic development, residing 20-60μm below the embryo surface [15]. The organ first constricts halfway along its length, then constricts again to subdivide into four chambers. Within $75-90$ minutes after the onset of the first fold, the constrictions are fully formed, and the organ beings to adopt a

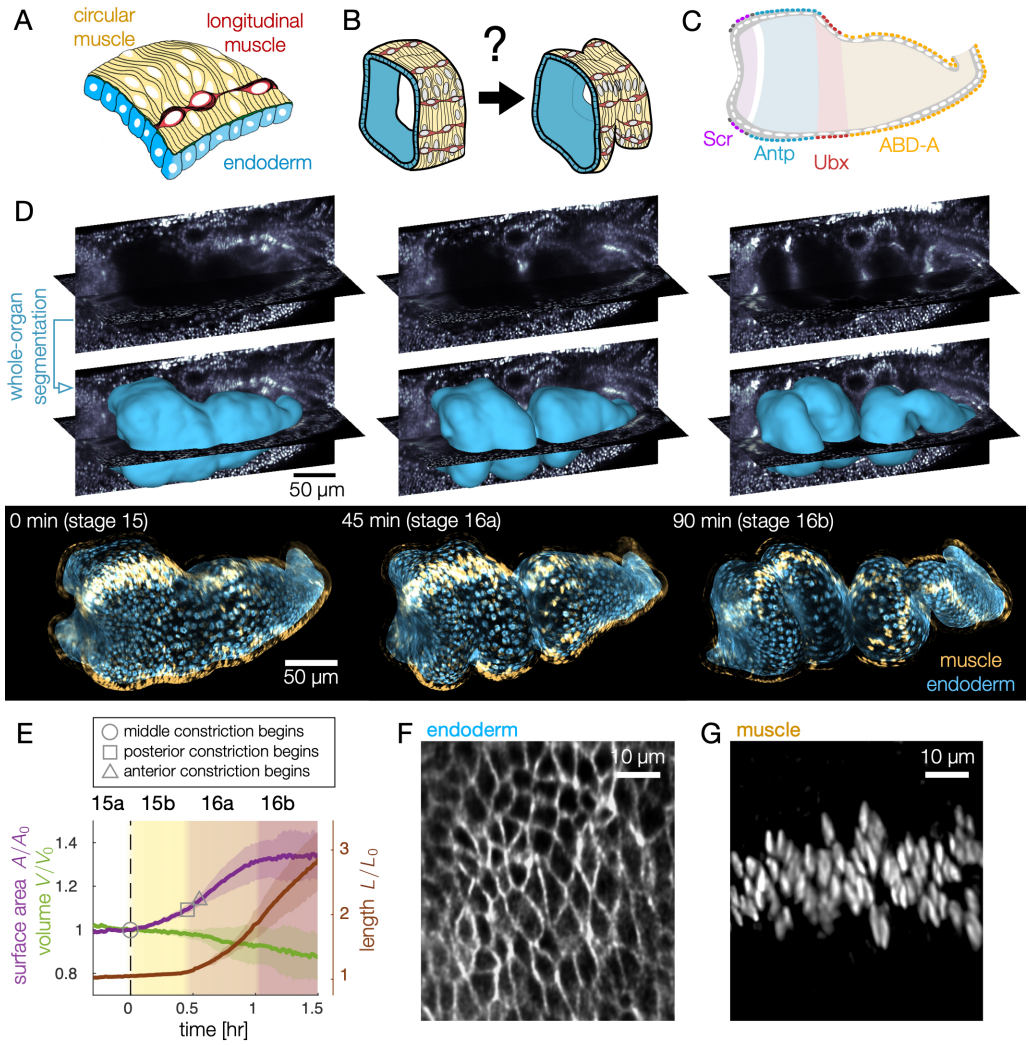

Figure 4.1: **Deep tissue live imaging reveals bilayer gut morphogenesis.** (*A-B*) Muscle and endoderm layers compose the midgut and interact to generate 3D shape. (*C*) Genetic patterning of hox transcription factors that govern midgut morphogenesis appears in the circumferential muscles. (*D*) Automatic segmentation using morphological snakes level sets enables layer-specific imaging, here shown for muscle (yellow) and endoderm (blue) for a *w,Hand>GAL4;UAS-Hand:GFP;hist:GFP* embryo. Morphogenesis proceeds first with a constriction cleaving the gut into two chambers (stage 15b). Two more constrictions form a total of four chambers (16a) before the gut begins to coil (16b onward). Stages follow [15]. (*E*) Surface area of the apical surface increases gradually during constrictions, but levels off by stage 16b. The enclosed volume decreases gradually, while the effective length of the organ – computed via the length of a centerline – nearly triples. Solid curves denote mean and shaded bands denote standard deviation ($N = 6$). (*F-G*) Segmentation of the endoderm layer from MuVi-SPIM imaging resolves individual cells, both in the endoderm and muscle layers, shown here at stage 15a.

contorted shape.

Quantitative characterization of these dynamics requires extraction of the full organ's geometry, which is challenging due to tissue scatter. We overcome this challenge by *in toto* live imaging using confocal multi-view light sheet microscopy [62]. In conjunction, we express tissue-specific markers using the GAL4-UAS system [29] in *klarsicht* embryos [259], which exhibit genetically-induced optical clearing (see Appendix E). To translate this volumetric data into dynamics of the midgut surface, we combine machine learning [18] with computer vision techniques [168, 42] using an analysis package dubbed 'TubULAR' [164]. In this way, we are able to resolve sub-cellular structures with 1 minute temporal resolution (Fig. 1.4, Fig. 4.1D and Fig. E.1).

We find that gut morphogenesis is stereotyped and exhibits reproducible stages (Fig. 4.1E). The surface area grows by $\sim 30\%$ during folding (stages 15a-16a) and remains constant by the time constrictions are fully formed (16b), despite continued shape change. The enclosed volume within the midgut decreases only gradually during this process, while the effective length of the organ – the length along its curving centerline – triples (Fig. 4.1E, Appendix E).

4.3 Endodermal cell shape change underlies tissue shape change

How does this 3D shape change occur at the tissue and cellular scale? We first analyzed the endoderm layer. Inspection of these cells reveals strikingly anisotropic cell shapes before constrictions begin (Fig. 4.1F and Fig. 4.2A-B). In order to quantify cell shape on this dynamic surface, we cartographically project into the plane using TubULAR [164]. This projection generates a global coordinate system in which we

unambiguously define the anterior-posterior (AP) and circumferential axes for all time points, even when the organ exhibits deep folds and contortions (Fig. E.3 and [164]).

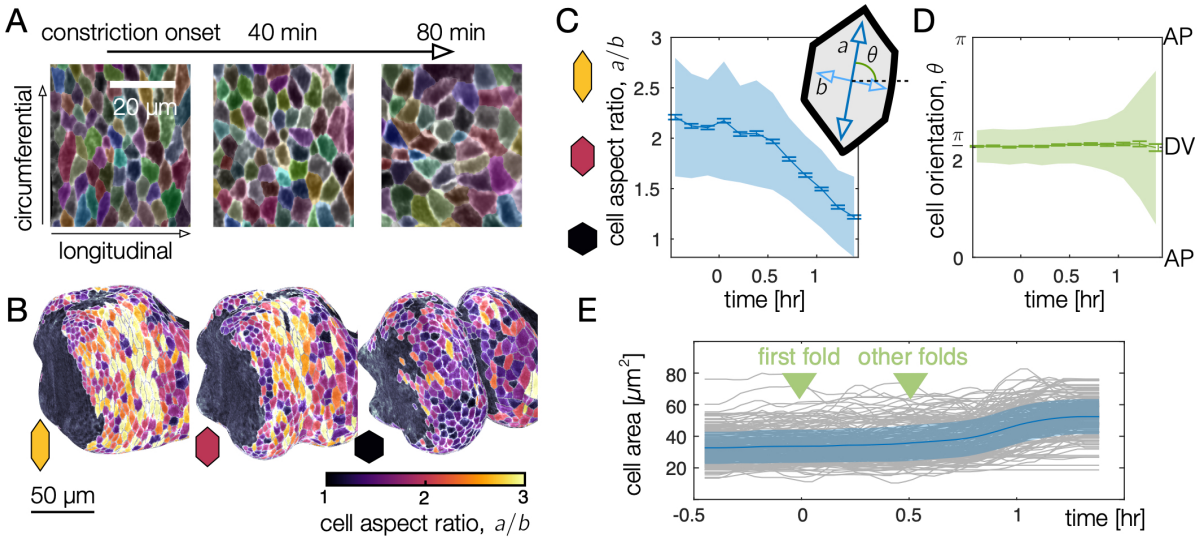

Figure 4.2: **Endodermal cell shape changes underlie organ shape change.** (A) Cell segmentation in a computationally flattened coordinate patch shows endodermal cells are initially elongated along the circumferential direction but change their shape during organ folding. $(B\text{-}C)$ Cell aspect ratios evolve from $a/b > 2$ to $a/b \approx 1$, shown in 3D for cells near the anterior fold. (C) Colored bands denote area-weighted standard deviations for 600-1300 segmented cells per timepoint, and tick marks denote standard error on the mean. (D) As cells change their aspect ratio, their orientations do not rotate. (E) Single-cell tracking shows gentle increase of cell areas through violent folding events, suggesting that cell area changes do not drive organ shape change. Blue curve and shaded region denote mean and standard deviation, with raw traces in gray.

By segmenting cell shapes, we find that endodermal cells are strongly anisotropic, with an average aspect ratio $a/b > 2$, and are globally aligned along the circumferential axis (Fig. 4.2A-C). As constrictions develop, cells loose this anisotropy and even become elongated along the AP axis in posterior regions (Fig. 4.2B-C and Fig. E.4A). Measurement of endodermal cell orientations reveal that this effect is not due to rotations (Fig. 4.2D). As shown in Fig. E.4A, the initial anisotropy is patterned along the AP axis so that cells near two of the constriction locations are most anisotropic. While we do not

presently know the mechanism of this patterning, it suggests these tissue regions may be primed for deformation by positional information before constrictions begin. Subsequent cell shape change is greatest near each constriction, as shown in Fig. E.4B.

Despite the large changes in aspect ratio, cell areas in the endoderm change only gradually (Fig. 4.2E), such that cells converge along the circumferential axis while extending along the folding longitudinal axis. On a larger scale, the observed cellular deformation would collectively generate tissue movement called convergent extension. At the same time, other processes – such as oriented divisions or cell intercalations – could also contribute or counteract tissue-scale convergent extension [74]. However, we find no signs of cell division during this process, confirming previous observations [15]. Moreover, though tracking quartets of cells in the anterior midgut revealed widespread intercalations (also called T1 transitions), the orientations of these events were not significantly biased for the early stages of constriction (Fig. E.5). This suggests that anisotropic cell shape change may be the primary contributor to tissue-scale shape change. We next tested this hypothesis, asking how in-plane, cell-scale shape change connects to out-of-plane, tissue-scale deformations during constrictions.

4.4 Tissue-scale convergent extension via constriction

To understand the kinematic mechanism underlying organ shape, we must bridge spatial scales from cell deformation to meso-scale tissue deformation. Given that the midgut tissue is thin compared to the organ radius, cells exert forces on one another primarily through in-plane interactions, but in-plane mechanical stress can couple to curvature to generate out-of-plane motion [6]. In a nearly incompressible tissue constricting out-

of-plane, cells do not change area, but may change shape, collectively driving in-plane motion. In such a situation, we make sense of dilatational flow and out-of-plane deformation and interpret their difference as the local area growth rate by the following argument. The surface changes according to its tissue velocity, which has tangential and normal components $\mathbf{v} = \partial_t \mathbf{X} = v_\parallel^i \mathbf{e}_i + v_n \hat{\mathbf{n}}$. The shape of the surface is encoded by the metric $g_{ij} = \partial_i \mathbf{X} \cdot \partial_j \mathbf{X}$, which describes lengths and angles measured in the tissue, and by the second fundamental form $b_{ij} = \partial_i \partial_j \mathbf{X} \cdot \hat{\mathbf{n}} = -\partial_i \mathbf{X} \cdot \partial_j \hat{\mathbf{n}}$, which contains information relating to both intrinsic and extrinsic measures of surface curvature [55]. The time rate of change of the metric, also called the rate-of-deformation tensor, is determined by the superposition of velocity gradients and normal motion where the surface is curved [6, 156]:

$$\partial_t g_{ij} = \nabla_i v_j + \nabla_j v_i - 2 v_n b_{ij}. \tag{4.1}$$

Here, ∇ denotes the covariant derivative operator defined with respect to the embedding metric $\mathbf{g}$. The covariant mass continuity equation gives [6]

$$0 = \frac{D\rho}{Dt} + \frac{\rho}{2} \mathrm{Tr}[\mathbf{g}^{-1} \dot{\mathbf{g}}] \tag{4.2}$$

$$= \frac{D\rho}{Dt} + \rho \nabla \cdot \mathbf{v}_\parallel - \rho 2 v_n H, \tag{4.3}$$

where ρ is the mass density in the physical embedding, and the material derivative is $D\rho/Dt = \partial_t \rho + \rho(\nabla \cdot \mathbf{v}_\parallel) + \mathbf{v} \cdot \nabla \rho$. Incompressibility ($D\rho/Dt = 0$) then implies

$$2 H v_n = \nabla \cdot \mathbf{v}_\parallel. \tag{4.4}$$

Such a kinematic constraint guides the shape changes that result from prescribed patterns of mechanical stresses in the tissue.

We hypothesized that the constricting midgut may behave as nearly incompressible,

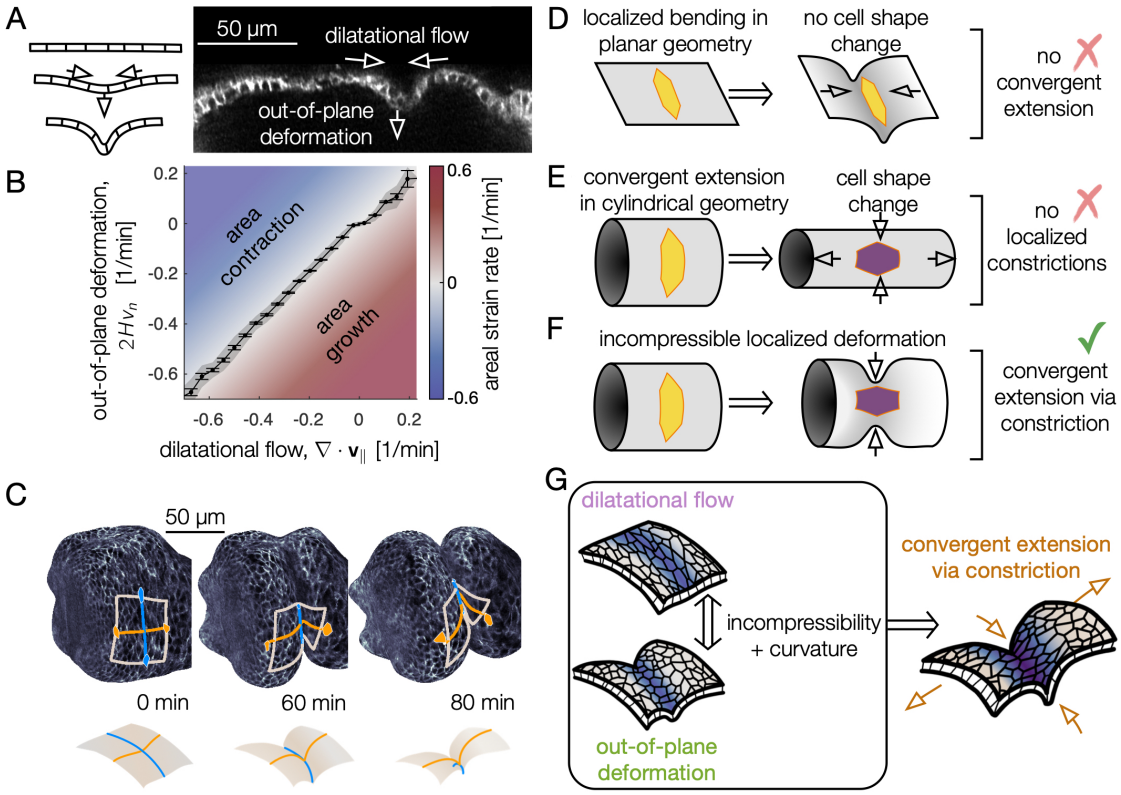

Figure 4.3: **Incompressible tissue dynamics reveal convergent extension via constrictions.** (A) Localized constrictions couple dilatational in-plane velocity patterns to out-of-plane deformation near folds. (B) In-plane divergence and out-of-plane deformation are correlated at the 97% level, signaling nearly incompressible behavior ($N = 3$ embryos, with kinematics sampled in 320 non-overlapping tissue patches per minute for $0 < t < 90$ min). Gray band denotes standard deviation and ticks denote standard error on the mean for each bin. Here, H denotes mean curvature, v_n is the normal (out-of-plane) velocity, and $\nabla \cdot \mathbf{v}_{\|}$ is the covariant divergence of the in-plane velocity. (C) The tissue converges along the circumferential direction as cells sink into the constriction (blue) and extends along the bending longitudinal profile (orange) to preserve the area of a tissue patch. (D) In contrast to the curved gut, localized bending of a flat, incompressible sheet requires no cell shape change, and thus no tissue-scale convergent extension. (E) Cell shape deformations converging along the circumferential axis and extending along the the AP axis would generate tissue convergent extension corresponding to uniform constriction of a tube, but no localized constrictions would form. (F) Localized constriction of an incompressible sheet exhibits cell shape change without cell area change in the absence of oriented divisions or oriented cell intercalations. The cell shape extends along the bending longitudinal (AP) axis. (G) Convergent extension via constriction follows as a geometric consequence of localized constrictions of the tubular organ without local area change.

given that we found cell areas to vary only gradually during constrictions. To test this, we extract whole-organ tissue deformation patterns and find strong out-of-plane motion and in-plane dilatational flows concentrated near folds (Fig. 4.3A, and Fig. E.6). Remarkably, we find that the pattern of out-of-plane deformation almost entirely accounts for in-plane dilatational motion in the gut, with only a small change in local tissue areas. This tight link suggests that the tissue behaves as an incompressible medium. As shown in Fig. 4.3B, these terms match with 97% correlation, leaving a residual in-plane growth residue at the level of $\sim$1% per minute. This slow residual area growth, which is primarily concentrated in the lobes of rounding gut chambers, accounts for both the surface area growth noted in Fig. 4.1E and the cellular area growth in Fig. 4.2E.

Because the organ is curved into a tube, constrictions converge the tissue along the circumferential axis, and tissue incompressibility couples inward motion to extension along the longitudinal axis to preserve areas (Fig. 4.3C). We dub this kinematic mechanism 'convergent extension via constriction': as the tissue constricts with an inward normal velocity, the length of the tissue along the circumferential direction shortens while curves along the longitudinal (AP) axis of the organ lengthen, keeping the areas of cells approximately constant (Fig. 4.3D-F and Fig. E.8). As a consequence of tissue incompressibility and localized constrictions, the resulting area-preserving deformations are largest near constrictions (Fig. E.9), mirroring the pattern of cell-scale deformations. Though the shape of the organ becomes increasingly complex, in-plane deformations remain globally aligned in the material coordinate system: the tissue converges and extends along the circumferential and longitudinal axes, respectively, even as these axes deform in 3D space as morphogenesis proceeds (Fig. E.9). A more detailed explanation of this mechanism, including some illustrative schematics, can be found in Appendix E.

Finally, we find that tissue convergent extension is accounted for primarily by our previous measurement of cell shape change. Since the early stages of midgut constric-

tions have no divisions or oriented cell intercalations, we hypothesized that cell shape change alone can explain the tissue scale convergent extension. Fig. 4.4 shows a quantitative match between cell shape changes and tissue convergent extension, indicating that local cell shape changes primarily mediate tissue-scale convergent extension during the early stages of constrictions. During stage 16b, the tight association between cell-scale and tissue-scale deformations loosens, corresponding to contributions from cell intercalations [26].

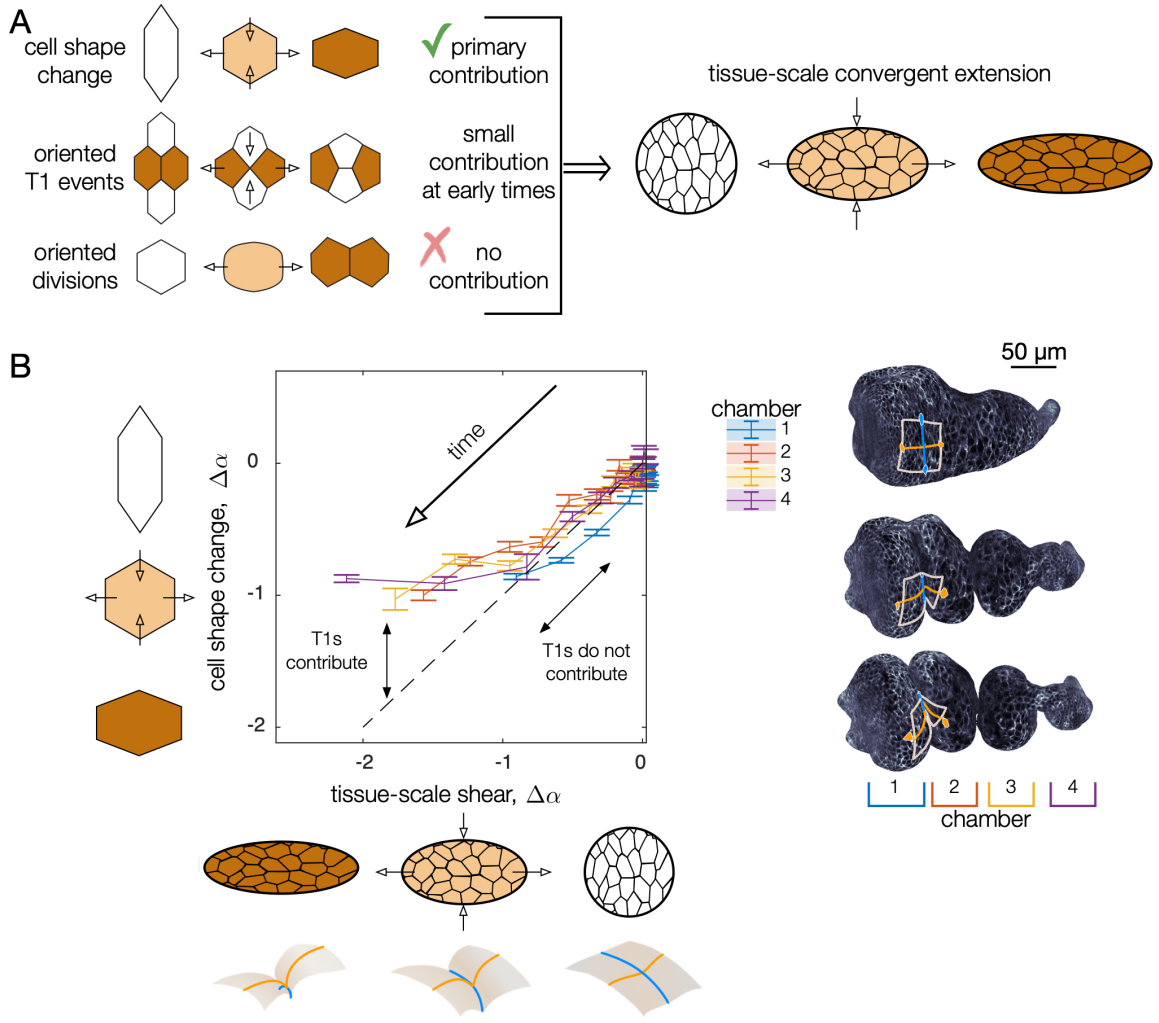

In short, we established a link from endodermal cell shape change to tissue-scale

Figure 4.4: **Cell shape change quantitatively accounts for tissue-scale convergent extension during early stages of midgut constrictions.** (A) As constrictions form, cells change shape from elongated circumferentially to elongated along the longitudinal axis of the organ. At the same time, the tissue deformation mirrors the cell shape change, converging along the circumference and elongating along the longitudinal axis of the organ. Cell intercalations (T1 events) could also contribute to convergent extension if oriented. We find these make a small contribution at early stages of constriction and a large contribution at later stages. No signs of divisions are present, so we rule out oriented cell divisions as contributors to convergent extension. (B) Tissue-scale deformation quantitatively tracks cell shape change at early times, while intercalations contribute to convergent extension at later stages. Change in cell shape anisotropy (assessed over all cells in each chamber) is plotted against the magnitude of tissue convergent extension (averaged over the same tissue positions in each chamber). On the vertical axis, we report cell shape change as the average cell shape anisotropy for all segmented cells in each chamber $\langle\alpha(t)\rangle$, minus the mean value for each chamber at the onset of the middle constriction $\langle\alpha(t=0)\rangle$, such that $\Delta\alpha(t) \equiv \alpha(t) - \langle\alpha(t=0)\rangle$. Given that cells' orientations are steady during constrictions, we use a scalar measure of oriented cell shape anisotropy, $\alpha = (1 - a/b)\cos 2\theta$, where a and b are the semimajor and semiminor axes of the ellipse capturing each cell's in-plane moment of inertia tensor and θ is the cell's angle with respect to the material frame's longitudinal axis. To compute a tissue-scale shape change for comparison, we advect the cell contours of the initial segmentation along the meso-scale tissue flow and compute the cell shape anisotropy of the advected segmentation [164]. Chambers are numbered from anterior (1) to posterior (4), separated by constriction locations. Tick marks denote standard errors on the mean for cell anisotropies within each chamber.

folding – in which incompressibility couples out-of-plane deformation to in-plane motion – resulting in convergent extension via constriction (Fig. 4.3G). What mechanical process drives strong, localized contractions at the folds?

4.5 Muscle contractions drive cell and tissue shape change

It is known that embryos with either disrupted muscle or endoderm structure fail to fold [24, 264, 229, 265], as do embryos lacking integrins linking the two layers [66]. This suggests that gut morphogenesis requires an interaction between muscle and endodermal layers. At the same time, hox genes – which are expressed exclusively in the muscle layer – have been linked to the successful formation of specific folds (Fig. 4.5A-B) [248]. In particular, *Antp* mutants lack the anterior fold lying near the center of the *Antp* domain (Fig. 4.5C), while *Ubx* mutants lack the middle fold lying at the posterior edge of the *Ubx* domain (Fig. 4.5D). In this system, genetic patterning of the endoderm occurs via genetic patterning from the muscle layer [21, 158], so it is possible that constrictions result from a *genetic* induction process. Alternatively, *mechanical* interactions between the layers could induce a program of convergent extension in the endoderm – with patterned deformation of the muscle layer sculpting a passive, tethered endoderm [203] or triggering active endodermal cell shape change.

To clarify the relationship between layers during constriction dynamics, we first measured relative motion of the muscle layer against the endoderm. By tracking both circumferential muscle nuclei and endoderm nuclei in the same embryo, we find that these two layers move together, with initially close nuclei separating by $\sim 5\mu$m per hour (Fig. 4.5E-F and Appendix E). This result is consistent with the notion that the two layers are tightly

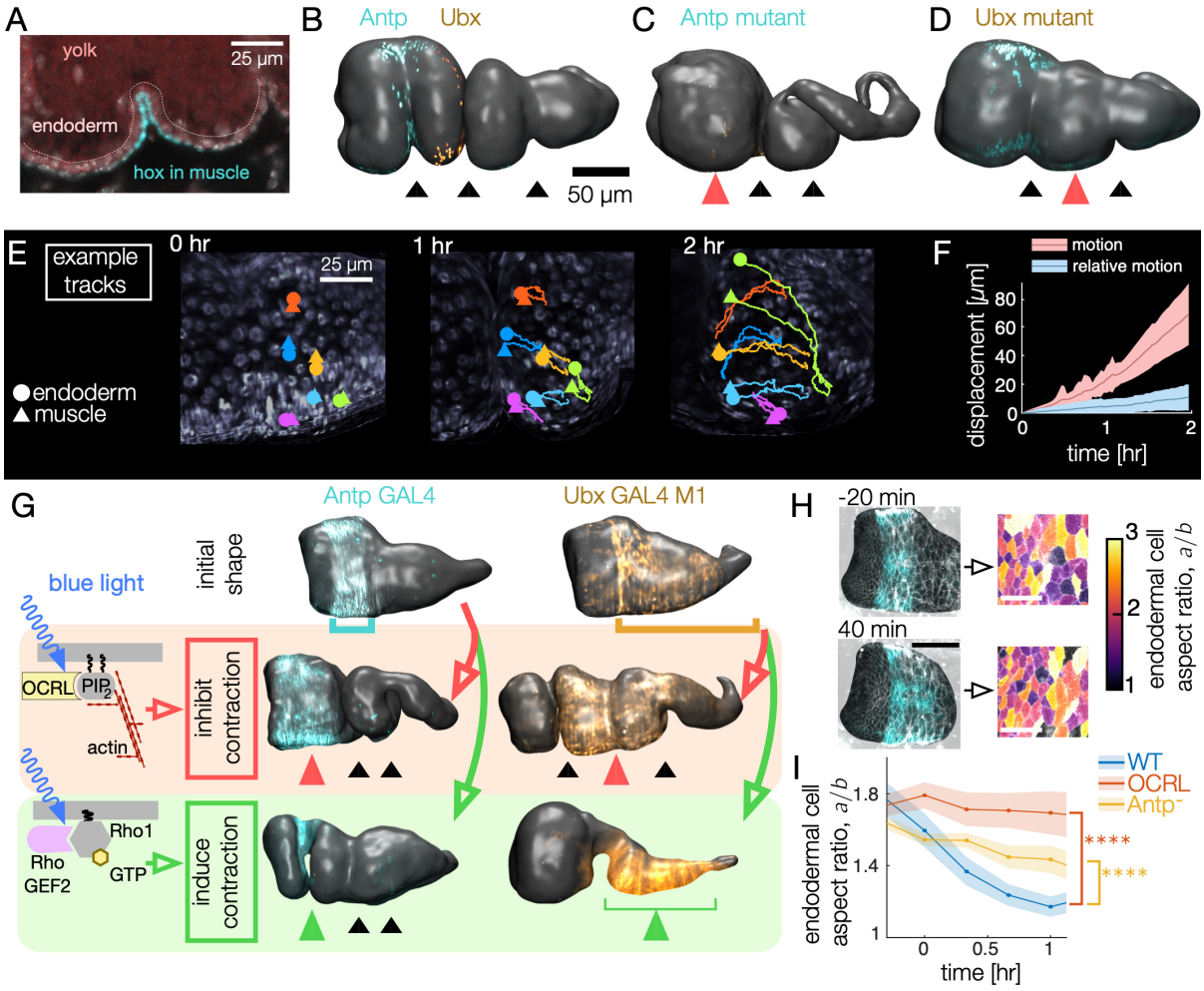
A
yolk
25 μm
endoderm
hox in muscle
B
Antp
Ubx
50 μm
C
Antp mutant
D
Ubx mutant
E
example tracks
endoderm
muscle
0 hr
25 μm
1 hr
2 hr
F
motion
relative motion
displacement [μm]
time [hr]
G
Antp GAL4
Ubx GAL4 M1
initial shape
blue light
OCRL
PIP2
actin
inhibit contraction
Rho GEF2
Rho1
GTP
induce contraction
H
-20 min
40 min
endodermal cell aspect ratio, a/b
I
endodermal cell aspect ratio, a/b
time [hr]
WT
OCRL
Antp⁻
****
****

Figure 4.5: **Muscle contractions mechanically couple to the endoderm layer, inducing cell shape change and convergent extension.** (*A-B*) Hox genes *Antp* and *Ubx* are expressed in the circumferential muscle in discrete regions, shown for surfaces extracted from light-sheet imaging. (*C-D*) Hox genes control organ shape: *Antp* and *Ubx* mutants lack anterior and middle constrictions, respectively. (*E*) Muscle and endoderm layers move together. By computationally extracting both muscle and endoderm layers in an embryo expressing both fluorescent circumferential muscle and endoderm (*w,Hand>GAL4;UAS-Hand:GFP;hist:GFP*), we track relative motion of initially close muscle-endoderm nuclei pairs. (*F*) Muscle-endoderm nuclei pairs show modest relative motion compared to the integrated motion of the tissue ($N = 81$ pairs, colored bands denote standard deviations). (*G*) Optogenetic inhibition of contractility via *CRY2-OCRL*, which dephosphorylates $PI(4,5)P_2$ [91], mimics hox mutant behaviors ($N = 11$ each), and stimulation of muscle contraction via recruitment of *CRY2-ρGEF2* to the plasma membrane [114] drives ectopic folding ($N = 5$ each). (*H*) Inhibiting muscle contraction via *CRY2-OCRL* prevents endoderm cell shape change, shown for snapshots before and after the anterior constriction would normally form. The black scale bar is 50 μm, and white scale bar in images of segmented cells is 25 μm. (*I*) Measurements of endodermal cell anisotropy over time confirm that mechanical inhibition in the muscle reduces cell shape change in the endoderm (blue, $p = 1 \times 10^{-22}$). *Antp* mutants also exhibit reduced endoderm cell shape change, consistent with *Antp* regulating muscle contraction (yellow, $p = 4 \times 10^{-9}$). Each datapoint is the weighted average of multiple adjacent timepoints from 2-3 embryos with at least 30 cells per timepoint segmented in each embryo. Colored bands denote standard error on the mean.

tethered by the integrins and extracellular matrix binding the heterologous layers [66].

Based on this tight coupling, we hypothesized that muscle mechanically induces shape change in the tethered endoderm. To test this hypothesis, we inhibited contractility of the muscle layer by driving *UAS-CIBN UAS-CRY2-OCRL*, a two-component optogenetic construct that recruits *OCRL* to the plasma membrane to dephosphorylate PI(4,5)P_2. This process has been shown to abolish actomyosin contractility in other developmental contexts by releasing actin from the plasma membrane [91]. Driving *CRY2-OCRL* with *Antp-GAL4* under continuous activation of blue light reliably prevented anterior folding (Fig. 4.5G). Likewise, driving *CIBN* and *CRY2-OCRL* under continuous blue light activation in muscle regions posterior to the anterior fold using *Ubx-GAL4 M1* locally inhibited constriction dynamics. We note that *Ubx-GAL4 M1* embryos express *Ubx* in a larger domain than the endogenous WT *Ubx* domain due to differences in its regulation [82], but *Ubx-GAL4 M1* embryos nonetheless execute all three constrictions in the absence of *UAS-CRY2-OCRL* under similar imaging conditions. Inhibiting contraction in selected regions therefore mimics the genetic mutants known to remove folds.

Given that muscle contractility is required, we asked if optogenetically inducing actomyosin contraction in the muscle is sufficient to induce constrictions. Indeed, optogenetic activation using the *CIBN UAS-ρGEF2* system in the *Antp* region generates an anterior fold on demand on the timescale of a few minutes, even if induced long before the constriction would normally begin (Fig. 4.5G). Similarly, activation of the *Ubx-GAL4 M1* domain results in a nearly uniform constriction that dramatically alters the shape of the organ, forcing the yolk to flow into the anterior chamber. Additional optogenetic experiments inhibiting contractility of all muscles likewise led to folding defects ($N = 13$, *w;UAS-CIBN::GFP;Mef2-GAL4 / UAS-CRY2-OCRL:mCherry*). We conclude that muscle contractility is necessary for constrictions and inducing contraction and the associated downstream behaviors is sufficient to generate folds.

We then asked how these macro-scale perturbations on organ shape are linked to cell shapes in the endoderm. In contrast with the wild-type, endodermal cell shape changes are significantly reduced under optogenetic inhibition of muscle contractility. As shown in Fig. 4.5H-I, cell segmentation of the endoderm during optogenetic inhibition of muscle contraction in the *Antp* domain reveals nearly constant aspect ratios: the endoderm cells near the *Antp* domain undergo reduced convergent extension when muscle contraction is locally disrupted (single-sided z-test: $p = 1 \times 10^{-6}$ for difference after 1 hr, $p = 1 \times 10^{-22}$ for sustained difference between curves, see Methods). We also observe analogous reduction of endodermal cell shape change in *Antp* mutants, which lack anterior folds (Fig. 4.5I, single-sided z-test: $p = 7 \times 10^{-3}$ for difference after 1 hr, $p = 4 \times 10^{-9}$ for sustained difference between curves). Thus, the endodermal program of convergent extension is induced by mechanical interaction with the contracting muscle layer.

4.6 Calcium pulses spatiotemporally pattern muscle contractility

What mechanism triggers muscle contractions, allowing such sharp folds to arise? Recent studies have shown that calcium signaling triggers muscle contractions in a wide range of contexts [128]. If hox genes use calcium signaling to pattern muscle contraction in the midgut, we would predict that calcium pulses appear near localized constrictions. Furthermore, hox gene mutants lacking folds would not exhibit localized calcium pulses, and inhibition of the cell biological mechanism translating calcium into mechanical contraction should likewise inhibit constrictions.

To test for a link from hox genes to organ shape through this mechanism, we fist imaged a fluorescent probe of calcium dynamics (*GCaMP6s*) in the muscle layer. As

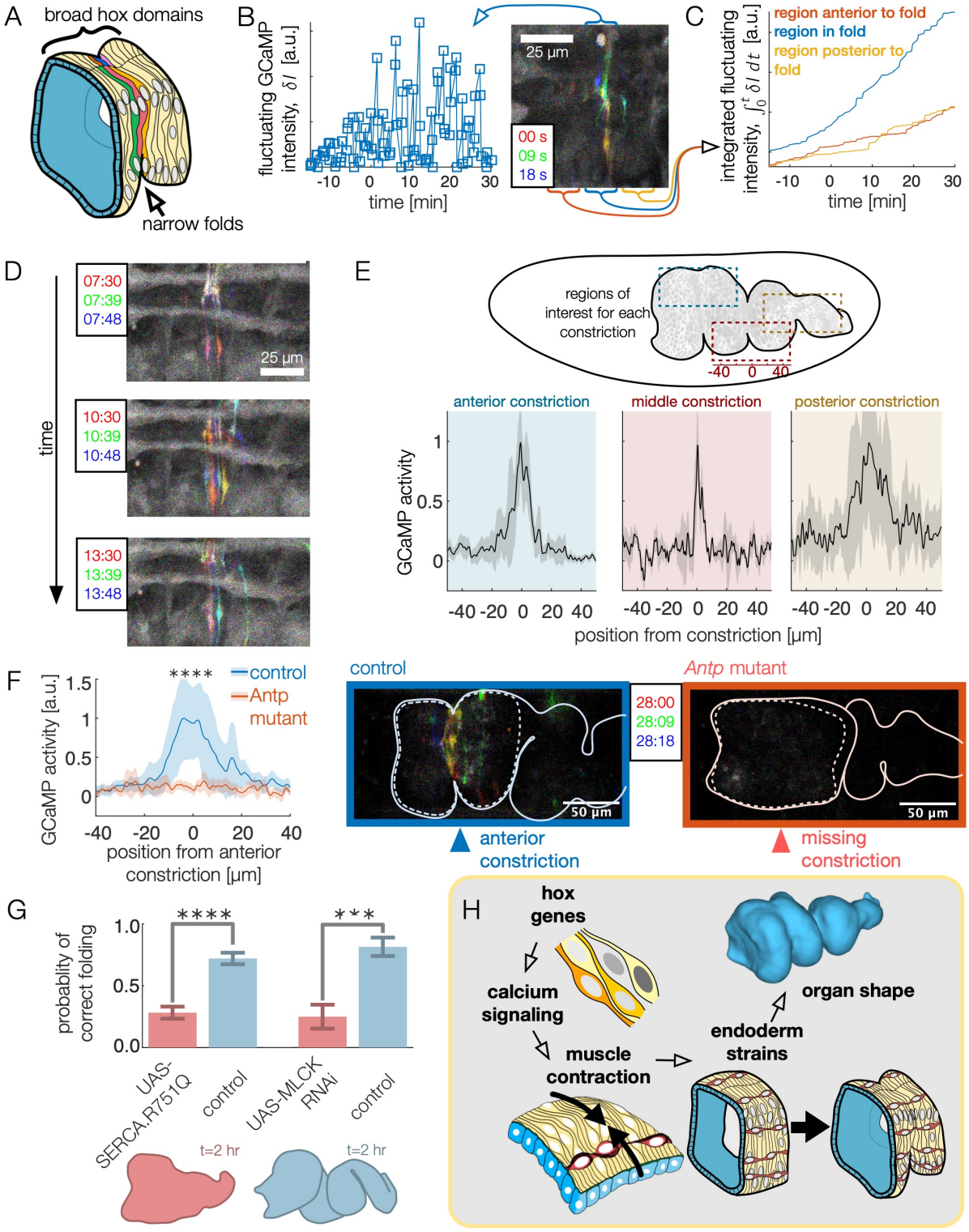
A
broad hox domains
narrow folds
B
fluctuating GCaMP intensity, δI [a.u.]
time [min]
25 μm
00 s
09 s
18 s
C
integrated fluctuating intensity, ∫δI dt [a.u.]
region anterior to fold
region in fold
region posterior to fold
time [min]
D
time
07:30
07:39
07:48
10:30
10:39
10:48
13:30
13:39
13:48
25 μm
E
regions of interest for each constriction
anterior constriction
middle constriction
posterior constriction
GCaMP activity
position from constriction [μm]
F
control
Antp mutant
GCaMP activity [a.u.]
position from anterior constriction [μm]
control
Antp mutant
28:00
28:09
28:18
50 μm
anterior constriction
missing constriction
G
probability of correct folding
UAS-SERCA.R751Q
control
UAS-MLCK RNAi
control
t=2 hr
t=2 hr
H
hox genes
calcium signaling
muscle contraction
endoderm strains
organ shape

Figure 4.6: **High frequency calcium pulses mediate muscle contraction, linking hox genes to organ shape through tissue mechanics.** (A) Dynamic calcium pulses appear near the anterior fold, localized to a region more narrow than the *Antp* domain. (B) Transient pulses in *GCaMP6s* intensity occur on the timescale of seconds and increase in amplitude when folding begins ($t = 0$). Red, green, and blue channels of images represent maximum intensity projections of confocal stacks separated in time by 9 seconds, here and below. (C) Integrated transient pulses for the embryo in (B) show calcium pulses are localized near the fold: *GCaMP6s* signals 20μm in front (red) or behind the fold (yellow) are less intense. (D) Snapshots of *GCaMP6s* fluorescence in muscle cells demonstrate calcium activity near constrictions. Each frame is a composite of three subsequent snapshots in red, green, and blue, so that transient pulses appear as colored signal, while background appears gray. Different muscle cells report calcium activity in adjacent frames. (E) Average fluorescent activity during the first 15 minutes of folding show localized signatures at each constriction, with particularly sharp peaks in the middle and anterior constrictions ($N = 5$, $N = 2$, and $N = 7$ for anterior, middle, and posterior folds, respectively). (F) In *Antp* mutants, *GCaMP6s* fluorescence is significantly reduced ($p = 2 \times 10^{-8}$) and is not localized in space. Snapshots of *GCaMP6s* expression 28 minutes after posterior fold onset (right) show almost no activity in the anterior region compared to the control (left). (G) Disruption of calcium regulation in muscle cells inhibits constrictions. The probability of forming three folds is reduced under heat-shock induced expression of the dominant negative mutant allele *SERCA.R751Q* with a muscle-specific driver *Mef2-GAL4* ($N = 130$, $p = 7 \times 10^{-9}$), and is likewise reduced under RNA interference of MLCK driven by *tub67-GAL4; tub16-GAL4* ($N = 37$, $p = 2 \times 10^{-4}$). (H) Altogether, we infer that hox genes are upstream of patterned calcium pulses, which generate muscle contraction that is mechanically coupled to the endoderm, driving tissue strains and ultimately organ shape.

shown in Fig. 4.6A-E, dynamic calcium pulses appear in the muscle layer in regions localized near all three midgut constrictions. Additionally, these calcium pulses are patterned in time, appearing only at the onset of constriction for each fold (Fig. E.13).

To test whether hox genes pattern shape change through calcium dynamics, we measured *GCaMP6s* activity in flies mutant for *Antp* that lack an anterior constriction. As shown in Fig. 4.6F, we found that calcium activity was almost entirely absent during stages 15-16. Calcium activity is strongly reduced at the location of the missing anterior constriction (single-sided z-test: $p = 2 \times 10^{-8}$) and subsequent calcium pulses are repressed within the vicinity of the region for the hour after the constriction would normally initiate (single-sided z-test: $p = 1 \times 10^{-13}$ within 50 μm (Fig. E.14). The hox gene *Antp* is therefore upstream of dynamic calcium pulses.

Importantly, we also find that in wild-type embryos, knock-downs of calcium signaling remove folds. In smooth muscle cells, calcium is known to trigger muscle contraction by binding to calmodulin, which in turn binds to myosin light chain kinase (MLCK) to trigger myosin light chain phosphorylation [103], and cytoplasmic calcium is transported from the cytosol into the sarcoplasmic reticulum for storage under regulation of SERCA [128]. Driving a dominant negative form of SERCA previously shown to exhibit temperature-sensitive expression under *Mef2-GAL4* [116], we find that disrupting calcium signaling via heatshock beginning at stages 13-15a suppressed midgut constrictions ($p = 7 \times 10^{-9}$, Fig. 4.6G). Separately, interrupting the production of MLCK in the muscle via RNA interference demonstrates a similar reduction in folding behavior ($p = 2 \times 10^{-4}$, Fig. 4.6G). From this we infer that spatially localized calcium dynamics – under the control of hox gene patterning – triggers MLCK signaling leading to muscle contractions (Fig. 4.6H).

4.7 Discussion

Here we studied morphogenesis of an organ in which heterologous tissue layers generate complex shape transformations. We found that convergent extension and sharp folds in the endodermal layer are triggered by mechanical interaction of muscle contractility together with tissue incompressibility, and patterns of calcium signaling regulate contractility in muscle cells according to hox-specified information (Fig. 4.6H).

Though correspondences between hox genes and cell fates have been established for decades [15], understanding the physical processes driven by hox genes remains an active area of research. Here we demonstrated a link from genes to tissue morphodynamics through active forces, connecting hox genes to a mechanical induction cascade across layers that integrates high frequency calcium pulses to advance reproducible morphogenesis of complex 3D shape. While calcium dynamics have known roles in early developmental stages of diverse organisms [254, 237, 147, 33] – including influencing the organization of muscle fibers in the midgut [108] and determining cell fates in heart valves [80] – our findings suggest a direct influence of calcium on shape, wherein pulses trigger a program of irreversible tissue deformation. These calcium-patterned muscle contractions control 3D shape through a mechanical cascade across tissue layers, with broad relevance to tissue engineering and organ morphogenesis in other organisms.

At the cellular level, a remaining question is how the midgut selects precise positions and times for localized calcium activity despite broad hox gene domains that vary slowly with time. For example, the anterior fold forms near the center of the *Antp* domain. Do cells sense subtle gradients of *Antp*, or does more refined patterning downstream of hox gene expression specify this location [25]? One available avenue for the latter possibility is that hox genes govern the formation of anatomical structures that may transmit signals from the soma to trigger calcium pulses [14].

At the tissue level, a remaining question is to what extent endodermal cells actively respond to muscle contraction, rather than passively deforming. For instance, there could be a mechanical signaling pathway provoking contractile behavior in endodermal cells, or even a mechanical induction loop between layers regulating morphological progression. Our findings open new avenues to study how dynamic interactions between layers encode complex shapes of visceral organs.

Chapter 5

A morphogenetic action principle for thin tissues

How does growth encode form in developing organisms? Many different spatiotemporal growth profiles may sculpt 2D epithelial sheets into the same target 3D shapes, but only specific growth patterns are observed in animal and plant development. The criteria that select for these stereotypic growth patterns and the ubiquity of anisotropic growth remain poorly understood. We propose that nature settles on the 'simplest' growth patterns. Using the geometric formalism of quasiconformal transformations, we demonstrate that growth pattern selection can be formulated as an optimization problem and solved for the trajectories that minimize spatiotemporal variation in areal growth rates and deformation anisotropy. The result is a complete prediction for the growth of the surface, including not only a set of intermediate shapes, but also a prediction for how cells flow along those surfaces. Optimization of growth trajectories for both idealized surfaces and experimentally acquired data show that relative growth rates can be uniformized at the cost of introducing anisotropy. Minimizing complexity can therefore be viewed as a generic mechanism for growth pattern selection and may help to understand the

prevalence of anisotropy in developmental programs.

5.1 Introduction

Morphogenesis, the process through which genes generate form, transforms simple initial configurations of cells into complex and specific shapes [246]. In order to accomplish this monumental task of self-organization, morphogenetic programs must coordinate spatiotemporal fields of genetic expression, cellular behaviors, and tissue scale forces, all of which feedback and couple to each other in nontrivial ways [13]. These interdependent motifs collectively force cells to flow and tissues to buckle and change shape, tracing out trajectories in the enormous 'morphospace' of possible shapes and configurations that living systems can assume (Fig. 5.1). From a purely geometric perspective, an infinite family of different growth patterns may all generate the same final, coarse-grained shape. Despite this degeneracy, typical individuals of the same species all employ the same stereotypic growth patterns to generate their organs and appendages. Generating a quantitiative understanding of how these stereotypic growth patterns are selected remains a foundational open question at the interface between mechanics and developmental biology.

We address this problem in the context of epithelial morphogenesis. Epithelia are the fundamental tissue scale building block of multicellular systems and regularly undergo dramatic shape changes during development [86, 92]. These tissue scale transformations are instructed by the collective input of a limited set of cell scale motifs, including cell shape change, cell rearrangements, and cell division (Fig. 5.2A) [26, 74, 93]. These various motifs can combine in nontrivial ways to produce markedly different signatures of motion. If the collective action of these cellular process has no mean preferred direction, then growth will be isotropic. If, on the other hand, the integrated cell-sclae con-

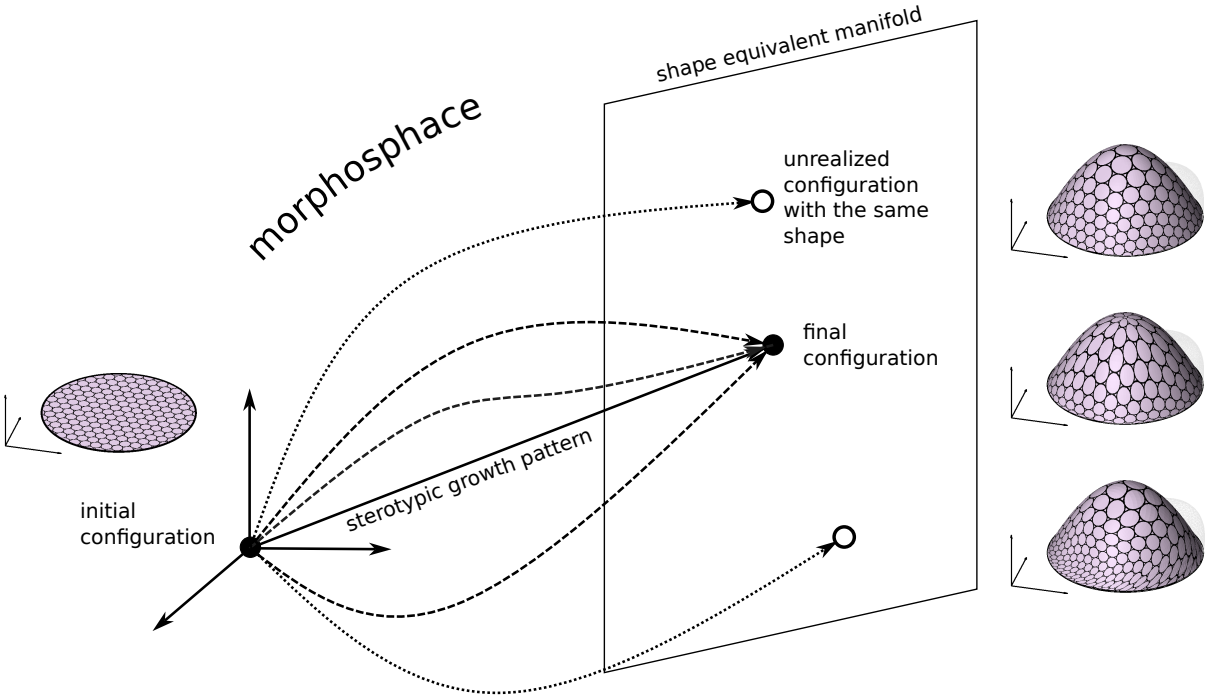

Figure 5.1: **Dynamic growth patterns are trajectories in 'morphospace'.** Morphogenetic programs transform simple initial configurations into complex target shapes. We define a configuration to comprise both a shape and a parameterization, i.e. a distribution of material patches over the surface. Different growth patterns may generate the same final shape, but with dissimilar distributions of material regions. Even growth patterns that generate the same final configuration may differ drastically in terms of the realized intermediate configurations. A complete machinery for understanding growth pattern selection must be able to quantiatively resolve this degeneracy.

tribuionts exhibit an average orientation, then growth will be anisotropic. Anisotropy is a ubiquitous hallmark in the growth and development of plants and animals. Numerous morphogenetic processes, including organogenesis [16], appendage formation [263] and vertebrate gastrulation [85], have been shown to feature anisotropic components. Fig. 5.2B illustrates the different final configurations produced by an isotropic and an anisotropic growth pattern with the same initial configuration and uniform growth rates. If we allow gowth rates to vary in space and time, we can produce the same final coarse grained shape through both isotropic and anisotropic growth, although the distribution of clonal regions within that tissue will be different. A comprehensive characterization of morphogenetic tracjectories must therefore be able to distinguish growth patterns in terms of both shape and flow.

In order to make sense of the complex interplay among these cellular processes, we construct a coarse-grained, effective theory that integrates collective cell behavior into smooth tissue scale deformations. Updates to the cell scale configuration of the tissue are integrated into changes to a coarse-grained *intrinsic geometry*. As the intrisic geometry is updated, the physical geometry changes in an attempt to match the target configuration [3]. Trajectories in morhphospace a can then be quantified at the tissue scale through the time dependence of the intrinsic geometry. Flows of cells become smooth time-dependent maps. In particular, flows due to isotropic growth are angle-preserving conformal maps, whereas flows due to anisotropic growth are described by quasiconformal maps, i.e. smooth transformations of bounded anistropic distortion.

Quasiconformal transformations provide natural language for describing anisotropic growth [1]. Using this formalism, we show how changes to the intrinsic geometry of a thin tissue can be uniquely expressed in terms of areal growth rates and shear anisotropy. We further demonstrate how complex, nonlinear deformations can be decomposed into simple infinitesimal updates. We use this machinery to forumlate a simple action principle for

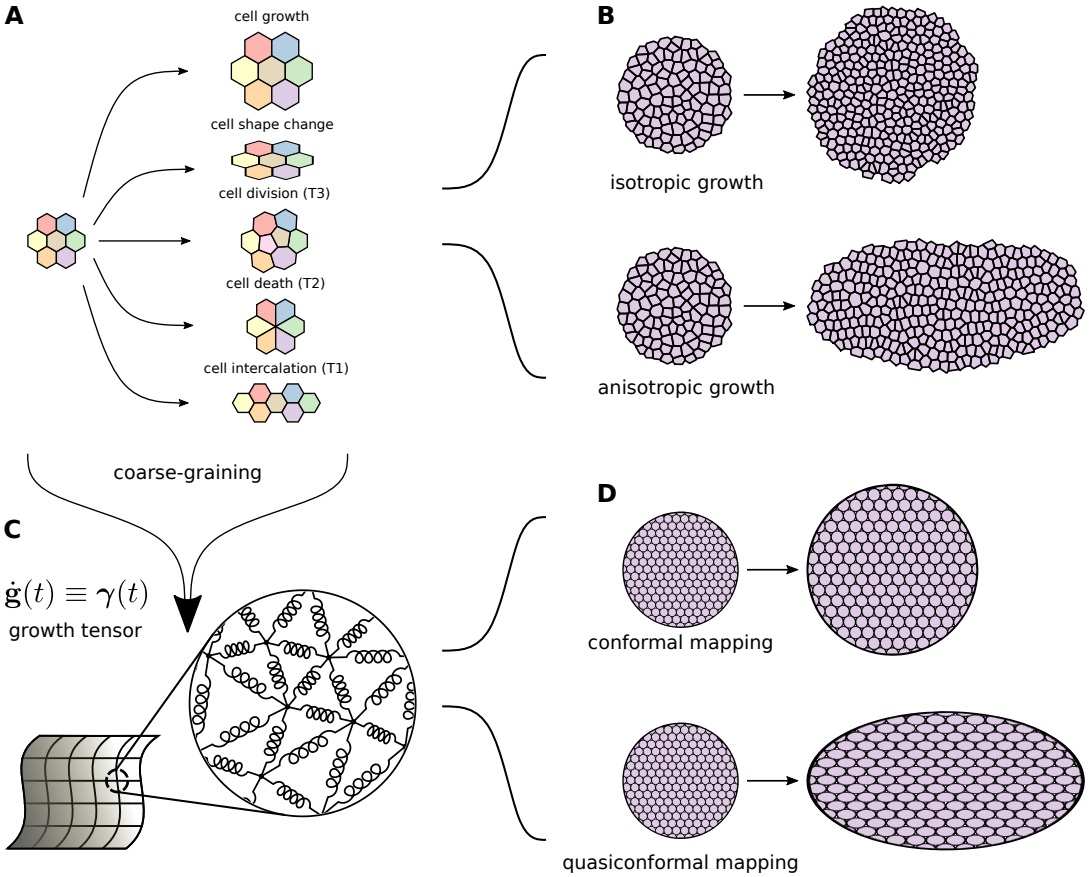

Figure 5.2: **Coarse-grained effective theory integrates cellular behaviors into tissue scale deformations.** (A) A schematic illustration of the cellular behaviors mediating epithelial morphogenesis. These behaviors can be delineated between geometric motifs, e.g. cell growth and cell shape change, and topological motifs, which rearrange the connectivity of cells within the tissue. (B) Processes at the cell scale are combined to collectively induce tissue scale shape change. Tissue scale growth will be isotropic hen the underlying cell scale behaviors have no average preferred direction (e.g. uniformly random cell division orientations). Conversely, the tissue will deform anisotropically when the underlying cellular processes align along a partiuclar orientation. (C) Coarse-graining the cellular motifs yields the *growth tensor*, $\boldsymbol{\gamma}(t)$, a tensorial representation of the rate and orientation of the time rate of change of the tissue's intrinsic geometry. The intrinsic geometry, represented by the target metric tensor $\bar{\mathbf{g}}(t)$, can be conceptualized as a time-dependent field of target lengths and angles between nearby points on the surface. (D) Changes in the intrinsic geometry induce tissue scale flows. In the schematic, circular patches represent material parcels of tissue that deform along Lagrangian pathlines. In the continuum, isotropic growth translates into conformal mappings, which preserve angles and map infinitesimal circles into re-scaled infinitesimal circles. Anisotropic growth translates into *quasiconformal* mappings, which transform infinitesimal circles into infinitesimal ellipses.

growth pattern selection. We propose that stereotypic growth patterns are the 'simplest' growth patterns, in the sense that they minimize spatiotemporal variation in growth rates and anistropy. In other words, they are the growth patterns which require the least amount of *a priori* information to specify. Optimizing this functional for a given input produces a complete, testable prediction for the full time course of a dynamic growth pattern.

Focusing on the case of constant growth, in which growth rates can vary in space, but are held constant throughout the growth process, we apply this formalism to deduce the optimal growth trajectories for a variety of synthetic shapes. We further demonstrate how varying the 'texture' of the anisotropy in the growth pattern can produce different morphological features, even if the areal growth rates are held fixed. Finally we apply our formalism to deduce optimal growth trajectories for limb morphogenesis in the crustacean *Parhyale hawaiensis* and compare the results to alternative growth pattern possibilities.

5.2 Quasiconformal parameterizations of anisotropic growth patterns

We represent a growing, thin tissue with a continuous curved surface $S_t \subset \mathbb{R}^3$. We assign to each material parcel in the tissue a set of curvilinear Lagrangian coordinates $\vec{\mathbf{x}} = (x^1, x^2) \in \mathcal{B}$ defined over a planar domain of parameterization $\mathcal{B} \subset \mathbb{R}^2$.The embedding of the surface is time-dependent map $\vec{\mathbf{R}}(\vec{\mathbf{x}}, t) : \mathcal{B} \to \mathbb{R}^3$. Each point $\vec{\mathbf{R}}(\vec{\mathbf{x}}, t) \in \mathcal{S}_t$ is characterized by its tangent vectors $\vec{\mathbf{e}}_1 = \partial\vec{\mathbf{R}}/\partial x^1$, $\vec{\mathbf{e}}_2 = \partial\vec{\mathbf{R}}/\partial x^2$ and its unit normal vector $\hat{\mathbf{n}} = \vec{\mathbf{e}}_1 \times \vec{\mathbf{e}}_2/||\vec{\mathbf{e}}_1 \times \vec{\mathbf{e}}_2||$. In what follows, Greek indices vary in the set $\{1, 2\}$. We also drop the explicit dependence on time for $\vec{\mathbf{R}}(t)$ and related functions in situations where it is obvious from context. This description is illustrated in Fig. 5.3.

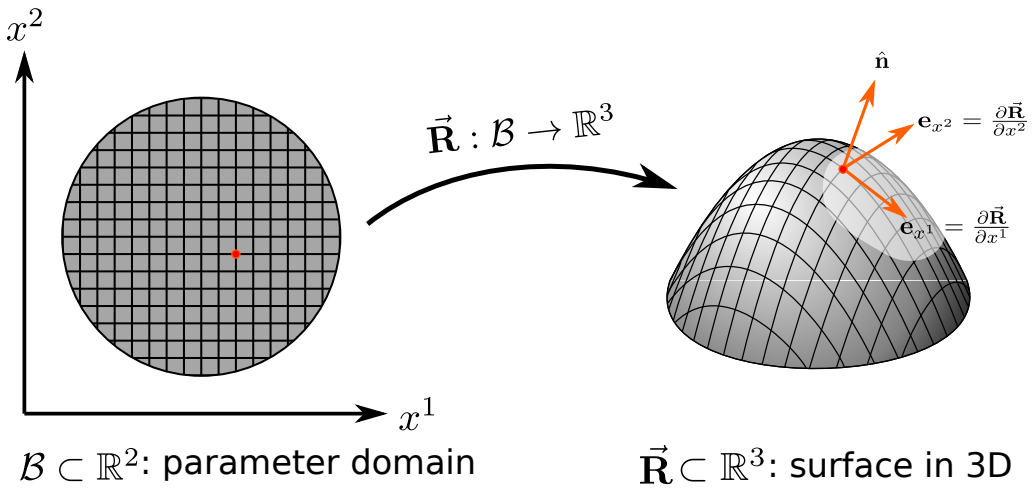

Figure 5.3: **Surface geometry.** The surface $\mathcal{S}$ is defined as an embedding $\vec{\mathbf{R}}$ of an arbitrary region of the plane $\mathcal{B} \subset \mathbb{R}^2$ into $\mathbb{R}^3$.

The covariant geometry of the surface is captured by the metric tensor

$$g_{\alpha\beta}(\vec{\mathbf{x}}, t) = \frac{\partial \vec{\mathbf{R}}(t)}{\partial x^\alpha} \cdot \frac{\partial \vec{\mathbf{R}}(t)}{\partial x^\beta}, \tag{5.1}$$

which quantifies lengths and angles between points on the surface. Notice that this quantity provides information both about the overall shape and the distribution of material patches on the surface. As the developmental program unfolds, tissue's physical shape will change as it tries to match the evolving target geometry. Any mismatch between these geometries will result in mechanical stresses [3]. If the time scale of mechanical relaxation is fast compared to the time scale of growth, then the tissue will effectively always be in mechanical equilibrium. For simplicity, we assume that the physical geometry is always an isometric embedding of the instantaneous target geometry, i.e. a stress-free equilibrium configuration. Strictly speaking, it is also necessary to provide a target curvature tensor, $b_{\alpha\beta} = \partial_\alpha \partial_\beta \vec{\mathbf{R}} \cdot \hat{\mathbf{n}}$, in order to uniquely specify the surface up to a rigid motion. For thin tissues, however, the energy associated between any metric mismatch dominates any bending energy. Moving forward with this in mind, we represent the full

dynamic growth of shape and flow using the tie course of the target metric $\mathbf{g}(t)$.

Quasiconformal mappings are generalizations of conformal mappings that allow for shear deformations of bounded distortion. We now briefly demonstrate how the language of quasiconformal maps can greatly clarify the problem of growth pattern selection. More detailed coverage of the subject matter can be found in [1, 7, 83]. Let $w = w(z)$ be a C^1 homeomorphism of one subregion of $\mathbb{C}$ to another, defined in terms of a pair of complex variables $z = x^1 + ix^2$ and $w = u^1 + iu^2$. The map $w(z) : \mathbb{C} \to \mathbb{C}$ is considered quasiconformal if it is a solution to the *complex Beltrami equation*

$$\frac{\partial w}{\partial \bar{z}} = \mu(z, \bar{z}) \frac{\partial w}{\partial z} \tag{5.2}$$

where where $\bar{z} = x - iy$ and the *Beltrami coefficient*, μ, is a Lebesgue-measurable function with $||\mu||_\infty < 1$. This latter constraint is sufficient to ensure that the Jacobian of the mapping $J = |\partial_z w|^2 - |\partial \bar{z} w|^2 > 0$ everywhere. Hence, by the inverse function theorem, w is a sense-preserving diffeomorphism. The geometric properties of quasiconformal transformations can be elucidated by comparison with conformal mappings. Locally, around a point, a conformal transformation maps infinitesimal circles into similar circles. A conformal map therefore does not introduce any preferred local orientation and is necessarily isotropic. In contrast, a quasiconformal transformation maps infinitesimal circles into infinitesimal ellipses. The Beltrami coefficient encodes the magnitude and directionality of this distortion, and thereby the anisotropy of the transformation. This geometric intuition is illustrated in Fig. 5.4. Notice that when $\mu = 0$, the Beltrami equation reduces to the Cauchy-Riemann equation, $\partial_{\bar{z}} w = 0$, the necessary and sufficient conditions for the conformality of a complex map.

For simplicity, we now restrict our consideration to surfaces with disklike topology (although virtually identical arguments hold true for both topological cylinders and topo-

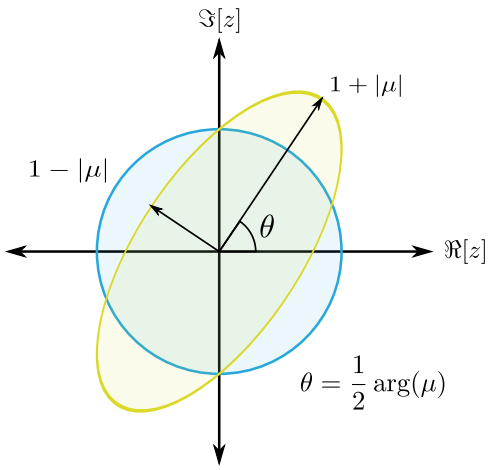

Figure 5.4: **The Beltrami coefficient encodes deformation anisotropy** An illustration of the shearing induced by a quasiconformal transformation. Locally, around a point, a planar quasiconformal transformation $w : \mathbb{C} \to \mathbb{C}$ maps infinitesimal circles into infinitesimal ellipses. The distortion associated with this map is encoded by the Beltrami coefficient, a complex valued function μ with $||\mu||_\infty < 1$ that is defined via the complex Beltrami equation: $\partial_{\bar{z}} w = \mu\, \partial_z w$. The angle of maximal stretching is $\theta = \arg(\mu)/2$ with an associated magnification factor of $1+|\mu|$. The angle of maximal shrinking is the orthogonal angle, $\theta + \pi/2$, with a compression factor of $1 - |\mu|$.

logical spheres). An arbitrary diffeomorphic parameterization of a disklike surface $\mathcal{S}_t$ is a quasiconformal map and can be constructed according to the following prescription. First, we calculate a conformal mapping $\vec{\mathbf{R}}(\vec{\mathbf{u}}) : \mathbb{D} \to \mathcal{S}_t$ from the unit disk, $\mathbb{D} = \{\vec{\mathbf{u}} : ||\vec{\mathbf{u}}|| < 1\}$, to the surface in 3D . The Riemann mapping theorem assures us that such a mapping is always possible and that it is unique up to a Möbius automorphism of the unit disk [171]. All Möbius automorphisms of the unit disk, $\varphi : \mathbb{D} \to \mathbb{D}$, share the following form

$$\varphi(z) = e^{i\theta} \frac{z - z_0}{1 - \bar{z}_0 z}, \tag{5.3}$$

for some angle $\theta \in [-\pi, \pi)$ and a complex constant $z_0 \in \mathbb{D}$. Effectively, a mapping like $\varphi(z)$ allows us to re-arrange the points $z = 0$ and $z = 1$ in such a way that $\mathbb{D}$ is preserved and no anisotropy is introduced. In these intermediate coordinates, the metric tensor

takes the following diagonal form

$$g_{\alpha\beta} = e^{\Omega(\vec{\mathbf{u}})}\,\delta_{\alpha\beta}. \tag{5.4}$$

Next, we generate a quasiconformal automorphism of the unit disk $w(z) : \mathbb{D} \to \mathbb{D}$, fixing the points $z = 0$ and $z = 1$. All of the anistropy in the parameterization is contained within this quasiconformal transformation and is described by the associated Beltrami coefficient $\mu(t) = \partial_{\bar{z}} w(t)/\partial_z w(t)$. This construction is illustrated in Fig. 5.5A. The complete metric tensor in these coordinates is given by

$$g_{\alpha\beta} = e^{\Omega(w \circ z)} |\partial_z w|^2 \begin{pmatrix} |1+\mu|^2 & -i(\mu - \bar{\mu}) \\ -i(\mu - \bar{\mu}) & |1-\mu|^2 \end{pmatrix}. \tag{5.5}$$

This construction benefits from several useful mathematical properties. The measurable Riemann mapping theorem assures us that there is a unique solution $w(z)$ to the complex Beltrami equation, fixing the points $z = 0$ and $z = 1$, for each μ with $||\mu||_\infty < 1$ [7]. As demonstrated by Eq (5.3), the intermediate conformal parameterization of the surface is totally constrained by the motion of the points $z = 0$ and $z = 1$. In practice, the motion of these points in 3D may be determined by tracking individual cells or distinguishable features. Therefore, given a 3D surface and the motion of a single point on the boundary and a single point in the bulk, each μ corresponds to a unique parameterization of that surface.

It is straightfoward now to see that we can decompose growth into a coupled contribution from anistroic and conformal growth. Given the anisotropy μ we can uniquely solve for the associated quasiconformal mapping $w(z)$. The 3D area of a small material

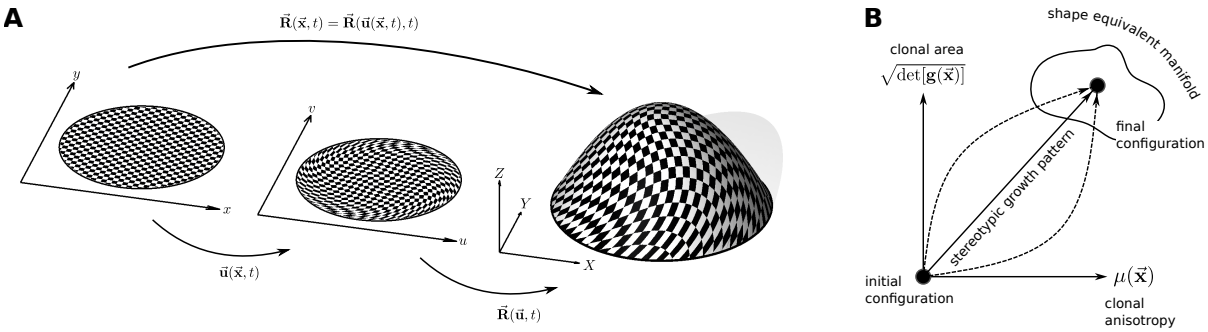

Figure 5.5: **Quasiconformal parameterization of a 3D surface provides quantitative structure for morphogenetic trajectories.** (A) An arbitrary parameterization of a topological disk in 3D can be expressed as the composition of a quasiconformal automorphism of the unit disk $\vec{\mathbf{u}} : \mathbb{D} \to \mathbb{D}$ fixing the points $\vec{\mathbf{x}} = (0,0)$ and $\vec{\mathbf{x}} = (1,0)$ followed by a conformal mapping into 3D $\vec{\mathbf{R}} : \mathbb{D} \to \mathbb{R}^3$. The parameterization is unique if both a Beltrami coefficient μ and the motion of two material points are specified. (B) An arbitrary intrinsic geometry can be reconstructed from the time dependent area and anisotropy of material regions. It is therefore possible to quantitatively characterize morphogenetic trajectories in terms of the dynamic profiles of these Lagrangian fields.

patch at $\vec{\mathbf{x}} \in \mathcal{B}$ is related to the quantity

$$\sqrt{g} = e^{\Omega(w \circ z)} |\partial_z w|^2 (1 - |\mu|^2), \tag{5.6}$$

where g is a shorthand for $\det[\mathbf{g}]$. If we know the anisotropy, μ. and the 3D area, A, of a material patch, we can uniquely construct the associated metric tensor, which serves as a proxy for both shape and flow. This decomposition enables us to assign a simple, concrete structure to the abstract morphospace alluded into in the introduction. Morphogenetic trajectories of thin tissues are simply time-dependent profiles of anisotropy and areal growth (Fig. 5.5B).

We now turn our attention to the parameterization of entire dynamic growth trajectories. We assume that internal biological processes set the rates at which the intrinsic geometry changes, rather than determining the cumulative state of the intrinsic geometry. For example, biological processes may set rate of cell division, rather than directly

controlling the cumulative target area of a clonal region. The crucial object under consideration is the time derivative of the target metric, $\dot{\mathbf{g}}(t) \equiv \boldsymbol{\gamma}$, which we call the *growth tensor* (Fig. 5.2C). Intuitively, $\boldsymbol{\gamma}$ is a coarse-grained tensorial representation of cell-scale growth procesess, i.e. rates and orientations of cell divisions. The aforementioned parameterization construction guides us towards a scheme for quantifying dynamic changes to the intrinsic geometry. Since a growth pattern can be described in terms of anistropy and area, it must also be possible to describe changes to the intrinsic geometry in terms of updates to these dynamical fields. The relevant quantities are the time rate of change of anisotropy, $\dot{\mu}(t)$, and the relative rate of area change

$$\Gamma = \frac{d}{dt}\log\left[\sqrt{\det[\mathbf{g}]}\right] = \frac{1}{2}\,\mathrm{Tr}\left[\mathbf{g}^{-1}\boldsymbol{\gamma}\right]. \tag{5.7}$$

The next task is to explicitly deduce how variation in these quantities induce changes in the intrinsic geometry.We know that, under suitable normalization, a Beltrami coefficient μ is uniquely associated to a quasiconformal mapping $w(z) : \mathbb{D} \to \mathbb{D}$. Therefore, as $\mu(t)$ changes in time it must induce a corresponding flow in the associated $ws(z)$. The precise form of this correspondence is given by the *Beltrami holomorphic flow*.

Theorem 1: (Beltrami Holomorphic Flow on $\mathbb{D}$) *There is a one-to-one correspondence between the set of quasiconformal diffeomorphisms of $\mathbb{D}$ that fix the points 0 and 1 and the set of smooth complex-valued functions μ on $\mathbb{D}$ for which $||\mu||_\infty = k < 1$. Furthermore, the solution w^μ depends holomorphically on μ. Let $\{\mu(t)\}$ be a family of Beltrami coefficients depending on a real or complex parameter t. Suppose also that $\mu(t)$ can be written in the form*

$$\mu(t)(z) = \mu(z) + t\nu(z) + t\epsilon(t)(z) \tag{5.8}$$

for $z \in \mathbb{D}$, with suitable μ in the unit ball of $C^\infty(\mathbb{D})$, ν, $\epsilon(t) \in L^\infty(\mathbb{D})$ such that $||\epsilon(t)||_\infty \to$

0 *as* $t \to 0$. *Then for all* $z \in \mathbb{D}$

$$w^{\mu(t)}(z) = w^{\mu}(z) + tV[w^{\mu}, \nu](z) + o(|t|) \tag{5.9}$$

locally uniformly on $\mathbb{D}$ *as* $t \to 0$, *where*

$$V[w^{\mu}, \nu](z) = -\frac{w^{\mu}(z)\,(w^{\mu}(z)-1)}{\pi} \quad \times \\ \left(\int_{\mathbb{D}} \frac{\nu(\zeta)\,(\partial_{\zeta} w^{\mu}(\zeta))^2 \; d\eta^1\, d\eta^2}{w^{\mu}(\zeta)\,(w^{\mu}(\zeta)-1)\,(w^{\mu}(\zeta)-w^{\mu}(z))} + \int_{\mathbb{D}} \frac{\overline{\nu(\zeta)}\,\overline{(\partial_{\zeta} w^{\mu}(\zeta))}^2 \, d\eta^1\, d\eta^2}{\overline{w^{\mu}(\zeta)}\left(1-\overline{w^{\mu}(\zeta)}\right)\left(1-\overline{w^{\mu}(\zeta)}\,w^{\mu}(z)\right)} \right) \tag{5.10}$$

A proof of this theorem can be found in [151]. For notational conveniece, we let

$$V[w^{\mu}, \nu](z) = \int_{\mathbb{D}} K(z, \zeta)\, d\eta^1\, d\eta^2 \tag{5.11}$$

where

$$K(z, \zeta) = -\frac{w^{\mu}(z)\,(w^{\mu}(z)-1)}{\pi} \quad \times \\ \left(\frac{\nu(\zeta)\,(\partial_{\zeta} w^{\mu}(\zeta))^2}{w^{\mu}(\zeta)\,(w^{\mu}(\zeta)-1)\,(w^{\mu}(\zeta)-w^{\mu}(z))} + \frac{\overline{\nu(\zeta)}\,\overline{(\partial_{\zeta} w^{\mu}(\zeta))}^2}{\overline{w^{\mu}(\zeta)}\left(1-\overline{w^{\mu}(\zeta)}\right)\left(1-\overline{w^{\mu}(\zeta)}\,w^{\mu}(z)\right)} \right) \tag{5.12}$$

We can also write $V[w^{\mu}, \nu](z)$ as

$$V[w^{\mu}, \nu](z) = \int_{\mathbb{D}} \begin{pmatrix} G_1\nu_1 + G_2\nu_2 \\ G_3\nu_1 + G_4\nu_2 \end{pmatrix} \, d\eta^1\, d\eta^2 \tag{5.13}$$

where $\zeta = \nu_1 + i\nu_2$ and G_1, G_2, G_3, G_4 are real valued functions defined on $\mathbb{D}$. Here, we

identify $A + iB$ as $\begin{pmatrix} A \\ B \end{pmatrix}$. The Beltrami holomorphic flow (BHF) provides an explicit construction for the calculation of the variation of f under the variation of μ.

Identifying the quantity ν with the physical rate of change of anistropy $\dot{\mu}$, the prescription for quantifying dynamic growth patterns becomes clear. At time $t = 0$, we can construct a conformal Lagrangian parameterization of the initial surface. A short time later, internal growth procesess update the intrisic anistropy of the system according to $\dot{\mu}$. This change induces a corresponding flow of the quasiconformal mapping captured by the quantity $V[w^{\mu}, \dot{\mu}]$. Simultaneously, these processes also induce a change in the 3D area of material patches, which is captured by the quantity Γ. We can calculate a corresponding update to $\mathbf{g}(t)$ in terms of $\dot{\mu}$ and Γ. This geometry can be embedded into 3D to find the new configuration of the system. We can string these infinitesimal transformations together to construct any arbitrary growth trajectory. This construction is illustrated in Fig. 5.6.

5.3 Growth pattern selection as an optimization problem

As we have already stated, there is an infinite degeneracy of possible growth trajectories linking an initial configuration and a final shape. How does nature settle on a specific developmental program? We propose that the time course of growth can be found as the solution to the following optimization problem. Given a an initial configuration $\mathcal{S}_0$ (interpreted as a fixed initial shape AND a fixed initial parameterization) and a final shape $\mathcal{S}_T$ (a fixed final shape BUT NOT a fixed final parameterization), the optimal

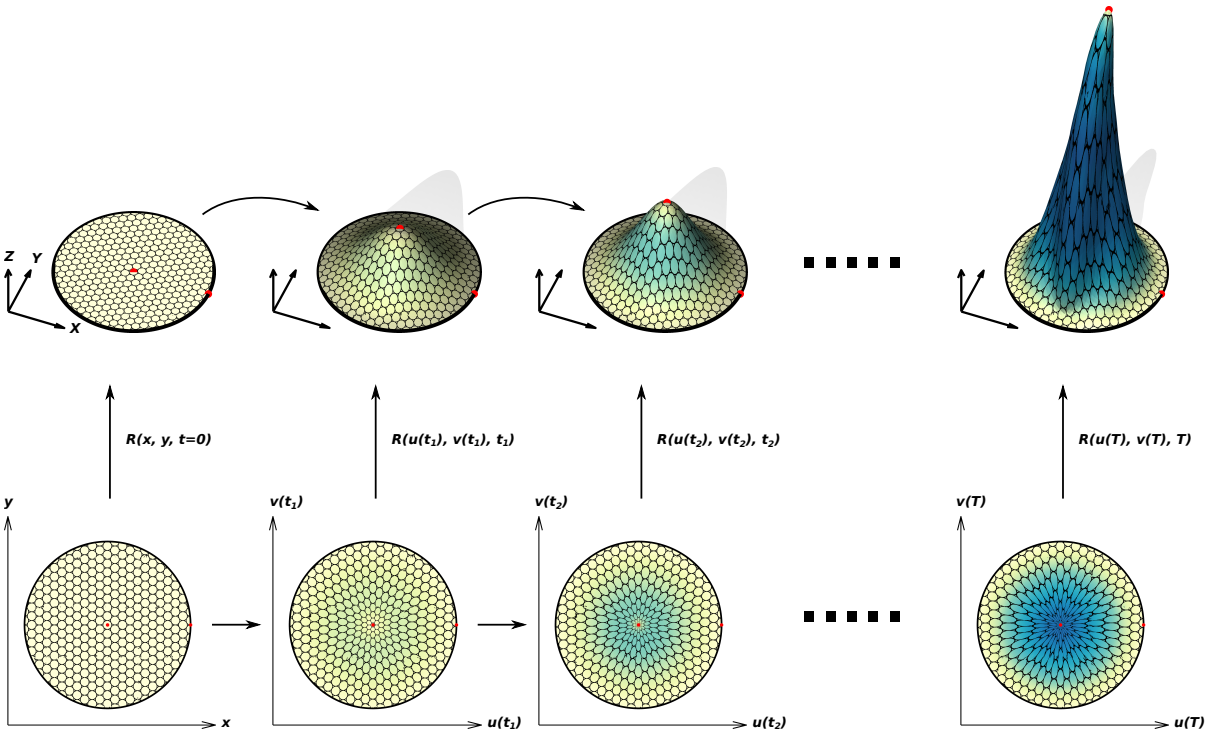

Figure 5.6: **Quasiconformal parameterization of dynamic growth patterns.** Complicated growth patterns for 3D surfaces can be built by stringing together simple infinitesimal updates to the system's intrinsic geometry. Beginning with a conformal parameteriztion of the initial configuration, new configurations are generated by calculating the contributions of changes in the system's intrinsic anistropy and target areas. A time course of $\dot{\mu}$ and Γ are sufficient to fully reconstruct arbitrary growth patterns.

growth trajectory $\boldsymbol{\gamma}^*$ is the minimizer of

$$\min_{\boldsymbol{\gamma}(\vec{\mathbf{x}},t)} \mathcal{E} = \int_0^T dt\, C\left[\boldsymbol{\gamma}(\vec{\mathbf{x}},t);\, \mathcal{S}_0\right] = \int_0^T dt \int_{\mathcal{B}} d^2\vec{\mathbf{x}}\, \sqrt{g}\; \mathcal{C}\left[\boldsymbol{\gamma}(\vec{\mathbf{x}},t);\, \mathcal{S}_0\right] \tag{5.14}$$

subject to

$$\mathbf{g}(\vec{\mathbf{x}}, t=T) \in \Sigma_{\mathcal{S}_T}. \tag{5.15}$$

where $\Sigma_{\mathcal{S}_T}$ is the space of *shape equivalent metrics* for the final surface $\mathcal{S}_T$ (more on this shortly). We also include the implicit constraint that the target metric, which is given by

$$\mathbf{g}(\vec{\mathbf{x}}, t) = \mathbf{g}(\vec{\mathbf{x}}, t=0) + \int_0^T dt\, \boldsymbol{\gamma}(\vec{\mathbf{x}}, t), \tag{5.16}$$

remain a valid metric at all times during the growth process. The precise form of the cost function density $\mathcal{C}[\boldsymbol{\gamma}]$ will be filled in shortly.

We will now explain the constraints in greater detail. The requirement that $\mathbf{g}(\vec{\mathbf{x}}, t)$ be a valid metric simply means that $\mathbf{g}(\vec{\mathbf{x}}, t)$ is a symmetric, positive-definite type-(0,2) tensor defined over $\mathcal{B}$. The constraint in Equation (5.15) requires some definitions and a little more thought. Suppose we endow the final surface $\mathcal{S}_T$ with a different set of coordinates $\vec{\mathbf{u}} \in \mathbb{D}$. In particular, suppose that $\vec{\mathbf{x}}$ and $\vec{\mathbf{u}}$ are related by a sense-preserving diffeomorphism of $\mathbb{D} \to \mathbb{D}$, i.e. $\vec{\mathbf{u}} = \vec{\mathbf{u}}(\vec{\mathbf{x}})$ where the Jacobian matrix $\partial u^\alpha / \partial x^\beta$ is invertible and has a positive determinant. This relationship is identital to the quasiconformal re-parameterization of the unit disk illustrated in Fig. 5.5A. The first fundamental form in these new coordinates $\mathbf{a}$ has components given by

$$a_{\alpha\beta} = \frac{\partial \vec{\mathbf{R}}}{\partial u^\alpha} \cdot \frac{\partial \vec{\mathbf{R}}}{\partial u^\beta}. \tag{5.17}$$

We say that $\mathbf{a}$ and $\mathbf{g}$ are *Shape Equivalent Metrics* (SEMs). In other words, they are

both induced metrics of the *same* surface, but corresponding to *different* coordinate parameterizations. Notice that SEMs must agree on lengths and angles on $\mathcal{S}$ which can be demonstrated as follows

$$\langle\langle \vec{\mathbf{v}}_1, \vec{\mathbf{v}}_2 \rangle\rangle_{\mathbf{g}} = g_{\sigma\tau}(v_1')^\sigma (v_2')^\tau = \left(\frac{\partial x^\alpha}{\partial u^\sigma}\frac{\partial x^\beta}{\partial u^\tau} a_{\alpha\beta}\right)\left(\frac{\partial u^\sigma}{\partial x^\alpha} v_1^\alpha\right)\left(\frac{\partial u^\tau}{\partial x^\beta} v_2^\beta\right) = a_{\alpha\beta} v_1^\alpha v_2^\beta = \langle\langle \vec{\mathbf{v}}_1, \vec{\mathbf{v}}_2 \rangle\rangle_{\mathbf{a}} \tag{5.18}$$

We denote by $\Sigma_{\mathcal{S}}$ the space of all SEMs for the surface $\mathcal{S}$. Physically, we interpret these parameterizations as corresponding to different material flows on the surface. Recall that the time-independent material coordinates $\vec{\mathbf{x}}$ constitute a *Lagrangian parameterization* of the growth trajectory. Each point $\vec{\mathbf{x}} \in \mathcal{B}$ is a fixed label for a material parcel that flows along with that material parcel through time as it moves, grows, and deforms. Therefore, modulating the intermediate mappping $\vec{\mathbf{u}}(\vec{\mathbf{x}}, t)$ amounts ro re-arranging cells on the surface in 3D. In order to generate an unbiased answer to the question of optimial growth, it is critical that we allow $\mathbf{g}(\vec{\mathbf{x}}, T)$ to search the entire space of $\Sigma_{\mathcal{S}_T}$. Anything less results in overly restrictive demands on the material flows during growth. We can formulate this constraint as a Lagrange multiplier by constructing a continuous distance metric that can determine if a given target metric is an element of the SEM space for a given surface. We define the shape equivalent metric distance for a test metric $\mathbf{a}$ and a surface $\mathcal{S}$

$$D_{SEM}[\mathbf{a};\, \mathcal{S}] = \min_{\mathbf{a}\in\Sigma_{\mathcal{S}}} \int_{\mathbb{D}} d_{SEM}[\mathbf{a}, \mathbf{g}]\, \sqrt{a}\, d^2\vec{\mathbf{x}} = \min_{\mathbf{a}\in\Sigma_{\mathcal{S}}} \int_{\mathbb{D}} ||(\mathbf{a} - \mathbf{g})/2||\, \sqrt{a}\, d^2\vec{\mathbf{x}} \tag{5.19}$$

where $d_{SEM}[\mathbf{a}, \mathbf{g}]$ is some local measurement of similarity between two metrics, taken here to be the Frobenius norm of a strain tensor $\boldsymbol{\varepsilon} = (\mathbf{a} - \mathbf{g})/2$. The functional $D_{SEM}[\mathbf{a}]$ will vanish if and only if $\mathbf{a} \in \Sigma_{\mathcal{S}}$.

Finding $D_{SEM}[\mathbf{a};\, \mathcal{S}]$ requires optimizing a distinct subproblem over the space of parameterizations of the final surface. In general, the complicated nature of this funtional space makes variational problems of this type immensely challenging. However, we can exploit the BHF to make crucial simplifications that enable us to solve this problem with relative ease. Recall that Measurable Riemann Mapping Theorem assures us that each mapping $w(z) : \mathbb{D} \to D$ that fixes $z = 0, 1$ is uniquely specified by a Beltrami coefficient μ. A corollary then assures us of the following equivalence

$$\frac{\text{Beltrami coefficients}}{\text{Möbius}} \cong \text{diffeomorphisms} \cong \Sigma_{\mathcal{S}}. \tag{5.20}$$

We can therefore simply explore the space of Beltrami coefficients, rather than directly searching the space of surface diffeomorphisms. In other words the optimization problem in Eqn (5.19) can be reformulated as

$$D_{SEM}[\mathbf{g};\, \mathcal{S}] = \min_{\mu} \int_{\mathbb{D}} d_{SEM}[\mathbf{a}, \mathbf{g}(\mu)]\, \sqrt{a}\, d^2\vec{\mathbf{x}} \tag{5.21}$$

The space of Beltrami coefficients is a much simpler functional space than the space of surface diffeomorphisms. There are no restrictions that Beltrami coefficients must be on-to-one, onto, or satisfy any constraints on their Jacobians. The BHF provides an explicit calculation of the variation of $w(z)$ under the variation of μ. We can therefore search the space of shape equivalent metrics by moving along a flow that decreases $D_{SEM}[\mathbf{g};\, \mathcal{S}]$. The constrained problem takes the form

$$\min_{\boldsymbol{\gamma}(\vec{\mathbf{x}},t)} \mathcal{L} = \int_0^T dt \int_{\mathcal{B}} d^2\vec{\mathbf{x}}\, \sqrt{g}\, \mathcal{C}\left[\boldsymbol{\gamma}(\vec{\mathbf{x}}, t); \mathcal{S}(t=0)\right] + \lambda\, D_{SEM}[\mathbf{g}(\vec{\mathbf{x}}, T);\, \mathcal{S}_T] \tag{5.22}$$

Solving this constrained problem ensures that the target metric at the final time $\mathbf{g}(\vec{\mathbf{x}}, T)$ corresponds to the desired final target shape, without placing any unnecessary constraints

on the final parameterization.

We must now address the specifc form of the cost functional defining optimal growth trajectories. We propose that optimal growth patterns minimize spatiotemporal variation in growth rates and anistropy:

$$\min_{\{\Gamma(\vec{\mathbf{x}},t),\dot{\mu}(\vec{\mathbf{x}},t)\}} \mathcal{E} = \int_0^T dt \int_{\mathcal{B}} d^2\vec{\mathbf{x}}\,\sqrt{g}\ \left[c_1||\nabla\Gamma||^2 + c_2|\nabla\dot{\mu}|^2 + c_3\dot{\Gamma}^2 + c_4|\ddot{\mu}|^2\right], \tag{5.23}$$

subject to appropriate constraints. Given an initial configuration and a final target shape, we can form the constrained problem by including the $D_{SEM}[\mathbf{g}(T)]$ term, as in Eq. (5.21). For simplicity and expediency, we focus on a the special case of *constant growth*. We define a constant growth pattern to be one in which Γ and $\dot{\mu}$ may vary spatially, but are held constant for all time, i.e. $\dot{\Gamma} = \ddot{\mu} = 0$. The first implication of these demands is that constant growth patterns linearly interpolate between the anisotropy of the initial configuration and the final configuration. Since we are always free to choose a conformal parameterization for our initial time point, this means that the Beltrami coefficient as a function of time is simply $\mu(\vec{\mathbf{x}},t) = t\,\dot{\mu}(\vec{\mathbf{x}})$. Additionally, constant growth implies that each material patch grows expontially with a time-independent rate constant. We can clearly see this by calculating the time-dependent area of a material element $dA(\vec{\mathbf{x}},t) = \sqrt{g(\vec{\mathbf{x}},t)}\,d^2\vec{\mathbf{x}}$. From Eq (5.7), we have

$$\sqrt{g(t)} = e^{\Gamma t}\,\sqrt{g(t=0)} \implies dA(t) = e^{\Gamma t} dA(t=0), \tag{5.24}$$

where we have exploited the fact that Γ is constant in time. The cost function for a constant growth pattern is simply

$$\min_{\{\Gamma(\vec{\mathbf{x}}),\dot{\mu}(\vec{\mathbf{x}})\}} \mathcal{E} = \int_0^T dt \int_{\mathcal{B}} d^2\vec{\mathbf{x}}\,\sqrt{g}\ \left[c_1||\nabla\Gamma||^2 + c_2|\nabla\dot{\mu}|^2\right] \tag{5.25}$$

The next crucial simplification is that, for a constant growth pattern, we can neglect the time dependence of the functional and simply minimize over the parameters of the *final* configuration. The modified constant growth functional is given by

$$\min_{\{\Gamma(\vec{\mathbf{x}}),\dot{\mu}(\vec{\mathbf{x}})\}} \tilde{\mathcal{E}} = \int_{\mathcal{B}} d^2\vec{\mathbf{x}}\,\sqrt{g}\ \left[c_1||\nabla\Gamma||^2 + c_2|\nabla\dot{\mu}|^2\right]. \tag{5.26}$$

This solving this reduced problem is completely analagous to the substep in the full time-dependent problem where we calculate D_{SEM}. In other words, given an initial configuration and final target shape, we can optimize over the space of parameterizations of the final shape to find the fields Γ and $\dot{\mu}$ that minimize the reduced energy function in Eq (5.26). Since we are directly optimizing over the space of parameterizations of the final shape, the shape constraint is satisfied by construction. We then can find all of the intermediate metric tensors using the previously discussed properties of constant growth patters. With these intermediate metrics in hand, we can embed the time dependent target geometries. The result is a complete prediction for both the shape and flow of a growing tissue over time.

5.4 Results

We now apply our formalism to compute the optimal constant growth patterns for a variety of synthetic and experimental systems. Even for simple systems, solving the optimization problem is intractable by hand. Instead, we generate numerical solutions using a geometric finite difference method. Smooth surfaces are approximated by mesh triangulations. The discrete metric tensor is a set of target lengths for each edge in the triangulation that satisfy the triangle equality. Smooth quasiconformal mappings become piecewise constant affine transformations of triangles with associated piecewise constant

Beltrami coefficients on each face. The relative areal growth rates are determined from the 3D areas of triangles in the mesh. The final ingredient for our optimization procedure is a non-parametric representation of the final target shape using natural neighbor interpolation [227, 76]. By storing the final shape as an interpolant, we can query dynamical fields in arbitrary parameterizations of the final shape. Furthermore, natural neighbor interpolation has C^1 continuous derivatives, which means that we can analytically calculate gradients of the optimal growth energy with respect to quasiconformal parameterizations. Composing this technique with the discrete Beltrami holopmorphic flow [151] allows us to employ gradient descent methods to efficiently find the paramterization corresponding to the optimal constant growth pattern. Once we have the final target metric, the properties of constant growth patterns allow us to calculate all intermediate metrics. We can then embed each metric individually using a method based on relaxing a mechanical energy from geometric elasticity to find a full time course of growth patterns. Details of these numerical procedures can be found in Appendix F. In all of the experiments that follow, we set the constants $c_1 = c_2 = 1$.

We begin by calculating optimal growth patterns for a set of simple synthetic target shapes grown from an initially flat disklike configuration (Fig. 5.7). In particular, we solve the optimal growth problem for a hemisphere and an elliptic paraboloid using a conformal parameterization as our initial guess. For all systems studied, growth rates in the optimal configuration are uniformized at the cost of introducing anisotropy. These results suggest that growth rate uniformization may be a generic mechanism explaining why anisotropic growth patterns are so commonly observed in living systems.

Our formalism allows us to make quantitative insights into the physical characteristics of various growth patters. Fig. 5.8, A and B shows the cumulative final anistropy of the constant growth pattern transforming a flat disk into a hemispherical shell. Displaying the local direction along which tissue parcels extend dur to anistropic deformation

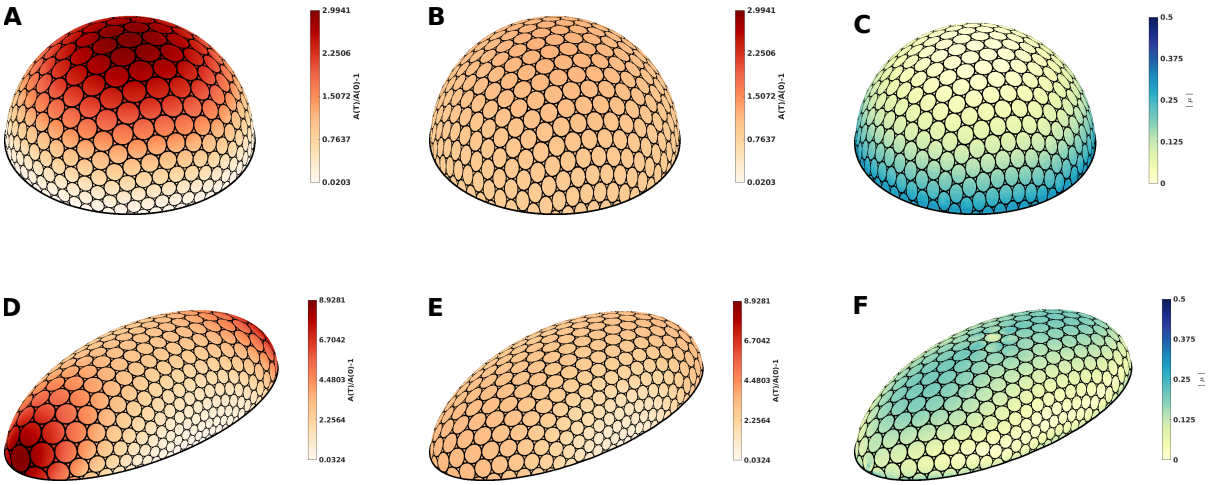

Figure 5.7: **Growth rates can be uniformized by introducing anisotropy.** A set of optimized constant growth patterns for set of synthetic surfaces. Initial configuration for all surfaces is the flat unit disk. Circular texture on the surfaces represents the deformation of material patches under the flow. (A) A conformal growth pattern linking the unit disk and the hemispherical surface. Growth occurs primarily at the apex of the dome. (B) The optimized constant growth rates for the same final shape. Growth rates are heavily uniformized relative to the conformal growth pattern. (C) The absolute value of the Beltrami coefficient for the optimized constant growth pattern. (D) A conformal growth pattern linking the unit disk and an an elliptic paraboloid. Growth occurs primarily at the poles. (E) The optimized constant growth rates for the same final shape. Growth rates are uniformized, although not as completely as the case of the spherical surface. (F) The absolute value of the Beltrami coefficient for the optimized constant growth pattern.

results in a nematic texture with topological defects. Such textures have recently been studied in the context of epithelial morphogenesis coupled to active nematic biomolecular components [191, 251, 104]. The optimal growth texture is characterized by a +1 defect at the pole off the sphere. Modifying the anistropy texture, but keeping the areal growth rates exactly the same, produces an entirely new final shape (Fig. 5.8, C and D). This proof-of-principle demonstrates how our methods can be used as a platform for growth pattern design in terms of nematic textures.

Next, we applied our machinery directly to an experimentally observed growth pattern in the crustacean *Parhyale hawaiensis*. *Parhyale* are direct developers that grow externally visible appendages and deep surface folds during embryogenesis when live imaging is readily possible [262, 34]. Recent work characterized the growth of the T2 appendage by tracking individual cells in 3D [263]. Analysis of individual cell behaviors is informative, but produce limited insights about the dynamics of tissue-scale deformations. Using a combination of computer vision and discrete differential geometry, we extracted the continuous, quasiconformal growth pattern generating the limb. We were then able to apply our machinery to calculate the optimal growth pattern linking the initial configuration and the final shape of the limb. The optimal growth pattern qualitatively reproduces the large scale features of biological limb morphogenesis. In both the measured and calculated growth patterns, areal growth occurs primarily at the distal tip of the nascent appendage. The anisotropic deformations generating the limb are also similar. For both the measured and calculated growth patterns, the tissue stretches along the proximodistal axis away from the animal's body. The most obvious quantitative discrepancy is that the optimal growth pattern underpredicts the maximum areal growth rates at the distal tip of the limb. Note that the *Parhyale* limb is comprised of relatively few cells (approximately 15 cell lengths long at 109.1h AEL). The observed discrepancy may indicate that the optimal growth principle should be modified to ac-

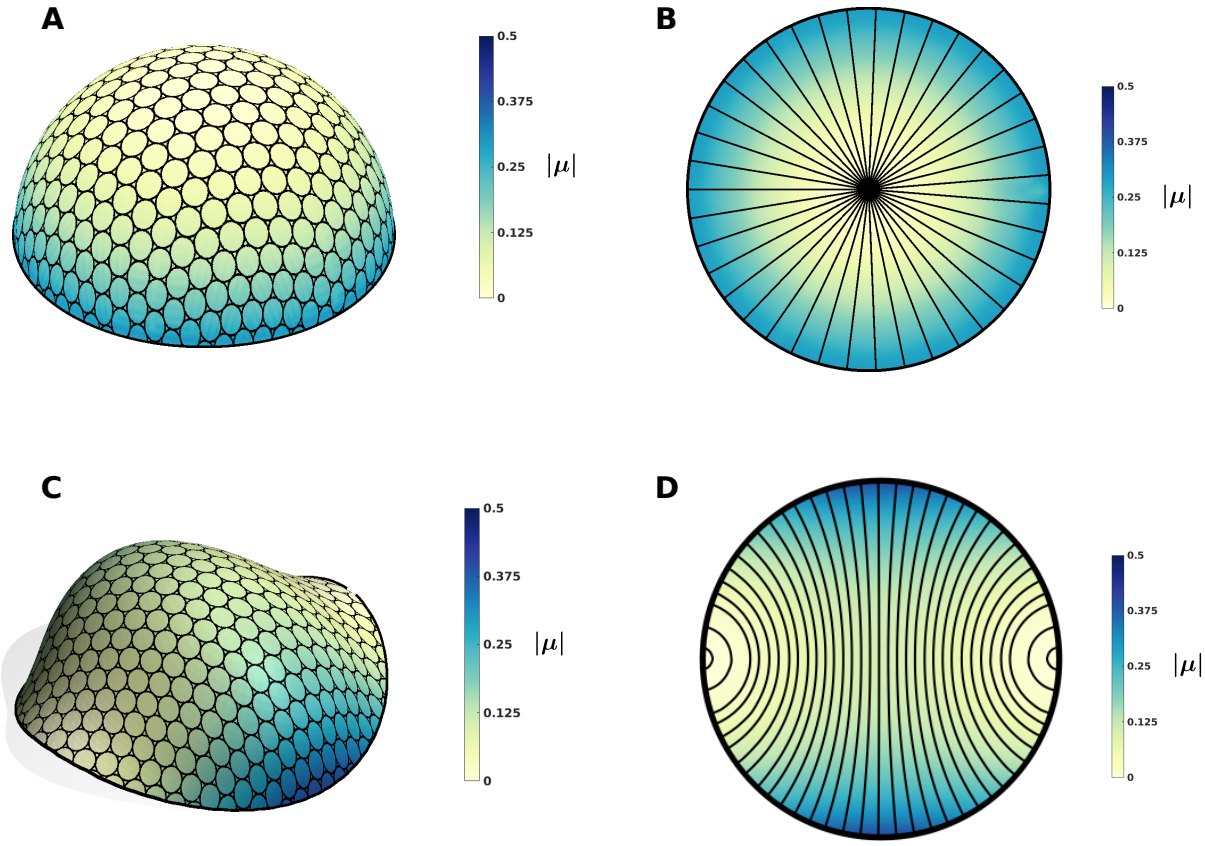

Figure 5.8: **3D surface features are reflected in nematic anistropy textures.** (A) The absolute value of the Beltrami coefficient for the optimized constant growth pattern transforming a flat disk into a hemispherical surface. (B) The nematic field denoted the direction along which material patches extend. The texture is reminiscient of a $+1$ defect with phase $\psi = 0$. (C) A different surface grown using the exact same growth rates as the surface in (A), but with a different anistropy texture. (D) The anistropy texture for the surface in (C). The texture is constructed by placing two $+1$ defects with phase $\psi = \pi/2$ at opposite poles of the disk boundary.

count for the discrete cellular structure of such tissues, rather than naively optimizing for smooth gradients of proliferation.

Finally, we made quantitative comparisons of different types of dynamic growth patterns to the observed developmental trajectory. In particular, we compared the constant growth pattern to another growth pattern that linearly interpolated between the initial and final optimal metric tensor, i.e. $\tilde{\mathbf{g}}(t) = (1 - t/T)\,\mathbf{g}(t = 0) + (t/T)\,\mathbf{g}(t = T)$ for $t \in [0, T]$. We see that the constant growth pattern produces a significantly more accurate result at intermediate times than the linearly interpolated geometry.

5.5 Discussion

This study puts forth a theoretical and computational machinery for tackling the problem of growth pattern selection in epithelial morphogenesis. By exploiting the mathematical formalism of quasiconformal transformations, we enable the characterization of arbitrary growth patterns in terms of simple contributions with straightfoward physical interpretations.We can therefore make quantitiative comparisons between different growth patterns, opening the door to a predicitive understanding of growth pattern selection.

We propose a simple action priniciple for growth pattern selection, wherein stereotypical growth trajectories minimize spatiotemporal variation in growth rates and anisotropy. The prediction of this model was shown to reproduce important qualitative features of experimentally measured growth patterns in limb morphogenesis. Crucially, our optimization machinery is both modular and adaptible. Different optimality criteria tailored to specific situations may be substituted and explored in a controlled fashion. This portability invites applications beyond morphogenesis to the design of synthetic surface structures and bioinspired materials.

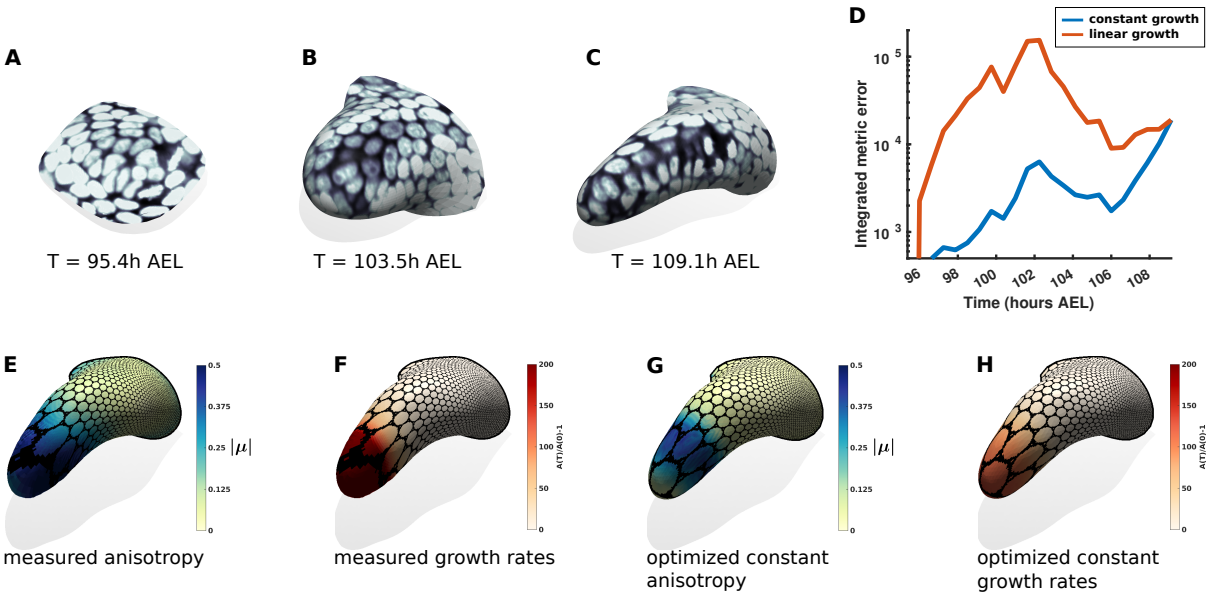

Figure 5.9: **Optimal growth platform captures features of experimentally quantified limb morphogenesis.** $(A\text{-}C)$ Surface of a growing appendage in a *Parhyale hawaiensis* embryo captrured using light-sheet microscopy. Time is measured in hours after egg lay (AEL). Signal displayed on the surface is a transgenic fluorescent nuclear marker. (D) Instantaneous integrated metric error between two different growth patterns. The blue curve is the prediction error for the constant growth pattern linking the initial configuration and the optimized final configuration holding $\dot{\mu}$ and Γ constant. The orange curve links the same initial and final configurations, but does so by linearly interpolating the initial and final target geometries, i.e. $\tilde{\mathbf{g}}(t) = (1 - t/T)\,\mathbf{g}(t = 0) + (t/T)\,\mathbf{g}(t = T)$ for $t \in [0, T]$. (E) The measured anistropy for the appendage growth pattern. (F) The measured growth rates for the appendage growth pattern. (G) The anistropy associated with the optimized constant growth pattren generating the final appendage shape. (H) The growth rates associated with the optimized constant growth pattern generating the final appendage shape.

One compelling generalization of our simple optimality condition would be the inclusion of mechanical and geometric feedback. By relaxing the constraint that the physical geometry be an isometric embedding of the target geometry, we could directly explore how dynamical mechanical fields, such as in-plane stress, may modulate the feasibility of particular growth patterns with respect to optimality. Another possibility would be the direct inclusion of morphogen fields. Our machinery is well suited to analyze a variety of geometrically distinct classes of morphegens, including scalar fields (e.g. molecular concentration), vector fields (e.g. concentration gradients), and nematic tensor fields (e.g. contractile actomyosin networkds). Essentially arbitrary interactions between mechanics, geometry, and signalling could be incorporated into novel optimality criteria. The result is a step towards generating a quantitative understanding of how morphogenetic programs decompress genetic information into shape and form.

Chapter 6

Conclusions and Outlook

It is ceaselessly astonishing to consider the variety and beauty of physical forms living systems achieve. The furling of a flower's petals, the streamlined contours of birds in flight, our own bodies, and every shape in between are all made possible by developmental programs that instruct single cells transform into complex multicellular structures. Determining how morphogensis transduces genetic information into physical shape is one of the most compelling frontiers in science. By now, it is clear that morphogenesis marries biology, biochemistry, physics, and geometry in a way that transcends centuries-old delineations of scientific fields and challenges us to evolve new paradigms for understanding life. Recent revolutionary advances in experimental and computational techniques have heralded an explosion of quantitative data on developmental programs. We are rapidly transforming these insights into an increasingly cohesive and predictive understanding of morphogenesis. In a practical sense, this presents the tantalizing prospect of new medicines and cures for developmental defects [110]. Less pragmatically, this enterprise offers glipmses of nature that simultaneously underscore both the deep interconnectedness of all life and the uniquess of our own place within that framework. In addition to the simple joy of solving problems, it is the occasional appreciation of these connections

that have maintained my curiosity and passion throughout my doctoral work and beyond as I carry this work with me into the future.

This dissertation has presented a collection of projects utilizing a combination of theoretical, computational, and experimental methods to investigate the growth and development of thin tissues. The result of each project have illuminated the vital role played by order, geometry, and mechanics in epithelial morphogenesis. The central function of these physical properties hints that the dizzying complexity of developmental programs may belie an emergent simplicity. Analogously to the discovery of universality in many-body physics, it is possible that individual growth patterns may be unified by a set of common, underlying principles. The elegance of this ideal, however, does not guarantee its veracity. It is conceivable that morphogenesis and other characteristics of living systems present a different type of complexity that will not yield the simplifications that have exemplified study of physical systems. With this in mind, the goal and outlook of future projects building upon this work will be to build quantative models of morphogenesis that produce testable predictions and, to whatever extent is possible, use these models to extract universal aspects of shape change and growth.

In Chapter 2, we presented a set of computational methods for the characterization and analysis of tissue deformation in tubelike surfaces. These methods, contained within the TubULAR package, enable users to extract dynamic surfaces, construct 2D parameterizations optimized for tracking tissue parcels, measure whole-organ tissue deformation, and compute signatures of 3D motion. Future directions for this work include expanding its functionality to address a greater variety of system topologies. In addition to simple tubes, thin tissues are frequently organized into disks (e.g. the early *Parhyale* embryo [34]), spheres (e.g. the mature *Hydra* body plan [155]), and complicated branching structures (e.g. airways in the vertebrate lung [183]). Moreover, tissue topology can change over the course of development. This occurs, for instance, during organogenesis in

Drosophila when disklike tissue fuses into the gut tube [165] and similarly during neural tube formation in vertebrate neurulation [119]. It is compelling to consider implementing a computational suite capabale of seamlesly constructing Lagrangian tissue paramaterizations of surfaces with time dependent topologies. A tool with this capability would also have applicability beyond morphogenesis, for instance, in the study of active cytoskeletal gels [240].

In Chapter 3, we demonstrated how actively choreographed cell divisions generate the ordered body plan in the *Parhyale* embryo from an initially fluid state. From a theoretical perspective, it would be interesting to further investigate the robustness and efficacy of this order generating mechanism. The capacity of oriented divisions to generate orientational order could be explored *in silico* for a variety of initial tissue configurations, material parameters, and topologies. There are also a variety of potential continuations and applications in various experimental models. The topological rearrangements of cell-cell connectivty induced by division enable the tissue to more rapidly explore the phase space of ordered states than through number-conserving rearrangements alone [8]. It has recently been shown that the typical shape of the *Drosophila* wing is preserved in mutants with randomized division orientations, with oriented T1 transitions supplying the necessary shear deformations to generate the anistropic final shape [277]. It would be interesting to compare the hexatic order of cells in these mutant wings to the typical hexagonal cell packings produced by wild type animals [48].

In our evaluation of *Parhyale* germband formation, we were able to show that the orientations and timing of cell divsions were not set by local mechanical or geometric signals and proposed instead that these properties are determined by biochemical symmetric breaking (i.e a morphogen gradient or planar cell polarity mechanism). Further investigation might seek to determine the precise identities of relvant biochemical agents, although the lack of genetic techniques in *Parhyale* make this a daunting task. One

exciting continuation would be to directly investigate the relationship of order within the ectodermal lattice and ensuing tissue scale shape change. We contend that the ordered cell lattice acts like a coordinate grid that enables the developing embryo to properly arrange and orient its many appendages. The sites of differential cleavage at which the orientational order breaks down were shown to correspond to the loci of nascent limb buds during subsequent limb development. This process provides a rich example of the interplay between geometry, mechanics, and shape change that would be interesting to explore. Finally, it would be worthwhile to investigate how typical ectodermal ordering is modifed during ectopic limb formation due to hox gene misexpression in transgenic *Parhyale* embryos [189].

In Chapter 4, we investigated how the complex shape of the *Drosophila* midgut is generated during embryonic organogenesis. The gut, which is initially a simple tube, first forms folds delineating distinct compartments and then elongates and coils into a compliated chiral structure. We found that hox gene expression patterns mediate calcium pulses that regulate muscle contractions at precise locations along the length of the gut. We showed that these contractions induce sharp folds and convergent extension of the gut endoderm constrained by tissue incompressibility. Taken together, these results demonstated a link from genes to tissue morphodynamics through active forces and continuum mechanics. A number of exciting aspects of this process remain to be understood. The observed hox gene expression domains are spatially broad and vary slowly in time. The mechanism by which this coarse positional information in translated into precise positions and timing of localized calcium activity is unclear. At the tissue level, an outstanding question is the the extent to which endodermal cells actively respond to muscle contraction, rather than passively deforming. Finally, since our work primarily investigated the formation of folds during the first stages of organogenesis, there are rich possibilities for future reserach into the subsequent coiling and chiral symmetry breaking.

In Chapter 5, we presented a theoretical and computational machinery for tackling the problem of growth pattern selection in epithelial morphogenesis. We showed that developmental programs can be quantified in terms of anistropy and areal growth rates. We proposed an action principle that selects for simple growth patterns minimizing spatiotemporal variation in these quantities. We then applied this formalism to seveal synthetic and experimental systems. The purpose of this work was not to claim discovery of a universal principle, but rather to demonstrate that cogent, quantitative questions can be asked about growth pattern selection. A great deal of future work remains. Firstly, it would be interesting to apply this formalism to a greater variety of experimental systems. Leaf growth in plants is a particularly exciting setting to study how the interplay between isotropic areal growth and anisotropic deformations generate shape and flow [4, 32]. On the theoretical front, our methods coul be augmented to handle a greaty variety of system topologies. The arguments we employed to quantify the growth patterns of topological disks generalize quite well for topological spheres and cylinders. Finally, we look forward to exploring new optimality criteria explicitly relating tissue geometry to mechanical feeback and morphogen expression patterns.

Appendix A

TubULAR implementation details

A.1 Overview of approach by example

In addition to detailed documentation and example pipelines available on GitHub, we summarize the steps in our approach in Fig. A.1. This gives a typical sequence of method calls to extract surfaces, create an initial sequence of parameterizations constrained for minimal tissue motion in the pullback plane, and compute covariant measures of tissue dynamics. Subsequent steps further refine the material coordinate definition to remove residual motion and read out measures of motion and strain in this Lagrangian frame (along 'material pathlines'). The last set of steps visualize the material motions, decompose them into divergence, curl, rate of area change, and measures of anisotropic deformation like the Beltrami coefficient. Finally, methods compute principal components of the tissue dynamics and decompose into eigenfunctions of the Laplace-Beltrami operator, akin to spherical harmonics for a sphere or Bessel functions for a cylinder but defined on an arbitrary surface. Fig. A.2, meanwhile, gives an overview of the class structures included in the toolkit.

Instantiation
Set experiment metadata and any custom options.....xp=struct(...); opts=struct(...);
Instantiate TubULAR.....tubi = TubULAR(xp, opts)

Surface extraction
Create downsampled volumes to use for iLastik & level sets.....tubi.prepareIlastik()
Extract the surfaces using level sets on output of iLastik or raw data..tubi.getMeshes()

Parameterization
Define global reference frame (APDV).....tubi.computeAPDVCoords()
Define endcap points and one point for a virtual seam.....tubi.computeAPDpoints()
Align meshes into global frame.....tubi.alignMeshesAPDV()
Optional: render data on dynamic surfaces (can be slow).....tubi.plotSeriesOnSurfaceTexturePatch()
Compute initial centerlines.....tubi.extractCenterlineSeries()
Temporally average centerlines and fix any inconsistencies.....tubi.generateCleanCntrlines()
Remove the endcaps.....tubi.sliceMeshEndcaps()
Clean up the mesh endcaps.....tubi.cleanCylMeshes()
Cut the meshes along virtual seams.....tubi.generateCurrentCutMesh()
Constrained parameterization of the mesh into (u,v) and (s,ϕ) frames....tubi.generateCurrentSPCutMesh()
Generate pullback images.....tubi.generateCurrentPullbacks()

Dynamics
Initial pass of smoothing embedding over time.....tubi.smoothDynamicSPhiMeshes()
Create pullbacks of smoothed (s,ϕ) frames.....tubi.generateCurrentPullbacks()
Tile the images in ϕ (as 'double-cover').....tubi.doubleCoverPullbackImages()
Measure any residual material motion in the parameterization.....tubi.measurePIV2d()
Translate pullback information into motion in 3D (embedding space).....tubi.measurePIV3d()

Refined processing of surface dynamics
Recommended: smooth the resulting 3D dynamics along material pathlines..tubi.timeAverageVelocities()
Compute material pathlines in 3D.....tubi.measurePullbackPathlines()
Measure rate of strain over the surface at each timepoint.....tubi.measureStrainRate()
Query the rate of strain along pathlines.....tubi.measurePathlineStrainRate()
Measure the integrated strain along pathlines.....tubi.measurePathlineStrain()

Interpretation and mode decomposition
Visualize flows.....tubi.plotTimeAvgVelocities()
Decompose into divergence and curl, scalar potential fields.....tubi.helmholtzHodge()
Compute areal rate of change.....tubi.measureMetricKinematics()
Mesaure anisotropic strain using Beltrami coefficient.....tubi.measureBeltramiCoefficient()
Decompose into Principal Component Analysis.....tubi.getPCAoverTime()
Decompose into eigenmodes of the Laplace-Beltrami operator.....tubi.getLBSoverTime()

Figure A.1: **Example high-level pipeline for data analysis using TubULAR passes through constrained parameterization, measurement of surface dynamics, refinement, and steps to interpret the results.** Descriptions of typical steps in a TubULAR pipeline are listed on the left, with the corresponding class method calls for each goal on the right.

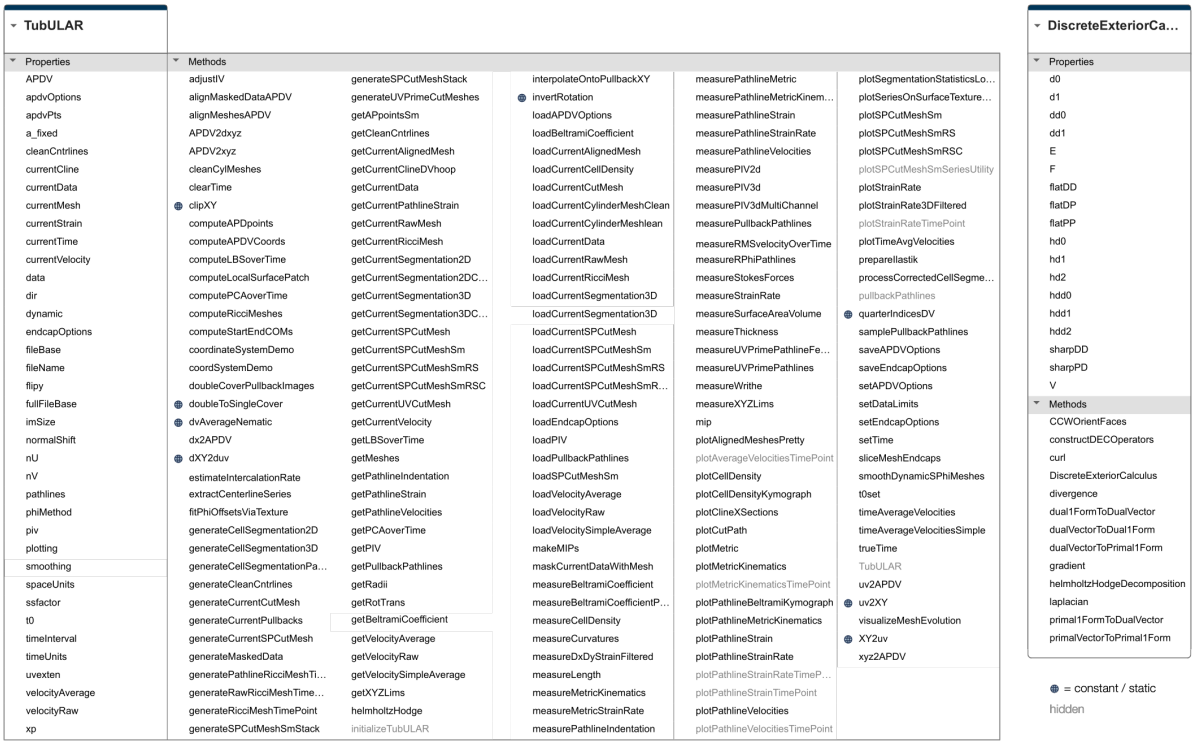

Figure A.2: **The TubULAR class and the DiscreteExteriorCalculus class within `DECLab` carry properties and methods, listed here for reference.**

A.2 Surface extraction using level sets

To extract whole-organ surfaces, we use a level sets approach, combined with marching cubes [149] and Laplacian smoothing. While the literature on level sets segmentation is vast [182], we give a brief overview of the relevant method here. The process of surface detection is mapped onto an optimization problem by defining a physics-inspired cost functional [168, 42]:

$$F[c_1, c_2, \mathcal{S}] = \mu \int_{\mathcal{S}} \mathrm{d}s + \nu \int_{\Omega} \mathrm{d}^3\mathbf{x} + \lambda_1 \int_{u>0} |I(\mathbf{x}) - c_1| \mathrm{d}\mathbf{x} + \lambda_2 \int_{u<0} |I(\mathbf{x}) - c_2| \mathrm{d}\mathbf{x}, \quad \text{(A.1)}$$

where c_1 and c_2 are the average values of the data inside and outside, respectively:

$$c_1(\mathcal{S}) = \langle I(\mathbf{x}) \rangle_{\text{inside}} \quad \text{(A.2)}$$

$$c_2(\mathcal{S}) = \langle I(\mathbf{x}) \rangle_{\text{outside}}. \quad \text{(A.3)}$$

The first term is a surface tension that tries to smooth out ruggedness in the surface. The second term is an effective pressure that penalizes blow up in the enclosed volume of the segmented regions. The final two attachment terms incorporate the actual measured data into the optimization procedure. The third term attempts to homogenize the intensities of voxels included in the interior of the segmented volume and the fourth term attempts to homogenize the intensities of the excluded voxels. A minimizer can be found by iteratively applying the Euler-Lagrange equation [168],

$$\partial_t u = |\nabla u| \left(\mu \nabla \cdot \left(\frac{\nabla u}{|\nabla u|} \right) - \nu - \lambda_1 (I - c_1)^2 + \lambda_2 (I - c_2)^2 \right), \quad \text{(A.4)}$$

or by using a sparse-field approach [260].

To segment the midgut and heart surfaces, we generate a level set solution for a

contiguous volume enclosing the interior of the tube, partitioning space into a topological sphere (the 'filled' tube) and its exterior. TubULAR then removes endcaps of the mesh at the interface to create a topological tube.

A.2.1 Segmentation of the zebrafish heart

The zebrafish heart data set posed particular challenges requiring the application of some non-standard segmentation procedures, which we summarize here. Rather than attempt to segment both the heart tissue and the space it enclosed, we used the level set methods to segment only the heart tissue. This resulted in a binary level set solution of toroidal topology. We then applied a homotopic thinning procedure slice-by-slice along the length of the tube to produce a point cloud approximating the mid-surface of the heart tissue. We then fed a smoothed, up-sampled version of this point cloud into our Poisson surface reconstruction algorithm to produce a closed, sphere-like mesh of the heart. The results at this point in the segmentation process were structurally identical to those produced in a typical pipeline.

A.3 Constrained mapping to the plane follows tissue motion

To follow tissue surfaces as they deform, we begin with an initial map at a reference timepoint that defines the material coordinates, then construct maps to minimize subsequent tissue motion in the pullback plane, remove any residual motion, and generate material pathlines in 3D. We denote the dynamic map from the evolving surface to a fixed 2D material coordinate system as $\varphi(t)$. This dynamic map is constructed as a composition of four steps: $\varphi(t) \equiv J \circ \Phi \circ Z \circ f$, each of which is detailed in this section. Briefly,

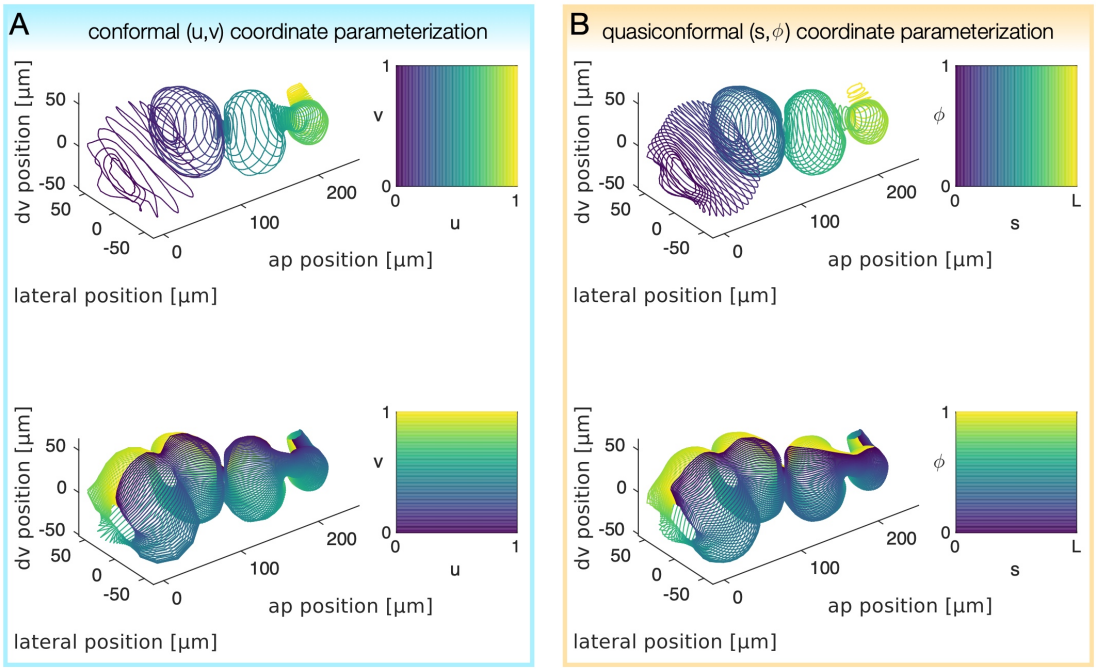

Figure A.3: **A quasiconformal mapping from (u, v) to (s, ϕ) aids in spatially uniform surface sampling and velocimetry for refined tissue tracking.** *(A)* The constrained conformal map to the plane at a time 90 minutes after the onset of constrictions ($t = 90$ min) demonstrates large variations in the sampling density along the longitudinal direction (top). Note the high density of circumferential hoops near constrictions and near the posterior tip. *(B)* After creating the conformal mapping to (u, v), the TubULAR workflow constructs an second map to a parameterization in which the surface is more evenly sampled along the longitudinal axis and in which motion in the v direction is subtracted off. Note the more uniform longitudinal density of circumferential hoops (top) and the difference in the curve $\phi = 0$ at this later timepoint, which matches the previous position of the material along $\phi = 0$ at earlier timepoints. At time $t = t_0 = 0$ min, $\phi = v$, while at this later timepoint, $\phi \neq v$.

$f : \mathcal{S}(\mathbf{x}) \to (u, v)$ is a conformal map of the surface $\mathcal{S}$ to the unit square (via Ricci flow or Dirichlet energy minimization). $Z : u \to s$ maps each longitudinal coordinate $u(t)$ to proper length $s(u(t))$ along the long axis of the tube-like surface. $\Phi : v \to \phi$ stabilizes motion of the tissue along the circumferential axis. Finally, $J : (s, \phi) \to (s_0, \phi_0)$ removes any residual motion of the material in the pullback plane. Let us turn to each component in turn.

A.3.1 Initial conformal map f

We homotopically flatten the 3D surface to the plane using one of two methods. The first (default) option is Ricci flow, which results in a precisely conformal output at the cost of being slow, while the second option is using a map minimizing a Dirichlet energy, which in general is faster, but produces less conformal results.

Ricci flow

Originally introduced by Hamilton in the context of geometric topology, Ricci flow is a tool that enables the design of Riemannian metrics with prescribed curvatures. Ricci flow deforms a Riemannian metric proportionally to its intrinsic curvature, such that the curvature evolves according to a nonlinear heat diffusion process and eventually becomes constant everywhere. In the continuous setting, Ricci flow on 2D surfaces can be defined as

$$\frac{dg_{ij}(t)}{dt} = -2(K(t) - \bar{K})\, g_{ij}(t), \tag{A.5}$$

where $g_{ij}(t)$ is the time dependent metric of the surface, $K(t)$ is the associated Gaussian curvature, and $\bar{K}$ is the target Gaussian curvature. It is immediately apparent from Eq. (A.5) that surface Ricci flow is conformal, i.e. preserves angles defined by $g_{ij}(t)$. It has also been demonstrated that the Gaussian curvature during the flow always remains

bounded.

Surface Ricci flow has intuitive geometric interpretations, which directly inform the design of data structures in the discrete setting. For instance, the surface can be represented as a mesh triangulation and the metric tensor can be simply represented as a set of positive edge lengths on this triangulation satisfying the triangle inequality. Crucially, it is possible to reformulate discrete surface Ricci flow as a convex optimization problem over the space of discrete metrics, which has a unique minimum and can be solved efficiently using Newton's method. Intuitively, given an initial metric, the method first constructs a circle-packing metric, i.e. it instantiates a set of circles living at mesh vertices with consistent conditions on how the circles intersect. Each variational step in the minimization process flows the discrete metric closer to the target curvature in a way that always maintains the integrity of the circle packing. The conformality of the discrete flow is ensured by construction since it always maps (discrete) infinitesimal circles into (discrete) infinitesimal circles. For a comprehensive review of the method, please consult [276].

Annular orbifold map

The annular orbifold map follows the formalism of Aigerman & Lipman [2], but applies these ideas to a topological cylinder mapped to a rectangle that is periodic along one dimension. Essentially, we produce a parameterization that minimizes the Dirichlet energy (see next section), enforcing certain boundary conditions so that the resulting parameterization is both seamless and globally bijective.

For a parameterization $\vec{u} = (u, v)$, the Dirichlet energy is defined as

$$E_D = \frac{1}{2} \int ||\nabla \vec{u}||^2 \mathrm{d}A. \tag{A.6}$$

This energy penalizes ruggedness in $\vec{u}$ and, as a result, its minimizers are smooth, well-behaved parameterizations. Extrema of this energy functional can be found according to a variational principle by solving the associated Euler-Lagrange equation:

$$\nabla^2 \vec{u} = 0. \tag{A.7}$$

This is, of course, simply the vector Laplace equation. The associated solutions are called *harmonic maps*. In practice, since $\vec{u}$ is unknown, the operator ∇^2 is taken to be the Laplace-Beltrami operator defined on the input 3D surface. Additionally, we demand that the anterior and posterior endcaps of the cylindrical mesh are mapped to vertical lines $u = 0$ and $u = 1$. We also enforce the orbifold condition that corresponding vertex pairs on each cut path map to the same location in the planar parameterization space, modulo a vertical offset corresponding to the periodic spacing along the azimuthal direction of the tube. These boundary constraints ensure that the planar parameterization retains the cylindrical topology of the 3D surface under proper tiling of the plane. This entire problem, including the constraints, can be cast as a single linear system

$$A\vec{u} = b. \tag{A.8}$$

Any conformal parameterization of the surface will be a minimizer of the Dirichlet energy. To see this, let us specialize for a moment to the case of planar transformations $f : \mathbb{C} \to \mathbb{C}$. Let $z = x + i\,y$ denote a complex coordinate defined over the input domain being parameterized (the analogue of the input 3D surface) and let $f = u + i\,v$ be a complex representation of the parameterization. A conformal parameterization must satisfy the Cauchy-Riemann condition

$$\partial_{\bar{z}} f = 0. \tag{A.9}$$

It is therefore clear that any conformal mapping must also be harmonic since $\nabla^2 f = 4\partial_z \partial_{\bar{z}} f = 0$. Similar generalized arguments prove the harmonicity of 2D conformal parameterizations of 3D surfaces. In practice, the boundary conditions we enforce preclude the possibility of a truly conformal mapping. However, the results are generally a good approximation of a discrete conformal mapping, especially in the bulk away from the mesh boundaries. The high quality of Dirichlet energy minima as approximations to discrete conformal mappings has also been observed in a variety of settings [2]. While such methods are not currently implemented in TubULAR, we note that the conformality of the parameterizations can be improved by replacing the Dirichlet energy with the so-called *conformal energy*, $E_C = E_D - A(\vec{u})$, where $A(\vec{u})$ denotes the area of the domain of parameterization [194]. This improvement in conformality comes at the expense of increased computational cost and usually do not preserve angles as well the conformal Ricci maps anyway.

Independence of mapping on choice of longitudinal seam

The choice of cut path along the long axis of the organ for unrolling the cylinder should intuitively be immaterial to the position of the mapped surface coordinates. For the Ricci flow case, this is true by construction: we map to an annular domain (with one endcap boundary mapped to the unit circle and one near the origin), then take a logarithm of these coordinates to acquire a rectilinear representation. For the annular orbifold map, we must enforce this path independence.

Inspired by the topology-preserving orbifold mappings of spherical surfaces [2], we enforce a set of boundary conditions to ensure that the parameterization in the plane respects the cylindrical topology of the 3D surface. Namely, we demand continuity in the boundary components of the 2D meshes associated with the virtual seam, such that, if one were to tile these meshes in the plane, moving across this boundary from one tile

into another would be physically indistinguishable from crossing over the virtual seam on the 3D cylindrical surface. This mapping ensures that the edges composing the cut path takes on a unique shape in the domain of parameterization, and the shape of these edges would be identical whether or not the edges are components of the cut path.

There is one caveat to this independence: the cut path will change the output pullback map if it winds around the tube relative to the centerline with a different winding number. Therefore, we take measures to enforce this topological constraint. For the first timepoint mapped to the plane (t_0), we choose a cut path to be the geodesic connecting the two endcaps. For subsequent (and previous) timepoints, we ensure the winding number does not change relative to this path's winding.

While several options are available for enforcing this constraint, the default behavior uses a crude approximation to the centerline and measures the winding of the cut path around this curve. The details of this centerline construction are not particularly important, since the curve's purpose is to provide a topological constraint – not a geometric one – on the cut path chosen, whose own geometry is immaterial so long as it does not wind around the centerline. Nevertheless, we give a brief description here: Briefly, for each timepoint, we measure a crude pathline via fast marching (Fig. A.4B). We connect the endpoints by a curve that spans the interior of the mesh found by minimizing the 'time of travel' with a speed of travel through any given voxel determined by the distance transform of the segmented data volume [53]. If a geodesic path is found to change its winding from one timepoint to the next, the path is perturbed to more closely match the previous one in space until the topology is preserved. We found this 'trial and error' approach to be far faster than constructing an explicitly-topologically-equivalent curve (for example, after Ricci flow to an annular domain). The relevant TubULAR methods provide options for choosing different approaches if needed, including the explicit construction method.

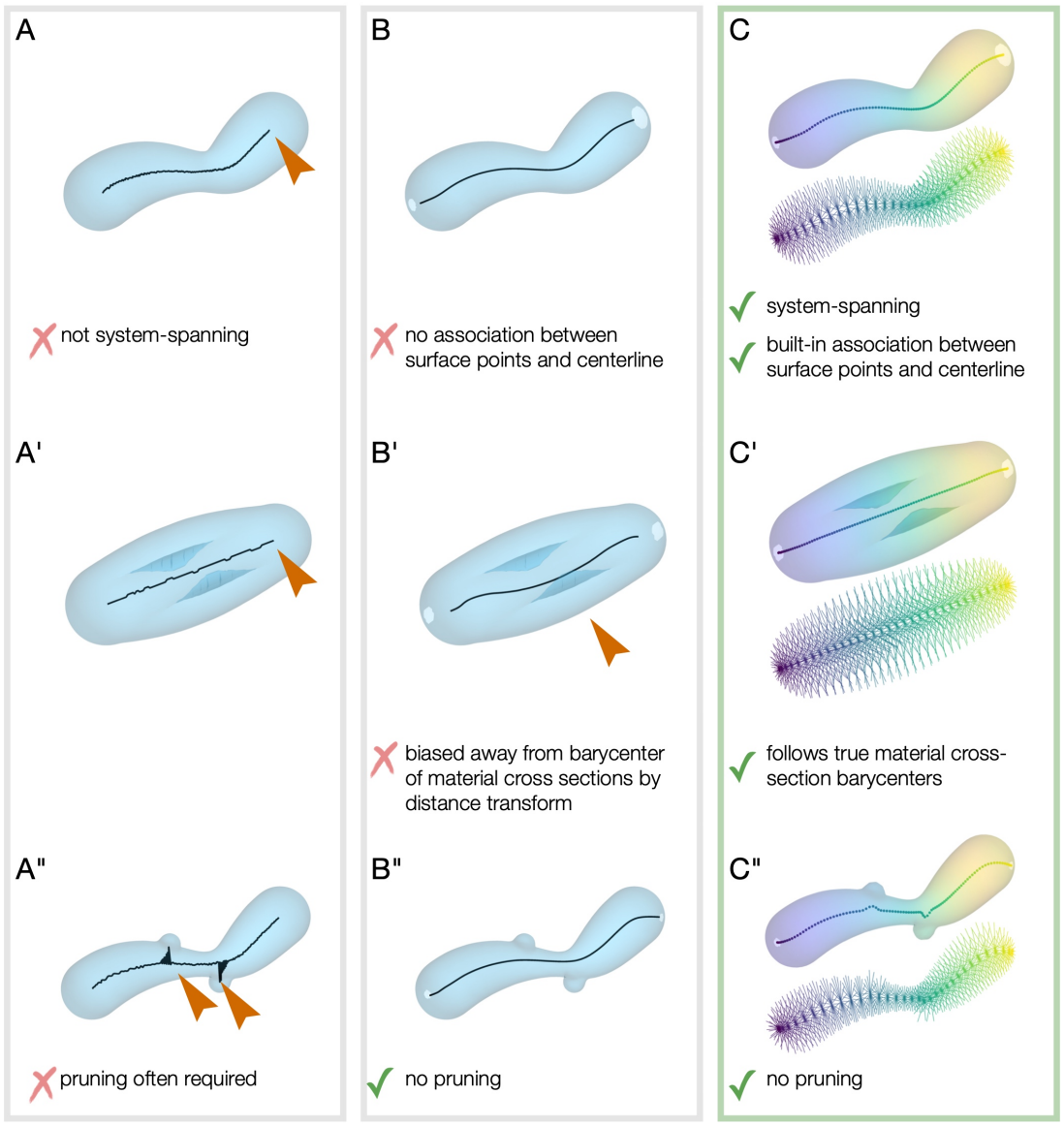
A
not system-spanning
A'
A"
pruning often required
B
no association between surface points and centerline
B'
biased away from barycenter of material cross sections by distance transform
B"
no pruning
C
system-spanning
built-in association between surface points and centerline
C'
follows true material cross-section barycenters
C"
no pruning

Figure A.4: **Our method provides a geometric route to centerline extraction which offers several benefits over traditional approaches.** *(A-A")* An approximate centerline can be built from homotopic thinning methods [141]. This simple method has several downsides, including that the curves do not span the whole system, and pruning of the curve is needed when the surface is not sufficiently smooth. Associating the mesh surface and the curve poses conceptual challenges as well. *(B-B")* An alternative – which is implemented in an auxiliary step for constraining surface parameterization in TubULAR – minimizes the 'time of travel' within the segmented volume from selected endpoints, where the speed of travel through a given voxel is weighted by its signed distance from the mesh surface [53]. While this offers system-spanning centerline curves, the curves deviate from the center of the object when the surface is puckered, as in panel B'. Additionally, no association between the mesh surface the the curve is given by this method. For contorted tubes such as the fly midgut, nearest distance matching gives spurious associations. *(C-C")* Constructing centerlines based on the coordinate parameterization to the material frame offers advantages for finding a single curve without branching with explicit associations between surface points and the centerline. This construction enables examination of the constriction cross sections in the Chapter 2.

A.3.2 Quasiconformal map $\Phi \circ Z$ to (s, ϕ) coordinates

We then introduce a further coordinate transformation which we found aids in surface stabilization. Because directly measuring optical flow in (u, v) coordinates is often too crude and does not uniformly sample tissue motion across the embedding surface, we followed a more constrained approach to remove motion, which we found to aid in subsequent refinement of the tissue stabilization. We denote this second planar parameterization (s, ϕ), shown in Fig. A.3B. We find this (s, ϕ, t) parameterization aids in both visualization and enables more accurate velocimetry measurements than other choices we considered, particularly when large variations appear in the effective radius of the surface along its long axis. This second map, which we denote $\Phi \circ Z$ is a quasi-conformal transformation (i.e. a smooth transformation with finite anisotropic distortion [1]) of the initial (u, v) coordinates.

For the reference timepoint t_0 considered first, the coordinate directions $(\hat{s}, \hat{\phi})$ are the same as the conformal mapping to the plane (u, v) at a reference time $t = 0$. Furthermore,

at this initial timepoint, ϕ is identical to the intrinsic circumferential axis of the conformal map. The sole difference is that s parameterizes a longitudinal position along the long axis of the organ at $t = 0$. In particular, we compute s as the average geodesic length along the surface from the anterior endcap to a set of uniformly-sampled points with fixed horizontal coordinate in the conformal pullback space (Fig. 2.2A-D). Intuitively then, s this is the average path length required to travel on the surface from the anterior face to a given location along curves of constant ϕ.

In more detail, we define the (s, ϕ) domain of parameterization, which is less conformal but which more equally represents different patches of tissue that initially experience vastly different dilation in the map f from 3D embedding $\vec{x}$ to 2D pullback $\vec{u} = (u, v)$. This empirically improves measurements of tissue velocity in plane for our shapes, and we expect the additional transformation will improve other tissues that are elongated in quasi-axisymmetric geometries. Circumferential 'hoops' of tissue surrounding the centerline that are equally sampled *along* the centerline will be equally spaced in the pullback coordinates. The map $\Phi \circ Z$ from the previous (conformal) frame (u, v) to the (s, ϕ) coordinate system is defined by

$$s(u) = \int_0^u \langle \mathrm{d}s(u') \rangle_{u'=\mathrm{const}} du', \tag{A.10}$$

and

$$\phi(u, v) = v - \phi_0(u). \tag{A.11}$$

Equation A.10 ensures that circumferential hoops sampled at equally spaced distances (as measured by their average proper distance) along the longitudinal axis are equally spaced in pullback space.

Equation A.11 removes tissue motion along ϕ at each longitudinal position s. The

form of $\phi_0(u)$ is such that motion of the tissue along each hoop is cancelled out in the pullback to acheive a more Lagrangian parameterization. For $t = t_0$, $\phi_0(u) = 0$. For other timepoints, $\phi_0(u)$ is chosen to minimize the difference in positions of material points at the current timepoint relative to the previous (next) timepoint for $t > t_0$ ($t < t_0$). To minimize the difference in material positions, we maximize the correlation of circumferential 'hoops' defined by $s_i < s < s_j$ to the mapped positions at a previously-solved timepoint closer to t_0. These hoops can be visualized in pullback space as vertical strips in the (s, ϕ) pullback coordinates. If optical flow is well constrained, the user may toggle the option for stabilization method so that $\phi_0(u)$ is defined by maximizing the cross correlation between the intensity data lying within each circumferential hoop and the intensity data in the previous pullback lying near the same u coordinate. This option uses phase correlation of the pullback image itself and compares each strip in pullback space (corresponding to a hoop in 3D data space) to the previous image. If optical flow is an unreliable measure in this step, we have found that shifting these slices along ϕ (which is a periodic dimension) to minimize the difference in 3D space defines $\phi_0(u)$ gives satisfactory results, and further processing in the next stages of the pipeline remove any residual material motion in the (s, ϕ) plane.

A.3.3 Constrained parameterization defines a system-spanning centerline of the surface

Centerline construction leverages the surface parameterization in 3D space already created from the previous step. Hoops for which $s =$ constant define an effective circumference for increments along the length of the organ, and the average 3D position of each hoop defines its centerline point. Connecting mean points of adjacent hoops along the length of the organ defines the centerline of the object. This construction offers several

advantages to previous methods of centerline construction.

A.3.4 Constrained parameterization defines an effective radius along the surface

We define an effective radius as the average distance from each point in a uniform sampling of a ring of constant s (computed via the mapping to the pullback plane) to the centerline, which is composed of the mean positions of all circumferential rings. We then identified constriction locations as rings of constant s whose effective radii $r(s)$ are local minima (so that $\partial_s r(s) = 0$). Local minima in effective radius are tracked starting at the onset of folding forward in time to define constriction locations. Before the onset of folding, presumptive constriction locations are inferred by back-tracing the onset location to earlier timepoints.

We note that this measurement of effective radius could be done on the (u, v) coordinate parameterization and would give identical results, since curves of constant u are also curves of constant s. The effective radii $r(s)$ are therefore equal to those indexed by u: $r(s(u)) = r(u)$.

A.3.5 Refined Lagrangian parameterization of the surface, $\varphi = J \circ \Phi \circ Z \circ f$

After the previous constrained parameterization into the plane via $\Phi \circ Z \circ f$, which minimizes much of the tissue motion in the parameterization plane, we accomplish further refinement via computing pathlines in the domain of parameterization using particle image velocimetry (PIV). Advecting mesh vertices along these pathlines, then inverting the dynamic map to the plane gives the 3D positions of material points as they deform. This provides the surface shown in Fig. 2.1D, for instance.

A.3.6 Surface velocities and discrete exterior calculus

3D velocity vectors arise naturally from our approach via mapping the endpoints of 2D PIV vectors into their respective 3D surfaces. Geometrically, displacement vectors $\mathbf{v}$ extend from one coordinate $\mathbf{x}_0$ in 3D on the surface at time t_0 to a different coordinate $\mathbf{x}_1$ on the deformed surface at time t_1. When t_0 and t_1 are adjacent timepoints, this defines the 3D tissue velocity at t_0 as $\mathbf{v} = (\mathbf{x}_1 - \mathbf{x}_0)/(t_1 - t_0)$. We then decompose the velocity into a component tangential to the surface $\mathbf{v}_{\|}$ and a normal component v_n.

The tangential velocity fields $\mathbf{v}_{\|}$ can then be further analyzed using our implementation of the discrete exterior calculus (DEC). DEC discretizes the methods of exterior calculus in the continuous setting for application on simplicial complexes such as mesh triangulations. DEC is built using a straightforward set of discrete differential forms, defined on mesh vertices, edges, and faces. On a 2D surface, the only such forms are 0-forms (scalars), 1-forms (analogues of vector fields), and 2-forms (oriented areas). The DEC also defines representations of the exterior derivative d and the Hodge star $\star$ in terms of simple linear operations. These elemental operations are maps between the different spaces of k-forms on the mesh ($k \in \{0, 1, 2\}$). This technology can be exploited for a wide variety of applications in discrete geometry processing. In particular, it allows us to easily compute gradients of the velocity field (or other vector/tensor fields) on curved surfaces.

For a given mesh, instantiating `DECLab`'s `DiscreteExteriorCalculus` class generates the elemental operators, d and $\star$, for each possible pairing of k-form types, i.e. for a one form ω the operation $d\omega = \alpha$ generates a 2-form α. When strung together, these operators generate familiar mathematical operations such as the divergence, curl, and Laplacian – except now these operators take care to incorporate the curvature and geometry of the triangulated surface. For completeness, we enumerate some familiar

differential operations in the language of exterior calculus. Let φ denote a scalar field (0-form), let $\vec{v}$ denote a vector field, and let $\flat/\sharp$ denote the musical isomorphisms that transform vector fields into 1-form fields and 1-form fields into vector fields, respectively.

$$\nabla\varphi \to (d\varphi)^\sharp \tag{A.12a}$$

$$\nabla^2\varphi \to \star d \star d\varphi \tag{A.12b}$$

$$\nabla \cdot \vec{v} \to \star d \star (\vec{v}^\flat) \tag{A.12c}$$

$$\nabla \times \vec{v} \to (\star d(\vec{v}^\flat))^\sharp \tag{A.12d}$$

$$\nabla^2\vec{v} = ((\star d \star d + d \star d\star)\, \vec{v}^\flat)^\sharp \tag{A.12e}$$

Fig. A.2 shows the properties and methods of this class, and the online GitHub documentation provides example usage and benchmarks for accuracy.

A.3.7 Helmholtz-Hodge decomposition of vector fields on dynamic surfaces

Our `DECLab` implementation includes a simple interface to generate a Helmholtz-Hodge decomposition of tangential vector fields [55], i.e. a decomposition into dilatational (curl-free), rotational (divergence-free), and harmonic parts. Let v denote the 1-form field associated with the tangential surface velocity. In general, any surface velocity field can be decomposed in the following way

$$v = d\varphi + \delta\alpha + h, \tag{A.13}$$

where d is the exterior derivative, $\star$ is the Hodge star, and $\delta = \star d \star$ is the co-differential acting on 2-forms. The dilatational part of the velocity field, $d\varphi$, is given by the exterior derivative of the scalar potential φ. The rotational part of the velocity field, $\delta\alpha$, is given by co-differential of the vector potential α (confusingly α is actually a 2-form despite the common naming convention). Finally, h is a harmonic 1-form (i.e. $(d\delta + \delta d)h = 0$) encompassing the remaining aspects of v that are neither dilatational nor rotational. Each term and potential function is given by the method `helmholtzHodgeDecomposition()`.

A.4 Example of inferring intercalation rates ('tissue tectonics') using TubULAR

Our approach aids in measurement of the contributions to tissue-scale convergent extension by cell shape change and oriented cell intercalation for dynamic curved surfaces. As illustrated in Fig. A.5, in the absence of oriented cell divisions, cell shape change and oriented cell intercalations (or 'T1 transitions') both contribute to tissue-scale shear, in which different axes of the tissue converge and extend. An example of tracked cells demonstrating these two contributions is shown in Fig. A.5. Note that each cell changes neighbors (through cell intercalations) and also changes its shape in a way to extend along the longitudinal (horizontal) axis and converge along the circumferential (vertical) axis.

As in [165], by imprinting the cell segmentation at time $t_0 = 0$ hr onto the surface and advecting the polygonal segmentation along material pathlines in 3D, we find a cell-by-cell measure of the tissue shear. This measures tissue shear by virtue of using a meso-scale measure of tissue flow from PIV in the pullback plane – providing a local measure of tissue-scale shear at each tissue patch on the surface. We can then directly

compare the tissue-scale shear to the cell's actual shape change of cells segmented over time without explicitly tracking cells. The difference between the tissue-scale shear and the cell shape change is attributed to net oriented cell intercalations. Note that this method measures *net* intercalations, where one T1 event forming a new cell-cell junction aligned with the longitudinal direction can be canceled by a T1 event forming a new cell-cell junction aligned with the circumferential direction. Indeed, in the midgut many more cell intercalations occur than are measured by the net difference [165].

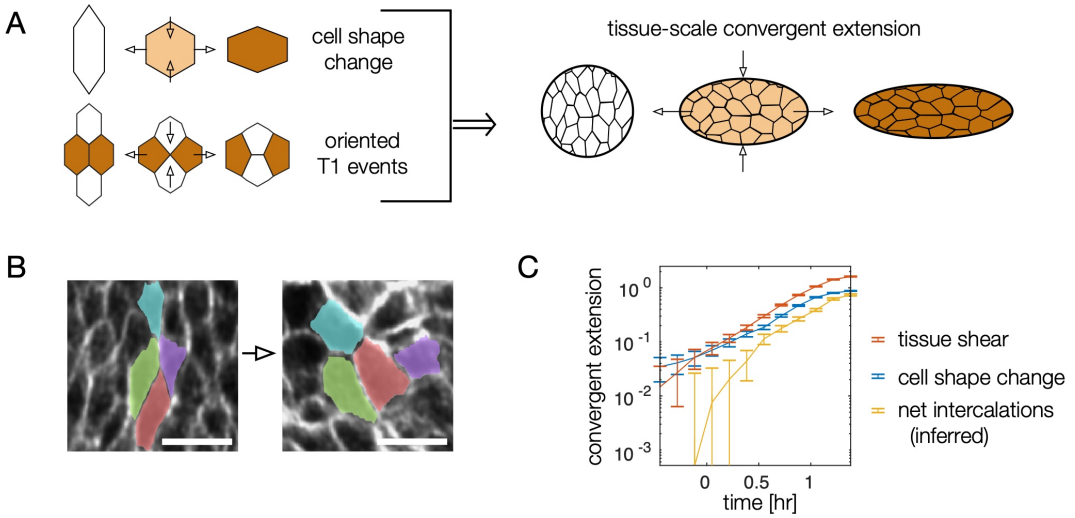

Figure A.5: **TubULAR aids in measurement of cell intercalations' contribution to tissue-scale convergent extension.** *(A)* In the absence of cell divisions, in-plane tissue-scale convergent extension occurs due to the changing shape of cells as well as the occurrence of oriented cell intercalations ('T1 events'). *(B)* During constrictions in the fly midgut, no cell divisions take place, but cells change shape and also intercalate in the endodermal layer. Scale bars are 10 μm. *(C)* We can then compare the cumulative effect of each contribution (blue and yellow) to the total tissue-scale convergent extension (orange, constricting along ϕ and extending along s). In the midgut endoderm, we directly measure tissue shear from the deviatoric component of the integrated strain computed from Lagrangian pathlines in 3D. This shear strain is almost entirely oriented along the longitudinal axis s. In order to compare directly this quantity to the cell shape change, we imprint the shapes of cells at $t = 0$ on the tissue surface, follow the outlines of these cells along tissue pathlines from coarse-grained particle image velocimetry measurements, and compute the cell shape anisotropy $\alpha \equiv (1 - a/b)\cos 2\theta$, where a and b are the semimajor and semiminor axes of the ellipse capturing each cell's moment of inertia tensor and θ is the cell's angle with respect to the material frame's longitudinal axis.

A.5 Analysis of beating zebrafish heart dynamics

In the absence of cell proliferation, the relationship between local tissue area rate of change, in-plane divergence, and out-of-plane motion is [6]:

$$\nabla \cdot \mathbf{v}_{\parallel} - 2Hv_n = \frac{1}{2}\mathrm{Tr}\left[\mathbf{g}^{-1}\dot{\mathbf{g}}\right], \tag{A.14}$$

where $\nabla \cdot \mathbf{v}_{\parallel}$ is the in-plane covariant divergence of the in-plane tissue velocities $\mathbf{v}_{\parallel}$, H is the mean curvature of the surface, v_n is the normal (out-of-plane) velocity, and $\mathrm{Tr}\left[\mathbf{g}^{-1}\dot{\mathbf{g}}\right]/2$ is the rate of local area change. We find the two terms on the left hand side are not equal, and in fact are anti-correlated. We measure their cross correlation between their circumferentially-averaged values, each of which is a function of the longitudinal coordinate, s, and of time, t: $\langle \nabla \cdot \mathbf{v}_{\parallel} \rangle_{\phi}(s,t)$ and $\langle 2Hv_n \rangle_{\phi}(s,t')$. Fixing the spatial coordinate but varying the time delay between measured values $\Delta = t - t'$ returns a sinusoidal correlation function parameterized by the time delay Δ. This curve fits well to

$$C(\Delta) \approx A\cos\left(2\pi(\Delta - \tilde{\Delta})/T\right). \tag{A.15}$$

The time shift corresponding to the maximum correlation – such that the in-plane and out-of-plane deformations would be in phase – is $\tilde{\Delta}$, which we report in the main text. This analysis gives insight into the kinematic properties of the tissue: tissue compressibility dominates the kinetics, prompting further modeling of the heart's mechanical cycle.

A.6 A cytoskeletal gel actively deforms liquid droplets

Figure 1L shows a snapshot of a DNA droplet in an active microtubule gel. Briefly, DNA droplets are assembled from multi-armed DNA nanostructures with self-interacting

complementary overhangs [23]. Active flows are generated by microtubule filaments depleted through non-adsorbing polymers such as polyethylene glycol (PEG) and powered by clusters of kinesin motors. Kinesin motors convert chemical energy from the environment and generate inter-filament sliding [213]. The DNA droplets are covalently bound to kinesin motors resulting in mechanical coupling between the microtubule bundles and the surface of the droplets. Active stresses are exerted through the microtubule flows, generating droplet deformation and eventually eventually leading to pinch-off of the elongating neck and preventing coarsening of the DNA droplets. Further details of the experimental design and imaging are given in [240].

Appendix B

Materials and methods for analysis of germband extension in *Parhyale*

B.1 Light sheet microscopy

For live imaging of transgenic parhyale embryos, we utilized a custom built MuVi SPIM [127]. This microscope has two excitation and two detection branches. Both used water dipping objectives (App LWD 5x, NA 1.1, Nikon Instruments Inc. for detection, and CFI Plan Fluor 10x, NA 0.3 for excitation). Furthermore, each detection branch consisted of a filter wheel (HS-1032, Finger Lakes Instrumentation LLC), with emission filters (BLP02-561R25, Semrock Inc.), tube lens (200 mm, Nikon Instruments Inc.) and a camera (sCMOS - Hamamtsu Flash 4.0 V2), with effective pixel size of 0.262 mm. The illumination branches featured a tube lens (200 mm, Nikon Instruments Inc.), scan lens (S4LFT0061/065, Sill optics GmbH and Co. KG), galvanometric mirror (6215 hr, Cambridge Technology Inc.), and discrete laser line (561LS OBIS 561nm). Optical section employed a translation stage from Physik Instrumente GmbH and Co. KG (P-629.1CD with E-753 controller), a rotation stage (U-628.03 with C-867 controller), and a linear

actuator (M-231.17 with C-863 controller).

B.2 Data post processing and microscope automation

To operate the microscope, we used Micro Manager [70], installed on a Super Micro 7047GR-TF Server, with 12 Core Intel Xeon 2.5 GHz, 64 GB PC3 RAM, and hardware Raid 0 with 7 2.0 TB SATA hard drives. For each sample we recorded 4 views, separated by 90 rotated views, with optical sectioning of 2 μm, and temporal resolution of 5 min. We embedded the embryos in agarose containing beads as a diagnostic specimen. This was used to register individual views into a common frame by utilizing the Fiji multi view deconvolution plugin [195], resulting in a final image with isotropic resolution of .2619 μm.

B.3 Extraction of dynamical surfaces of interest

The output of the lightsheet microscope is a time series of 3D grids whose voxel values correspond to intensity of the nuclear label or lipid dye. Extraction of the dynamical surface of interest from these data sets was performed in two stages: (1) 3D surface extraction and (2) 2D pullback map construction. In the surface extraction stage, the volumetric data of a representative time point was classified over the nuclear label/dye using the machine learning software Ilastik [18]. The resultant probability map was then fed into MATLAB and a static surface of interest was extracted using the morphological active contours method [168] (Fig. B.1), a type of level-set based segmentation algorithm well suited to segmented complicated, closed surfaces. The output of this segmentation is a 3D binary level-set, with identical dimensions to the data, where '1' values

corresponded to the interior of the closed surface (all embryonic tissue and yolk) and '0' values corresponded to regions external to the *Parhyale* egg. The boundary of this binary level-set is point cloud, a subset of which included voxels corresponding to the embryonic tissue. This point cloud was subsequently triangulated using Poisson surface reconstruction [121]. The result was a topologically spherical mesh triangulation.

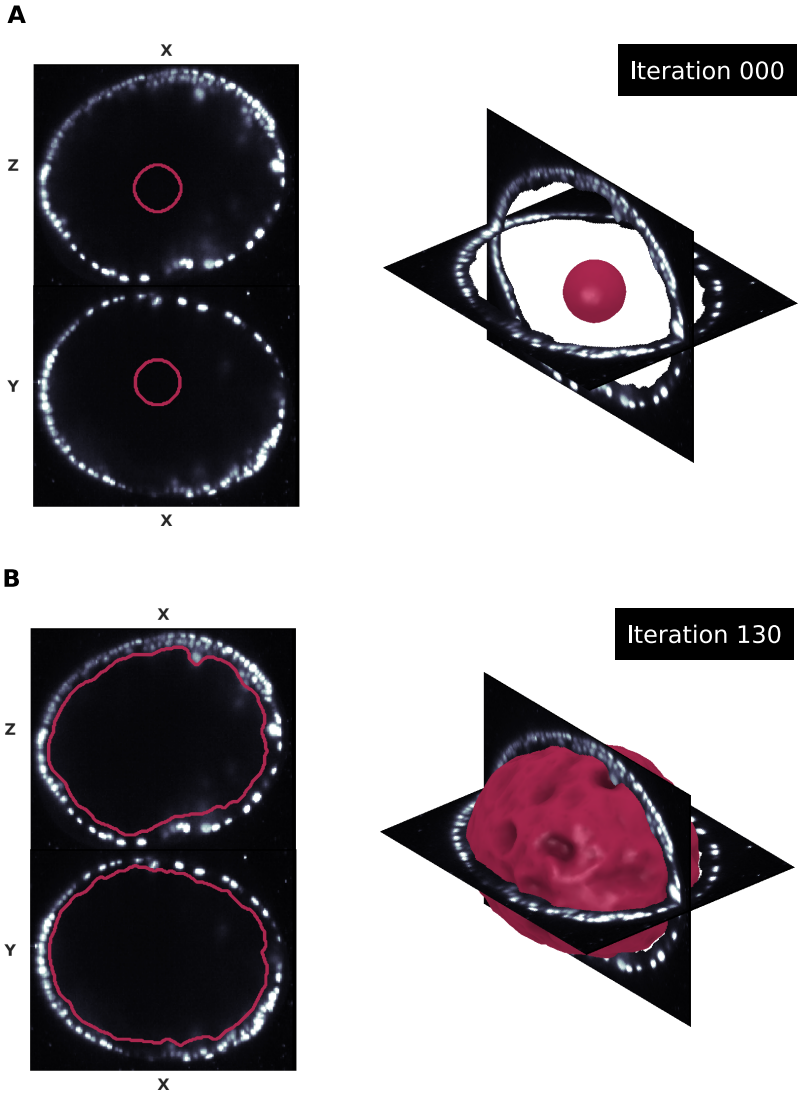

Figure B.1: **Surface extraction via level sets.** An illustration of the morphological snakes method used to extract the surface of interest in the growing embryo. (A) The spherical initial condition (zero completed iterations). (B) The segmented surface.

In the next processing step, this static surface was used as a seed to extract the dy-

namically changing surface at each time point. Recall that at this developmental stage the embryonic tissue is a topological disk sitting on top of a spherical yolk. The embryonic tissue was therefore contained in a disk-like subregion of the sphere-like surface triangulation. In order to extract this region of interest, the entire sphere-like mesh was mapped into the plane using the orbifold Tutte embedding method [2]. This method generates a topologically consistent parameterization of the sphere in the plane allowing us to view the entire surface at once with minimal geometric distortion. Next, a static submesh of the region of interest on the static surface was selected by hand using the orbifold pullbacks. Although static, this region of interest was large enough that it contained all relevant sections of the embryo as it grew and deformed over time. A set of 'onion layers' was then created by displacing the submesh along its positive and negative normal directions. A stack of pullback images was then created for each time point with one image in the stacks for each displaced onion layer. The number of layers and the inter-layer spacing was chosen so that all of the geometric features of the dynamic surfaces were captured for the various time points somewhere within the image stack. These stacks were then fed back into Ilastik and batch processed again over the nuclear label/dye. The result was a time dependent field of normal displacements over the static seed surface that transformed the static surface into the corresponding dynamic surface for each time point. These dynamic triangulations of the evolving region of interest were then separately mapped into the unit disk conformally via Ricci flow [276]. Such a conformal mapping is only unique up to a Möbius automorphism of the unit disk. In other words, unless care is taken to register the pullbacks, the resultant images may be wildly misaligned in pullback space from time point to time point. With this in mind, the time series of conformal pullbacks was iteratively registered to fix the conformal degrees of freedom within the pullbacks. Essentially, corresponding mesh vertices at subsequent times were approximately matched in 2D by finding an optimal Möbius automorphism

of the unit disk that registered as many points as possible without sacrificing the conformality of the parameterization [137]. The final result was a sequence of maximally aligned conformal pullbacks of the growing embryo to the plane. The conformality of these discrete parameterizations is illustrated in Fig. B.2.

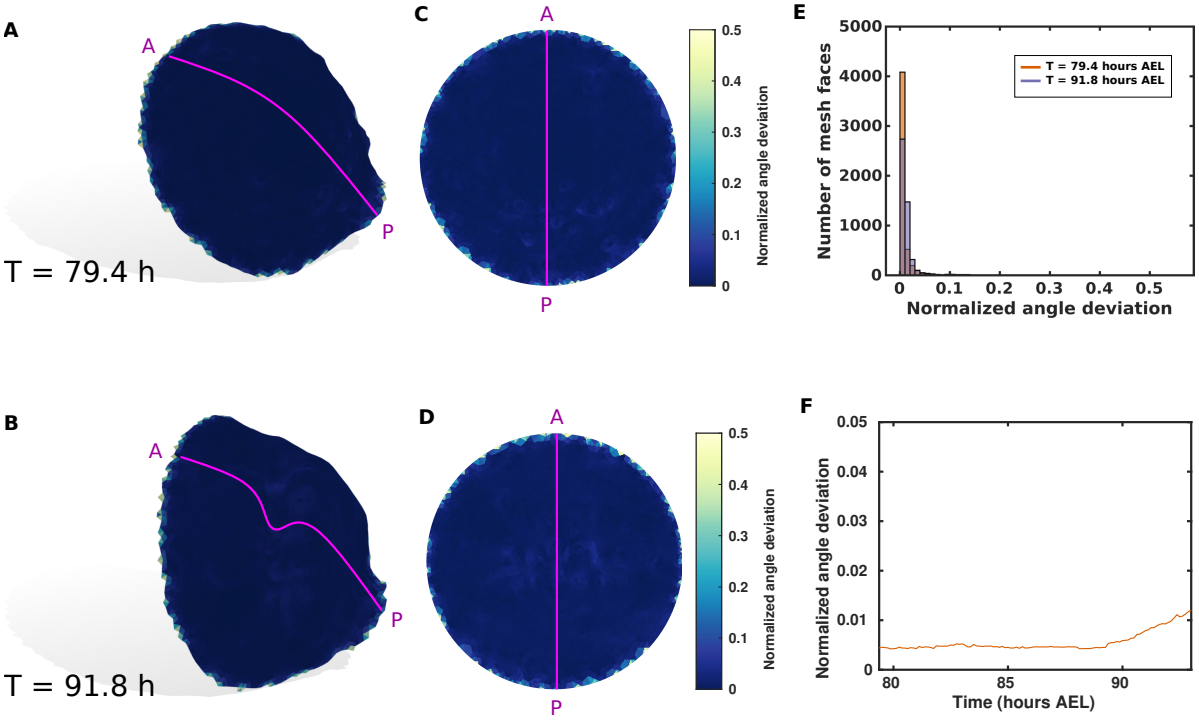

Figure B.2: **Discrete conformal parameterization of 3D surfaces.** The results of our discrete Ricci flow method in producing conformal parameterizations of the midsurface of the growing ectoderm. (A to D) Normalized angle deviation, $(|\theta_1^{3D} - \theta_1^{2D}| + |\theta_2^{3D} - \theta_2^{2D}| + |\theta_3^{3D} - \theta_3^{2D}|)/\pi$, defined on each mesh face reporting the conformality of the mapping. The quantities $\theta_i^{2D}, \theta_i^{3D}$ are the ith internal angle of each face in 2D and 3D, respectively. Mapping remains almost perfectly conformal in the bulk of the mesh, even at late times when the curvature of the tail fold is pronounced. (A) Normalized angle deviation on the 3D surface at T = 79.4 hours AEL. (B) Normalized angle deviation on the 3D surface at 91.9 hours AEL. (C) Normalized angle deviation displayed in the 2D pullback space at T = 79.4 hours AEL. (D) Normalized angle deviation displayed in the 2D pullback space at 91.8 hours AEL. (E) Histograms of the normalized angle deviation at the two representative time points. (F) Median normalized angle deviation over the full time course of the data set.

It is worthwhile here to briefly discuss the constraints of visualizing curved surfaces

in the plane via their parameterizations. Gauss' celebrated Theorema Egregium forbids the construction of a globally isometric planar parameterization for a 2D surface with non-zero Gaussian curvature [78]. In other words, if you want to map curved surface into the plan, you can do so in a way that preserves angles (a conformal map) or you can do so in a way that preserves areas (an authalic or isoareal map) or you can do so in a way that balances both non-zero angle distortion and non-zero area distortion, but you can never do so in a way that perfectly preserves angles and areas everywhere. The central focus of this work is the orientational order of cells within a curved tissue. As such, we generally choose to visualize surfaces using conformal maps which preserve the angles between neighboring cells from which the orientational order can be constructed. This means that some area distortion within the figures is inevitable. For instance, in Fig. 3.3C it appears that lateral cells are larger than cells near the ventral midline. However, calculating cell areas using tissue cartography reveals that cell size is essentially uniform in the tissue at a given time point (Fig. 3.6, E and F). Cell size varies instead primarily as a function of location in the cell cycle (recently divided cells are smaller - see Fig. B.10B).

B.4 In-plane cell segmentation and pathline reconstruction

One primary benefit of tissue cartography is that processing data in low dimensions greatly reduces the computational complexity of various analysis procedures. We exploited this benefit by segmenting nuclei directly in the 2D pullback images. Images were first classified in Ilastik. The resultant probability maps were then fed in MATLAB where the nuclei were segmented using a custom built version of the watershed algorithm

[161]. Custom additions to MATLAB's built-in `watershed` functionality were necessary to account for spatially proximal nuclei which were initially undersegmented, i.e. many nuclei were counted only as a single object. Special care was taken during this step in adjusting watershed parameters to ensure that adjacent nuclei were properly distinguished from each other. Connectivity among segmented cells could be inferred using a Voronoi tessellation (Fig. B.3).

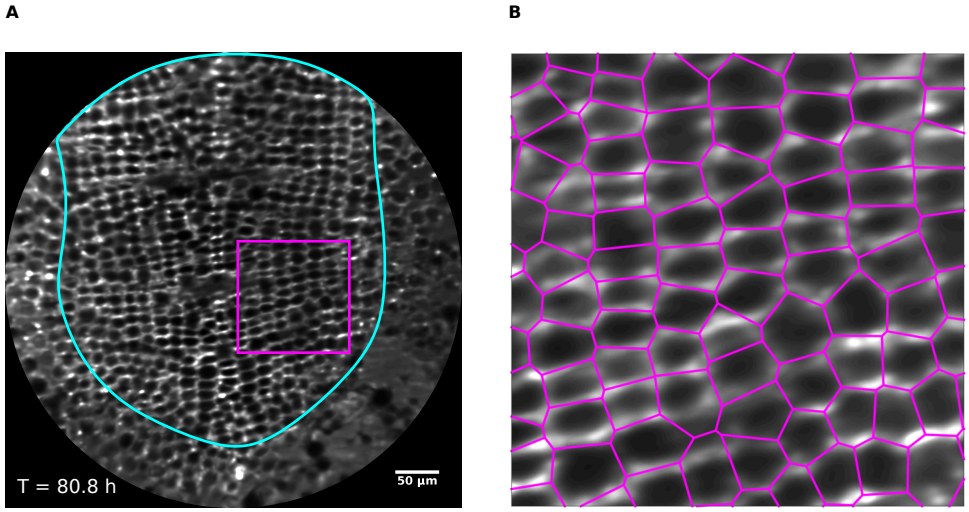

Figure B.3: **Visualizing cell membranes in the growing embryo.** (*A*) The trunk segmental ectoderm pulled to the plane and visualized with a lipid dye. Outer cyan marking delineates embryo from extra embryonic tissue. Inner magenta marking delineates the boundary of the region visualized in Fig. B.3B. (*B*) A close up visualization of a region of the trunk segmental ectoderm and a comparison to the Voronoi tessellation produced using the cell centers extracted from our cell segmentation pipelines.

Once segmented, nuclei were tracked semi-automatically using an enhanced point-matching procedure. For a given time point, the input to this procedure included a pullback image and segmentation at time t and another subsequent pullback image and segmentation at time $t+1$. First, the subsequent pullback image was registered onto the previous image using the Demon's deformable image registration algorithm [255]. The resultant displacement fields were then applied to the nuclei locations at time $t+1$. Point matching was then used to associate the nuclei locations at time t with the displaced

nuclei at $t + 1$. Displacing the nuclei locations at $t + 1$ to align more closely with the locations at t reduced discrepancies in the point matching associated with large nuclear motions. This process was applied iteratively until pathlines were generated for all cell lineages at all time points. Despite the enhancements, some manual correction was still necessary. Manual corrections were applied using a custom built MATLAB GUI. The pathlines were outputted as a digraph where nodes represented particular cells at particular time points and edges stored the information about the temporal relationships between nodes. Cell divisions could then be extracted from this tracking structure by locating events where single tracks split into two lineages.

Another benefit of tissue cartography is that the geometric information reflecting the fact that in-plane dynamics are occurring on a 2D surface embedded in 3D space are properly preserved. In particular, knowing the 2D locations of nuclei in pullback space provides an explicit correspondence to their locations on the surface in 3D. Therefore, once the tracks were constructed in 2D, it was trivial to extract full 3D nuclear pathlines. Velocities were constructed as simple backward differences between 3D nuclei locations. A backward difference was used since forward differences can generate ambiguities at cell division events where the forward difference velocities of the children sum to zero. 3D velocities were decomposed into tangential and normal components relative to the dynamic surface. Tangential velocities were then consistently transformed back into pullback space for display purposes using a discretization of the Jacobian on mesh triangulation faces.

B.5 Region of interest selection for dynamical quantities

For any quantity depending on measured cell tracking, with specific emphasis on the theoretical predictions of tissue velocities induced by cell divisions displayed in Fig. 3.9, the region of interest was always defined to be the maximal set of PSPRs that we could accurately track and follow through at least one round of mitotic wave divisions. All other segments were either already significantly progressed into their second mitotic wave or had not completed their first mitotic wave by the end of our recordings. As time progresses, the region of interest expands to include all clonal progeny of these chosen segments. The lateral extent of each PSPR was also carefully considered. It is understood that many cells at the dorsal boundary of the ventral ectoderm are in fact extra-embryonic and do not remain in the tissue as morphogenesis proceeds [262, 263]. On these grounds, any cell near the dorsal boundary of the tissue that appeared to detach from the ectoderm or that could not be confidently associated with a particular PSPR was excluded from any subsequent analysis.

B.6 Calculation of discrete curvatures

The discrete curvature was calculated for each dynamic mesh triangulation as a function of time using standard discrete constructions Fig. B.4 [27]. The Gaussian curvature $K(v_i)$ of a mesh vertex v_i was taken to be

$$K(v_i) = \frac{1}{A_i}\left(2\,\pi - \sum_{F_j \in \mathcal{N}_F(v_i)} \theta_{F_j}\right), \tag{B.1}$$

where A_i is the area associated to each vertex via barycentric subdivision of the triangles attached to that vertex, $\mathcal{N}_F(v_i)$ is the set of incident faces F_j attached to v_i, and θ_{F_j} is the internal angle of face F_j corresponding to v_i. The mean curvature $H(v_i)$ of a vertex v_i was calculated according to

$$\Delta\vec{\mathbf{x}}_i = 2\,H(v_i)\,\hat{\mathbf{n}}_i, \tag{B.2}$$

where $\vec{\mathbf{x}}_i$ is the 3D location of vertex v_i, $\hat{\mathbf{n}}_i$ is the unit normal vector corresponding to vertex v_i, and Δ denotes the Laplace-Beltrami operator. The discrete Laplace-Beltrami operator was implemented using the familiar cotangent discretization [27]

$$\Delta\vec{\mathbf{x}}_i = \frac{1}{2A_i}\sum_{v_j\in\mathcal{N}_v(v_i)}(\cot\alpha_{ij}+\cot\beta_{ij})\;(\vec{\mathbf{x}}_j-\vec{\mathbf{x}}_\mathbf{i}), \tag{B.3}$$

where $\mathcal{N}_v(v_i)$ is the neighborhood of vertices attached to vertex v_i and α_{ij} and β_{ij} are the two internal angles of the triangles opposite the edge shared by vertex v_i and v_j. In order to extract $H(v_i)$ from Eq. (B.2), it was first necessary to calculate $\hat{\mathbf{n}}_i$, which was taken to be the angle-weighted average of the face unit normal vectors of the triangles incident to vertex v_i assuming a counter-clockwise orientation of vertices in the faces. This choice breaks the degeneracy in the orientation of the unit normal and allowed for simple extraction of a signed mean curvature. The panels in Fig. B.4, were constructed by averaging together the Gaussian and mean curvatures, respectively, of all vertices found to lie within a particular Voronoi polygon corresponding to a specific cell after mapping the dynamic meshes conformally into the plane.

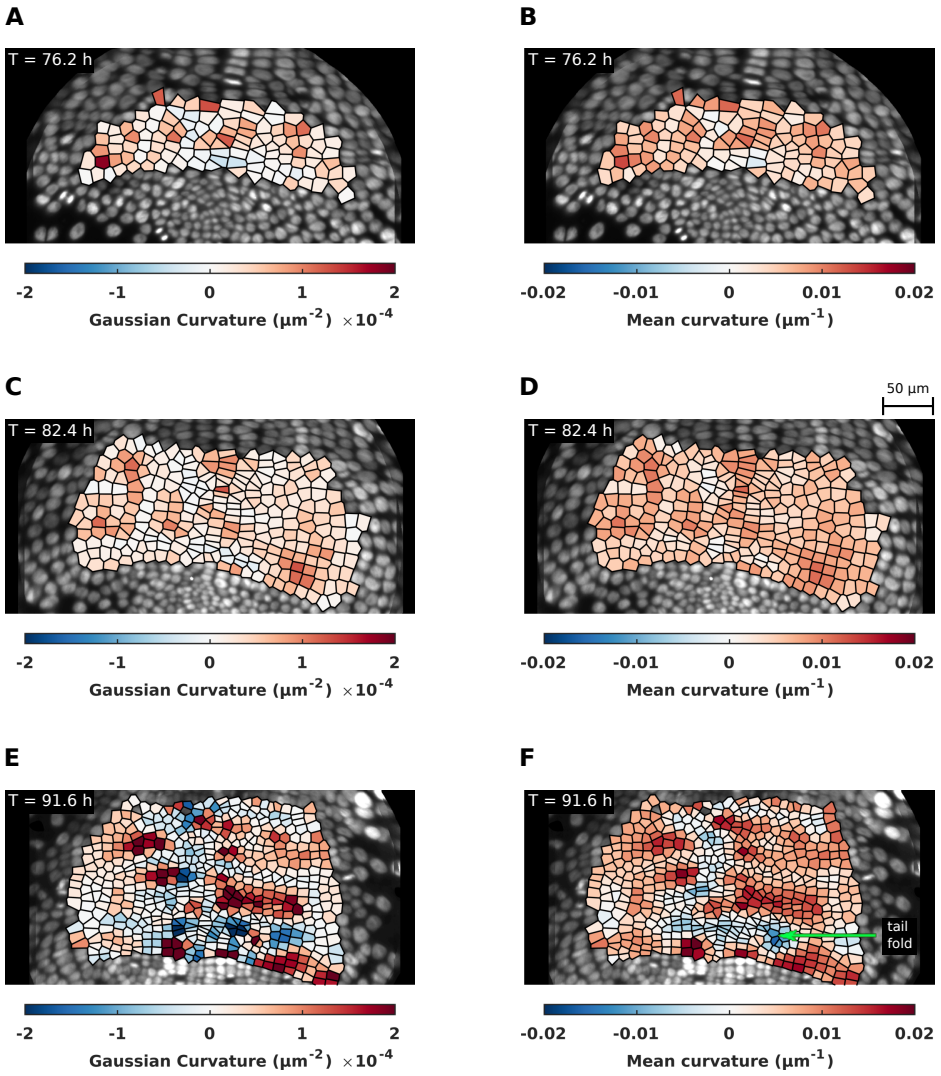

Figure B.4: **Surface curvatures in the growing *Parhyale* embryo.** (*A*) Per-cell Gaussian curvature at early times. (*B*) Per-cell mean curvature at early times. (*C*) Per-cell Gaussian curvature at intermediate times. (*D*) Per-cell mean curvature at intermediate times. (*E*) Per-cell Gaussian curvature at late times. (*F*) Per-cell mean curvature at late times.

B.7 Construction of correlation functions

In order to construct the two-point orientational order correlation functions, we first calculated the fourfold and sixfold orientational order parameters for each cell at a particular time point. Next, for each pair of cells, denoted here by their locations $\mathbf{x}_1$ and $\mathbf{x}_2$, we calculated the intercellular distance. This distance was taken to be the geodesic distance along the dynamic surface between the locations of the cell centroids on the 3D mesh triangulation [270]. We also calculated the product $\psi_n(\mathbf{x}_1)\,\psi_n^*(\mathbf{x}_2)$ for each pair of cells, where $n \in \{4, 6\}$. We then partitioned the intercellular distances into a set of bins. All pairs whose spacing lay between r and $r + dr$, where dr was the width of a bin, were then averaged together to calculate the two-point orientational order correlation function $< \psi_n(\mathbf{x}_1)\,\psi_n^*(\mathbf{x}_2) >$. It was assumed for this calculation that this quantity depended only on the scalar distance r between pairs of cells, i.e. $< \psi_n(\mathbf{x}_1)\,\psi_n^*(\mathbf{x}_2) >=< \psi_n(r_{12})\,\psi_n^*(0) >$. Note that under averaging, only the real part of the product $\psi_n(\mathbf{x}_1)\,\psi_n^*(\mathbf{x}_2)$ contributed, since $\psi_n(\mathbf{x}_1)\,\psi_n^*(\mathbf{x}_2) + \psi_n(\mathbf{x}_2)\,\psi_n^*(\mathbf{x}_1) = 2\mathrm{Re}[\psi_n(\mathbf{x}_1)\,\psi_n^*(\mathbf{x}_2)]$. Finally, the intercellular distances distances were normalized by an average cell length scale, calculated as the square root of the average area contained by each cells Voronoi polygon mapped back into 3D.

Following previous work [19, 188], information about translational order was extracted using variations of the pair correlation function $g(r)$ (also known as the radial distribution function). In addition to the radially symmetric pair correlation function $g(r)$, we also considered constructed anisotropic distributions that only aggregated information about oriented pairwise separations along the A-P and D-V axes ($g_{AP}(r)$ and $g_{DV}(r)$, respectively). The construction of all of these distributions proceeded similarly to the construction of the orientational order correlation function and also relied on the calculation of the pairwise geodesic distance between cells. All pairs of cells whose separation lay between r and $r + dr$, and whose relative orientation lay along the appropriate axes

in the case of $g_{AP}(r)$ and $g_{DV}(r)$, were consolidated into histograms within a set of bins (of width dr) segmenting the intercellular spacing. The histograms were then normalized using an 'effective volume method' that directly accounts for and ameliorates finite size effects [134]. In the following explanation we focus on the radially symmetric pair correlation function $g(r)$ for simplicity. Naively, the pair correlation function is normalized by the expected number of cell pairs predicted by a Poisson distribution, i.e.

$$g(r) = \sum_{i=1}^{N} \frac{n_i(r)}{N\,\rho\,dV}, \tag{B.4}$$

where $n_i(r)$ is a count of the number of cells having their centers a distance between $r - dr/2$ and $r + dr/2$ from the center of the ith cell in the measurement volume, N is the total number of cells in the measurement volume, $\rho = N/V$ is the raw number density of cells in the measurement volume, V is the total measurement volume, and dV is the volume of the generalized shell between $r - dr/2$ and $r + dr/2$ ($dV = 2\pi r dr$ for a 2D shell). Instead, we report the quantity

$$g(r) = \sum_{i=1}^{N} \frac{n_i(r)}{N\,\rho\,dV_i}, \tag{B.5}$$

where now, dV_i is defined as the intersection of the shell $dV(r)$ centered on cell i with the finite measurement volume V. This intersection volume therefore had to be calculated individually for each cell and for each distance bin. The final reported quantities were $g(r) - 1$ since this quantity decays to zero in a disordered system. An analysis of the finite size effects present in both the orientational and translational correlation functions can be found in Fig. B.5.

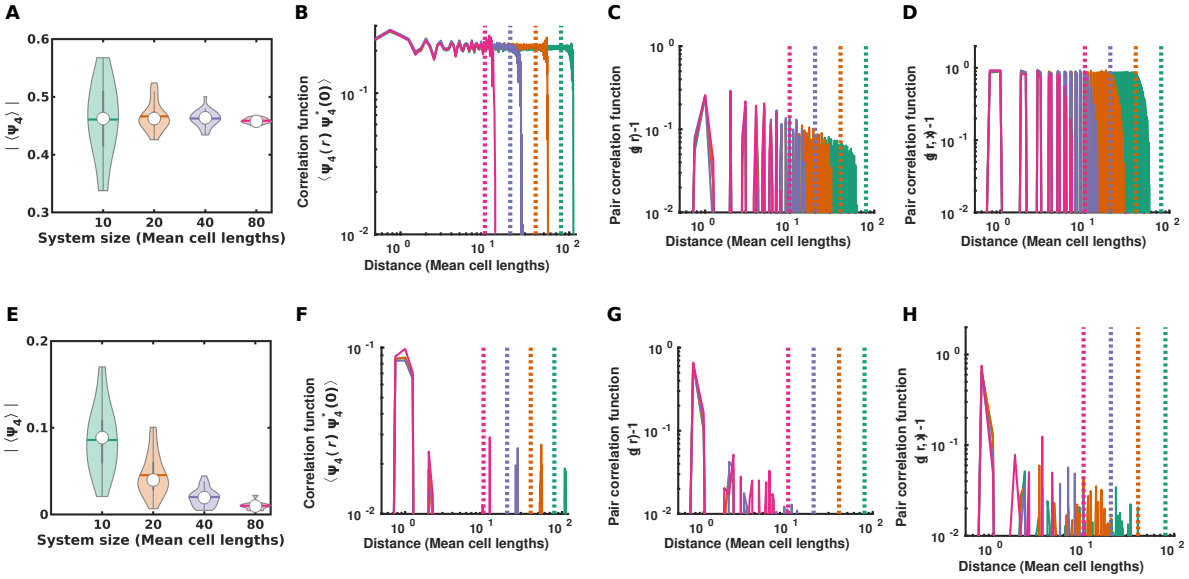

Figure B.5: **Finite size effects on orientational and translational order.** Finite size effects were investigated using synthetic data sets describing both fourfold ordered (A-D) and totally disordered systems (E-H). Systems were generated with square aspect ratios and system sizes $L = 10, 20, 40, 80$ cell lengths. $N = 25$ synthetic data sets for each system size. (A) Distributions of the mean global fourfold order parameter $|\langle\psi_4\rangle|$ for an orientationally ordered system. Distributions are much more closely packed around the mean for larger systems, but the mean of the distributions are constant for all system sizes. (B) Fourfold orientational correlation function for an ordered system. Vertical dotted lines indicate system size. Correlations approach and maintain a constant value over the entirety of the system. (C) Radially symmetric pair correlation function $g(r) - 1$. Pair correlation function decays algebraically over most of the system size. (D) Horizontal cut of the pair correlation function $g(r, x) - 1$. Correlations also decay algebraically, albeit extremely slowly. (E) Distributions of the mean global fourfold order parameter $|\langle\psi_4\rangle|$ for a disordered system. The mean value for each distribution is more variable across system size than in the ordered case, but all values are still consistent with a disordered system. Mean values appear to monotonically approach zero as system size in increased. (F) Fourfold orientational correlation functions decay exponentially for all system sizes. Some erroneous spikes are observed at distances larger than the system size. (G) Radially symmetric pair correlation function $g(r) - 1$ decays exponentially for all system sizes. (H) Horizontal cut of the pair correlation function $g(r, x) - 1$ decays exponentially for all system sizes.

B.8 Circular statistics for division events

In order to properly analyze the distributions of division events, it was necessary to construct measures of statistical properties that properly accounted for the nematic nature of division events, i.e. a division event with orientation θ is physically identical to a division event with orientation $\theta \pm \pi$. Extending familiar measures of circular distributions [275], the modified circular mean of the orientations of a set of division events, $\{\theta_n\}$ where $n = 1, \ldots N$, was defined to be

$$\overline{\theta} = \frac{1}{2} \arg \left[\sum_{n=1}^{N} e^{2i\theta_n} \right] \in [-\frac{\pi}{2}, \frac{\pi}{2}], \tag{B.6}$$

which is invariant under the transformation $\theta_n \rightarrow \theta_n \pm \pi$ for any θ_n. If the division orientations are tightly distributed around a single value, then this quantity will also be close to that particular value. We also define a modified measure of angular dispersion

$$s = \sqrt{2 \left(1 - \frac{1}{N} \sum_{n=1}^{N} e^{2i\theta_n} \right)}. \tag{B.7}$$

Note that this is a dimensionless quantity. Our measure of angular dispersion varies between $s = 0$ for perfectly oriented divisions ($\theta_n = \overline{\theta}$ for all n and $s = \sqrt{2}$ for totally isotropic divisions).

B.9 Determination of the average division velocity

Division events were extracted from the tracking structure and the resulting sample set was pruned for quality (sufficiently far from the boundary of the tissue, sufficiently far from another division event, etc). In order to compare different events, divisions were translated and rotated so that the center of mass of the daughter cells lay at the

origin and the division axis lay along the y-axis. The measured velocities of the daughter cells and of cells in the third-order natural neighborhood of the daughter cells were then interpolated onto a fine mesh triangulation using generalized Hessian-energy scheme that minimizes distortion in the interpolated field at the boundary of the triangulation [234]. The interpolated velocity fields were then averaged across division events to find the mean velocity induced by divisions (Fig. 3.7). Gradients of the resultant velocity fields were calculated on the mesh triangulation using `DECLab` (see Chapter 2) (Fig. 3.8 and Fig. B.6).

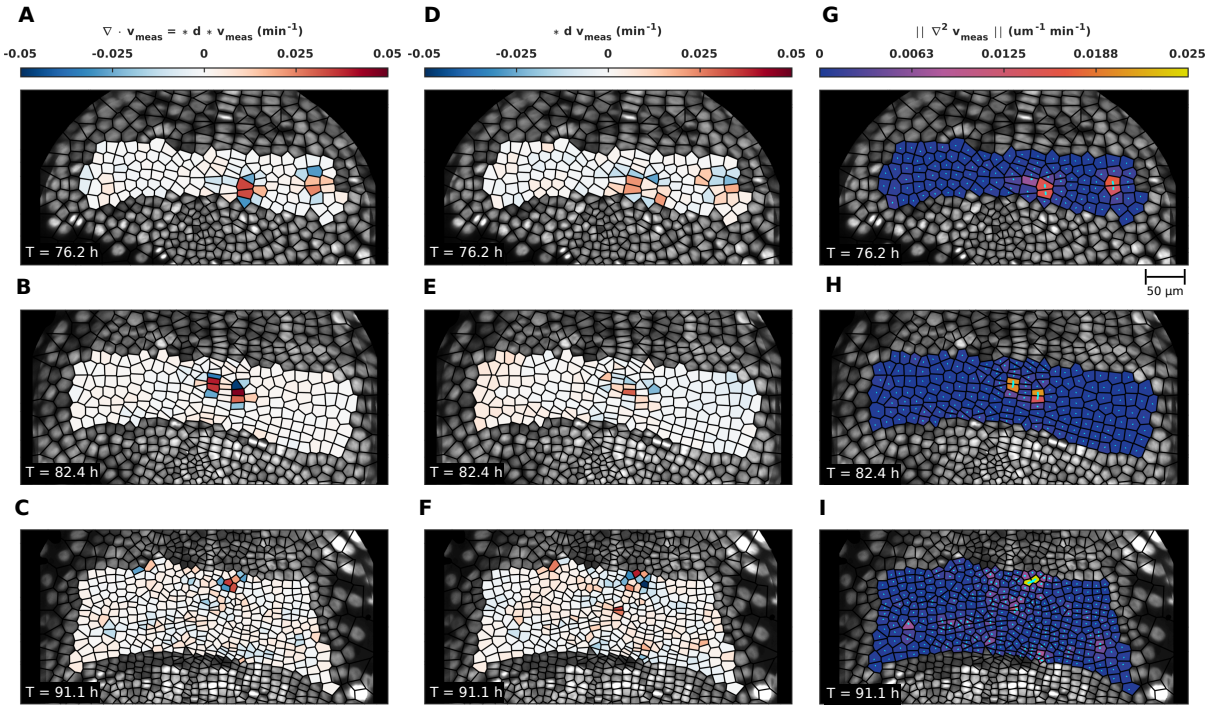

Figure B.6: **Gradients of the measured tissue velocity fields.** (A to C) The divergence of the measured tissue velocity fields for three representative time points. Explicit construction in term of exterior derivatives and Hodge stars is shown in (A). (D to F) The 'curl' of the measured tissue velocity fields for three representative time point. Explicit construction in terms of exterior derivatives and Hodge stars is shown in (D). (G to I) The Laplacian of the measured tissue velocity fields for three representative time points.

B.10 Generation of synthetic data sets and comparison with measured data

The synthetic data sets were generated to understand the extent to which the measured order was statistically significant and how the finite size of the germband effected the order. First, the length and width of the germband at each time was extracted. These were determined by tagging representative rows and columns of cells, following these rows and columns over time, and calculating the geodesic length along each row and columns. The average geodesic length of the rows (columns) was taken to be the width (length) of the germband at a particular time. We also extracted a mean cell density at each time point by averaging the inverse 3D areas of cells. One thousand synthetic data sets were generated for each time point within rectangles with the same length and width as the germband. Points representing cell centroids were generated to exhibit the same cell density as the germband using a fast Poisson-disk sampling method [31]. The connectivity of these randomly generated points was approximated using Voronoi tesselation. This connectivity allowed for the calculation of the order parameters and orientational correlation functions over the finite size samples. We also calculated the radial distribution functions along the A-P axis (length of the rectangle) and the D-V axis (width of the rectangle) for each synthetic data set Fig. B.7 using the same method of construction as for the measured data.

Additionally, we compared the corresponding measured and synthetic distributions of orientational order parameters according to the two-sample Kolmogorov-Smirnov (K-S) test [157] using MATLAB's `kstest2`. This implementation of the K-S test returns two measurements that assess the confidence with which one can assert that two sets of observed random variables are drawn from the same distribution. The first is the K-S statistic, which is simply the maximum difference between the empirical CDFs of the two

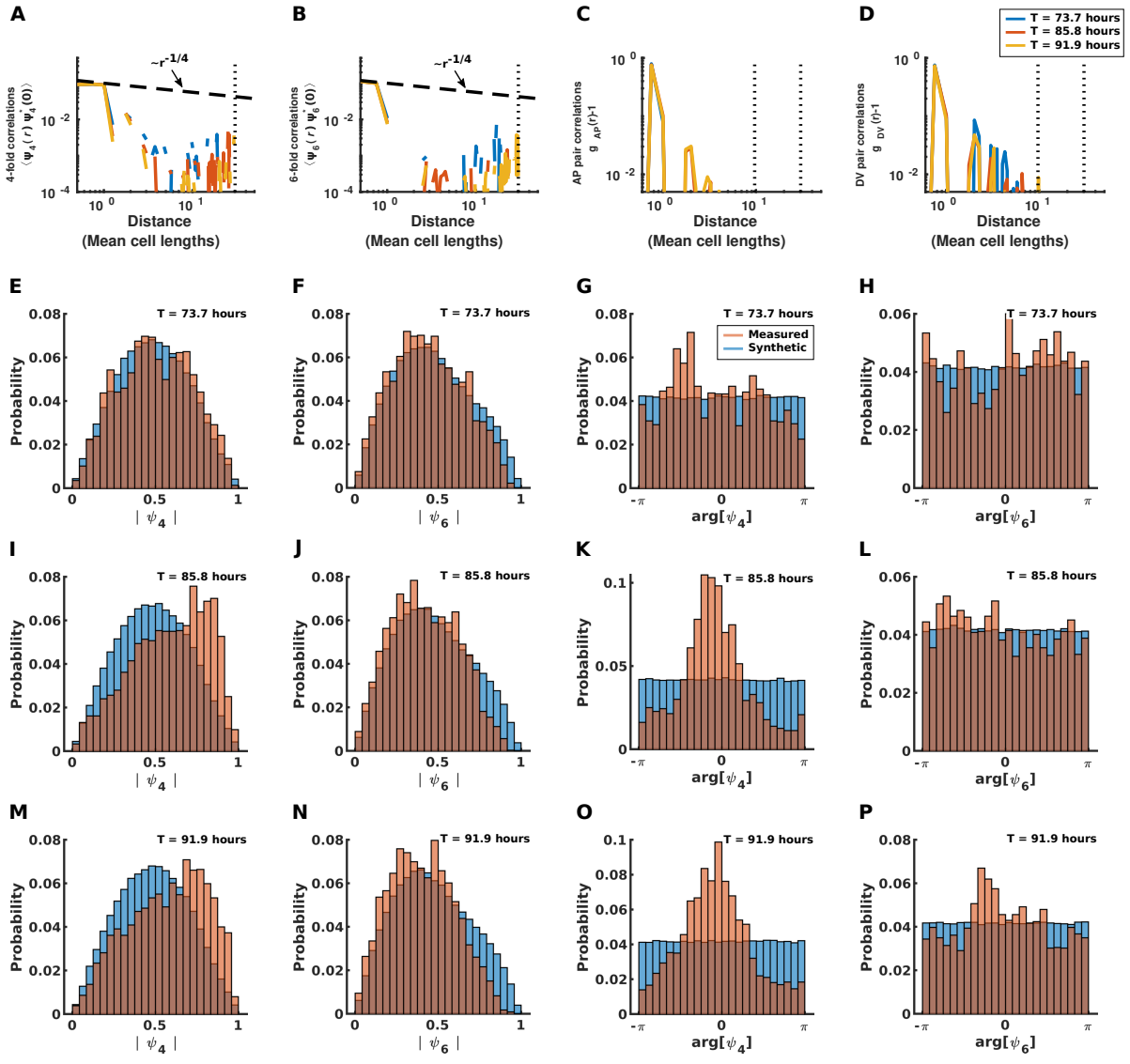
A
B
C
D
~r^-1/4
4-fold correlations
6-fold correlations
AP pair correlations
DV pair correlations
Distance
(Mean cell lengths)
T = 73.7 hours
T = 85.8 hours
T = 91.9 hours
E
F
G
H
I
J
K
L
M
N
O
P
Probability
Measured
Synthetic
arg[ψ4]
arg[ψ6]

Figure B.7: **Observed order in the embryo is significant compared to disordered synthetic data sets.** (*A* to *D*) Correlation functions for synthetic datas sets with the same system sizes and cell densities as the representative time points in Fig. 3.3. (*A*) The two-point fourfold orientational correlation function. (*B*) The two–point sixfold orientational correlation function. (*C*) The pairwise radial distribution function measured along the A-P axis of the synthetic data set. (*D*) The pairwise radial distribution function measured along the D-V axis of the synthetic data set. (*E* to *H*) Comparison of the fourfold and sixfold order parameters of the measured and synthetic data sets at early times. (*E*) The magnitude of the fourfold order parameter. (*F*) The magnitude of the sixfold order parameter. (*G*) The phase of the fourfold order parameter. (*H*) The phase of the sixfold order parameter. (*I* to *L*) Comparison of the fourfold and sixfold order parameters of the measured and synthetic data sets at intermediate times. (*I*) The magnitude of the fourfold order parameter. (*J*) The magnitude of the sixfold order parameter. (*K*) The phase of the fourfold order parameter. (*L*) The phase of the sixfold order parameter. (*M* to *P*) Comparison of the fourfold and sixfold order parameters of the measured and synthetic data sets at late times. (*M*) The magnitude of the fourfold order parameter. (*N*) The magnitude of the sixfold order parameter. (*O*) The phase of the fourfold order parameter. (*P*) The phase of the sixfold order parameter.

sample sets. The larger the K-S statistic, the greater the discrepancy between the two sample sets. The second measurement is the asymptotic p-value, which is the probability of observing a test statistic as extreme as, or more extreme than, the observed value under the null hypothesis that both samples are drawn from the same distribution. All K-S statistics and p-values are reported in Table B.1. At the confidence level $\alpha = 0.05$, the null hypothesis is rejected for all distributions, indicating it is unlikely that the observed order at any time point is due to chance. We note that the p-values for fourfold order at intermediate and late times are vastly smaller than the corresponding p-values at early times, while the p-values for sixfold order do not change as drastically. This implies that while it is still improbable that the observed fourfold order at early times is due to chance, it is hugely more likely when compared to intermediate and late times after the order generating choreography has unfolded.

Similar methods were used to generate the synthetic illustration of a translationally ordered system Fig. B.8. We patterned perfect square lattices on rectangles with the same

	p-Value	K-S Statistic
$T = 73.7\,\mathrm{h}:\ \lvert\psi_4\rvert$	9.23e-05	0.0475
$T = 73.7\,\mathrm{h}:\ \arg[\psi_4]$	5.64e-08	0.0627
$T = 73.7\,\mathrm{h}:\ \lvert\psi_6\rvert$	1.11e-06	0.0571
$T = 73.7\,\mathrm{h}:\ \arg[\psi_6]$	2.50e-06	0.0555
$T = 85.8\,\mathrm{h}:\ \lvert\psi_4\rvert$	1.05e-106	0.2016
$T = 85.8\,\mathrm{h}:\ \arg[\psi_4]$	7.55e-100	0.1949
$T = 85.8\,\mathrm{h}:\ \lvert\psi_6\rvert$	6.61e-20	0.0863
$T = 85.8\,\mathrm{h}:\ \arg[\psi_6]$	2.21e-06	0.0477
$T = 91.9\,\mathrm{h}:\ \lvert\psi_4\rvert$	2.62e-95	0.1804
$T = 91.9\,\mathrm{h}:\ \arg[\psi_4]$	4.86e-89	0.1744
$T = 91.9\,\mathrm{h}:\ \lvert\psi_6\rvert$	3.45e-41	0.1183
$T = 91.9\,\mathrm{h}:\ \arg[\psi_6]$	1.12e-07	0.0499

Table B.1: **Statistical comparison of orientational order in measured and synthetic data sets.** The Kolmogorov-Smirnov (K-S) statistic and asymptotic p-values for the distributions shown in Fig. B.7.

length and width as the germband for the same representative time points. The lattice spacing was set to match the measured cell density at the corresponding time point. We then generated one hundred synthetic data sets for each time point by adding Gaussian white noise to the lattice site positions with a signal-to-noise ratio of 5. Calculation of the orientational order parameters, the orientational correlation functions, and the radial distribution functions were performed in the same manner as the other synthetic data sets.

B.11 Timing and orientation of cell divisions is not predicted by local mechanical or geometric signals

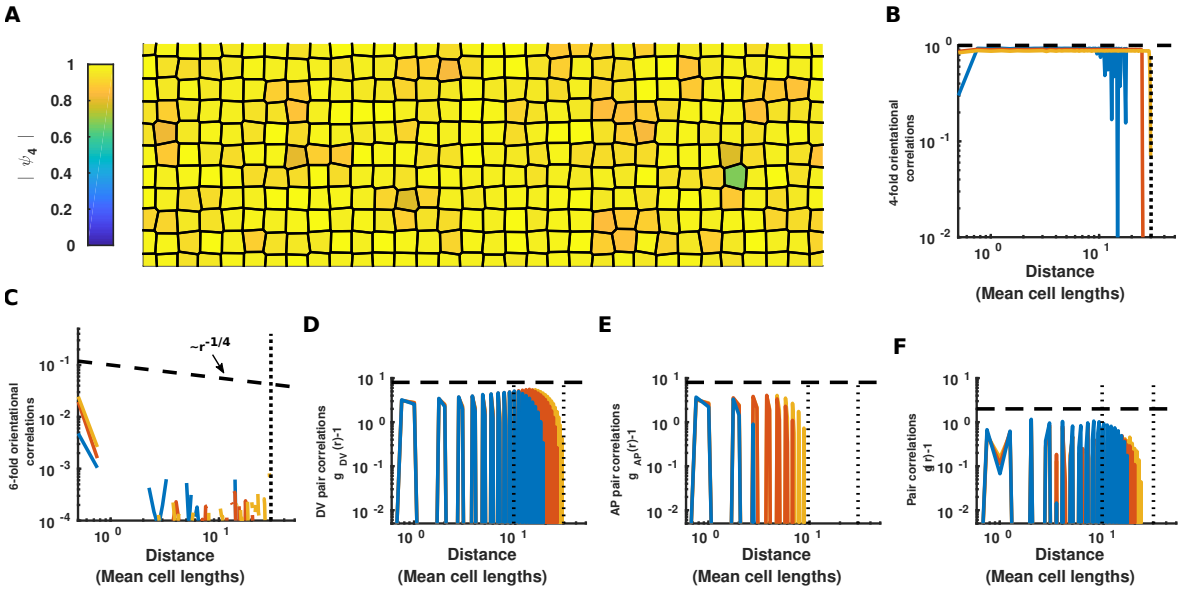

Figure B.8: **The germband does not exhibit translational order.** (*A*) An example translationally ordered synthetic data set with the same spatial dimensions and cell density as the germband at $T = 91.9$ hours after egg lay. Color of cells indicates the magnitude of the fourfold orientational order parameters. (*B* to *F*) Correlation functions for synthetic data sets with the same system sizes and cell densities as the representative time points in Fig. 3.3. (*B*) The two-point fourfold orientational correlation function. (*C*) The two-point sixfold orientational correlation function. (*D*) The pairwise radial distribution function measured along the D-V axis of the synthetic data set. The horizontal dashed line is a guide for the eye. (*E*) The pairwise radial distribution function measured along the A-P axis of the synthetic data set. (*F*) Radially symmetric pair correlation function

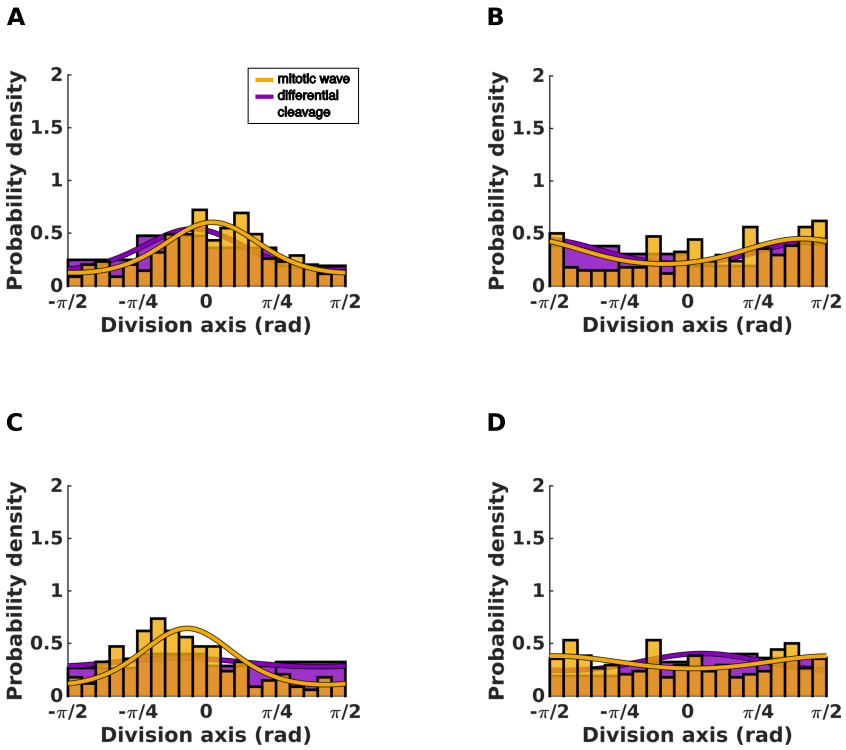

Figure B.9: **Orientations of cell divisions are not predicted by local mechanical or geometric signals.** (A) Histogram of orientations of cell divisions relative to the principal axis of the strain-rate of the corresponding parent cell integrated over the hour preceding cell division. (B) Histogram of the orientations of cell divisions relative to the axis of elongation of the corresponding parent cell averaged over the hour preceding cell division. (C) Histogram of the orientations of cell divisions relative of the orientation of the fourfold order parameter of the corresponding parent cell averaged over the hour preceding cell division. (D) Histogram of the orientations of cell divisions relative to the orientation of the sixfold order parameter of the corresponding parent cell averaged over the hour preceding cell division.

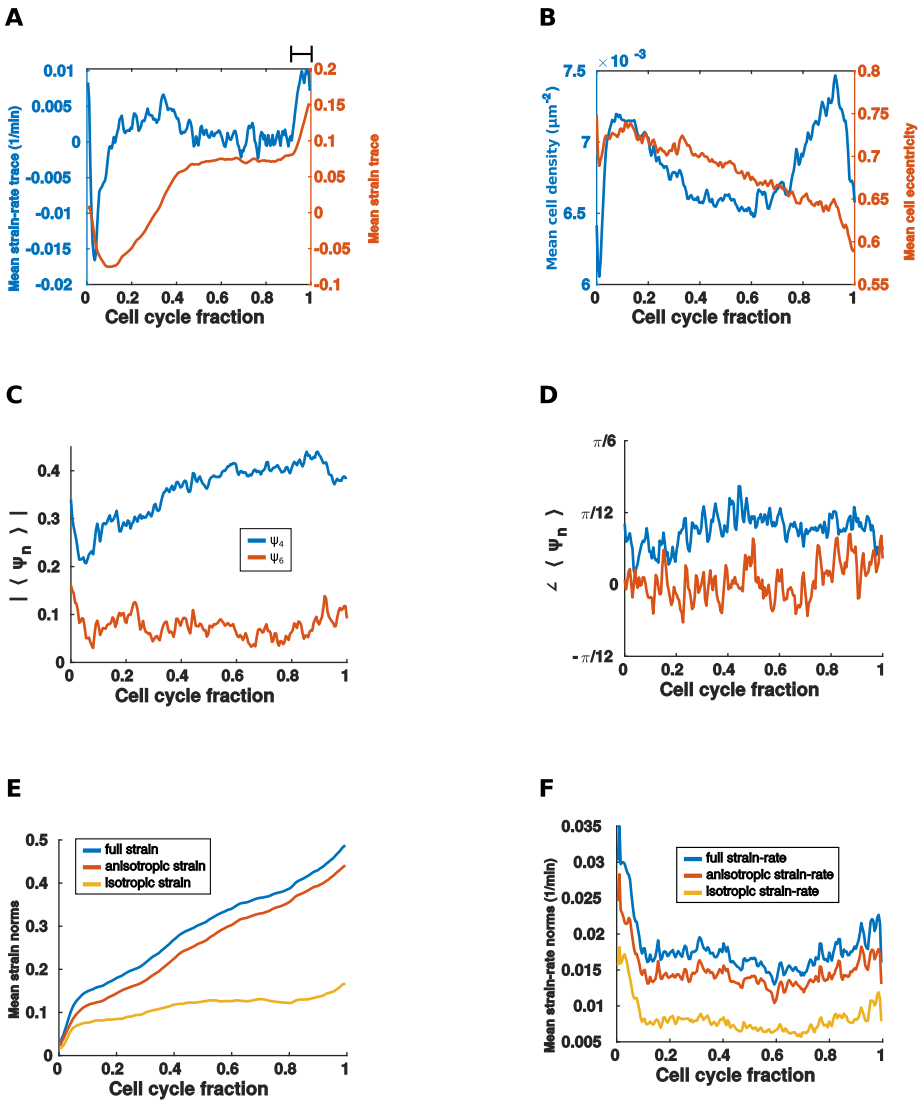

Figure B.10: **Timing of cell divisions are not predicted by local mechanical or geometric signals.** (*A* to *F*) Various geometric and mechanical fields averaged over a normalized cell cycle. Average includes cell cycles from both mitotic waves and differential cleavage. (*A*) The trace of the mean strain-rate tensor (left) and the trace of the mean cumulative strain tensor (right). The black bar in the upper right hand corner indicates the growth phase preceding cell division, i.e. cell division has already been initiated in this phase. (*B*) Mean cell density (left) and mean eccentricity of an ellipse fit to each cell (right). (*C*) The magnitude of the average fourfold and sixfold order parameters. (*D*) The orientation of the average fourfold and sixfold order parameters relative to the A-P axis. (*E*) The Frobenius norm of the average full cumulative strain tensor, the anistropic part of the the average strain tensor, and the isotropic part of the average strain tensor. (*F*) The Frobenius norm of the full average strain-rate tensor, the anisotropic part of the average strain-rate tensor, and the isotropic part of the average strain-rate tensor.

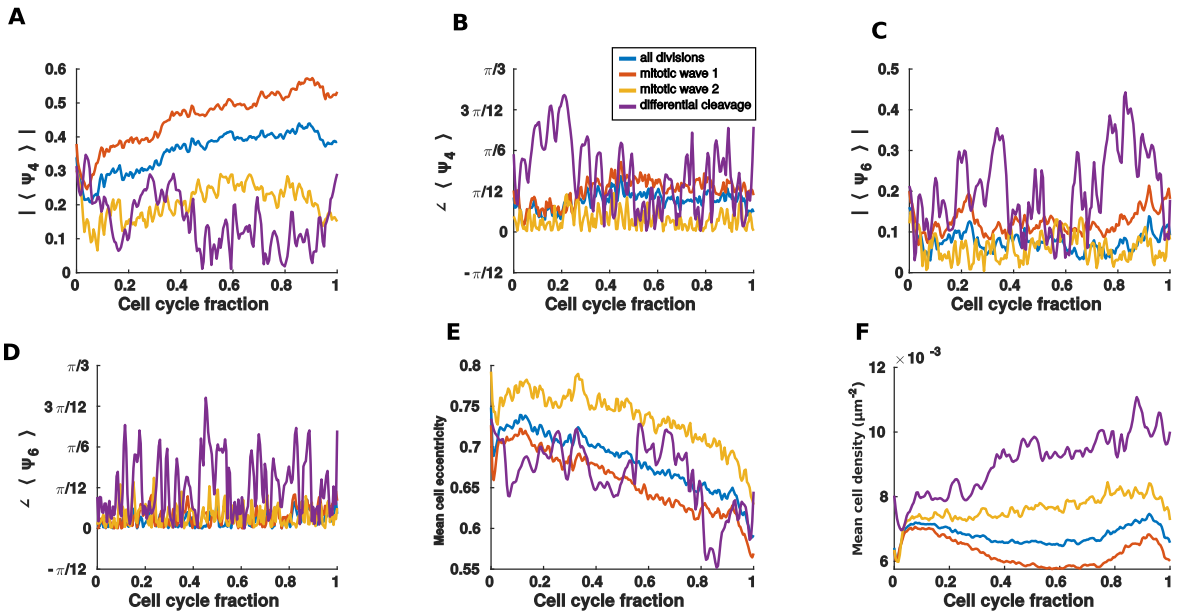

Figure B.11: **Timing of cell divisions are not predicted by local geometric signals (cont.).** (A to F) Various geometric fields averaged over a normalized cell cycle. Separate averages are included for each mitotic wave and differential cleavage. (A) The magnitude of the mean fourfold orientational order parmeter. (B) The orientation of the mean fourfold orientational order parmeter. (C) The magnitude of the mean sixfold orientational order parameter. (D) The orietnation of the mean sixfold orientational order parameter. (E) The mean eccentricity of an ellipse fit to each cell. (F) The mean cell density.

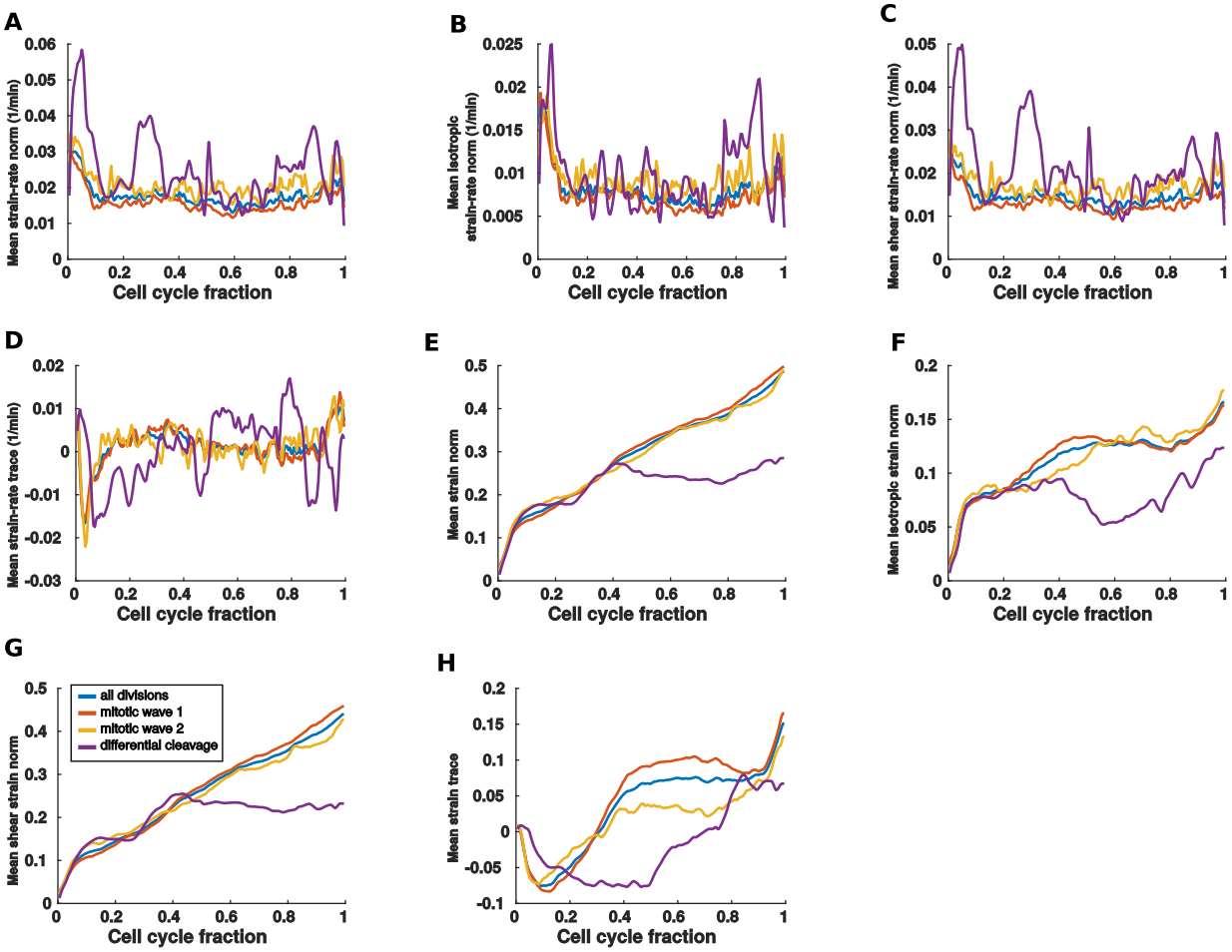

Figure B.12: **Timing of cell divisions are not predicted by local mechanical signals (cont.).** (*A* to *H*) Various mechanical fields averaged over a normalized cell cycle. Separate averages are included for each mitotic wave and differential cleavage. (*A*) The Frobenius norm of the mean strain-rate tensor. (*B*) The Frobenius norm of the isotropic part of the mean strain-rate tensor. (*C*) The Frobenius of the anisotropic part of the mean strain-rate tensor. (*D*) The trace of the mean strain-rate tensor. (*E*) The Frobenius norm of the mean cumulative strain tensor. (*F*) The Frobenius norm of the isotropic part of the mean cumulative strain tensor. (*G*) The Frobenius norm of the anisotropic part of the mean cumulative strain tensor. (*H*) The trace of the mean cumulative strain tensor.

B.12 Additional figures for Chapter 3

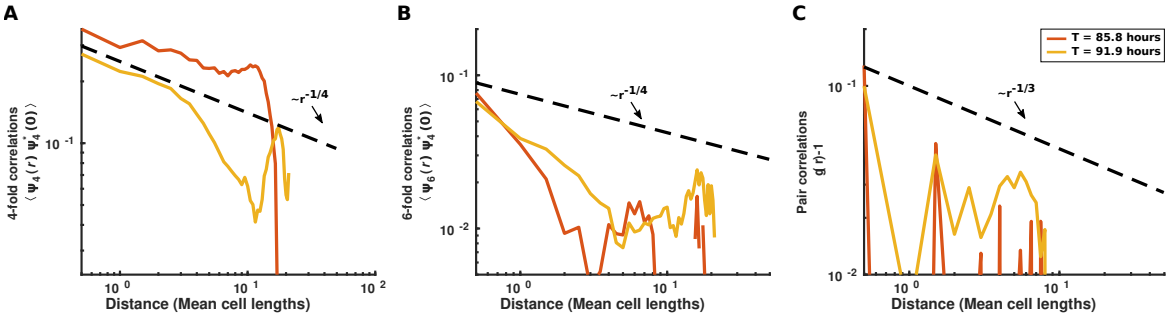

Figure B.13: **Trunk ectodermal germband exhibits neither sixfold nor translational/smectic order (cont.).** Orientational order correlation functions and isotropic pair correlation function for a separate embryo at the same representative times. (*A*) The two-point fourfold orientational correlation functions at two representative time points. Tissue exhibits quasi-long range order at the at T = 85.8 h. (*B*) The two-point sixfold orientational correlation functions at three representative time points. All time points exhibit exponential decay. (*C*) The isotropic pair correlation function. All time points exhibit exponential decay, implying no isotropic translational order.

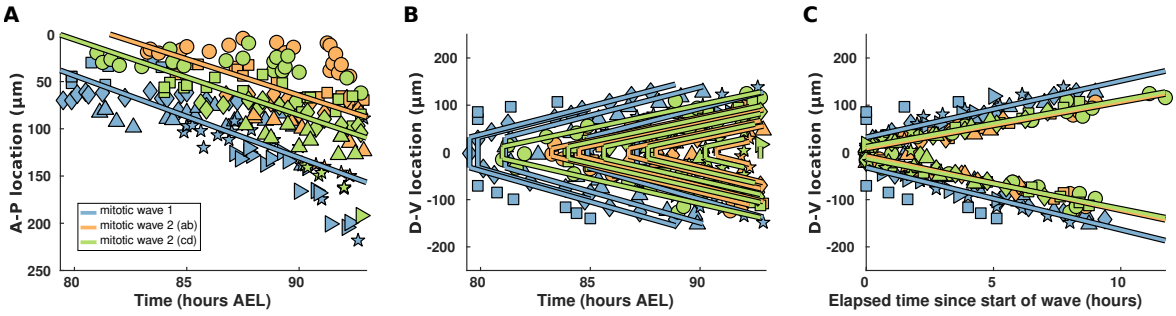

Figure B.14: **Division wave pattern is preserved across embryos.** (A to C) The location of mitotic wave division events over time in a different embryo than the one shown in (Fig. 3.4, E to G). Shapes indicate the parasegment within which a division occurs. Indicated lines are linear fits to all division events associated to a particular mitotic wave. (A) shows the location of each division along the A-P axis. The speed of mitotic wave 1 is 8.7 ± 0.8 μm/hr. The speed of mitotic wave 2 (AB) is 7.7 ± 1.6 μm/hr. The speed of mitotic wave 2 (CD) is 8.0 ± 1.2 μm/hr. (B) and (C) show the location of each division along the D-V axis. Division times in (C) have been normalized to the occurrence of the first division event associated with a particular wave in a specific parasegment. The speed of mitotic wave 1 is 12.6 ± 1.1 μm/hr. The speed of mitotic wave 2 (AB) is 10.7 ± 0.5 μm/hr. The speed of mitotic wave 2 (CD) is 10.3 ± 0.6 μm/hr.

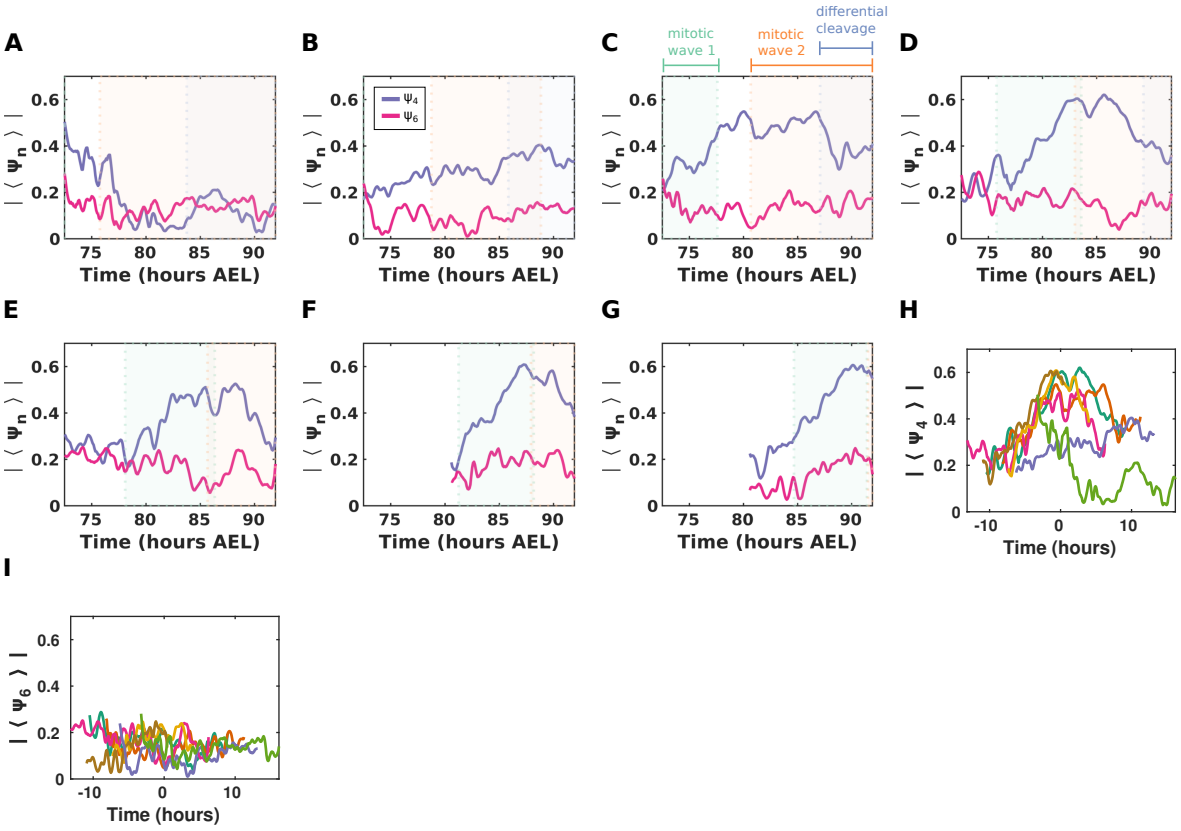

Figure B.15: **Temporal profile of orientational order is similar across different parasegments.** (A to G) Per-parasegment profile of of the magnitude of the average fourfold and sixfold orientational order parameters over time. Ordering of panels (A to G) mirrors anterior to posterior ordering of the physical segments (i.e. the parasegment shown in (A) is anterior to the parasegment shown in (B), etc.). (H) The magnitude of the average fourfold orientational order parameter for each parasegment shifted in time so that $T = 0$ corresponds to the first cell division of mitotic wave 2. (I) The magnitude of the average sixfold orientational order parameter for each parasegment shifted in time so that $T = 0$ corresponds to the first cell division of mitotic wave 2.

Appendix C

Derivation of hydrodynamic model for active stress due to cell divisions

The tissue scale mechanics of epithelia is best understood as emerging from the collective mechanics of the tissue's constituent cells [139]. The cell scale mechanics are dominated by the influence of intracellular cytoskeletal cortices [256, 152]. These structures are capable of supporting stresses throughout the cell's bulk interior and can deform the cell either actively or in response to external stresses. The individual cortices of neighboring cells are coupled together by cadherin mediated adherens junctions [98] into a global trans-cellular mechanical network. Crucially, these networks are both 'active' and 'adaptive'. Active contributions, such as cell divisions [68] or the contraction of trans-cellular actomyosin networks [236], act both locally and over large scales to deform the tissue. These active deformations generate passive stress distally from the activity via the coupling between cells. Stresses created in this fashion can then be relaxed either locally, via internal rearrangement of the cytoskeletal cortex [120, 269], or at the tissue scale, via cell rearrangements [74]. The result is an exotic type of viscoelasticity, wherein the tissue responds elastically to active stresses over short timescales and then reverts to a fluidlike

flow at longer timescales as the tissue adaptively relaxes stress. When the timescale of growth (i.e. rate of cell division, etc.) is long compared to the timescale of mechanical relaxation, the tissue essentially behaves like a slowly creeping fluid in quasistatic mechanical equilibrium with both the active and external forces. For our purposes, a detailed description of the complex cellular processes mediating the active stresses and adaptive relaxation is unimportant. Instead, we adopt an approximate continuum scale description of the tissue that captures the relevant behaviors of the system.

At short time scales, the tissue behaves elastically [75, 220]. Incremental increases in strain generate corresponding increases in stress. These stresses are then subsequently relaxed over a time scale τ_R. The total stress $\boldsymbol{\sigma} = \boldsymbol{\sigma}^e + \boldsymbol{\sigma}^a$ can be decomposed into a sum of the elastic stresses $\boldsymbol{\sigma}^e$ and the active stresses $\boldsymbol{\sigma}^a$. For simplicity, we assume that the tissue is a flat two-dimensional surface. Supposing the tissue behaves like a Maxwell viscoelastic fluid, the time-evolution of the elastic stress is given by

$$\dot{\boldsymbol{\sigma}}^e = \mu \left(\nabla \mathbf{v} + (\nabla \mathbf{v})^T\right) + \lambda \left(\nabla \cdot \mathbf{v}\right) \mathbb{I} - \tau_R^{-1} \boldsymbol{\sigma}^e, \tag{C.1}$$

where $\dot{\boldsymbol{\sigma}}^e = \partial_t \boldsymbol{\sigma}^e + \mathbf{v} \cdot \nabla \boldsymbol{\sigma}^e$ denotes a convective time derivative, $\mathbf{v}$ is the local velocity or rate of displacement, and μ and λ are the Lamé parameters characterizing a linear isotropic stress-strain relationship. The Lamé parameters are assumed to be spatially homogeneous, but may depend on time. A more complete description would include the corotational time derivatives of $\boldsymbol{\sigma}^e$ on the left hand side, but we omit them for simplicity. The first two terms on the right hand side describe the generation of stress in proportion to the rate of strain. The final term parameterizes the relaxation of the elastic stress. We have made the assumption that $\dot{\boldsymbol{\sigma}}^e$ only depends on $\boldsymbol{\sigma}^a$ implicitly through the final term $\tau_R^{-1}\boldsymbol{\sigma}^e$ (see the force balance condition below). This is not meant to imply that adaptive cell behaviors do not actually depend explicitly on the active stresses. It is

merely a mathematical simplification. In reality, there may exist a complex interplay between mechanics, gene expression/cell fate, and adaptive cellular behaviors, but this lies beyond the scope of this work.

In general, the tissue flow velocity can be described by the Cauchy momentum equation [133]

$$\begin{aligned} \rho\,\dot{\mathbf{v}} &= \nabla\cdot\boldsymbol{\sigma} + \mathbf{F}^{EXT} \\ &= \nabla\cdot\boldsymbol{\sigma}^{e} + \nabla\cdot\boldsymbol{\sigma}^{a} + \mathbf{F}^{EXT}, \end{aligned} \tag{C.2}$$

where ρ denotes the material density and $\mathbf{F}^{EXT}$ denotes any external body forces acting on the system. If the rate of mechanical relaxation is sufficiently fast to reach quasi-equilibrium, $\dot{\boldsymbol{\sigma}}^{e}$ vanishes, leaving us with

$$\tau_R^{-1}\boldsymbol{\sigma}^{e} \approx \mu\left(\nabla\mathbf{v} + (\nabla\mathbf{v})^{T}\right) + \lambda\left(\nabla\cdot\mathbf{v}\right)\mathbb{I}. \tag{C.3}$$

Substituting this into Eq. (C.2), we find that

$$\rho\,\dot{\mathbf{v}} = \tau_R\,\mu\,\nabla^2\mathbf{v} + \tau_R\left(\mu+\lambda\right)\nabla(\nabla\cdot\mathbf{v}) + \nabla\cdot\boldsymbol{\sigma}^{a} + \mathbf{F}^{EXT}. \tag{C.4}$$

In other words, the transient elasticity of the system gives rise to fluidlike behavior in the quasi-stationary regime parameterized by a set of effective viscosities. The effective shear viscosity $\nu_1 \equiv \tau_R\,\mu$ tends to resist shearing motion, while the effective bulk viscosity $\nu_2 \equiv \tau_R\left(\mu+\lambda\right)$ resists the isotropic compressible part of the flow. If the effective viscosities are sufficiently large and the corresponding motion is sufficiently slow we can neglect the inertial term relative to the viscous terms ($\rho\dot{\mathbf{v}} << \nu\nabla^2\mathbf{v}$). If, for simplicity, we furthermore assume that there are no external forces acting on the system, we are left with the following force balance condition defining the tissue flow velocities in terms of

the active stresses

$$\nu_1 \nabla^2 \mathbf{v} + \nu_2 \nabla(\nabla \cdot \mathbf{v}) = -\nabla \cdot \boldsymbol{\sigma}^a \equiv -\mathbf{F}^a, \tag{C.5}$$

which can be solved given suitable boundary conditions.

C.1 Cell divisions and active stresses

In general, there may be numerous different types of active stresses acting within the tissue during growth [68, 177, 236]. These various sources of active stress will likely not contribute with equal importance to the shaping of the nascent tissue. Our observations of the cell division choreography indicate that cell proliferation is the primary factor mediating tissue velocities. In order to simplify our model, we assume that the only relevant active stresses are due to these cell divisions.

Our first consideration in modeling active stresses due to cell divisions is to understand how division events might be incorporated into a spatiotempoally coarse grained scheme. With respect to timing, daughter cell separation in real cell division events occurs over a short, but finite time [35]. We ignore the complexity of the rapid subcellular properties mediating mitosis and model cell divisions as instantaneous events (for our purposes any process that occurs faster than 5 min, the time resolution of our microscope data, is considered instantaneous). Real cell divisions push on the surrounding tissue, which responds elastically over the short time scale of the actual division, before remodeling to relax the resulting stress. In our model, both the plastic strain due to a division and the subsequent relaxation are assumed to occur instantaneously so that the fluid is always in quasistatic mechanical equilibrium. With respect to spatial coarse graining, we note that the length scale of a single cell division is small compared to the scale of the entire germband. Numerical experimentation showed that approximating division events as

point force dipoles produced inaccurate flow fields. We therefore model divisions as small, but finite size events to regularize this inconsistency. We also make the approximation that the inclusion lives in an infinite, otherwise quiescent medium in order to make analytic progress.

The mathematical structure of the fluid mechanical equations of motion in Eq. (C.5) is identical to the structure of the Navier equations of linear elasticity. Exploiting this similarity, we can model the instantaneous displacement (read velocity) due to a cell division as that of an Eshelby inclusion. In the context of classical elasticity, an Eshelby inclusion is a finite subregion of an elastic body which undergoes a permanent plastic deformation [73]. Eshelby inclusions, and the associated theories of elastic multipoles [214], have proved useful in numerous applications including understanding shear localization in amporphous solids [59] and the properties of mechanical metamaterials [10]. In the current context of viscoelastic tissue growth, this displacement corresponds to both the plastic deformation and the subsequent viscous relaxation, which are assumed to both occur instantaneously on time scales relevant to growth. Relying on the well-trodden mathematical history of Eshelby inclusions, we may, in the following derivation, use terminology similar to Eshelby's original exposition for elastic materials (e.g. eigenstrain). For clarity, we emphasize again that we are modeling the tissue as a viscoelastic fluid, not an elastic solid, and that the parameters of our model are effective viscosities, not elastic moduli which would vanish in an orientationally ordered phase.

In particular, we choose to model the division as a circular Eshelby inclusion of radius a and eigenstrain $\epsilon^*_{\alpha\beta} = (M/2)\,\delta_{\alpha\beta} + q\,(2\,\hat{n}_\alpha\hat{n}_\beta - \delta_{\alpha\beta})$, where $\delta_{\alpha\beta}$ is the Kronecker delta and $\hat{\mathbf{n}}$ is a unit vector along the division axis. Here, M is a parameter controlling the isotropic contribution of the divisions, mediating area growth, and q controlling the deviatoric contribution, mediating constant area shear. Note that we have adopted an index notation to better account for the high-rank tensorial nature of the following

calculations. Greek indices vary in the set $\{x, y\}$. We also adopt the Einstein summation notation so that all repeated indices are summed. It was shown by Eshelby that the constraining medium generates a constant strain within the inclusion $\epsilon^c_{\alpha\beta} = S_{\alpha\beta\gamma\delta}\,\epsilon^*_{\gamma\delta}$, where $S_{\alpha\beta\gamma\delta}$ is a constant tensor for any elliptical inclusion. For a circular inclusion

$$S_{\alpha\beta\gamma\delta} = \frac{\lambda-\mu}{4(\lambda+2\mu)}\,\delta_{\alpha\beta}\delta_{\gamma\delta} + \frac{\lambda+3\mu}{4(\lambda+2\mu)}\,(\delta_{\alpha\gamma}\delta_{\beta\delta} + \delta_{\alpha\delta}\delta_{\beta\gamma}), \tag{C.6}$$

which yields the following constrained strain within the inclusion

$$\begin{aligned}\epsilon^c_{\alpha\beta} &= \frac{\lambda-\mu}{4(\lambda+2\mu)}\,\delta_{\alpha\beta}\,\epsilon^*_{\gamma\gamma} + \frac{\lambda+3\mu}{2(\lambda+2\mu)}\,\epsilon^*_{\alpha\beta} \\ &= \frac{M\,(\lambda+\mu)}{2\,(\lambda+2\mu)}\,\delta_{\alpha\beta} + \frac{q\,(\lambda+3\mu)}{2\,(\lambda+2\mu)}\,(2\,\hat{n}_\alpha\hat{n}_\beta - \delta_{\alpha\beta}).\end{aligned} \tag{C.7}$$

Thanks to the linearity of the system, the corresponding velocity, i.e. instantaneous displacement, within the inclusion can now be computed as

$$\begin{aligned}v^{in}_\alpha(\mathbf{x}) = \epsilon^c_{\alpha\beta}x_\beta &= \frac{\lambda-\mu}{4(\lambda+2\mu)}\,\epsilon^*_{\beta\beta}\,x_\alpha + \frac{\lambda+3\mu}{2(\lambda+2\mu)}\,\epsilon^*_{\alpha\beta}\,x_\beta \\ &= \frac{M\,(\lambda+\mu)}{2\,(\lambda+2\mu)}\,x_\alpha + \frac{q\,(\lambda+3\mu)}{2\,(\lambda+2\mu)}\,(2\,\hat{n}_\alpha\,(\hat{n}_\beta x_\beta) - x_\alpha).\end{aligned} \tag{C.8}$$

The velocity outside of the inclusion will satisfy the biharmonic equation $\nabla^2\nabla^2 v^{out}_\alpha(\mathbf{x}) = 0$, subject to continuity at the surface of the inclusion and must also tend to zero as $r \to \infty$ where $r \equiv ||\mathbf{x}||$. Recalling the radial solutions of the biharmonic equation in 2D (i.e., 1, $\ln r$, r^2, and $r^2 \ln r$), we construct the general solution by considering all combinations of derivatives of the radial solutions that are linear in the eigenstrain, tend to zero at infinity, and transform like a vector field:

$$v^{out}_\alpha(\mathbf{x}) = A\,\epsilon^*_{\alpha\beta}\,\frac{\partial \ln r}{\partial x_\beta} + B\,\epsilon^*_{\beta\beta}\,\frac{\partial \ln r}{\partial x_\alpha} + C\,\epsilon^*_{\beta\gamma}\,\frac{\partial^3 \ln r}{\partial x_\alpha \partial x_\beta \partial x_\gamma} + D\,\epsilon^*_{\beta\gamma}\,\frac{\partial^3 (r^2 \ln r)}{\partial x_\alpha \partial x_\beta \partial x_\gamma} \tag{C.9}$$

where A, B, C, and D are constants to be determined. Recall that the velocity outside of the inclusion is a solution to the equation

$$\mu\,\partial_\beta^2\, v_\alpha^{out}(\mathbf{x}) + (\mu+\lambda)\,\partial_\alpha(\partial_\beta\, v_\beta^{out}(\mathbf{x})) = 0. \tag{C.10}$$

The fact that $\nabla^2\nabla^2 v_\alpha^{out}(\mathbf{x}) = 0$ is a necessary, but insufficient condition on any solution of Eq. (C.10). With this fact in mind, we begin to calculate the constants by first computing

$$\frac{\partial^2 v_\alpha^{out}}{\partial x_\beta \partial x_\beta} = D\,\epsilon^*_{\eta\lambda}\,\frac{\partial^3}{\partial x_\alpha \partial x_\eta \partial x_\lambda}\left[\frac{\partial^2 (r^2 \ln r)}{\partial x_\beta \partial x_\beta}\right] = 4\,D\,\epsilon^*_{\eta\lambda}\frac{\partial^3 \ln r}{\partial x_\alpha \partial x_\eta \partial x_\lambda}. \tag{C.11}$$

In the first equality, we used the identity

$$\frac{\partial^2 \ln r}{\partial x_\beta \partial x_\beta} = 0 \tag{C.12}$$

to cancel the terms proportional to A, B, and C. In the second equality, we made use of the fact that

$$\frac{\partial^2 (r^2 \ln r)}{\partial x_\beta \partial x_\beta} = 4\,(\ln r + 1). \tag{C.13}$$

Next we compute

$$\begin{aligned}
\frac{\partial^2 v_\beta^{out}}{\partial x_\alpha \partial x_\beta} &= \frac{\partial}{\partial x_\alpha}\Bigg[A\,\epsilon^*_{\beta\eta}\,\frac{\partial^2 \ln r}{\partial x_\beta \partial x_\eta} + B\,\epsilon^*_{\eta\eta}\,\frac{\partial^2 \ln r}{\partial x_\beta \partial x_\beta} + \\
&\qquad\qquad C\,\epsilon^*_{\eta\lambda}\,\frac{\partial^4 \ln r}{\partial x_\beta \partial x_\beta \partial x_\eta \partial x_\lambda} + D\,\epsilon^*_{\eta\lambda}\,\frac{\partial^4 (r^2 \ln r)}{\partial x_\beta \partial x_\beta \partial x_\eta \partial x_\lambda}\Bigg] \\
&= \frac{\partial}{\partial x_\alpha}\left[A\,\epsilon^*_{\beta\eta}\,\frac{\partial^2 \ln r}{\partial x_\beta \partial x_\eta} + 4\,D\,\epsilon^*_{\eta\lambda}\,\frac{\partial^2 (\ln r + 1)}{\partial x_\eta \partial x_\lambda}\right] \\
&= (A + 4D)\,\epsilon^*_{\eta\lambda}\,\frac{\partial^3 \ln r}{\partial x_\alpha \partial x_\eta \partial x_\lambda},
\end{aligned} \tag{C.14}$$

where we have once again made use of both Eq. (C.12) and Eq. (C.13). Substituting

these results into Eq. (C.10) yields

$$4\,\mu\,D\,\epsilon^*_{\eta\lambda}\frac{\partial^3 \ln r}{\partial x_\alpha \partial x_\eta \partial x_\lambda} + (\lambda+\mu)\,(A+4D)\,\epsilon^*_{\eta\lambda}\frac{\partial^3 \ln r}{\partial x_\alpha \partial x_\eta \partial x_\lambda} = 0, \tag{C.15}$$

which, when simplified, reveals that

$$D = -\frac{A\,(\lambda+\mu)}{4\,(\lambda+2\mu)}. \tag{C.16}$$

The velocity outside the inclusion can therefore be written as

$$v^{out}_\alpha(\mathbf{x}) = A\,\epsilon^*_{\alpha\beta}\frac{\partial \ln r}{\partial x_\beta} + B\,\epsilon^*_{\beta\beta}\frac{\partial \ln r}{\partial x_\alpha} + C\,\epsilon^*_{\beta\gamma}\frac{\partial^3 \ln r}{\partial x_\alpha \partial x_\beta \partial x_\gamma} - \frac{A\,(\lambda+\mu)}{4\,(\lambda+2\mu)}\,\epsilon^*_{\beta\gamma}\frac{\partial^3 (r^2 \ln r)}{\partial x_\alpha \partial x_\beta \partial x_\gamma}. \tag{C.17}$$

The following identities are now required to make further progress:

$$\frac{\partial \ln r}{\partial x_\beta} = \frac{x_\beta}{r^2}, \tag{C.18}$$

$$\frac{\partial^3 \ln r}{\partial x_\alpha \partial x_\beta \partial x_\gamma} = \frac{-2r^2(x_\alpha\delta_{\beta\gamma} + x_\beta\delta_{\alpha\gamma} + x_\gamma\delta_{\alpha\beta}) + 8x_\alpha x_\beta x_\gamma}{r^6}, \tag{C.19}$$

$$\frac{\partial^3 (r^2 \ln r)}{\partial x_\alpha \partial x_\beta \partial x_\gamma} = \frac{2r^2(x_\alpha\delta_{\beta\gamma} + x_\beta\delta_{\alpha\gamma} + x_\gamma\delta_{\alpha\beta}) - 4x_\alpha x_\beta x_\gamma}{r^4}. \tag{C.20}$$

Substituting these identities directly into Eq. (C.17) and simplifying allows us to re-write the velocity in the following form

$$\begin{aligned} v^{out}_\alpha(\mathbf{x}) = &\left[\frac{A}{r^2} - \frac{4C}{r^4} - \frac{A(\lambda+\mu)}{(\lambda+2\mu)r^2}\right]\epsilon^*_{\alpha\beta}x_\beta + \\ &\left[\frac{B}{r^2} - \frac{2C}{r^4} - \frac{A(\lambda+\mu)}{2(\lambda+2\mu)r^2}\right]\epsilon^*_{\beta\beta}x_\alpha + \left[\frac{8C}{r^6} + \frac{A(\lambda+\mu)}{(\lambda+2\mu)r^4}\right]\epsilon^*_{\beta\gamma}x_\alpha x_\beta x_\gamma. \end{aligned} \tag{C.21}$$

The remaining constants can be computed by enforcing continuity of the velocity field at the boundary of the inclusion where $r = a$. First, we know that the third term that is cubic in $\mathbf{x}$ must vanish when $r = a$ since the velocity within the inclusion is linear in $\mathbf{x}$.

$$\frac{8C}{r^6} + \frac{A(\lambda+\mu)}{(\lambda+2\mu)r^4} = 0 \implies C = -\frac{a^2 A(\lambda+\mu)}{8(\lambda+2\mu)}. \tag{C.22}$$

The dependence of $\mathbf{v}^{out}(\mathbf{x})$ on C can now be removed yielding

$$\begin{aligned} v_\alpha^{out}(\mathbf{x}) = \frac{A}{2(\lambda+2\mu)r^2}&\left[2\mu + \frac{a^2(\lambda+\mu)}{r^2}\right]\epsilon^*_{\alpha\beta}x_\beta \\ &+ \frac{1}{4r^2(\lambda+2\mu)}\left[-2(A(\lambda+\mu) - 2B(\lambda+2\mu)) + \frac{a^2A(\lambda+\mu)}{r^2}\right]\epsilon^*_{\beta\beta}x_\alpha \\ &+ \frac{A(r^2-a^2)(\lambda+\mu)}{(\lambda+2\mu)r^6}\epsilon^*_{\beta\gamma}x_\alpha x_\beta x_\gamma. \end{aligned} \tag{C.23}$$

Referencing Eq. (C.8), we continue to enforce continuity at the boundary of the inclusion and match the coefficients of the velocities inside and outside the inclusion term by term. The term proportional to $\epsilon^* x_\beta$ tells us

$$\frac{A}{2(\lambda+2\mu)a^2}\left(2\mu + (\lambda+\mu)\right) = \frac{\lambda+3\mu}{2(\lambda+2\mu)} \implies A = a^2, \tag{C.24}$$

and the term proportional to $\epsilon^*_{\beta\beta}x_\alpha$ tells us

$$\begin{aligned} &\frac{1}{4a^2(\lambda+2\mu)}\left[-2(A(\lambda+\mu) - 2B(\lambda+2\mu)) + A(\lambda+\mu)\right] = \\ &\frac{1}{4a^2(\lambda+2\mu)}\left[-2(a^2(\lambda+\mu) - 2B(\lambda+2\mu)) + a^2(\lambda+\mu)\right] = \frac{\lambda-\mu}{4(\lambda+2\mu)} \\ &\implies B = \frac{a^2\lambda}{2(\lambda+2\mu)}. \end{aligned} \tag{C.25}$$

Finally we arrive at the following form for the velocity outside of the inclusion

$$\begin{aligned} v_\alpha^{out}(\mathbf{x}) =& \frac{q(\lambda+\mu)}{2(\lambda+2\mu)}\left(\frac{a^2}{r^2}\right)\left(\frac{2\mu}{\lambda+\mu}+\frac{a^2}{r^2}\right)(2\hat{n}_\alpha(\hat{n}_\beta x_\beta)-x_\alpha) \\ &+\frac{M(\lambda+\mu)}{2(\lambda+2\mu)}\left(\frac{a^2}{r^2}\right)^2 x_\alpha \\ &+\frac{\lambda+\mu}{\lambda+2\mu}\left(\frac{a^2}{r^2}\right)\left(1-\frac{a^2}{r^2}\right)\left(\frac{M}{2}+q\left(\frac{2(\hat{n}_\beta x_\beta)^2}{r^2}-1\right)\right)x_\alpha. \end{aligned} \tag{C.26}$$

In summary, the instantaneous velocity induced by a cell division is has the following vectorial form

$$\mathbf{v}(\mathbf{x}) = \begin{cases} \frac{M(\lambda+\mu)}{2(\lambda+2\mu)}\mathbf{x}+\frac{q(\lambda+3\mu)}{2(\lambda+2\mu)}\left(2\,\hat{\mathbf{n}}\,(\hat{\mathbf{n}}\cdot\mathbf{x})-\mathbf{x}\right) & \text{for } r\le a \\ \frac{q(\lambda+\mu)}{2(\lambda+2\mu)}\left(\frac{a^2}{r^2}\right)\left(\frac{2\mu}{\lambda+\mu}+\frac{a^2}{r^2}\right)\left(2\,\hat{\mathbf{n}}\,(\hat{\mathbf{n}}\cdot\mathbf{x})-\mathbf{x}\right) & \\ +\frac{M(\lambda+\mu)}{2(\lambda+2\mu)}\left(\frac{a^2}{r^2}\right)^2\mathbf{x} & \text{for } r>a \\ +\frac{\lambda+\mu}{\lambda+2\mu}\left(\frac{a^2}{r^2}\right)\left(1-\frac{a^2}{r^2}\right)\left(\frac{M}{2}+q\left(\frac{2\,(\hat{\mathbf{n}}\cdot\mathbf{x})^2}{r^2}-1\right)\right)\mathbf{x}, & \end{cases} \tag{C.27}$$

or, in terms of the effective viscosities $\nu_1=\tau_R\,\mu$ and $\nu_2=\tau_R\,(\lambda+\mu)$

$$\mathbf{v}(\mathbf{x}) = \begin{cases} \frac{M\,\nu_2}{2\,(\nu_1+\nu_2)}\mathbf{x}+\frac{q\,(2\,\nu_1+\nu_2)}{2\,(\nu_1+\nu_2)}\left(2\,\hat{\mathbf{n}}\,(\hat{\mathbf{n}}\cdot\mathbf{x})-\mathbf{x}\right) & \text{for } r\le a \\ \frac{q\,\nu_2}{2\,(\nu_1+\nu_2)}\left(\frac{a^2}{r^2}\right)\left(\frac{2\,\nu_1}{\nu_2}+\frac{a^2}{r^2}\right)\left(2\,\hat{\mathbf{n}}\,(\hat{\mathbf{n}}\cdot\mathbf{x})-\mathbf{x}\right) & \\ +\frac{M\,\nu_2}{2\,(\nu_1+\nu_2)}\left(\frac{a^2}{r^2}\right)^2\mathbf{x} & \text{for } r>a \\ +\frac{\nu_2}{\nu_1+\nu_2}\left(\frac{a^2}{r^2}\right)\left(1-\frac{a^2}{r^2}\right)\left(\frac{M}{2}+q\left(\frac{2\,(\hat{\mathbf{n}}\cdot\mathbf{x})^2}{r^2}-1\right)\right)\mathbf{x}. & \end{cases} \tag{C.28}$$

This equation can be non-dimensionalized by introducing the dimensionless parameter

$$\tilde{\nu} \equiv \frac{\lambda}{2\,(\lambda+\mu)} = \frac{\nu_2 - \nu_1}{2\,\nu_2}, \tag{C.29}$$

in terms of which the division velocity is

$$\mathbf{v}(\mathbf{x}) = \begin{cases} \frac{M}{4\,(1-\tilde{\nu})}\,\mathbf{x} + \frac{q\,(3-4\,\tilde{\nu})}{4\,(1-\tilde{\nu})}\,(2\,\hat{\mathbf{n}}\,(\hat{\mathbf{n}}\cdot\mathbf{x}) - \mathbf{x}) & \text{for } r \le a \\ \frac{q}{4\,(1-\tilde{\nu})}\,\left(\frac{a^2}{r^2}\right)\left(2\,(1-2\,\tilde{\nu}) + \frac{a^2}{r^2}\right)(2\,\hat{\mathbf{n}}\,(\hat{\mathbf{n}}\cdot\mathbf{x}) - \mathbf{x}) & \\ +\frac{M}{4\,(1-\tilde{\nu})}\left(\frac{a^2}{r^2}\right)^2\mathbf{x} & \text{for } r > a \\ +\frac{1}{2\,(1-\tilde{\nu})}\left(\frac{a^2}{r^2}\right)\left(1-\frac{a^2}{r^2}\right)\left(\frac{M}{2} + q\left(\frac{2\,(\hat{\mathbf{n}}\cdot\mathbf{x})^2}{r^2} - 1\right)\right)\mathbf{x}. & \end{cases} \tag{C.30}$$

C.2 Numerical prediction of tissue velocities from cell divisions

In order to simplify numerical analysis, this model in Eq.(C.5) was reformulated as

$$\nabla^2\mathbf{v} + \frac{1}{1-2\,\nu}\,\nabla\,(\nabla\cdot\mathbf{v}) = -\tilde{\mathbf{F}}^a, \tag{C.31}$$

where now $\tilde{\mathbf{F}}^a$ is a renormalized set of active forces and ν is the analogous to the Poisson ratio obtained by treating the tissue as an idealized thin 3D material, i.e. as opposed to a true 2D material. Note that ν is not the same as the dimensionless parameter $\tilde{\nu}$ introduced in Eq. (C.29). Per the discussion in the previous section, the (renormalized) active forces induced by each division event were modeled as resulting from a circular

Eshelby inclusion of radius a and eigenstrain

$$\boldsymbol{\epsilon}^* = (M/2)\,\mathbf{I} + q\,(2\,\hat{\mathbf{n}} \otimes \hat{\mathbf{n}} - \mathbf{I}), \tag{C.32}$$

where $\mathbf{I}$ is the 2×2 identity matrix and $\hat{\mathbf{n}}$ is a unit vector along the division axis. Here, M is a parameter controlling the isotropic contribution of the divisions, mediating area growth, and q controlling the deviatoric contribution, mediating constant area shear.

The model was solved numerically for actual data using custom FEM machinery. First, a fine mesh triangulation was constructed over a subset of tracked cells at a particular time Fig. C.1A. Circular holes containing cells about to divide were then removed from the triangulation. These holes represented the finite-size circular Eshelby inclusions used to model the velocities induced by cell divisions (supplementary text). The size of the holes was chosen so that the area of the circular holes equaled the area of the Voronoi polygons of the corresponding cells. Removing the inclusions from the mesh renders the task of predicting velocities a simple boundary value problem with Dirichlet boundary conditions. The velocities on the interior boundary vertices were set to match the analytical predictions of the model (i.e. the displacement field induced by the inclusion) plus a constant term equal to the average measured velocity of the entire tissue in order to account for the advection of the dividing cell with the tissue scale flow. The velocities on the exterior boundary were set to the measured velocities. Using the measured velocities on the exterior boundary captured how cells not included in the subregion contributed to the relevant motion within the region over which the velocities were predicted. The results of the numerical solution was a velocity vector for each triangulation vertex. For cells that did not divide, all vertices contained within each corresponding Voronoi polygon were then averaged to produce a single cell velocity vector. Note that many vertices were averaged for each polygon, so that prescribing Dirichlet boundary conditions on

the triangulation did not correspond to prescribing cell-scale velocities. Note that under deformation the circular inclusions were deformed into ellipses. The locations of the foci of these ellipses were given directly by the fluid mechanical model. The velocity of cells that divided were set to be the displacement of these foci from the center of the undeformed circular inclusion. For our purposes, we set $\nu = 1/3$ for all time points and the parameters M and q were fit separately for each time point containing divisions using MATLAB's `lsqnonlin` in order to minimize the resulting velocity residuals. In order to produce the 'division only' predictions presented in Fig. C.2, we simply summed the contribution of the analytical prediction for each division event at each time point without solving the boundary value problem using the measured data on the domain boundary.

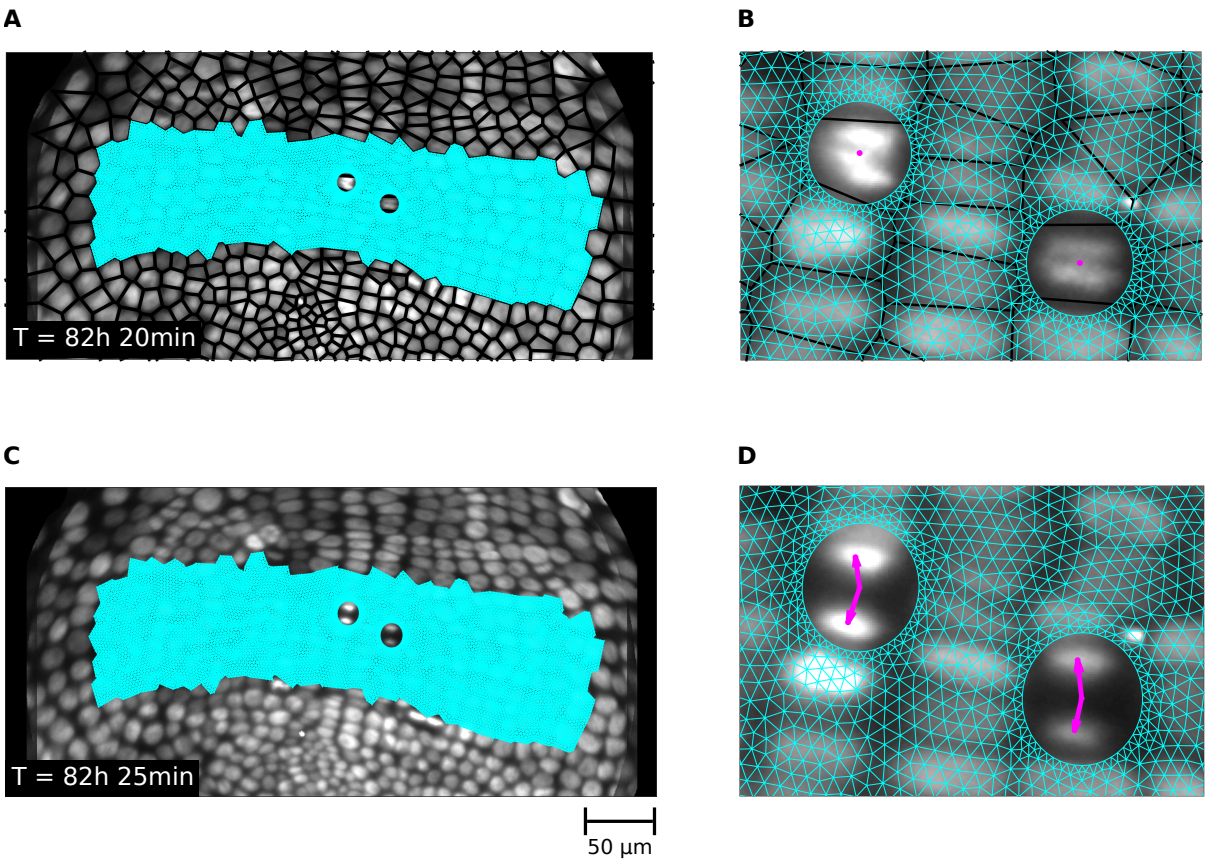

Figure C.1: **Numerical solution of the fluid mechanical equations of motion.** Examples of the triangular mesh used to implement a finite element method (FEM) solution to the equations of motion predicting tissue velocities from cell divisions. (A) The undeformed mesh triangulation. Circular holes have been removed surrounding cells about to divide. (B) A zoomed-in visualization of the undeformed mesh near the cells about to divide. (C) The deformed mesh at the subsequent time. Mesh vertex velocities have been scaled by a constant pre-factor (x5) to improve visibility. (D) A zoomed-in visualization of the mesh near the recently divided cells. Note that the initially circular holes are deformed into ellipses.

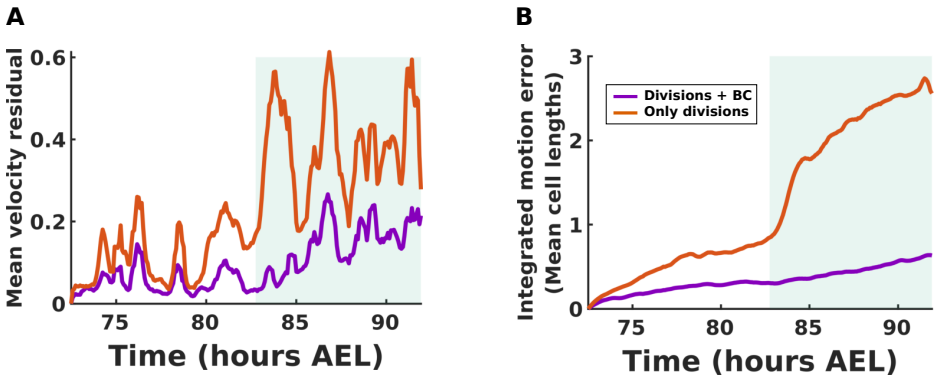

Figure C.2: **Hydrodynamic model of cell divisions predicts cell positions during mitotic wave.** (A) Mean residual between the measured cell velocities and the cell velocities predicted by the active hydrodynamic model using the measured boundary conditions (purple) and without any imposed boundary conditions (orange), i.e. simply the sum of the velocities predicted using our inclusion model. The prediction with no boundary conditions performs reasonably well during the first stage of growth, but breaks down during convergent extension. (B) The error in the predictions for the locations of cell centers generated by integrating measured velocities and calculated velocities, i.e. $||\vec{\mathbf{x}}_{meas}(t) - \vec{\mathbf{x}}_{calc}(t)||$ in units of mean cell lengths. The prediction with no boundary conditions stays within a single cell length of the true position for the first stage of growth, but grows large during convergent extension.

Appendix D

Vertex model simulations of orientational order generation

We simulate a simple vertex model with energy

$$E = \sum_c \left[\frac{k_{A,c}}{2} (A_c - A_{0,c})^2 + \frac{k_{P,c}}{2} (P_c - P_{0,c})^2 \right], \tag{D.1}$$

where c labels the cells, $k_{A,c}$ is the area stiffness parameter for cell c, A_c is the cell area, $A_{0,c}$ is the target cell area, $k_{P,c}$ is the perimeter stiffness parameter, P_c is the cell perimeter, and $P_{0,c}$ is the target cell perimeter. The first term in the sum is an elastic energy that tries to force each cells area to match its target area and the second term is a similar contribution that tries to force each cell to obtain a specified target perimeter. The code used to simulate the vertex model was based on the publicly available code used in [185]. For simplicity, in all of our simulations, we set $k_{A,c} = k_{P,c} = 1$ and fix the target areas, $A_{0,c} = A_0$, and perimeters, $P_{0,c} = P_0$, to be uniform for all cells yielding the simplified energy

$$E = \frac{1}{2} \sum_c \left[(A_c - A_0)^2 + (P_c - P_0)^2 \right]. \tag{D.2}$$

The simulation algorithm is detailed in Algorithm 1.

Algorithm 1 Vertex Model Simulation Algorithm

Require: Initial cell lattice, initial division order for first wave

```
Relax initial cell lattice
for Each division wave do
    Update division order for current wave
    for Each cell in the division order do
        for Number of growth steps do
            Update A_0, P_0 for the next cell in the division order
            Update mesh connectivity due to T1 transitions
            Relax cell lattice
            Enforce confinement
        end for
        Re-set A_0, P_0 for the cell about to divide
        Update mesh connectivity due to T1 transitions
        Randomly choose division axis orientation
        Divide cell along division axis
        Relax cell lattice
        Enforce confinement
    end for
end for
```

D.1 Initial lattice construction

For the division wave/random division simulations, the initial lattices were generated by first constructing a perfect hexagonal lattice with a specified length and height. Row identities were extracted from this initial stage and a subset of the rows in the middle of the lattice were selected to be a part of the division order generated using the row identities. For the random division simulations, this initial division order was then randomly permuted. All simulations were run with an initial set of five dividing rows. Gaussian white noise with a signal-to-noise ratio of 18 was then added to cell positions to produce

a nonuniform hexatically ordered initial state (i.e. quasi-long range sixfold orientational order and no translational order). The decision to use a hexatically ordered initial state was due to the necessity of having an initial configuration with well defined rows and with no fourfold orientational order. Properties of the initial lattices are displayed in Fig. D.1. After the initial lattice was constructed, the parameter A_0 was set to be the mean area of all the cells in the lattice and $P_0 = 4A_0$. Lattices were constructed so that all cells had an approximate initial length scale = 1.

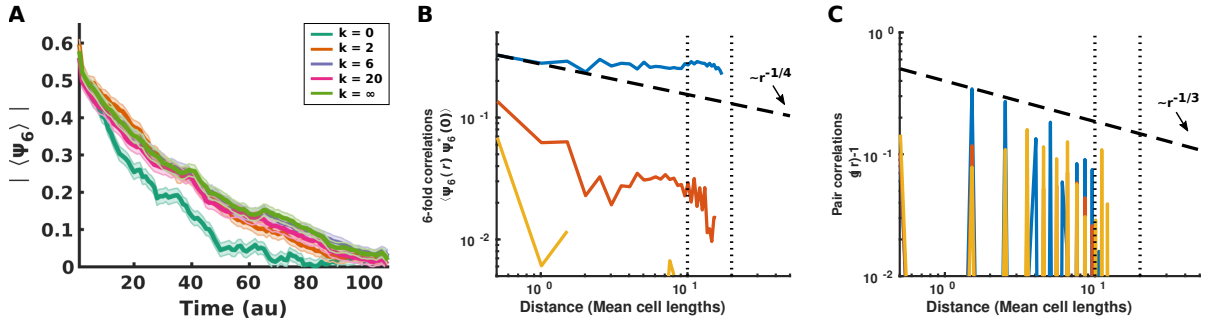

Figure D.1: **Additional division wave simulation properties.** (A) The absolute value of the mean sixfold order parameter during division wave simulations. Different curves correspond to different concentrations k of distributions from which division orientations were randomly drawn (see Fig. 3.10F). Sixfold order degrades completely for all values of k. (B) The two-point correlation function of the sixfold orientational order parameter generated by division wave simulations with $k = \infty$. Vertical lines indicate the length and width of the tissue, respectively. Initial configurations display quasi-long range sixfold order. (C) The isotropic pair correlation function generated by division wave simulations with $k = \infty$. No configuration displays algebraically decaying order over the entire tissue indicating that the initial and final configurations are sixfold and fourfold orientationally ordered, respectively, but not translationally ordered.

D.2 Growth, division, relaxation, and confinement

After the initial lattice was constructed, simulations begin with the first division wave. The cell that is next to divide in the division order undergoes a series of growth steps. In each growth step, the parameters $P_{0,c}$ and $A_{0,c}$ were increased, fixing $P_{0,c} = 4A_{0,c}$. Lattice

connectivity was then updated by implementing T1 transitions for all edges below a user specified length threshold. Boundary edges whose shared external angle dropped below a user specified threshold were then fused together to prevent self-interpenetration of the tissue and other physically erroneous configurations. For all of our simulations, we set the T1 edge length threshold $\ell_{min} = 0.05$, the edge merger threshold $\theta_{min} = 20$, and the number of growth steps $N_{growth} = 50$. The geometric parameters $P_{0,c}$ and $A_{0,c}$ were increased so that $A_{0,c} = 1.5\,A_0$ after N_{growth} growth steps. Additionally, for all of our numerical experiments T1 transitions were prohibited in the bulk.

After all parameter updates and topological corrections, the lattice was then relaxed to an equilibrium configuration. The energy was minimized with the GNU Scientific Library Multidimensional Minimizer, using the Polak-Ribiere conjugate gradient algorithm. The wrapper to this minimization procedure was extended from the code used in [185]. Following relaxation, confinement was enforced by clipping the x-coordinates of lattice vertices to remain within a user specified domain, equal to the width of the original lattice domain plus one cell length. Using a large number of growth steps ensured that no more complicated constraint enforcement procedure was necessary.

After all of the growth steps were concluded, the cell was then forced to divide. Division orientations were drawn from a circular von Mises distribution given by

$$f(x|\mu, k) = \frac{1}{\pi I_0(k)}\, e^{k\,\cos\left(2(x-\mu)\right)}, \tag{D.3}$$

where μ is the center of the distribution, k is its concentration, and $I_0(k)$ is a modified Bessel function of the first kind. We set $mu = \pi/2$ for all of our simulations, i.e. a vertically oriented division along the A-P axis. See Fig. 4F for a visual depiction of the distributions for all values of k used in the simulations. Following division, the tissue was relaxed and confined again and the whole procedure continued for the next cell in

the division order.

Once all of the cells in the division order had divided, the division order was updated for the subsequent wave so that the new order would also proceed as a division wave. We only simulated a single division wave in our numerical experiments. Visualization and order parameter calculations were performed on the Voronoi tessellation of the centroids of each cell polygon in order to be consistent with the methodology used to analyze the data.

Appendix E

Materials and methods for analysis of *Drosophila* midgut morphogenesis

E.1 Microscopy

For light sheet imaging of live and fixed embryos, we used a custom multi-view selective plane illumination microscope drawn schematically in Fig. 1.4A. This setup has been previously described in [236].

Subsequent registration, deconvolution, and fusion using the methods presented in [196] results in a single, deconvolved data volume per timepoint with isotropic resolution (0.018 μm^3 per voxel). For most experiments in this work, we acquire one volume per minute. The optimal number of deconvolution iterations varied between 8 and 20 for different fluorescent reporters. We used 6 or 8 views for most datasets.

To peer deep inside the developing embryo, we leverage the UAS-GAL4 system [193] to express fluorescent proteins in gut-specific tissues and use embryos with the *klarsicht* mutation [259], which reduces scatter without altering gut morphogenesis. We used confocal microscopy (Leica SP8) for more detailed characterization of calcium dynamics,

live imaging of *Ubx* and *Antp* mutants, and supplementary optogenetic experiments

E.2 Parameterization of organ shape

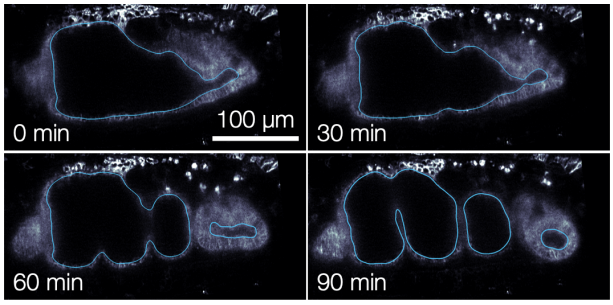

Figure E.1: **Organ segmentation via morphological snakes level sets.** Automatic segmentation of the apical (inner) surface of the endoderm minimizes a non-local Chan-Vese energy functional [42, 168] to encapsulate yolk without enclosing midgut tissue, shown for four snapshots of mid-sagittal sections using TubULAR [164]. Blue contours mark the surface intersection with the mid-sagittal plane.

The geometry of organ shape and deformation was quantified using the TubULAR package (see Chapter 2 and [164]). We begin by using TubULAR's surface detection methods to extract the organ shape with a morphological snakes level set analysis [168, 42] on the output of an iLastik training [18] against midgut tissue (membrane, nuclei, actin, or myosin). Example results from this segmentation performed on a *w;48Y GAL4 / UAS-CAAX::mCh* embryo are shown in midsagittal sections in Fig. E.1. We then use TubULAR's cartographic mapping functions to map the surface to the plane and stabilize noise in the mappings' dynamics (Chapter 2). For visualization, we use a pullback parameterization (s, ϕ) such that the coordinate directions $(\hat{s}, \hat{\phi})$ are determined by the conformal mapping to the plane at the onset of the first constriction ($t = 0$). In this way, ϕ parameterizes the intrinsic circumferential axis and s parameterizes a longitudinal position along the long axis of the organ at $t = 0$. In subsequent timepoints, the difference in parameterization coordinates in 3D space are minimized to match the previous time-

point, such that the coordinates follow the shape change of the organ (Chapter 2). We find this (s, ϕ, t) parameterization aids in both visualization and enables more accurate velocimetry measurements than other choices.

We define the 'material frame' of a given midgut as the tissue configuration at the onset of the middle constriction, which is the first constriction that appears.

We compute the centerline using the TubULAR package (Chapter 2), wherein the organ is divided into circumferential 'hoops' based on its planar parameterization (Fig. 2.2E and Fig. E.2). Hoops for which s = constant define an effective circumference for increments along the lengths of the organ, and the average 3D position of each hoop defines its centerline point. Connecting mean points of adjacent hoops along the length of the organ defines the centerline of the object (brown curve) whose length is reported in Fig. 4.1E.

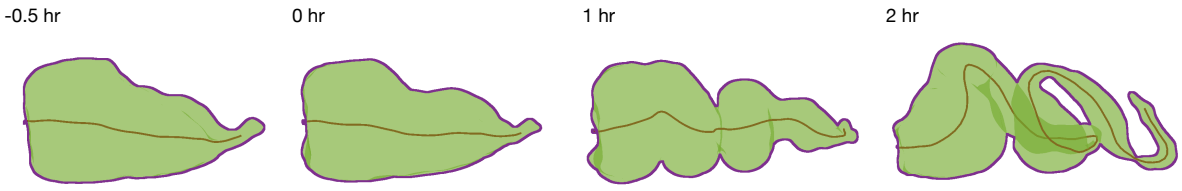

Figure E.2: **A centerline measures an effective length of the organ.** We compute the centerline (brown curve) using the TubULAR package for extracted shapes (green with purple boundary for clarity). The cumulative length of these curves defines the effective length of the organ reported in Fig. 4.2.

E.3 Endodermal cell segmentation and shape change

Using a single slice of the gut surface projected into stabilized (s, ϕ) pullback coordinates, we segmented 600-1300 cells per timepoint (Fig. E.3) using a semi-automated procedure:

1. We first perform adaptive histogram equalization over patches of the pullback containing several cells in width.

2. We then perform two passes of morphological image reconstruction (see MATLAB's `imreconstruct` function) punctuated by morphological dilation and erosion steps.

3. The result is binarized and skeletonized via a watershed algorithm.

4. We overlay this skeleton on the original image to enhance the membrane contrast, convolve with a narrow Gaussian (with a standard deviation of $\sim 0.2\%$ of organ length), and pass the result through the previous three steps.

This gives us an estimate for the image segmentation. We then manually correct any spurious segmentation artifacts in GIMP [241] by overlaying the segmentation with the original pullback images. To resolve some ambiguous cell junctions, we examine not only a single slice of the endodermal cell layer near the apical side (about 2.5μm beyond the apical side), but also the maximum intensity projection of several microns along the surface normal direction.

We compute cell anisotropy by finding segmented cell shapes in 2D, embedding those polygons in 3D, projecting each cell onto a local tangent plane, and measuring the moment of inertia tensor of this polygon in the material coordinate system. This procedure is shown schematically in Fig. E.3. We then embed the Lagrangian coordinate directions $(\hat{s}, \hat{\phi})$ from a conformal mapping of the whole organ at the onset of the initial (middle) constriction $t = t_0$ onto the cell's centroid in 3D (in the deformed configuration at time $t \neq t_0$). The moment of inertia tensor for the cell polygon is expressed in the local coordinate system from the embedded $(\hat{s}, \hat{\phi})$ directions in the local tangent plane of the tissue. The eigenvalues I_1 and I_2 of the moment of inertia tensor and their associated eigenvectors then provide an effective ellipse for the cell with orientation θ with respect to the local $\hat{\mathbf{s}}$ direction and an aspect ratio $a/b \equiv \sqrt{I_1/I_2}$. Fig. E.3 shows the raw data of these measurements without computing statistics.

We then average the cellular anisotropy over the organ surface to report a mean,

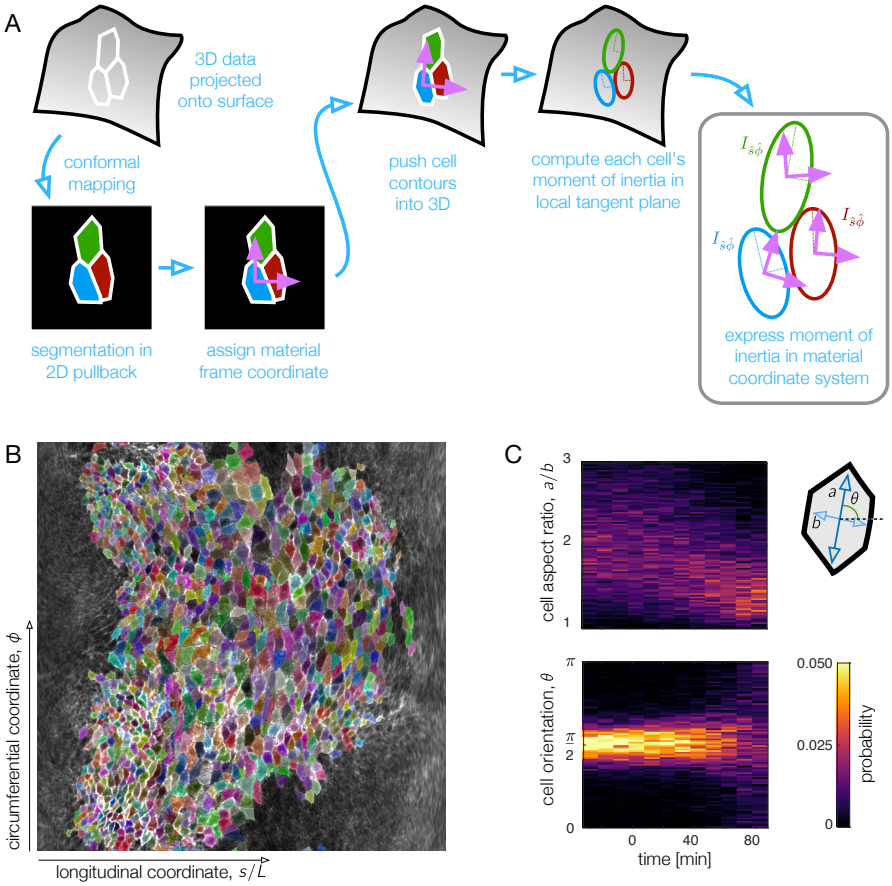

Figure E.3: **Surface projection aids in quantifying cell shape change in the 3D tissue surface.** (*A*) To measure cell shapes, we trace cell membrane contours in a conformal mapping to a 2D pullback plane and re-embed cells into local tangent planes in 3D for shape quantification. After surface extraction, we project the data on a midgut surface ∼2.5 μm beyond the apical side of the endoderm to the plane for segmentation. The pullback plane also defines material coordinate directions in which we can measure orientation of cells, θ. By projecting cell contours back into 3D, we compute moment of inertia tensors for each cell in a local tangent plane. The eigenvalues and eigenvectors of the moment of inertia tensors define the cell anisotropy a/b and the orientation of their long axis, θ, with respect to material coordinate directions $\hat{s}$ and $\hat{\phi}$. (*B*) Example segmentation in the pullback plane at a time near the onset of the first constriction. Each cell polygon is given a random, distinguishable color to demonstrate the segmentation quality. (*C*) Here shown in raw histograms, cell aspect ratios decrease and condense close to 1 (isotropic shapes) by ∼80 minutes after the onset of the first (middle) constriction. During this time, the cells do not rotate, as evidenced by the sustained peak in cell orientation near zero. At late times, when the cells are nearly isotropic, the orientation becomes less clearly defined and the distribution broadens.

standard deviation, and standard error for both the cellular aspect ratio and cell orientation. In this averaging, we weight each cell's contribution to the observable (aspect ratio a/b or orientation θ) by its area, so that all material points on the organ are given equal weight. The results reported in Fig. 4.2, C and D in the main text are the weighted mean and weighted standard deviation for each distribution. The weighted means of the aspect ratio a/b and orientation θ are

$$\langle a/b \rangle = \frac{\sum_{i=1}^{N} A_i a_i/b_i}{\sum_{i=1}^{N} A_i} \tag{E.1}$$

$$\langle \theta \rangle = \tan^{-1}\left[\frac{\sum_{i=1}^{N} A_i \sin\theta_i}{\sum_{i=1}^{N} A_i \cos\theta_i}\right], \tag{E.2}$$

where A_i is the area of the i^{th} cell, and N is the total number of cells. We note that we obtain similar results by weighting each cell equally, which would correspond to setting $A_i = 1$ for all i above.

We obtain standard errors by bootstrapping. In detail, we subsample our collection of measurements, compute the weighted mean for the subsample, and repeat with replacement 1000 times. The variance of these 1000 means decreases in proportion to the number of samples n included in our subsampling, so that $\sigma_{\bar{x}}^2(n) = \tilde{\sigma}_{\bar{x}}^2/n + \sigma_0^2$. Fitting for $\sigma_{\bar{x}}^2$ across 50 values of n ($N/4 < n < N$) and evaluating this fit for $n = N$ gives an estimate for the standard error on the mean $\sigma_{\bar{x}} = \sqrt{\sigma_{\bar{x}}^2}$. In practice, the result is nearly identical to measuring the means of many weighted subsamplings of $n = N$ cells with replacement and computing the standard deviation of this collection of means.

E.4 Single-cell tracking

We tracked 175 cells from -27 min $< t < 83$ minutes of development relative to the onset of the middle constriction in a *w; 48Y GAL4;klar* × *w; UAS-CAAX::mCh* embryo

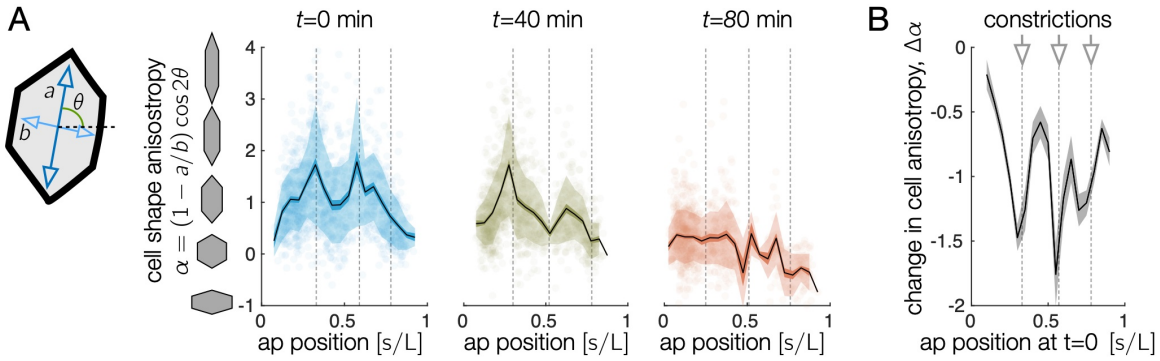

Figure E.4: **Endodermal cells are initially most elongated near anterior and middle constrictions, and cell shape change is greatest near constrictions.** (*A*) The oriented cell anisotropy varies along the anterior-posterior axis. We define the cell shape anisotropy to be a signed quantity varying from positive for cells elongated along the circumferential axis and negative for cells elongated along the longitudinal axis. This signed measure of oriented anisotropy shows that some cells become elongated along the longitudinal (AP) axis, particularly near the posterior end of the midgut by $t = 80$ min. In particular, the signed shape anisotropy of a cell is $\alpha \equiv (1 - a/b)\cos 2\theta$, where a and b are the semimajor and semiminor axes of the ellipse capturing each cell's moment of inertia tensor and θ is the cell's angle with respect to the material frame's longitudinal axis. Locations of the constrictions or constriction precursors are marked in dashed gray vertical lines. Cells near the anterior and middle constrictions are initially elongated along the circumferential axis more than cells in the interstitial regions. Cell anisotropy changes dramatically first at the middle constriction, then at the anterior and posterior constrictions. Shaded error bars denote standard deviations (semi-transparent bands) and standard error on the mean (opaque colored bands), while black curves denote the mean. (*B*) The total change in signed cell shape anisotropy over the 80 minute timecourse shows strong, negative values near each constriction. We here parameterize cells' anterior-posterior positions at $t = 80$ by mapping to their locations at $t = 0$ in order to compare measurements made in the same tissue patches.

imaged using confocal MuVi-SPIM. First, we segmented the same 175 cells in the first chamber of the gut every two minutes using the same procedure as in the previous section. We tracked their positions over time using iLastik manual tracking workflow using 2D (s, ϕ) pullback projections. From these segmented polygons, we project back into 3D onto the gut surface and measure the cell areas in a local tangent plane for Fig. 4.2E in the main text.

E.5 Topological cell rearrangements in the endoderm

Cell rearrangements are also present in the endodermal tissue, and these 'T1' events could also contribute to the large-scale shear [74]. To estimate their contribution, we performed manual tracking of 175 segmented cells in the first chamber and identified T1 transitions from $-27 < t < 83$ minutes relative to the onset of the middle constriction. Importantly, the orientation of T1 transitions is not significantly aligned with the elongation axis at early times, suggesting that the endoderm is fluidized and that T1s are not a tightly controlled process directing morphogenesis.

To identify T1 transitions, we leveraged our single-cell tracking previously used in Fig. 4.2E – a contiguous region of cells in the anterior chamber of the midgut, extending from the anteriormost portion of the midgut up to the anterior fold. We query all cell pairs which share an edge in the endoderm at any time during the morphogenetic process. We then filter out any pairs that remain neighbors for all timepoints, since their shared edges do not participate in topological rearrangements. The remaining pairs reflect a cell-cell interface which either appears or vanishes during morphogenesis. We perform additionally screening of these candidate events to confirm that the change in cell topological is not an artifact from possible segmentation error by coloring the two cells participating and visually inspecting their motion. Fig. E.5 shows an example sequence of T1 transitions

tracked using this scheme.

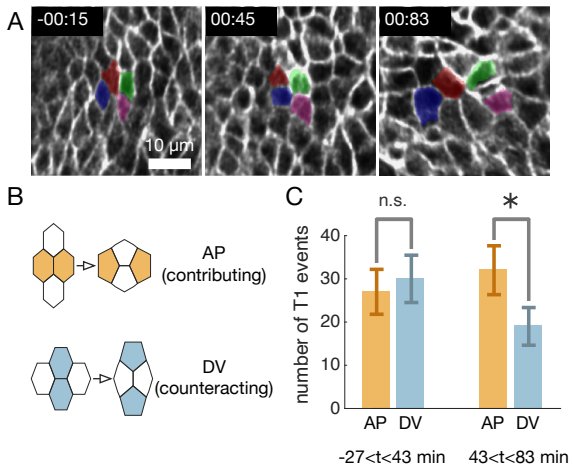

Figure E.5: **Topological rearrangements occur in the endoderm but are not aligned during the earliest stages of gut constrictions, consistent with cell shape change being the dominant contributor to tissue deformation at the onset of constrictions.** (A) An example rosette of four tracked cells. The tissue patch is flattened to a plane such that the longitudinal and circumferential axes of the organ in the material frame aligns with the horizontal and vertical axis, respectively. The mapping to the plane is an as-rigid-as-possible map constrained so that the ratio of lengths in the longitudinal and circumferential directions is preserved near the center of the image (so the diagonal metric tensor components are equal $g_{11} \approx g_{22}$). (B) Here we define T1 events to be AP oriented if the cells that lose contact are within 45° of the longitudinal axis of the organ in the material frame. Conversely, in DV oriented T1 events, the cells that lose contact are within 45° of the circumferential axis of the organ in the material frame. (C) In a collection of 175 tracked cells in the anterior midgut, we find no significant difference between the rate of cell intercalations oriented along the longitudinal direction versus the circumferential direction during stages 15-16a of constrictions ($-27 < t < 43$ min), while we find a bias in T1 orientations during later stages of 16a and 16b ($43 < t < 83$ minutes) among the tracked cells. Uncertainties are taken as the square root of the count, and $* = p < 0.05$

For each junction lost or gained, we measure the axis of the associated T1 transition by computing the centroid of each cell in the pair that is gaining or losing a junction. Fig. E.5B shows a histogram of these axes' angles with respect to the anterior-posterior axis of the organ defined in a locally conformal coordinate patch, with the AP axis orientation inferred from the material (Lagrangian) frame. We find that T1 transitions oriented along the AP axis (converging along DV) occur about as frequently as T1 tran-

sitions oriented along the DV axis (converging along AP) for our collection of tracked cells in the first lobe, suggesting that topological cell rearrangements are not a principal driver of convergent extension in the tissue. These rearrangements are therefore unlikely to drive shape change, as predicted by the quantitative similarity between tissue shear and cell shape change (Fig. 4.4).

E.6 Quantification of tissue deformation

To compute a coarse-grained tissue velocity over the gut surface, we again used the TubULAR package (Chapter 2 and [164]). This resource enables velocimetry and discrete exterior calculus measurements [55] on the evolving surface. The result is a fully covariant measurement of the compressibility and shear of the tissue spanning the whole organ.

Briefly, given our (s, ϕ, t) coordinate system defined in the TubULAR pipeline, we then run particle image velocimetry (PIV) using PIVLab [242, 243] and map tissue velocities in the domain of parameterization to the embedding space. Geometrically, displacement vectors $\mathbf{v}$ extend from one $\mathbf{x}(s_0, \phi_0, t_0)$ coordinate in 3D on the surface at time t_0 to a different $\mathbf{x}(s_1, \phi_1, t_1)$ coordinate on the deformed surface at time t_1. When t_0 and t_1 are adjacent timepoints, this defines the 3D tissue velocity at $\mathbf{x}(s_0, \phi_0, t_0)$ as $\mathbf{v}(s_0, \phi_0, t_0) = (\mathbf{x}(s_1, \phi_1, t_1) - \mathbf{x}(s_0, \phi_0, t_0))/(t_1 - t_0)$. We decompose the velocity into a component tangential to the surface $\mathbf{v}_{\|}$ and a normal component $\mathbf{v}_n = v_n \hat{\mathbf{n}}$ for measuring divergence via discrete exterior calculus and for measuring out-of-plane deformation $2Hv_n$, where H is the mean curvature obtained via computing the Laplacian of the mesh vertices in (embedding) space: $\Delta \mathbf{X} = 2H\hat{\mathbf{n}}$ (see [55]). As shown in Fig. E.6, the in-plane dilatational flow almost perfectly matches the out-of-plane deformation during the morphogenetic process.

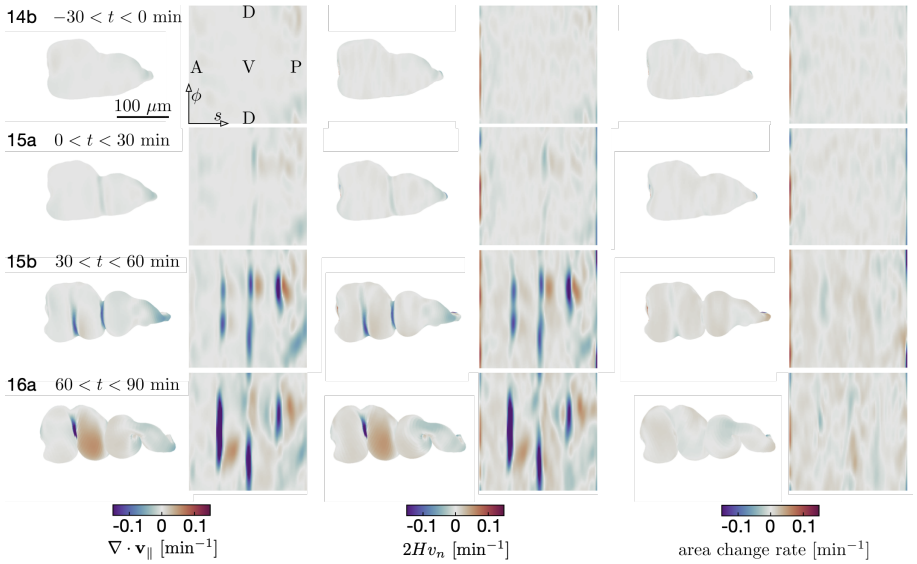

Figure E.6: **Dilatational flow patterns are tightly coupled to bending throughout midgut constrictions, indicating a nearly incompressible tissue behavior.** Resulting divergence of in-plane tissue motion ($\nabla \cdot \mathbf{v}_\parallel$) and out-of-plane deformation measurements ($2Hv_n$) on an representative embryo, plotted both on the midgut surface in 3D and in pullback coordinates, show strong correlation. The difference of the two patterns gives the local area change (right columns). Each image is the average of patterns over a 30 minute timespan. The pullback representation uses the surface Lagrangian parameterization (s, ϕ), such that the ventral tissue is in the midline of the image, anterior is to the left, posterior is to the right, and deformation of the organ shape in 3D is subtracted out from the pullback coordinates of subsequent timepoints [164]. The s position in the pullback representation is proportional to the proper distance along the organ's longitudinal axis.

E.7 Minimal ingredients demonstrate geometric interplay between compressibility and shear

A flat, nearly incompressible sheet demonstrates a kinematic coupling between dilatational in-plane flow ($\nabla \cdot \mathbf{v}_{\parallel}$) and out-of-plane deformation ($2Hv_n$). Contracting such a sheet as in Fig. E.8A leads to out-of-plane bending to preserve surface area of the sheet. This out-of-plane motion leaves cells unchanged in their aspect ratio: no in-plane deformation is necessary.

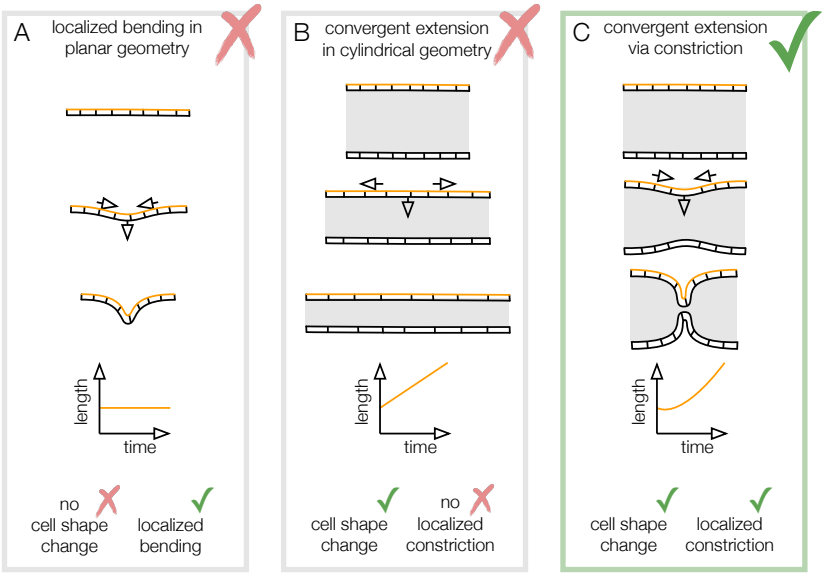

Figure E.7: **Convergent extension via constriction links in-plane tissue shape change with out-of-plane deformation.** (A) An initially flat, incompressible sheet may bend in a localized region without deforming the tissue in-plane. Distances between cells in plane are preserved, illustrated by the constant length between the ends of the sheet along the orange geodesic. (B) A uniformly constricting, incompressible tube exhibits convergent extension but has no localized folds. In the absence of cell intercalations, cells converge along the circumferential direction and elongate along the longitudinal direction, so an orange curve spanning several cells along the longitudinal axis lengthens over time. (C) In convergent extension via constriction, localized normal motion of the tube couples to in-plane tissue shape change. In a constricting, incompressible tube, the tissue converges along the circumference and extends along the bending longitudinal profile.

If the sheet is curved into a tube (so that mean curvature is nonzero, $|H| > 0$), then

constricting an sheet (with inward velocity $v_n > 0$) can generate deformation in the local tangent plane of the sheet. Such incompressibility couples to initial curvature to generate shear deformation. For example, an incompressible sheet of paper glued into a cylinder along one of its edges cannot be pinched in this fashion without crumpling, folding, or tearing. An elastic sheet, however, can be deformed in this manner even if local areas of material patches are required not to change. In particular, the sheet may stretch along the long axis while constricted circumferentially, such that a circular material patch is transformed into an elliptical patch with the same area, as in Fig. E.8B.

Finally, these two effects are coupled in the case of the pinched cylinder. In a given snapshot with an existing localized constriction, we can schematically understand the three ingredients by considering the pinched cylinder with a step-wise indentation shown in Fig. E.8C. First, active stresses constrict the neck, decreasing the surface area of the neck (blue) and dilating the interior faces (red). In order to restore the surface area of the cells in the neck, its length may increase, resulting in extension along the long axis of the tube. In tandem, to combat the dilation in the interior faces, cells flow into the constriction from the chambers. Note that if all three steps are instantaneously coupled, the order of events is immaterial to the outcome: contractile surface flows could increase the density of cells in the interior faces, which leads to neck constriction to restore cell density in the faces and results in convergent extension of the neck.

We note also that when the constriction is broad along the longitude or when the indentation is shallow, the mean curvature will be positive everywhere (cylinder-like, $H > 0$). In this case, inward motion of the incompressible tube causes an extensile surface flow ($\nabla \cdot \mathbf{v}_{\|} > 0$), rather than a contractile one. This is a qualitative difference between broad or uniform constrictions of a tube and localized constrictions such as those seen in the midgut. In principle, we predict a crossover between the two modes of behavior during the very onset of constriction in our system – from positive to negative

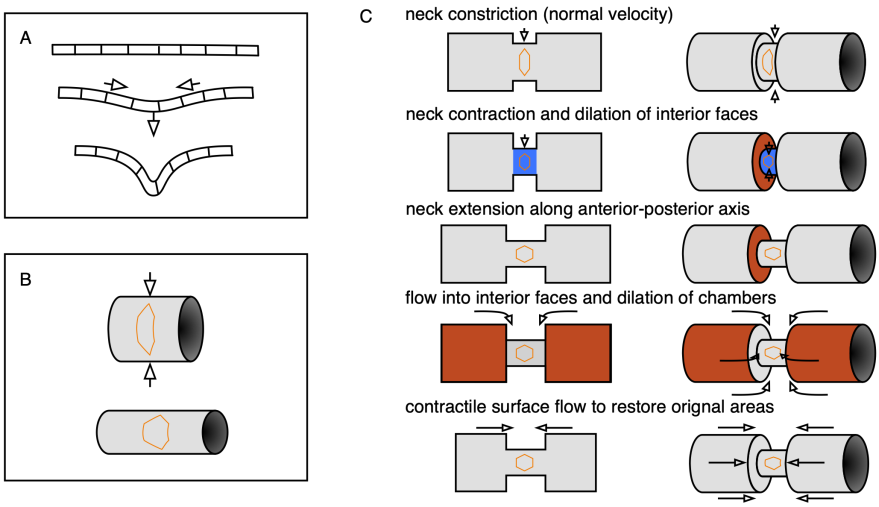

Figure E.8: **Three-component decomposition of kinematics elucidates coupling between compressibility and convergent extension.** (A) An initially flat incompressible sheet demonstrates kinematic coupling between in-plane dilatational flow and out-of-plane bending to preserve cells' 2D areas. (B) Constriction couples to convergent extension via curvature of the surface. As a tube constricts, the tube elongates in order to preserve surface area. Correspondingly, cells change their aspect ratio and undergo convergent extension. (C) The two effects shown in (A) and (B) couple in a pinching tube with a localized constriction. A tube with a step-like constriction is composed of deformable cells whose areas shall not change. Constriction of the narrow tube via inward normal velocities would decrease the neck area (blue), so the neck extends to keep its area fixed. This is convergent extension. The faces are now dilated, triggering flow into the interior faces to correct for the change in tissue density. In this way, convergent extension is linked to incompressibility, which couples in-plane dilatational flow to out-of-plane deformation.

divergence as the curvature changes sign. This is a subtle and transient feature, given the large radius of the midgut compared to the small axial length of the constrictions and the non-uniform initial curvature of the midgut before constrictions begin.

E.8 Quantification of tissue shear

We employ a geometric method of tissue-scale shear quantification that accounts for both the shear due to the changing shape of the gut and the shear due to the material flow of cells along the dynamic surface. The first step is to establish consistent material coordinates for all times, i.e. labels for parcels of tissue that follow those parcels as they move and deform. We prescribe these labels at the onset of midgut constrictions by endowing a cylindrical 'cut mesh' of the organ's surface at the that time with a planar parameterization. The cut mesh is first conformally mapped into a planar annular domain, $\{||\mathbf{x}|| : r \leq ||\mathbf{x}|| \leq 1\}$, using a custom Ricci flow code included in our TubULAR package (Chapter 2 and [164]). Fixing the outer radius of the annulus to 1, the inner radius r is a conformal invariant that is automatically determined from the geometry of the organ. Taking the logarithm of these intermediate coordinates then defines a rectangular domain, with a branch cut identifying the top and bottom horizontal edges of the domain in such a way the the cylindrical topology of the cut mesh in 3D is fully respected. The coordinates in this domain are taken to be the material ('Lagrangian') coordinate system, $(\tilde{\zeta}, \tilde{\phi})$. This conformal parameterization is, by construction, isotropic; the metric tensor is diagonal. This parameterization is therefore a suitable reference against which to measure all subsequent accumulation of anisotropy in the tissue. We note that at the reference time t_0 (at the onset of the first constriction), the material coordinates are similar to the (s, ϕ, t_0) coordinate system defined before, except that the coordinate s measures a proper length on the surface along curves of constant ϕ, while

$\tilde{\zeta}$ is a coordinate of the conformally mapped planar domain. We chose to use s instead of $\tilde{\zeta}$ for visualizations simply because deep constrictions exhibit extreme dilation in a conformal $(\tilde{\zeta}, \tilde{\phi})$ pullback plane, but these are attenuated in an (s, ϕ) pullback plane (see Chapter 2). We stress that all measurements account for the physical embedding of the surface: the coordinate system parameterizing the surface is a tool to define circumferential and longitudinal directions based on the organ's intrinsic geometry, and the choice of parameterization does not influence the magnitude of tissue deformation.

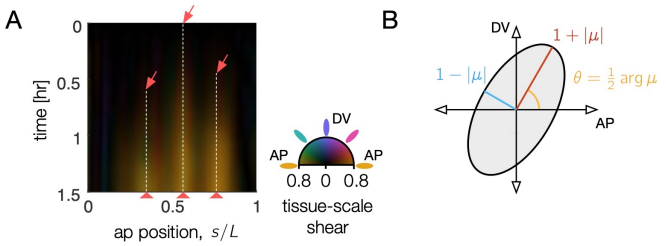

Figure E.9: **Tissue shear generates 3D convergent extension during constrictions, as captured in the Beltrami coefficient – a local measure of anisotropic, area-preserving deformation.** (A) Tissue-scale shear accumulates near each constriction, shown as a kymograph in the material coordinate frame averaged along the circumferential axis. As time increases (downward), orange streaks reflect area-preserving convergence of tissue patches along the organ circumference and extension along the folding AP axis near constrictions (red arrows). Here, the organ is parameterized by the position, s, at the onset of constriction ($t = 0$), measured in proper length along the surface, and deformation is averaged along the circumferential position in the kymograph. Color denotes the orientation of the anisotropic shear deformation in this material frame, such that shear which converges along the circumferential axis and extends along the AP axis is denoted by orange color (colorwheel). Larger magnitudes of tissue shear are brighter, reflecting the Beltrami coefficient averaged over the circumferential axis. (B) The Beltrami coefficient μ is defined as the amount of area-preserving shear transforming a circle into an ellipse with aspect ratio $1 + |\mu|/(1 - |\mu|)$ at an angle $\arg \mu/2$.

In order to recapitulate the material flow of the tissue, these coordinates are advected in the plane along the flow fields extracted using PIV [243, 242] and then mapped into 3D at each time point. This mapping defines a deformed mesh whose induced metric tensor, $\mathbf{g}' \equiv \mathbf{g}(t)$, can be computed relative to the material coordinates. All anisotropy in the mapping is encoded by the complex Beltrami coefficient, $\mu(t)$, defined in terms of

the components of the time-dependent metric tensor

$$\mu(t) = \frac{g'_{11} - g'_{22} + 2i\, g'_{12}}{g'_{11} + g'_{22} + 2\sqrt{g'_{11}\, g'_{22} - {g'_{12}}^2}}. \tag{E.3}$$

As illustrated in Fig. E.9B, μ describes how an initially circular infinitesimal patch of tissue is deformed into an elliptical patch under the action of the material mapping. The argument of μ describes the orientation of this ellipse. The magnitude $|\mu|$ is related to the ratio, K of the lengths of the major axis of this ellipse to its minor axis by

$$K = \frac{1 + |\mu|}{1 - |\mu|}. \tag{E.4}$$

When $|\mu| = 0$, the material mapping is isotropic, i.e. a circular patch of tissue remains circular under the mapping. Note that $|\mu| < 1$ and therefore provides a bounded description of both the magnitude and orientation of material anisotropy in the deforming surface.

The results of this measurement are shown as a kymograph in Fig. E.9 for a representative dataset. Constrictions begin to appear at times and locations marked by red arrows and continue to deepen. The Beltrami coefficient is averaged along the circumferential direction and plotted at the anterior-posterior position in tissue coordinates at the onset of the middle constriction (the first constriction to appear), so that the deformation of advected tissue patches are compared to their original shape. A single color dominates the kymograph, indicating that the deformation is globally aligned to extend along the local longitudinal axis (and contract along the material frame's circumferential axis), despite the contorting and complex shape. This is consistent with circumferential muscle orientations defining the axes for convergent extension in the midgut.

E.9 Relative motion between layers

To characterize relative motion between layers, we tracked 375 endodermal and 81 muscle nuclei in the same *w,Hand>GAL4;UAS-Hand:GFP;hist:GFP* embryo. Fig. E.10 shows measurements of relative displacement of initially-close nuclei pairs (< 5 μm apart at the onset of the first constriction). Two example tracks are highlighted in yellow and green. Fig. E.11 shows additional statistics of the relative motion over time.

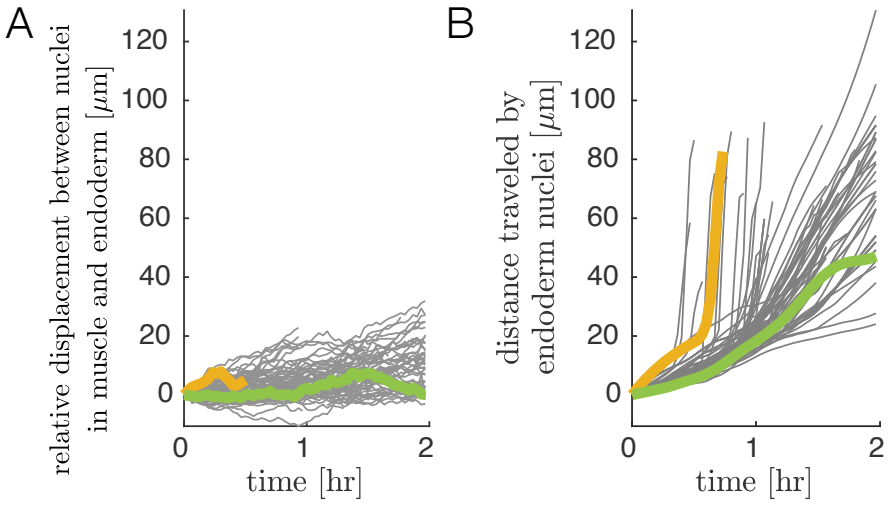

Figure E.10: **Relative motion of endodermal and mesodermal nuclei is small compared to motion of the tissue.** (*A*) Tracking muscle nuclei and counterpart nuclei in the endoderm reveals only a gradual increase in geodesic distance (distance along the gut surface) between initially close nuclei pairs over time. The mean displacement grows by $\sim$5 μm per hour during folding on average, regardless of whether nuclei are located in deep folds (as in the example pair marked by a yellow curve) or on the surface of the gut chambers (green curve). (*B*) In contrast, the tissue deformation leads to large displacements of cells. We measure distances in embedding space along pathline trajectories suitably smoothed to remove contributions from noise and transient motions. Distance traveled for example tracks invaginating into deep folds (yellow curve) or translating on gut chambers (green curve) are highlighted to match panel (*A*).

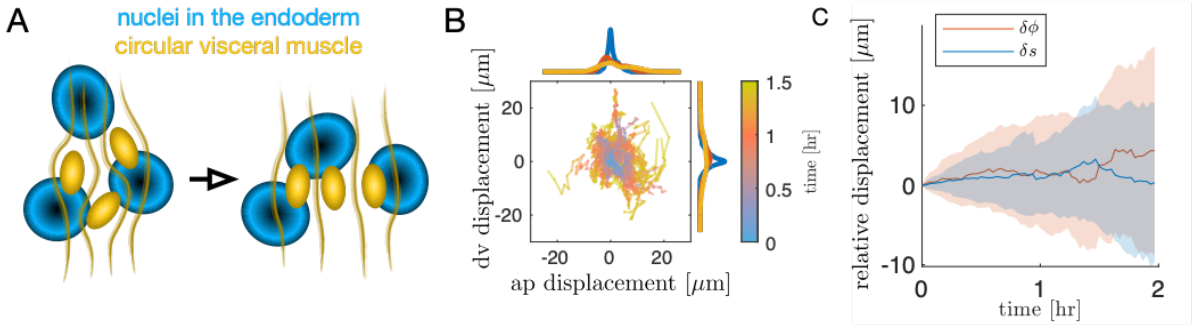

Figure E.11: **Motion of the muscle nuclei with respect to the endoderm is not coherent.** (*A*) Schematic of muscle nuclei configuration at early and late times. Muscle cells are positioned in bands along the AP axis and are initially clustered, such that each band is several cells wide along the circumferential axis. As constrictions form, circumferential muscle nuclei arrange in a nearly single-file configuration. (*B*) Motion of nuclei cells relative to the endodermal layer does not show strongly coherent (directional) motion, as demonstrated by individual tracks of relative displacement colored by timestamp. As before, the positions of 81 nuclei cells are measured relative to the center of mass of the endodermal nucleus that was nearest at the onset of constrictions. Distances are measured as geodesic lengths along the surface. Distances along the normal direction (through the thickness of the tissue) are ignored. That is, nuclear positions are projected along the thickness of the tissue onto the surface in which the endodermal nuclei reside. Histograms of accumulated displacements in either direction show the average over the first 30 minutes (blue), 30-60 minutes (red), and 60-90 minutes (yellow). (*C*) The same data shown in (*B*) is plotted as a distribution, with each component separated. The standard deviation of displacement coordinates (colored bands), either in the $\hat{\boldsymbol{s}}$ direction (along the folding longitudinal axis in the material frame, blue) or the $\hat{\boldsymbol{\phi}}$ direction (along the circumferential axis in the material frame, orange) show an increase of $\sim$5 μm per hour, with nearly zero mean displacement in either axis.

E.10 Optogenetic experiments

The *UAS-CRY2-OCRL* and *UAS-ρGEF2* constructs have been previously characterized [91, 114]. For optogenetic confocal microscopy experiments, we activated the optogenetic construct with continuous oblique illumination of a 470 nm LED at 6.2±0.1 mW/cm^2 power, in addition to periodic illumination with the 488 nm laser used to image the sample. Wild-type embryos developed normally under this illumination ($N = 18/19$). Variations by a factor of two in either the LED power or in the 488 nm laser power used to image the *GFP* channel did not result in differences in phenotype. For light sheet imaging, we illuminated with a 488 nm laser line at 1 mW for 30 seconds once per minute.

We quantified the endoderm cell shapes using a similar procedure as before. After deconvolution (Huygens Essential software), we perform 3D segmentation via a morphological snakes level set method on an iLastik pixel classification to carve out an approximate midsurface of the endoderm. We measured the endoderm shape dynamics for two-color *y,w,Antp-GAL4;;Gap*^{43} *mCherry* × *w;UAS-CIBN::GFP;UAS-CRY2-OCRL* embryos held under continuous optogenetic activation from oblique illumination of a 470 nm LED at 6.2±0.1 mW/cm^2 power as before. For comparison, we additionally measured endoderm shapes in *Antp* mutant embryos with a membrane marker driven in the midgut endoderm (*w;48Y GAL4/UAS-CAAX::mCh;Antp*$^{NS+RC3}$).

Fig. E.12A shows representative snapshots of this segmentation procedure for a two-color *y,w,Antp-GAL4;;Gap*^{43} *mCherry* × *w;UAS-CIBN::GFP;UAS-CRY2-OCRL* embryo at the onset of the first constriction and 40 minutes after the middle constriction began. Circumferential muscle localized near the anterior constriction expresses the optogenetic construct (cyan band), while the endoderm is imaged using a ubiquitous membrane marker (grayscale). Image regions masked in semi-transparent gray are the

deepest confocal plane acquired, while the rest of the image is a lateral view of the projected data on the segmented organ surface. Segmented endodermal cell polygons are colored by their aspect ratios. Cells are segmented in 2D and then projected into 3D for measurement of their aspect ratios. As shown in Fig. E.12C, there is no significant difference between cell orientations in wild-type (blue), optogenetic mutants (red), and *Antp* mutants (yellow).

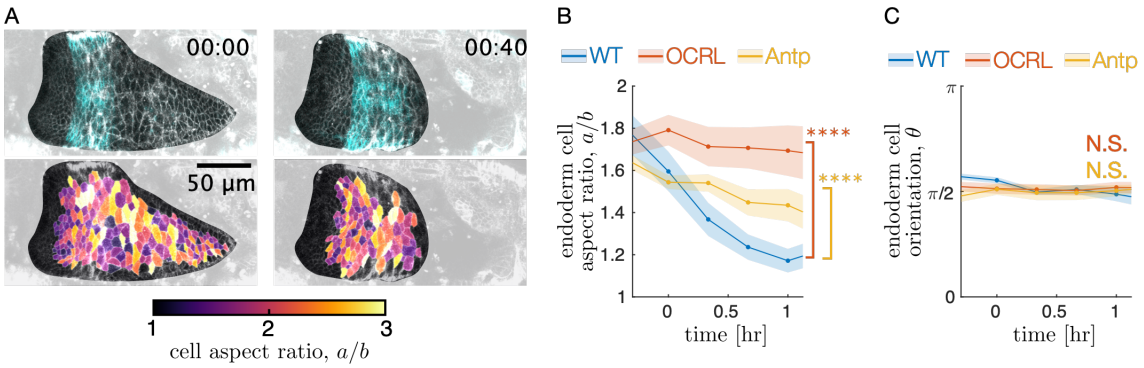

Figure E.12: **Optogenetic knockdown of muscle contractility inhibits endodermal shape changes, mimicking mutant behavior.** (*A*) Snapshots of single-cell shape measurements of embryos under optogenetic perturbations demonstrate that muscle contraction induces endoderm cell shape change. During optogenetic inhibition of muscle contractility in the *Antp* domain using *w,Antp-GAL4* × *w; UAS–CIBN::pmGFP;UAS-CRY2-OCRL*, cell shapes in the interior two chambers (which remain as a single chamber in the optogenetic mutant) remain steady. (*B*) Endodermal cells undergo less shape change in both *CRY2-OCRL* and *Antp* mutants, as reported in the main text. As before, **** denotes $p < 0.0001$, and N.S. denotes $p > 0.05$. (*C*) The endodermal cell orientation does not change significantly between conditions.

E.11 Wild-type calcium dynamics

We quantified calcium dynamics using the confocal microscopy (Leica SP8) of the live reporter *UAS GCaMP6s* driven by either the driver *Mef2-GAL4*, which is expressed across all muscles in the embryo, or *48Y GAL4*, which is expressed in the embryonic midgut both in endoderm and visceral muscles. Here, we used *Mef2-GAL4* as a driver for

characterizing anterior and middle constrictions. We used *48Y GAL4* for the posterior constriction since many fluorescent somatic muscles occlude the line of sight for the posterior constriction under *Mef2-GAL4*. We found that the two drivers yielded similar quantitative results for the anterior constriction.

To measure transient calcium activity without bias from variations in ambient fluorescent intensity due to spatially-dependent scattering, we imaged three confocal stacks with 2.5-3 μm step size in rapid succession (9 or 10 seconds apart) and subtracted subsequent image stacks from each other according to

$$\delta I \equiv |I_1 - I_2| + |I_2 - I_3| + |I_1 - I_3|, \tag{E.5}$$

where $I_i = I_i(x, y)$ is the maximum intensity projection (projected across $dz \approx 30\mu$m) of the i^{th} stack. Over such short timescales, motion of the midgut is small, but transient flashes of *GCaMP6s* are unlikely to span more than one acquisition. We then extract coherent features from δI using a Gaussian blur followed by a tophat filter, and sum the resulting signal along the circumferential direction.

While we interrogated *GCaMP6s* activity using many views of the gut, the quantification used three standardized views. For the anterior constriction, we used a dorsal view, since out-of-plane effects are smallest on the dorsal side and since the midgut is nearest to the surface on the dorsal side. For the middle constriction, we used ventrolateral views since there is a line of sight with fewer other muscles driven by *Mef2-GAL4* from this view. For the posterior constriction, we used a left lateral view for quantification.

To time-align the *GCaMP6s* experiments of the anterior and middle constrictions, we defined $t = 0$ as the first timestamp in which the constriction under observation showed localized bending along the longitudinal (AP) axis. For characterization of calcium dynamics at the posterior constriction, we defined the onset of constriction by the ventral

side of the gut visceral muscle having moved dorsally by ∼10 μm.

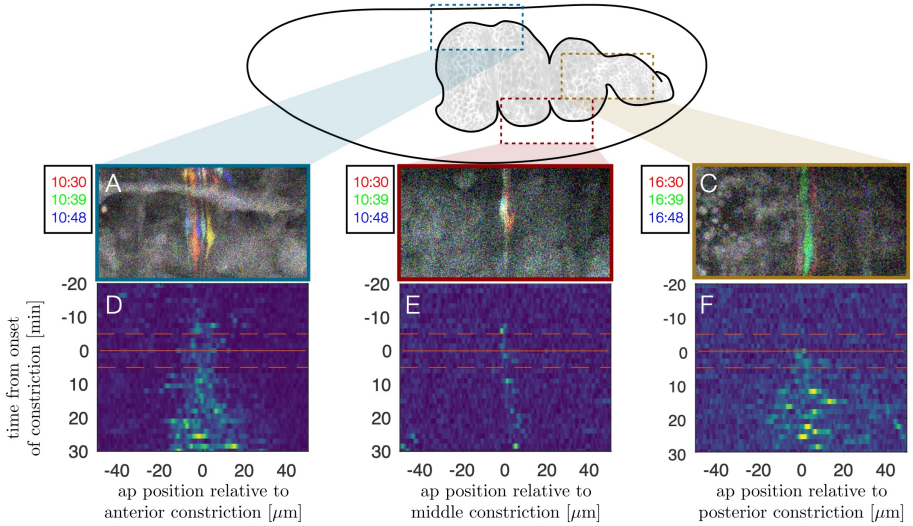

Figure E.13: **Kymographs of *GCaMP6s* dynamics show that calcium activity is initially localized in space to constrictions and begins near the time at which constrictions begin.** For each constriction, the transient signal is computed (colored signals in snapshots *A*-*C*) and averaged across the DV direction (in the lab frame) into a space-time heatmap (*D*-*F*). A time of $t = 0$ min for each panel corresponds to the time when localized constriction is visible in the bright-field channel at that constriction location and carries an uncertainty of ±5 minutes (dashed orange lines). The middle constriction (the sharpest fold, *B* and *E*) has the sharpest activity profile, and the posterior constriction (the widest fold, *C* and *F*) has the broadest activity profile.

Fig. E.13 shows kymographs of *GCaMP6s* dynamics averaged across biological repeats. In these kymographs, activity begins near the time when constrictions begin. In contrast, Fig. E.14 shows delayed and suppressed *GCaMP6s* activity in *Antp* mutants compared to the wild-type behavior of sibling embryos that are not homozygous mutants for *Antp*.

E.12 Calcium activity in *Antp* mutants

To compare calcium activity in *Antp* mutants against wild-type dynamics, we computed p values using a z-score measuring the difference between *Antp* heterozygotes

(controls) and *Antp* homozygotes (mutants) as

$$Z = \frac{\overline{\delta I}_{\text{mutant}} - \overline{\delta I}_{\text{control}}}{\sqrt{s^2_{\text{control}}/n_{\text{control}} + s^2_{\text{mutant}}/n_{\text{mutant}}}}, \tag{E.6}$$

where $\overline{\delta I}$ is the sample mean, s_{control} and s_{mutant} are the sample standard deviations, and n_{control} and n_{mutant} are the sample sizes. This score gives a single-sided p value via

$$p = \frac{1}{2}\text{erfc}\left(-Z/\sqrt{2}\right), \tag{E.7}$$

where erfc is the complementary error function.

To quantify the difference in overall activity between mutants and heterozygotes, we first estimate the expected fluorescent intensity for a given embryo under the null hypothesis that all embryos, whether mutant or not, will have similar *GCaMP6s* activity. Since embryos vary in opacity, we normalized each heterozygous embryo according to a value dependent on its background fluorescent intensity measured in regions within the embryo but far (45-50 μm) from the site of the putative constriction. The observed maximum fluorescent activity δI correlated with this background signal with a correlation coefficient of 78% and a mean signal-to-background ratio of 5.1$\pm$0.5. We then normalized each embryo's time-averaged $\delta I = \delta I(x)$ as

$$\delta I \to \frac{\delta I - \delta I_{\text{bg}}}{\delta I_{\text{max}} - \delta I_{\text{bg}}}. \tag{E.8}$$

This enabled us to reduce the confounding influence of variation in optical density between embryos in the mutant analysis and compare absolute curves δI rather than only their variation along the anterior-posterior axis.

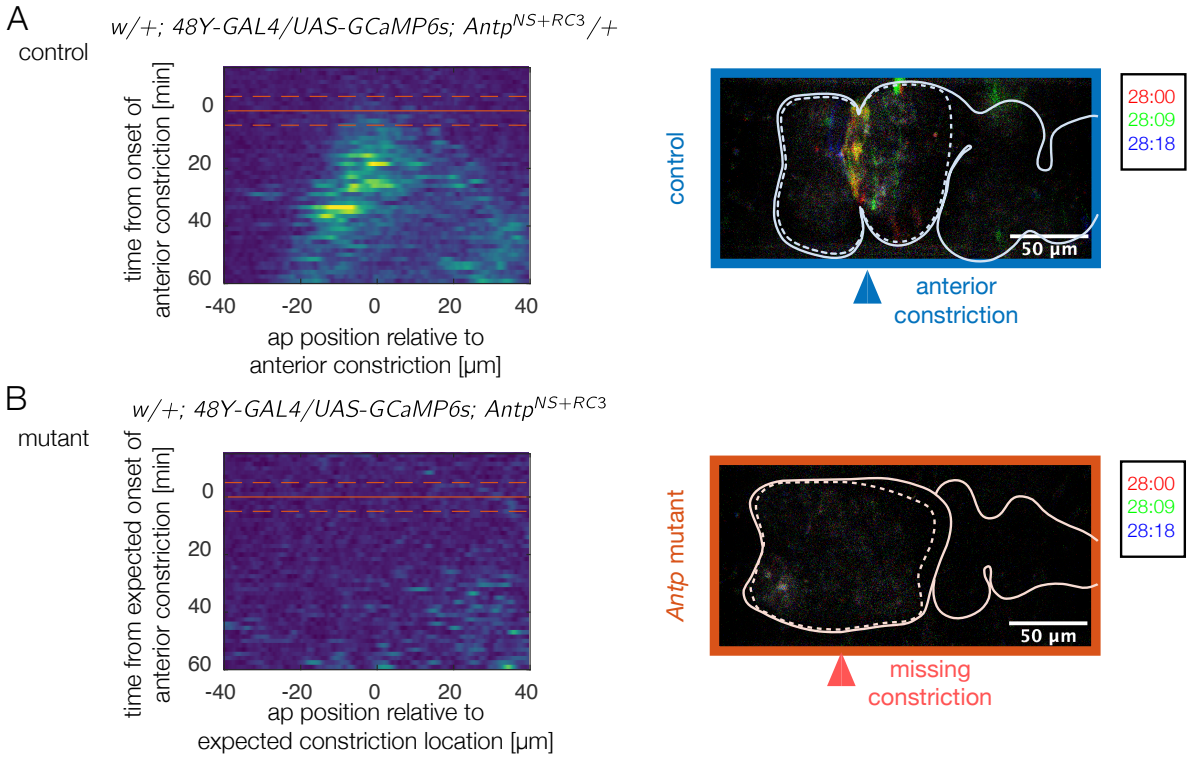

Figure E.14: ***Antp* mutants show reduced calcium activity in the anterior two chambers for over an hour.** (A) Kymographs of wild-type calcium dynamics near the anterior fold for $N = 13$ control embryos show fluctuating calcium activity beginning at the onset of folding at the site of the fold. The domain of calcium activity broadens anteriorly and posteriorly in time. A red solid line marks the onset of the anterior constriction, and dashed lines denote the precision with which this time is known. (B) In mutants, almost no calcium pulses are observed during the same timespan. A kymograph of average fluctuating *GCaMP6s* intensity for $N = 5$ *Antp* mutants remains quiescent (dark blue). Given that the anterior fold does not form, $t = 0$ was prescribed based on the depth of the posterior fold. The expected position of the anterior fold (which defines the horizontal axis of the kymograph) is inferred from the position of the anterior fold relative to the anterior face of the midgut in control embryos.

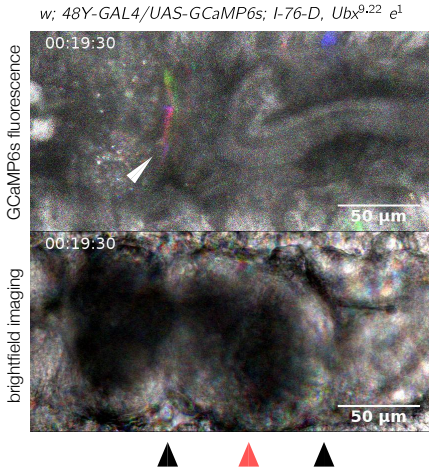

Figure E.15: **Calcium pulses appear at the unaffected anterior constriction in *Ubx* mutants.** A dorsal view snapshot of pulsing calcium activity (top panel) and the associated brightfield image (bottom panel) of a *Ubx* mutant shows calcium pulses in the anterior constriction (white arrowhead). Each image is an overlay of maximum intensity projections for three shallow confocal stacks taken 10 seconds apart and false-colored red, green, and blue for each respective stack. The colorful streak near the anterior constriction reflects the transient pulses at that location. As in Fig. 4.6F and Fig. E.14, the posterior constriction lies outside the confocal stack and is therefore not visible in the *GCaMP6s* channel. This data suggest the calcium dynamics at each constriction are regulated locally along the length of the midgut ($N = 5$).

E.13 MLCK RNAi and SERCA mutant analysis

To drive expression of MLCK RNAi or a dominant negative allele of *SERCA*, we administered heat shock by abruptly raising the temperature to 37°C using a stage-top incuabator (Okolab) and observing embryos staged such that they had not yet completed gut closure. The standard errors in the probabilities of successful constrictions are given by

$$SE = \sqrt{\frac{\hat{p}\,(1-\hat{p})}{N}}, \tag{E.9}$$

where $\hat{p}$ is the observed frequency of forming all three constrictions and N is the number of samples of a given genotype (for ex, *Mef2-GAL4* $\times$ *UAS-SERCA.R751Q::mtomato*) measured in the experimental heat shock conditions. We note that the result is not sensitive to the choice of analysis. For example, we also computed the mean number of folds formed – that is, the number of deep constrictions – for each condition and compare the two distributions, as shown in Fig. E.16A and B. The mean number of folds formed was reduced in both *Mef2-GAL4* $\times$ *UAS-SERCA.R751Q* embryos and *tub67-GAL4; tub16-GAL4* $\times$ *UAS-MLCK RNAi* embryos ($p = 3 \times 10^{-8}$ and $p = 0.002$, respectively).

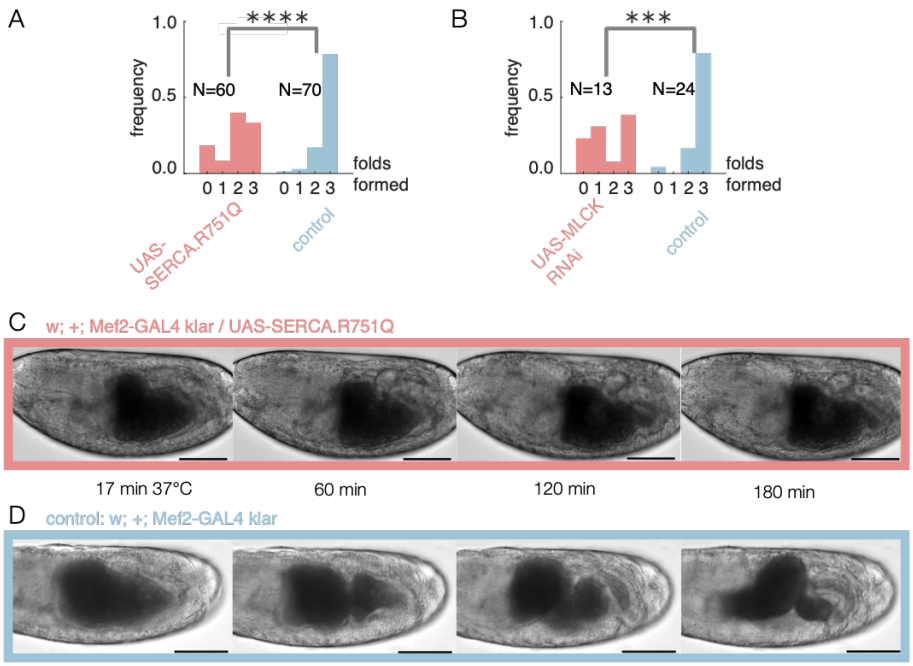

Figure E.16: **Disrupting calcium activity hinders constrictions.** (A) Embryos expressing a dominant negative form of SERCA have fewer successful constrictions on average (single tailed Z-test, $N = 130$, $p = 3 \times 10^{-8}$) using a muscle-specific driver, *Mef2-GAL4*, at elevated temperatures (continuous heatshock at 37°C). In adult flies, this dominant negative SERCA was previously shown to exhibit temperature-sensitive expression and inhibits muscle contractions at 37°C [116]. (B) Embryos expressing RNAi against MLCK have fewer successful folds on average (single tailed Z-test, $N = 37$, $p = 0.002$). Here we use a ubiquitous driver, *tub15-GAL4; tub67-GAL4* under continuous heatshock starting during or just after midgut closure, before constrictions appear. (C) Brightfield imaging of embryos expressing a mutant form of *SERCA* in muscles show reduced folding activity. Here, driving a mutant *SERCA* expression via heatshock starting at stage 15a shows no folds. (D) Control embryos without the mutant form of *SERCA*, in contrast, typically form three folds. Timestamps denote minutes since the onset of heatshock and scalebar is 100 μm.

Appendix F

Numerical methods for optimal growth pattern selection

F.1 Embedding intrinsic geometries in 3D

Consider a surface $S_t \subset \mathbb{R}^3$ parameterized in the usual way by a set of coordinates $\vec{\mathbf{x}} \in \mathbb{R}^2$. At each point $\vec{\mathbf{R}} \in S_t$, The geometry of the surface is captured by the first fundamental form, $g_{\alpha\beta} = \partial_\alpha \vec{\mathbf{R}} \cdot \partial_\beta \vec{\mathbf{R}}$, and the second fundamental form, $b_{\alpha\beta} = \partial_\alpha \partial_\beta \vec{\mathbf{R}} \cdot \hat{\mathbf{n}}$, where $\hat{\mathbf{n}}$ is the unit normal to the surface at $\vec{\mathbf{R}}$. We characterize the time-dependent intrinsic geometry of the surface in terms the target metric, $\overline{\mathbf{g}}(t)$, and the target curvature tensor, $\overline{\mathbf{b}}(t)$. We define the inverse target metric tensor by $\bar{g}^{\alpha\beta}$ by $\bar{g}^{\alpha\sigma}\bar{g}_{\sigma\beta} = \delta^\alpha_\beta$, so that indices of tensorial quantities are raised and lowered with respect to the target metric.

We utilize a method motivated by continuum mechanics to embed the target geometry

in $\mathbb{R}^3$. We assume that the tissue is an incompatible elastic shell with energy

$$\begin{aligned} E &= E_S + E_B \\ &= \frac{Y}{2(1-\nu^2)} \int d\vec{\mathbf{x}}^2 \sqrt{\bar{g}} \left\{ \frac{h}{4} \left[\nu \operatorname{Tr}[\bar{\mathbf{g}}^{-1}(\mathbf{g}-\bar{\mathbf{g}})]^2 + (1-\nu) \operatorname{Tr}[(\bar{\mathbf{g}}^{-1}(\mathbf{g}-\bar{\mathbf{g}}))^2] \right] \right. \\ &\qquad \left. + \frac{h^3}{12} \left[\nu \operatorname{Tr}[\bar{\mathbf{g}}^{-1}(\mathbf{b}-\overline{\mathbf{b}})]^2 + (1-\nu) \operatorname{Tr}[(\bar{\mathbf{g}}^{-1}(\mathbf{b}-\overline{\mathbf{b}}))^2] \right] \right\}, \end{aligned} \tag{F.1}$$

where h is the thickness of the tissue, Y is Young's modulus, and ν is the Poisson ratio. This mechanical energy has been studied both in the context of morphogenesis and the design and manipulation of synthetic surface structures [223, 71]. The stretching energy $E_S \propto h$ describes the mismatch between the target rest lengths and angles of the surface and the physical rest lengths and angles. Analogously, the bending energy $E_B \propto h^3$ describes the mismatch between the target and physical curvatures. Essentially, the system will adopt an equilibrium configuration that balances the comptition between stretching and the bending. Importantly, it is not assumed that $\bar{g}$ and $\bar{b}$ satisfy the Gauss-Codazzi-Mainardi-Peterson compatibility conditions [78]. If this is the case, then there is no attainable 3D configuration for which the energy vanishes identically. In this situation, the equilibrium configuration will harbor residual stresses.

Equilibrium configurations of this energy are computed using a geometric finite difference method. The 3D surface is approximated by a mesh triangulation. In order to maintain a fixed mesh topology, we choose to order the vertices describing each face in a counter-clockwise fashion, i.e. $F = [\vec{\mathbf{x}}_i, \vec{\mathbf{x}}_j, \vec{\mathbf{x}}_k]$ where a vertex $\vec{\mathbf{x}}_i \in \mathbb{R}^3$. The edges of the face are labelled by the vertex index opposite to that edge. The normal vector of the face, is simply given by $\vec{\mathbf{n}} = \vec{\mathbf{e}}_i \times \vec{\mathbf{e}}_j = \vec{\mathbf{e}}_j \times \vec{\mathbf{e}}_k = \vec{\mathbf{e}}_k \times \vec{\mathbf{e}}_i$. The unit normal vector is therefore $\hat{\mathbf{n}} = \vec{\mathbf{n}}/2A$ where A is the area of the face. For simplicity, we define the three in-plane mid-edge normals, $\vec{\mathbf{t}}_i$, $\vec{\mathbf{t}}_j$, and $\vec{\mathbf{t}}_k$, which are simply the corresponding edge vectors rotated by $\pi/2$ radians, i.e. $\vec{\mathbf{t}}_i = \vec{\mathbf{e}}_i \times \hat{\mathbf{n}}$. This construction is illustrated in Fig. F.1.

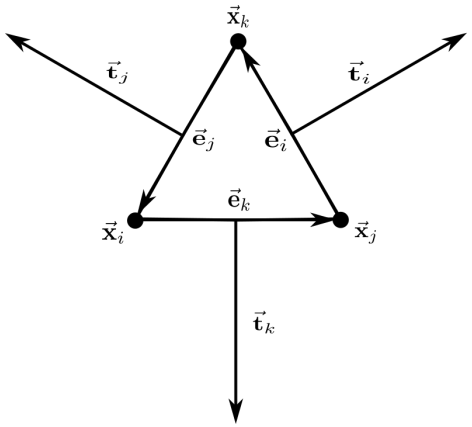

Figure F.1: Notation for triangle vectors.

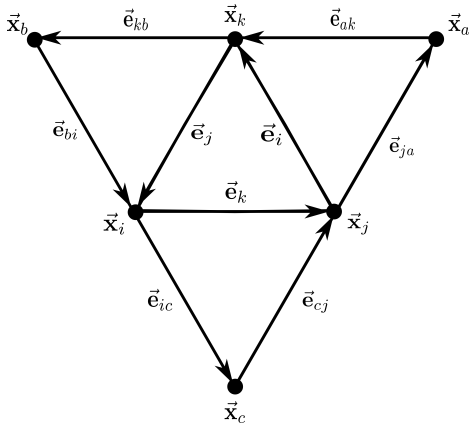

Figure F.2: The 'face-with-flaps' stencil over which the energy is evaluated.

Since the total elastic energy of the surface is calculated by evaluating an integral, we must choose a stencil of finite area to serve as the discrete analog of the integral measure. For, this purpose we choose a 'face-with-flaps' stencil. The structure and nomenclature associated with this stencil is shown in Fig. F.2. The extra flaps are included in order to evaluate the bending energy. Here, the bending energy is evaluated at the shared edges of the triangulation, i.e. along the triangulation hinges. The structure of a single hinge is shown in Fig. F.3 and Fig. F.4. Notice that θ denotes the *bending* or *hinge* angle between the unit normal vectors of adjacent faces. The dihedral angle of the edge is therefore $\pi - \theta$. In general, θ is a *signed* quantity which depends on edge orientation. The sign of θ for a given edge orientation is chosen arbitrarily, but consistently, to be the same as the sign of $(\hat{\mathbf{n}}_1 \times \hat{\mathbf{n}}_2) \cdot \vec{\mathbf{e}}_0$, where $\hat{\mathbf{n}}_1$ is the unit normal of the current face, $\hat{\mathbf{n}}_2$ is the unit normal of the adjacent face flap, and $\vec{\mathbf{e}}_0$ is the associated edge with orientation defined counter-clockwise relative to $\hat{\mathbf{n}}_1$. In this way, θ is positive when the normals point away from each other and negative when they point towards each other.

Our goal is to build a discrete formulation of the energy in Eq (F.1). The target geometry of the system can be represented by a set of target edge lengths and bending angles. The target edge lengths must satisfy the triangle inequality on each face in

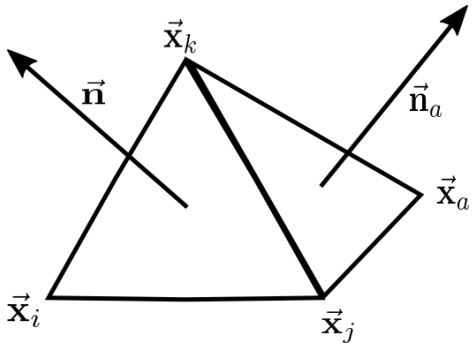

Figure F.3: A single hinge viewed from above.

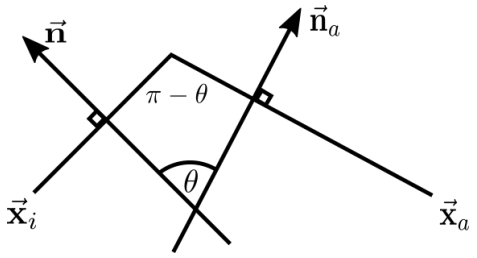

Figure F.4: The notation describing the bending angle of a single hinge.

order to constitue a valid geometry. In the discrete setting, the tensors $\mathbf{g}$ and $\mathbf{b}$ are approximated by piecewise constant symmetric 2×2 matrices defined on mesh faces. The components of any such matrix defined over a subset of $\mathbb{R}^2$ can be uniquely determined by the its action on three linearly independent vectors in the plane. Analogously to its function in the continuous setting, the discrete metric tensor on a face is the unique matrix that returns $\vec{\mathbf{e}}_i^T\,\mathbf{g}\,\vec{\mathbf{e}}_i = \ell_i^2$ for each edge $\vec{\mathbf{e}}_\mathbf{i}$ in the face with length ℓ_i. Similarly, the discrete curvature tensor should encode the bending angles on each edge. In terms of these representations, we define the discrete strain tensor

$$\begin{aligned}
\boldsymbol{\varepsilon} &= \bar{\mathbf{a}}^{-1}\left(\mathbf{a}-\bar{\mathbf{a}}\right) \\
&= -\frac{1}{8\bar{A}^2}\sum_{(ijk)}\left[\ell_i^2-\ell_j^2-\ell_k^2-\left(L_i^2-L_j^2-L_k^2\right)\right]\,\vec{\underline{\mathbf{t}}}_i\otimes\vec{\underline{\mathbf{t}}}_i \\
&= -\frac{1}{8\bar{A}^2}\sum_{(ijk)}\left[\varepsilon(\ell_i,L_i)-\varepsilon(\ell_j,L_j)-\varepsilon(\ell_k,L_k)\right]\vec{\underline{\mathbf{t}}}_i\otimes\vec{\underline{\mathbf{t}}}_i \\
&= -\frac{1}{8\bar{A}^2}\sum_{(ijk)}E_i\,\vec{\underline{\mathbf{t}}}_i\otimes\vec{\underline{\mathbf{t}}}_i
\end{aligned} \tag{F.2}$$

Here, ℓ_i is the length of edge i in the physical triangulation, L_i is the target length of that edge, $\bar{A}$ is the target area of the face and $\vec{\underline{\mathbf{t}}}$ is the in-plane mid-edge normal of the *target* geometry. The $\bar{A}$ may be calculated directly from the L_i without reference to an explicit

embedding of the target geometry. It may seem counter-intuitive to define this quantity in terms of the $\vec{\underline{\mathbf{t}}}_i$, since we do not have access to these target quantities directly. We will see that the final energy is formulated in way that can be calculated without an explicit embedding, just like the $\bar{A}$. The tensor product of two vectors $\vec{\mathbf{u}}$ and $\vec{\mathbf{v}}$ is computed in a matrix representation as $\vec{\mathbf{u}}_i \otimes \vec{\mathbf{v}}_i = \vec{\mathbf{u}}_i \, \vec{\mathbf{v}}_i^T$. The notation (ijk) implies a cyclic sum over the edges. We also define the function $\varepsilon(\ell_m, L_m) \equiv \ell_m^2 - L_m^2$. Here, E_i is a temporary shorthand we use to denote the cyclic sum $\varepsilon_i - \varepsilon_j - \varepsilon_k$. The discrete bending moment is

$$\begin{aligned}
\mathbf{B} &= \bar{\mathbf{a}}^{-1} \left(\mathbf{b} - \bar{\mathbf{b}} \right) \\
&= \sum_{(ijk)} \frac{1}{2\bar{A} L_i} \left[\underbrace{2 \tan(\frac{\theta_i}{2})}_{\varphi(\theta_i)} - \underbrace{2 \tan(\frac{\Theta_i}{2})}_{\varphi(\Theta_i)} \right] \vec{\underline{\mathbf{t}}}_i \otimes \vec{\underline{\mathbf{t}}}_i \\
&= \sum_{(ijk)} \frac{\Phi(\theta_i, \Theta_i)}{2\bar{A} L_i} \, \vec{\underline{\mathbf{t}}}_i \otimes \vec{\underline{\mathbf{t}}}_i
\end{aligned} \tag{F.3}$$

where Θ_i is the target bending angle for that edge and $\Phi(\theta_i) \equiv \varphi(\theta_i) - \varphi(\Theta_i)$.

Direct calculation shows that for any symmetric quadratic form $\mathbf{Q}$ defined on on a face (i.e. a section of $\mathbb{R}^2$) with the following form

$$\begin{aligned}
\mathbf{Q} &= \sum_{(ijk)} Q_i \, \vec{\underline{\mathbf{t}}}_i \otimes \vec{\underline{\mathbf{t}}}_i \\
&\implies \mathrm{Tr}[\mathbf{Q}] = \sum_i Q_i L^2 \\
&\implies \mathrm{Tr}[\mathbf{Q}^2] = \sum_i \sum_j Q_i Q_j (\vec{\underline{\mathbf{e}}}_i \cdot \vec{\underline{\mathbf{e}}}_j)^2
\end{aligned} \tag{F.4}$$

Putting all of this together, the (re-scaled) discrete elastic energy of a Non-Euclidean

shell is given by

$$\tilde{E} = E/h = \frac{1}{2}\sum_T \bar{A}_T \left\{ \frac{1}{4} \left[\nu \left(\sum_i \frac{-E_i}{8\bar{A}_T^2} L_i^2 \right)^2 + (1-\nu) \left(\sum_i \sum_j \frac{E_i\, E_j}{64\bar{A}_T^4} (\vec{\underline{\mathbf{e}}}_i \cdot \vec{\underline{\mathbf{e}}}_j)^2 \right) \right] \right.$$
$$\left. + \frac{h^2}{12} \left[\nu \left(\sum_i \frac{\Phi(\theta_i, \Theta_i) L_i}{2\bar{A}_T} \right)^2 + (1-\nu) \left(\sum_i \sum_j \frac{\Phi(\theta_i, \Theta_i)\, \Phi(\theta_j, \Theta_j)}{4\bar{A}_T^2 L_i L_j} (\vec{\underline{\mathbf{e}}}_i \cdot \vec{\underline{\mathbf{e}}}_j)^2 \right) \right] \right\} \tag{F.5}$$

where the sum is over the faces T of the triangulation and we have set $Y = 1 - \nu^2$ (Y is irrelevant to the computation of the equilibrium configuration since it simply rescales the energy). We minimuze this energy using a a custom build quasi-Newton method using an L-BFGS Hessian approximation [176].

Strictly speaking, the Bonnet theorem tells us necessary to specify both $\bar{\mathbf{g}}(t)$ and $\overline{\mathbf{b}}(t)$ to uniquely specify the surface up to a rigid motion [78]. For small h, howver, the bending energy is small relative to the stretching energy, i.e. $E_B << E_S$. In this regime, the system's tendency to match $\mathbf{g}(t)$ and $\bar{\mathbf{g}}(t)$ will overwhelm it's tendency to minimize the bending energy. The optimization of Eq. F.1 essentially becomes a machinery for producing isometric embeddings of the target metric $\bar{\mathbf{g}}(t)$ with E_B playing the role of a regularizer.

This machinery for computing the embeddings of an instantaneous target geometry can also be used to generate embeddings of entire time courses of growth patterns. When the timescale of growth in the system (i.e. rate of cell division, etc.) is long compared to the timescale of mechanical relaxation, the tissue will always effectively remain in mechanical equilibrium. In this quasistatic regime, the physical configuration will always be a minimizer of the energy Eq. (F.1) given an instantaneous target geometry. Over a short time Δt, the target geometry will change, i.e $\bar{\mathbf{g}}(t) \to \bar{\mathbf{g}}(t+\Delta t)$ and $\overline{\mathbf{b}}(t) \to \overline{\mathbf{b}}(t+\Delta t)$. At each new time step, we minimize the new elastic energy using the previous time point's

configuration as an initial guess. The result is a full time course of growth embedding the various target geometries.

F.2 Non-Parametric Representations of Discrete Surfaces as Smooth Interpolants

Computing the optimal growth pattern for a given input requires searching the space of parameterizations of the final target shape. We must therefore be able to evaluate surface configurations corresponding to arbitrary parameterizations. In order to do so, we store the final surface as a smooth interpolant over the unit disk $\mathbb{D}$ rather than as a fixed triangulation. In particular, utilize natural neighbor interpolation for scattered data points [227, 76]. We will now explain this formalism in its general form and then show how it is applied for the specific case of evaluating surface configurations.

Let $\mathcal{P} = \{\mathbf{p_1}, \ldots, \mathbf{p_n}\}$ be a set of n points in $\mathbb{R}^2$ and let $\vec{\mathbf{\Phi}}$ be a vector-valued function defined on the convex hull of $\mathcal{P}$. We assume that the function values are known at the points of $\mathcal{P}$. In the context of surface evaluation, these are simply the 3D locations od the data points, i.e. $\vec{\mathbf{R}}_i = \vec{\mathbf{\Phi}}(\mathbf{p}_i)$. The point set $\mathcal{P}$ defines a Voronoi tesselation of $\mathbb{R}^2$, Equivalently, there is a unique Delaunay triangulation associated to this point set. We also require knowledge of the gradient at each point $\mathbf{G}_i = \nabla\vec{\mathbf{\Phi}}(\mathbf{p}_i)$. If the user has analytic knowledge of the function $\vec{\mathbf{\Phi}}$ these gradients can be supplied as inputs. Otherwise, they are estimated by fitting high order Taylor polynomials to local neighboords of data poitns and extracting the first-order coefficients. Experiments show that fitting a 3rd order Taylor polynomial produces high quality results without being too computationally expensive.

The interpolation is carried out for an arbitrary query point $\mathbf{q}$ on the convex hull

of $\mathcal{P}$. When simulating the insertion of the query point $\mathbf{q}$ into the Voronoi diagram of $\mathcal{P}$ the virtual Voronoi cell of $\mathbf{q}$ "steals" some area from the existing existing cells. This construction is illustrated in Figure F.5. Let $A(\mathbf{q})$ denote the area of the virtual Voronoi

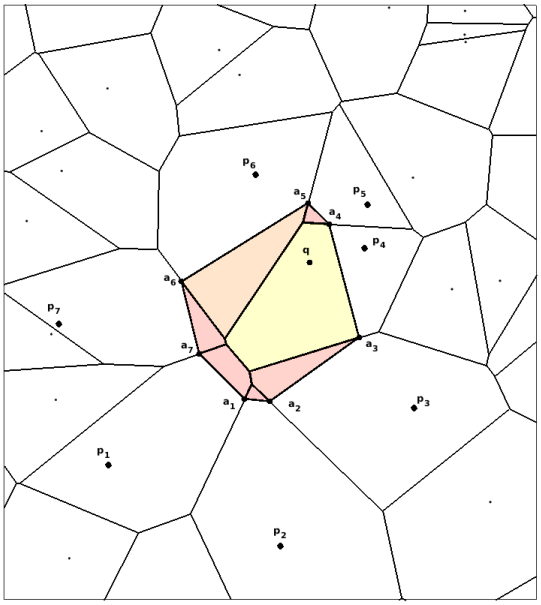

Figure F.5: Natural neighbor coordinate construction.

cell of $\mathbf{q}$ and let $A_i(\mathbf{q})$ denote the area of the sub-cell that would be stolen from the cell of $\mathbf{p}_i$ by the cell of $\mathbf{q}$. The natural neighbor coordinates of $\mathbf{q}$ with respect to the data point $\mathbf{p_i} \in \mathcal{P}$ are defined to be

$$\lambda_i(\mathbf{q}) = \frac{A_i(\mathbf{q})}{A(\mathbf{q})}. \tag{F.6}$$

These coordinates have the following properties

- $\mathbf{q} = \sum_{i=1}^{n} \lambda_i(\mathbf{q})\, \mathbf{p}_i$ (barycentric coordinate property)
- For any $i, j \leq n$, $\lambda_i(\mathbf{p}_j) = \delta_{ij}$
- $\sum_{i=1}^{n} \lambda_i(\mathbf{q}) = 1$ (partition of unity property)

Furthermore, the natural neighbor coordinates depend continuously on the planar coordinates of $\mathbf{q} = (q^x, q^y)$. In fact, one can calculate the gradient of the "stolen" sub-cell area $A_i(\mathbf{q})$ with respect to the components of $\mathbf{q}$. Let the m natural neighbors of $\mathbf{q}$ be denoted $\{\mathbf{p}_1, \ldots, \mathbf{p_m}\}$ and be arranged in counter-clockwise order around $\mathbf{q}$ (this numbering is for convenience in the calculation of local quantities with respect to $\mathbf{q}$ and does not have to match the global numbering scheme used in $\mathcal{P}$). Additionally let the set $\{\mathbf{a}_1, \ldots, \mathbf{a}_m\}$ refer to the counter-clockwise ordered vertices of the virtual Voronoi cell of $\mathbf{q}$. It can be shown that

$$\nabla A_k(\mathbf{q}) = \frac{f_k}{d_k}\left(\frac{\mathbf{a}_k + \mathbf{a}_{k+1}}{2} - \mathbf{q}\right) = \frac{f_k}{d_k}\left(\frac{\vec{\mathbf{v}}_k + \vec{\mathbf{v}}_{k+1}}{2}\right) \tag{F.7}$$

where $f_k = ||\mathbf{a}_{k+1} - \mathbf{a}_k||$, $d_k = ||\mathbf{p}_k - \mathbf{q}||$, and $\vec{\mathbf{v}}_k = \mathbf{a}_k - \mathbf{q}$. The gradient of $\lambda_i(\mathbf{q})$ follows trivially from application of the chain rule and the fact that $A(\mathbf{q}) = \sum_k A_k(\mathbf{q})$.

Having calculated the natural neighbor coordinates of $\mathbf{q}$, we can infer the function value $\vec{\mathbf{\Phi}}(\mathbf{q})$ via interpolation with respect to these coordinates. In particular, we choose to use Sibson's C^1 interpolant [227]. Let

$$\vec{\mathbf{Z}}^0(\mathbf{q}) = \sum_i \lambda_i(\mathbf{q})\, \vec{\mathbf{\Phi}}(\mathbf{p}_i) \tag{F.8}$$

denote the linear combination of the neighbors function values weighted by the natural neighbor coordinates. Furthermore, we define the functions

$$\vec{\boldsymbol{\xi}}_i(\mathbf{q}) = \vec{\mathbf{\Phi}}(\mathbf{p}_i) + \mathbf{G}_i^T(\mathbf{q} - \mathbf{p}_i), \qquad \vec{\boldsymbol{\xi}}(\mathbf{q}) = \frac{\sum_i \frac{\lambda_i(\mathbf{q})}{||\mathbf{q}-\mathbf{p}_i||}\vec{\xi}_i(\mathbf{q})}{\frac{\lambda_i(\mathbf{q})}{||\mathbf{q}-\mathbf{p}_i||}}, \tag{F.9}$$

$$\alpha(\mathbf{q}) = \frac{\sum_i \lambda_i(\mathbf{q})\, ||\mathbf{q} - \mathbf{p}_i||}{\frac{\lambda_i(\mathbf{q})}{||\mathbf{q}-\mathbf{p}_i||}}, \tag{F.10}$$

and

$$\beta(\mathbf{q}) = \sum_i \lambda_i(\mathbf{q}) \, ||\mathbf{q} - \mathbf{p}_i||^2. \tag{F.11}$$

In terms of these quantities, the interpolant is defined to be

$$\vec{\mathbf{Z}}^1(\mathbf{q}) = \frac{\alpha(\mathbf{q}) \, \vec{\mathbf{Z}}^0(\mathbf{q}) + \beta(\mathbf{q}) \, \vec{\boldsymbol{\xi}}(\mathbf{q})}{\alpha(\mathbf{q}) + \beta(\mathbf{q})} \tag{F.12}$$

Sibson noticed that this interpolant is C^1 continuous with respect to the coordinates of the query point $\mathbf{q}$. This means that we can calculate analytic gradients of $\vec{\mathbf{Z}}^1(\mathbf{q})$ with respect to $\mathbf{q}$ (making use of the gradient in Equation (F.7) in a series of chain rule calculations). This property makes $\vec{\mathbf{Z}}^1$ a suitable for use in gradient based optimization procedures.

The application of natural neighbor interpolation to storing surfaces is straight forward. We provide as input a set of points with defining a surface $\{V, U\}$. Here V are the 3D coordinates of the points and $U \in \mathbb{D}$ are the 2D coordinates. Note that we do not need to supply a face connectivity list F - any association between the points will be through the Delaunay triangulation of U in $\mathbb{R}^2$.We can now evaluate updated surface triangulations for *any* updated parameterization U'. This is shown in Figure F.6.

F.3 Discretization of the Beltrami holopmorphic flow

In this section, we explain our numerical computation of the variation in a quasiconformal map $w : \mathbb{D} \to \mathbb{D}$ under the variation of its associated Beltrami coefficient μ. This implementation is based on the one formulated in [151]. Consider a triangulation of the unit disk defined by a face connectivity list F and a set of vertex coordinates V, where $\vec{\mathbf{x}}_i \in \mathbb{D}$ denotes the coordinates of the ith vertex. Let $\vec{\mathbf{w}}_i = (u^1, u^2) \in \mathbb{D}$ denote the updated coordinates of the ith vertex as the result of a quasiconformal mapping.

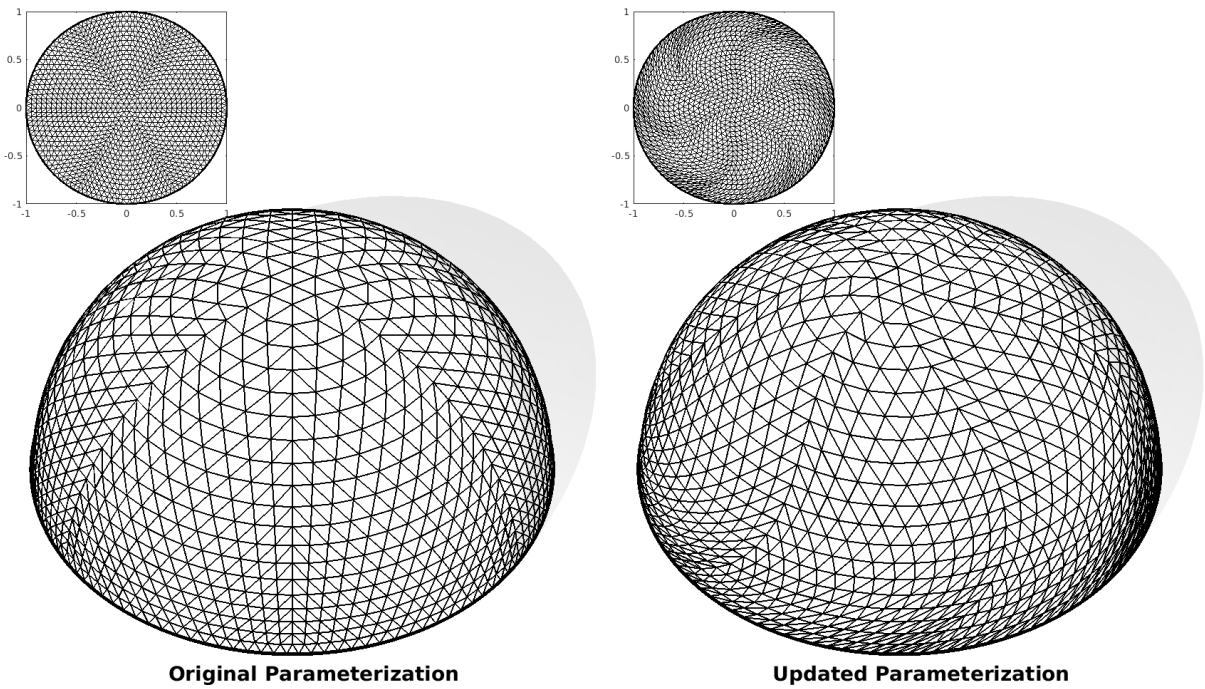

Figure F.6: Evaluation of surfaces via natural neighbor interpolation for different 2D parameterizations

Computation of the Beltrami coefficient

In the continuous setting, the map $w : \mathbb{D} \to \mathbb{D}$ has an associated Beltrami coefficient

$$\mu = \frac{\partial_{\bar{z}} w}{\partial_z w}, \tag{F.13}$$

where $z = x^1 + ix^2$ and $w = u^1 + iu^2$. In the discrete setting, the map $w : \mathbb{D} \to \mathbb{D}$, i.e. updated vertex coordinates, defines a set of piecewise constant affine transforations for each triangle in the mesh. We can define a Beltrami coefficient on each face f by discretizing Eq (F.13) in terms of the finite element method (FEM) gradient [27]. For a

face $f = [\vec{\mathbf{x}}_i, \vec{\mathbf{x}}_j, \vec{\mathbf{x}}_k]$, the gradient of a quantity h defined on each vertex is given by:

$$\nabla h = \begin{pmatrix} \partial_x h \\ \partial_y h \end{pmatrix} = \frac{1}{2A_f} \left((h_j - h_i)(\vec{\mathbf{x}}_i - \vec{\mathbf{x}}_k)^{\perp} + (h_k - h_i)(\vec{\mathbf{x}}_j - \vec{\mathbf{x}}_i)^{\perp} \right), \tag{F.14}$$

where A_f is the area of face f and the symbol $\perp$ denotes a counter-clockwise rotation by 90 in the plane of the face. Geometrically, this operation converts a scalar quantity defined on mesh vertices to a tangent vector defined on each mesh face. The Beltrami cofficient on each face is therefore given by

$$\mu_f = \frac{(\partial_{x^1} u^1 - \partial_{x^2} u^2) + i(\partial_{x^1} u^2 + \partial_{x^2} u^1)}{(\partial_{x^1} u^1 + \partial_{x^2} u^2) + i(\partial_{x^1} u^2 - \partial_{x^2} u^1)}. \tag{F.15}$$

For applications where we need to define the Beltrami coefficient on vertices, we can simply average the face-based quantity in Eq (F.15)

$$\mu_v = \sum_{f \in \mathcal{N}_v} \alpha_f \, \mu_f, \tag{F.16}$$

for a set of normalized weights $\{\alpha_f\}$. Experiments show that weighting this average by the normalized internal angle adjacent to the vertex within each face produces better results than simple averaging or area-weights. For notational convenience, we defined a modified partial derivative operator D that includes this angle weighted averaging step, i.e. $D_x h$ maps scalar vertex quantites to vectors in the tangent space of each vertex. We can define the vertex-based Beltrami coefficient directly in terms of these modified operators

$$\mu_v = \frac{(D_{x^1} u^1 - D_{x^2} u^2) + i(D_{x^1} u^2 + D_{x^2} u^1)}{(D_{x^1} u^1 + D_{x^2} u^2) + i(D_{x^1} u^2 - D_{x^2} u^1)}. \tag{F.17}$$

Computation of the BHF reconstruction

For both quasiconformal map reconstruction and surface function optimization, the key step is the computation of the variation $V[w^\mu, \nu]$ of the map w^μ under the variation of μ. From Eq (5.11) and Eq (5.12), we have

$$V[w^\mu, \nu](z) = \int_{\mathbb{D}} K(z, \zeta)\, d\eta^1\, d\eta^2 \tag{F.18}$$

where

$$K(z,\zeta) = -\frac{w^\mu(z)\,(w^\mu(z)-1)}{\pi} \quad \times \\ \left(\frac{\nu(\zeta)\,(\partial_\zeta w^\mu(\zeta))^2}{w^\mu(\zeta)\,(w^\mu(\zeta)-1)\,(w^\mu(\zeta)-w^\mu(z))} + \frac{\overline{\nu(\zeta)}\,\overline{(\partial_\zeta w^\mu(\zeta))}^2}{\overline{w^\mu(\zeta)}\left(1-\overline{w^\mu(\zeta)}\right)\left(1-\overline{w^\mu(\zeta)}\,w^\mu(z)\right)} \right). \tag{F.19}$$

The quantities w^μ and ν are defined on each vertex v. The derivative $\partial_z w^\mu$ can be approximated as

$$(\partial_z w^\mu)_v \approx \frac{(D_{x^1}u^1 + D_{x^2}u^2) + i(D_{x^1}u^2 - D_{x^2}u^1)}{2}. \tag{F.20}$$

For each pair of vertices (v_j, v_k), the kernel $K(v_j, v_k)$ can be assembled in terms of these quantities. When $K(v_j, v_k)$ is singular, we set $K(v_j, v_k) = 0$. Let A_v denote the barycentric area of each vertex, i.e.

$$A_v = \frac{1}{3} \sum_{f \in \mathcal{N}_v} A_f. \tag{F.21}$$

Then, $V[w^\mu, \nu]$ is can be approximated by

$$V[w^\mu, \nu](v_k) = \sum_{v_j} K(v_j, v_k)\, A_{v_j}. \tag{F.22}$$

It is frequently more convenient for computational implementations to re-express $V[w^\mu, \nu](z)$ in the following way

$$V[w^\mu, \nu](z) = \int_{\mathbb{D}} \begin{pmatrix} G_1\nu_1 + G_2\nu_2 \\ G_3\nu_1 + G_4\nu_2 \end{pmatrix} d\eta^1\, d\eta^2, \tag{F.23}$$

where G_1, G_2, G_3, and G_4 are real valued functions that can be derived from the form of $K(z, \zeta)$ and can be discretized in the obvious way in terms of w^μ and ν.

F.4 Evaluation and minimization of the optimal growth energy

From Eq (5.26), the optimal growth energy for constant growth patterns with $\dot{\Gamma} = \ddot{\mu} = 0$ is defined to be

$$\tilde{\mathcal{E}} = \int_{\mathbb{D}} d^2\vec{\mathbf{x}}\, \sqrt{g_0}\ \left[c_1||\nabla\Gamma||^2 + c_2|\nabla\dot{\mu}|^2\right], \tag{F.24}$$

where we have modified the energy so that the area element $\sqrt{g_0}$ is defined in terms of the area at the initial time $t = 0$. This modification greatly simplifies the calculation of the energy gradients and has the physical interpretation that contributions to the energy should be weighted by the initial clonal area rather than the clonal area at the final time. We use ∇ to denote the gradient of a quantity with respect to the fixed Lagrangian coordinates $\vec{\mathbf{x}}$.

The input to our numerical optimization method requires a mesh triangulation with an initial set of 3D vertex coordinates $\vec{\mathbf{X}}_0$, an initial set of 2D vertex coordinates defining the Lagrangian parameterization $\vec{\mathbf{x}}_0$, and a set of 3D vertex coordinates $\vec{\mathbf{X}}_T^{(0)}$ which will

be converted to a non-parametric representation of the final shape using natural neighbor interpolation. Let $A_f^{(0)}$ denote the 3D area of face f in the initial configuration and let A_f denote the 3D area of face f in the final configuration at time $t = T$. The growth rate Γ can be approximated on each face through

$$A_f = A_f^{(0)} \, e^{\Gamma_f \, T} \implies \Gamma_f = \frac{1}{T} \log \left[\frac{A_f}{A_f^{(0)}} \right], \tag{F.25}$$

and then mapped to values on vertices via the same angle-weighted averaging procedure described in the previous section for face-based Beltrami coefficients. The optimal growth energy can therefore be approximated as

$$\tilde{\mathcal{E}} = \sum_{f \in F} A_f^{(0)} \left(c_1 \left|\left| \frac{A_f^{(0)}}{A_f} \left(\nabla \frac{A}{A^{(0)}} \right)_f \right|\right|^2 + c_2 |(\nabla \mu)_f|^2 \right), \tag{F.26}$$

where we have exploited the fact that $\mu(T) = T\dot{\mu}$ for constant growth patterns with conformal initial conditions to replace write the energy in terms of μ and we have absorbed factors of $1/T$ into the constants c_1 and c_2. This energy can now be minimized using gradient descent methods over the space of vertex based Beltrami coefficients μ_v. The gradients of the 3D configuration vertices with respect to the 2D mapping w^μ are calculated according to our natural neighbor interpolation scheme and the gradient of the 2D mapping with respect to the Beltrami coefficients are computed according to the BHF prescription. The full gradients of the energy with respect to the μ_v are computed via the chain rule in terms of these quantities.

Bibliography

[1] L V Ahlfors. *Lectures on Quasiconformal Mappings*. University lecture series. American Mathematical Society, 2006.

[2] Noam Aigerman and Yaron Lipman. Orbifold Tutte embeddings. *ACM Transactions on Graphics*, 34(6):1–12, nov 2015.

[3] Sami C. Al-Izzi and Richard G. Morris. Active flows and deformable surfaces in development, mar 2021.

[4] Karen Alim, Shahaf Armon, Boris I. Shraiman, and Arezki Boudaoud. Leaf growth is conformal. *Physical Biology*, 13(5):05LT01, sep 2016.

[5] Joshua A. Anderson, James Antonaglia, Jaime A. Millan, Michael Engel, and Sharon C. Glotzer. Shape and symmetry determine two-dimensional melting transitions of hard regular polygons. *Physical Review X*, 7(2), apr 2017.

[6] Marino Arroyo and Antonio DeSimone. Relaxation dynamics of fluid membranes. *Physical Review E*, 79(3):031915, mar 2009.

[7] Kari Astala, Tadeusz. Iwaniec, and Gaven. Martin. *Elliptic partial differential equations and quasiconformal mappings in the plane*. Princeton University Press, Princeton, 2009.

[8] Ken Bagchi, Hans C Andersen, and William Swope. Computer Simulation Study of the Melting Transition in Two Dimensions. *Physical Review Letters*, 76(2):255–258, jan 1996.

[9] J. Bakkers. Zebrafish as a model to study cardiac development and human cardiac disease. *Cardiovasc Res*, 91(2):279–88, 2011.

[10] Yohai Bar-Sinai, Gabriele Librandi, Katia Bertoldi, and Michael Moshe. Geometric charges and nonlinear elasticity of two-dimensional elastic metamaterials. *Proceedings of the National Academy of Sciences of the United States of America*, 117(19):10195–10202, may 2020.

[11] Pierre Barbier de Reuille, Anne-Lise Routier-Kierzkowska, Daniel Kierzkowski, George W Bassel, Thierry Schüpbach, Gerardo Tauriello, Namrata Bajpai, Sören Strauss, Alain Weber, Annamaria Kiss, Agata Burian, Hugo Hofhuis, Aleksandra Sapala, Marcin Lipowczan, Maria B Heimlicher, Sarah Robinson, Emmanuelle M Bayer, Konrad Basler, Petros Koumoutsakos, Adrienne HK Roeder, Tinri Aegerter-Wilmsen, Naomi Nakayama, Miltos Tsiantis, Angela Hay, Dorota Kwiatkowska, Ioannis Xenarios, Cris Kuhlemeier, and Richard S Smith. Morphographx: A platform for quantifying morphogenesis in 4d. *eLife*, 4:e05864, may 2015.

[12] Pierre Luc Bardet, Boris Guirao, Camille Paoletti, Fanny Serman, Valentine Léopold, Floris Bosveld, YÛki Goya, Vincent Mirouse, François Graner, and Yohanns Bellaïche. PTEN Controls Junction Lengthening and Stability during Cell Rearrangement in Epithelial Tissue. *Developmental Cell*, 25(5):534–546, jun 2013.

[13] Michael J. F. Barresi and Scott F. Gilbert. *Developmental biology*. Sinauer Associates, an imprint of Oxford University Press, New York, twelfth ed edition, 2020.

[14] Laetitia Bataillé, Jean-Louis Frendo, and Alain Vincent. Hox control of Drosophila larval anatomy; The Alary and Thoracic Alary-Related Muscles. *Mechanisms of Development*, 138:170–176, nov 2015.

[15] Michael Bate and Alfonso Martinez Arias, editors. *The Development of Drosophila melanogaster*. Cold Spring Harbor Laboratory Press, 1993.

[16] Martine Ben Amar and Fei Jia. Anisotropic growth shapes intestinal tissues during embryogenesis. *Proceedings of the National Academy of Sciences of the United States of America*, 110(26):10525–30, jun 2013.

[17] Bertrand Bénazéraf and Olivier Pourquié. Formation and Segmentation of the Vertebrate Body Axis. *Annual Review of Cell and Developmental Biology*, 29:1–26, oct 2013.

[18] Stuart Berg, Dominik Kutra, Thorben Kroeger, Christoph N. Straehle, Bernhard X. Kausler, Carsten Haubold, Martin Schiegg, Janez Ales, Thorsten Beier, Markus Rudy, Kemal Eren, Jaime I. Cervantes, Buote Xu, Fynn Beuttenmueller, Adrian Wolny, Chong Zhang, Ullrich Koethe, Fred A. Hamprecht, and Anna Kreshuk. ilastik: interactive machine learning for (bio)image analysis. *Nature Methods*, 16(12):1226–1232, dec 2019.

[19] Etienne P Bernard and Werner Krauth. Two-Step Melting in Two Dimensions: First-Order Liquid-Hexatic Transition. *Physical Review Letters*, 107(15):155704, oct 2011.

[20] Sandeep Bhat, Jungho Ohn, and Michael Liebling. Motion-based structure separation for label-free high-speed 3-d cardiac microscopy. *IEEE Transactions on Image Processing*, 21(8):3638–3647, 2012.

[21] Mariann Bienz. Induction of the endoderm in Drosophila. *Seminars in Cell & Developmental Biology*, 7(1):113–119, feb 1996.

[22] Mariann Bienz and Gaby Tremml. Domain of Ultrabithorax expression in Drosophila visceral mesoderm from autoregulation and exclusion. *Nature*, 333(6173):576–578, jun 1988.

[23] Silvia Biffi, Roberto Cerbino, Francesca Bomboi, Elvezia Maria Paraboschi, Rosanna Asselta, Francesco Sciortino, and Tommaso Bellini. Phase behavior and critical activated dynamics of limited-valence dna nanostars. *Proceedings of the National Academy of Sciences*, 110(39):15633–15637, 2013.

[24] David Bilder and Matthew P. Scott. Genomic Regions Required for Morphogenesis of the Drosophila Embryonic Midgut. *Genetics*, 141(3):1087–1100, nov 1995.

[25] David Bilder and Matthew P. Scott. Hedgehog and Wingless Induce Metameric Pattern in the Drosophila Visceral Mesoderm. *Developmental Biology*, 201(1):43–56, sep 1998.

[26] Guy B Blanchard, Alexandre J Kabla, Nora L Schultz, Lucy C Butler, Benedicte Sanson, Nicole Gorfinkiel, L Mahadevan, and Richard J Adams. Tissue tectonics: morphogenetic strain rates, cell shape change and intercalation. *Nature Methods 2009 6:6*, 6(6):458–464, may 2009.

[27] M. Botsch, L. Kobbelt, M. Pauly, P. Alliez, and B. Levy. *Polygon Mesh Processing*. Ak Peters Series. Taylor & Francis, 2010.

[28] R. Bowley and M. Sánchez. *Introductory Statistical Mechanics*. Oxford science publications. Clarendon Press, 1999.

[29] A.H. Brand and N. Perrimon. Targeted gene expression as a means of altering cell fates and generating dominant phenotypes. *Development*, 118(2):401–415, jun 1993.

[30] Sebastian Brandstaeter, Sebastian L. Fuchs, Roland C. Aydin, and Christian J. Cyron. Mechanics of the stomach: A review of an emerging field of biomechanics. *GAMM-Mitteilungen*, 42(3):e201900001, 2019.

[31] Robert Bridson. Fast Poisson disk sampling in arbitrary dimensions. In *ACM SIGGRAPH 2007 sketches on - SIGGRAPH '07*, pages 22–es, New York, New York, USA, 2007. ACM Press.

[32] Martin Bringmann and Dominique C. Bergmann. Tissue-wide Mechanical Forces Influence the Polarity of Stomatal Stem Cells in Arabidopsis. *Current Biology*, 27(6):877–883, mar 2017.

[33] Pavel A. Brodskiy, Qinfeng Wu, Dharsan K. Soundarrajan, Francisco J. Huizar, Jianxu Chen, Peixian Liang, Cody Narciso, Megan K. Levis, Ninfamaria Arredondo-Walsh, Danny Z. Chen, and Jeremiah J. Zartman. Decoding Calcium Signaling Dynamics during Drosophila Wing Disc Development. *Biophysical Journal*, 116(4):725–740, feb 2019.

[34] William E. Browne, Alivia L. Price, Matthias Gerberding, and Nipam H. Patel. Stages of embryonic development in the amphipod crustacean,Parhyale hawaiensis. *genesis*, 42(3):124–149, jul 2005.

[35] Jan Brugués and Daniel Needleman. Physical basis of spindle self-organization. *Proceedings of the National Academy of Sciences*, 111(52):18496–18500, dec 2014.

[36] Lucy C Butler, Guy B Blanchard, Alexandre J Kabla, Nicola J Lawrence, David P Welchman, L Mahadevan, Richard J Adams, and Benedicte Sanson. Cell shape changes indicate a role for extrinsic tensile forces in Drosophila germ-band extension. *Nature Cell Biology*, 11(7):859–864, jul 2009.

[37] Paolo Caldarelli, Alexander Chamolly, Olinda Alegria-Prévot, Jerome Gros, and Francis Corson. Self-organized tissue mechanics underlie embryonic regulation. *bioRxiv*, 2021.

[38] J.A. Campos-Ortega and V. Hartenstein. *The Embryonic Development of Drosophila melanogaster*. Springer Berlin Heidelberg, 1997.

[39] Alessia Candeo, Ilenia Sana, Eleonora Ferrari, Luigi Maiuri, Cosimo D'Andrea, Gianluca Valentini, and Andrea Bassi. Virtual unfolding of light sheet fluorescence microscopy dataset for quantitative analysis of the mouse intestine. *Journal of Biomedical Optics*, 21(05):1, may 2016.

[40] Martin Chalfie, Yuan Tu, Ghia Euskirchen, William W Ward, and Douglas C. Prasher. Green Fluorescent Protein as a Marker for Gene Expression. *Science*, 263(5148):802–805, feb 1994.

[41] Kevin G. Chan, Sebastian J. Streichan, Le A. Trinh, and Michael Liebling. Simultaneous temporal superresolution and denoising for cardiac fluorescence microscopy. *IEEE Transactions on Computational Imaging*, 2(3):348–358, 2016.

[42] T.F. Chan and L.A. Vese. Active contours without edges. *IEEE Transactions on Image Processing*, 10(2):266–277, feb 2001.

[43] Soline Chanet, Callie J Miller, Eeshit Dhaval Vaishnav, Bard Ermentrout, Lance A Davidson, and Adam C Martin. Actomyosin meshwork mechanosensing enables tissue shape to orient cell force. *Nature Communications*, 8(1):15014, aug 2017.

[44] Ariel D. Chipman. The Evolution and Development of Segmented Body Plans. In *Evolutionary Developmental Biology*, pages 1–10. Springer International Publishing, Cham, 2018.

[45] Chia-Fu Chou, Anjun J. Jin, S. W. Hui, C. C. Huang, and John T. Ho. Multiple-Step Melting in Two-Dimensional Hexatic Liquid-Crystal Films. *Science*, 280(5368):1424–1426, may 1998.

[46] Dillon Cislo, Haodong Qin, Fengshuo Yang, Mark J. Bowick, and Sebastian J. Streichan. Active cell divisions generate exotic fourfold orientationally ordered phase in living tissue. *bioRxiv*, 2021.

[47] Dillon J. Cislo and Boris I. Shraiman. A morphogenetic action principle for the anisotropic growth of thin tissues. *In Preparation*, 2022.

[48] Anne Kathrin Classen, Kurt I. Anderson, Eric Marois, and Suzanne Eaton. Hexagonal packing of Drosophila wing epithelial cells by the planar cell polarity pathway. *Developmental Cell*, 9(6):805–817, dec 2005.

[49] Roie Cohen, Liat Amir-Zilberstein, Micha Hersch, Shiran Woland, Olga Loza, Shahar Taiber, Fumio Matsuzaki, Sven Bergmann, Karen B. Avraham, and David Sprinzak. Mechanical forces drive ordered patterning of hair cells in the mammalian inner ear. *Nature Communications*, 11(1):1–12, dec 2020.

[50] Sidney R. Coleman. Secret Symmetry: An Introduction to Spontaneous Symmetry Breakdown and Gauge Fields. *Subnucl. Ser.*, 11:139, 1975.

[51] J. Cooke and E. C. Zeeman. A clock and wavefront model for control of the number of repeated structures during animal morphogenesis. *Journal of Theoretical Biology*, 58(2):455–476, 1976.

[52] Alain F. Corcos and Floyd V. Monaghan. Mendel's work and its rediscovery: A new perspective. *Critical Reviews in Plant Sciences*, 9(3):197–212, 1990.

[53] Nicu D Cornea, Deborah Silver, and Patrick Min. Curve-skeleton properties, applications, and algorithms. *IEEE Transactions on visualization and computer graphics*, 13(3):530, 2007.

[54] Rodney Cotterill. *The Material World*. Cambridge University Press, 2 edition, 2008.

[55] Keenan Crane, Fernando de Goes, Mathieu Desbrun, and Peter Schröder. Digital geometry processing with discrete exterior calculus. In *ACM SIGGRAPH 2013 courses*, SIGGRAPH '13, New York, NY, USA, 2013. ACM.

[56] Francis H. C. Crick. Central Dogma of Molecular Biology. *Nature*, 227(5258):561–563, aug 1970.

[57] Wei Dai, Xiaoran Guo, Yuansheng Cao, James A Mondo, Joseph P Campanale, Brandon J Montell, Haley Burrous, Sebastian Streichan, Nir Gov, Wouter-Jan Rappel, and Denise J Montell. Tissue topography steers migrating Drosophila border cells. *Science*, 370(6519):987–990, nov 2020.

[58] Giovanni Dalmasso, Marco Musy, Martina Niksic, Alexandre Robert-Moreno, Claudio Badía-Careaga, Juan J. Sanz-Ezquerro, and James Sharpe. 4D reconstruction of developmental trajectories using spherical harmonics. *bioRxiv*, page 2021.12.16.472948, dec 2021.

[59] Ratul Dasgupta, H. George E. Hentschel, and Itamar Procaccia. Microscopic mechanism of shear bands in amorphous solids. *Physical Review Letters*, 109(25), 2012.

[60] Lance A. Davidson and Buzz Baum. Making waves: the rise and fall and rise of quantitative developmental biology. *Development*, 139(17):3065–3069, sep 2012.

[61] P.G. de Gennes and J. Prost. *The Physics of Liquid Crystals*. International Series of Monographs on Physics. Clarendon Press, 1993.

[62] Gustavo de Medeiros, Nils Norlin, Stefan Gunther, Marvin Albert, Laura Panavaite, Ulla-Maj Fiuza, Francesca Peri, Takashi Hiiragi, Uros Krzic, and Lars Hufnagel. Confocal multiview light-sheet microscopy. *Nature Communications*, 6(1):8881, nov 2015.

[63] Karl Deisseroth. Optogenetics. *Nature Methods*, 8(1):26–29, jan 2011.

[64] Marlis Denk-Lobnig and Adam C. Martin. Divergent and combinatorial mechanical strategies that promote epithelial folding during morphogenesis. *Current Opinion in Genetics and Development*, 63:24–29, aug 2020.

[65] Mathieu Desbrun, Anil N. Hirani, Melvin Leok, and Jerrold E. Marsden. Discrete Exterior Calculus. aug 2005.

[66] Danelle Devenport and Nicholas H. Brown. Morphogenesis in the absence of integrins: mutation of both Drosophila Beta subunits prevents midgut migration. *Development*, 131(21):5405–5415, nov 2004.

[67] Maria-del-Carmen Diaz-de-la Loza, Robert P. Ray, Poulami S. Ganguly, Silvanus Alt, John R. Davis, Andreas Hoppe, Nic Tapon, Guillaume Salbreux, and Barry J. Thompson. Apical and Basal Matrix Remodeling Control Epithelial Morphogenesis. *Developmental Cell*, 46(1):23–39.e5, jul 2018.

[68] Amin Doostmohammadi, Sumesh P. Thampi, Thuan B. Saw, Chwee T. Lim, Benoit Ladoux, and Julia M. Yeomans. Celebrating Soft Matter's 10th Anniversary: Cell division: a source of active stress in cellular monolayers. *Soft Matter*, 11(37):7328–7336, sep 2015.

[69] Marc Durand and Julien Heu. Thermally Driven Order-Disorder Transition in Two-Dimensional Soft Cellular Systems. *Physical Review Letters*, 123(18):188001, oct 2019.

[70] Arthur D Edelstein, Mark A Tsuchida, Nenad Amodaj, Henry Pinkard, Ronald D Vale, and Nico Stuurman. Advanced methods of microscope control using μManager software. *Journal of Biological Methods*, 1(2):e10, nov 2014.

[71] E Efrati, E Sharon, and R Kupferman. Elastic theory of unconstrained non-Euclidean plates. *Journal of the Mechanics and Physics of Solids*, 57(4):762–775, 2009.

[72] Efi Efrati, Eran Sharon, and Raz Kupferman. The metric description of elasticity in residually stressed soft materials. *Soft Matter*, 9(34):8187, aug 2013.

[73] John D. Eshelby. The determination of the elastic field of an ellipsoidal inclusion, and related problems. *Proceedings of the Royal Society of London. Series A. Mathematical and Physical Sciences*, 241(1226):376–396, aug 1957.

[74] Raphaël Etournay, Marko Popović, Matthias Merkel, Amitabha Nandi, Corinna Blasse, Benoît Aigouy, Holger Brandl, Gene Myers, Guillaume Salbreux, Frank Jülicher, and Suzanne Eaton. Interplay of cell dynamics and epithelial tension during morphogenesis of the Drosophila pupal wing. *eLife*, 4, jun 2015.

[75] Reza Farhadifar, Jens-Christian Röper, Benoit Aigouy, Suzanne Eaton, and Frank Jülicher. The Influence of Cell Mechanics, Cell-Cell Interactions, and Proliferation on Epithelial Packing. *Current Biology*, 17(24):2095–2104, dec 2007.

[76] Gerald Farin. Surfaces over dirichlet tessellations. *Computer Aided Geometric Design*, 7(1):281–292, 1990.

[77] Arian S. Forouhar, Michael Liebling, Anna Hickerson, Abbas Nasiraei-Moghaddam, Huai-Jen Tsai, Jay R. Hove, Scott E. Fraser, Mary E. Dickinson, and Morteza Gharib. The embryonic vertebrate heart tube is a dynamic suction pump. *Science*, 312(5774):751–753, 2006.

[78] Theodore Frankel. *The Geometry of Physics: An Introduction*. Cambridge University Press, 3 edition, 2011.

[79] Christian Frantz, Kathleen M. Stewart, and Valerie M. Weaver. The extracellular matrix at a glance. *Journal of Cell Science*, 123(24):4195–4200, dec 2010.

[80] Hajime Fukui, Renee Wei-Yan Chow, Jing Xie, Yoke Yin Foo, Choon Hwai Yap, Nicolas Minc, Naoki Mochizuki, and Julien Vermot. Bioelectric signaling and the control of cardiac cell identity in response to mechanical forces. *Science*, oct 2021.

[81] Kevin D. Gallagher, Madhav Mani, and Richard W. Carthew. Emergence of a geometric pattern of cell fates from tissue-scale mechanics in the Drosophila eye. *eLife*, 11, jan 2022.

[82] Daniel L. Garaulet, David Foronda, Manuel Calleja, and Ernesto Sánchez-Herrero. Polycomb-dependent Ultrabithorax Hox gene silencing induced by high Ultrabithorax levels in Drosophila. *Development*, 135(19):3219–3228, oct 2008.

[83] F.P. Gardiner, N. Lakic, and American Mathematical Society. *Quasiconformal Teichmuller Theory*. Mathematical surveys and monographs. American Mathematical Society, 2000.

[84] A. Gierer and H. Meinhardt. A theory of biological pattern formation. *Kybernetik*, 12(1):30–39, dec 1972.

[85] Taryn E. Gillies and Clemens Cabernard. Cell Division Orientation in Animals. *Current Biology*, 21(15):R599–R609, aug 2011.

[86] Darren Gilmour, Martina Rembold, and Maria Leptin. From morphogen to morphogenesis and back. *Nature*, 541(7637):311–320, jan 2017.

[87] Vitaly. L. Ginzburg and Lev. D. Landau. On the Theory of superconductivity. *Zh. Eksp. Teor. Fiz.*, 20:1064–1082, 1950.

[88] J. M. Girkin and M. T. Carvalho. The light-sheet microscopy revolution. *Journal of Optics*, 20(5):053002, may 2018.

[89] Guillermo A. Gomez, Robert W. McLachlan, and Alpha S. Yap. Productive tension: Force-sensing and homeostasis of cell-cell junctions. *Trends in Cell Biology*, 21(9):499–505, sep 2011.

[90] Jeremy B. A. Green and James Sharpe. Positional information and reaction-diffusion: two big ideas in developmental biology combine. *Development*, 142(7):1203–1211, apr 2015.

[91] Giorgia Guglielmi, Joseph D. Barry, Wolfgang Huber, and Stefano De Renzis. An Optogenetic Method to Modulate Cell Contractility during Tissue Morphogenesis. *Developmental Cell*, 35(5):646–660, dec 2015.

[92] Charlène Guillot and Thomas Lecuit. Mechanics of epithelial tissue homeostasis and morphogenesis. *Science (New York, N.Y.)*, 340(6137):1185–9, jun 2013.

[93] Boris Guirao, Stéphane U. Rigaud, Floris Bosveld, Anaïs Bailles, Jesús López-Gay, Shuji Ishihara, Kaoru Sugimura, François Graner, and Yohanns Bellaïche. Unified quantitative characterization of epithelial tissue development. *eLife*, 4(DECEMBER2015), dec 2015.

[94] B. I. Halperin and David R. Nelson. Theory of Two-Dimensional melting. *Physical Review Letters*, 41(2):121–124, jul 1978.

[95] Edouard Hannezo, Bo Dong, Pierre Recho, Jean-François Joanny, and Shigeo Hayashi. Cortical instability drives periodic supracellular actin pattern formation in epithelial tubes. *Proceedings of the National Academy of Sciences*, 112(28):8620–8625, 2015.

[96] Edouard Hannezo, Jacques Prost, and Jean-Francois Joanny. Theory of epithelial sheet morphology in three dimensions. *Proceedings of the National Academy of Sciences*, 111(1):27–32, 2014.

[97] Melissa M. Harrison, Brian V. Jenkins, Kate M. O'Connor-Giles, and Jill Wildonger. A CRISPR view of development. *Genes & Development*, 28(17):1859–1872, sep 2014.

[98] Andrea Hartsock and W. James Nelson. Adherens and tight junctions: Structure, function and connections to the actin cytoskeleton. *Biochimica et Biophysica Acta (BBA) - Biomembranes*, 1778(3):660–669, mar 2008.

[99] Idse Heemskerk and Sebastian J Streichan. Tissue cartography: compressing bio-image data by dimensional reduction. *Nature Methods*, 12(12):1139–1142, dec 2015.

[100] Idse Heemskerk and Sebastian J Streichan. Tissue Cartography: Compressing Bio-Image Data by Dimensional Reduction. *Nature methods*, 12(12):1139–1142, dec 2015.

[101] Carl-Philipp Heisenberg and Yohanns Bellaïche. Forces in Tissue Morphogenesis and Patterning. *Cell*, 153(5):948–962, may 2013.

[102] Sébastien Herbert, Léo Valon, Laure Mancini, Nicolas Dray, Paolo Caldarelli, Jérôme Gros, Elric Esposito, Spencer L. Shorte, Laure Bally-Cuif, Nathalie Aulner, Romain Levayer, and Jean-Yves Tinevez. LocalZProjector and DeProj: a toolbox for local 2D projection and accurate morphometrics of large 3D microscopy images. *BMC Biology*, 19(1):136, dec 2021.

[103] David C. Hill-Eubanks, Matthias E. Werner, Thomas J. Heppner, and Mark T. Nelson. Calcium Signaling in Smooth Muscle. *Cold Spring Harbor Perspectives in Biology*, 3(9):a004549, sep 2011.

[104] Ludwig A. Hoffmann, Livio Nicola Carenza, Julia Eckert, and Luca Giomi. Theory of defect-mediated morphogenesis. *Science Advances*, 8(15):2712, apr 2022.

[105] Stefan Hoppler and Mariann Bienz. Specification of a single cell type by a Drosophila homeotic gene. *Cell*, 76(4):689–702, feb 1994.

[106] Jonathon Howard. *Mechanics of Motor Proteins and the Cytoskeleton*. Sinauer Associates, Publishers, 2001.

[107] Chiu-Ju Huang, Chi-Tang Tu, Chung-Der Hsiao, Fong-Jou Hsieh, and Huai-Jen Tsai. Germ-line transmission of a myocardium-specific gfp transgene reveals critical regulatory elements in the cardiac myosin light chain 2 promoter of zebrafish. *Developmental Dynamics*, 228(1):30–40, 2003.

[108] Tyler R. Huycke, Bess M. Miller, Hasreet K. Gill, Nandan L. Nerurkar, David Sprinzak, L. Mahadevan, and Clifford J. Tabin. Genetic and Mechanical Regulation of Intestinal Smooth Muscle Development. *Cell*, 179(1):90–105.e21, sep 2019.

[109] Karin Immerglück, Peter A. Lawrence, and Mariann Bienz. Induction across germ layers in Drosophila mediated by a genetic cascade. *Cell*, 62(2):261–268, jul 1990.

[110] Donald E. Ingber and Michael Levin. What lies at the interface of regenerative medicine and developmental biology? *Development*, 134(14):2541–2547, jul 2007.

[111] Naoki Irie and Shigeru Kuratani. The developmental hourglass model: A predictor of the basic body plan? *Development*, 141(24):4649–4655, 2014.

[112] K.D. Irvine and E. Wieschaus. Cell intercalation during Drosophila germband extension and its regulation by pair-rule segmentation genes. *Development*, 120(4):827–841, apr 1994.

[113] Kenzo Ivanovitch, Susana Temiño, and Miguel Torres. Live imaging of heart tube development in mouse reveals alternating phases of cardiac differentiation and morphogenesis. *eLife*, 6, 2017.

[114] Emiliano Izquierdo, Theresa Quinkler, and Stefano De Renzis. Guided morphogenesis through optogenetic activation of Rho signalling during early Drosophila embryogenesis. *Nature Communications*, 9(1):2366, jun 2018.

[115] Ian Jolliffe. *Principal component analysis*. Springer Verlag, New York, 2002.

[116] Maki Kaneko, Bela S. Desai, and Boaz Cook. Ionic leakage underlies a gain-of-function effect of dominant disease mutations affecting diverse p-type atpases. *Nature Genetics*, 46(2):144–151, 2014.

[117] M. Kardar. *Statistical Physics of Particles*. Cambridge University Press, 2007.

[118] Eyal Karzbrun, Aimal H. Khankhel, Heitor C. Megale, Stella M. K. Glasauer, Yofiel Wyle, George Britton, Aryeh Warmflash, Kenneth S. Kosik, Eric D. Siggia, Boris I. Shraiman, and Sebastian J. Streichan. Human neural tube morphogenesis in vitro by geometric constraints. *Nature*, 599(7884):268–272, 2021.

[119] Eyal Karzbrun, Aimal H Khankhel, Heitor C Megale, Stella M. K. Glasauer, Yofiel Wyle, George Britton, Aryeh Warmflash, Kenneth S Kosik, Eric D Siggia, Boris I Shraiman, and Sebastian J Streichan. Human neural tube morphogenesis in vitro by geometric constraints. *Nature*, 599(7884):268–272, nov 2021.

[120] Karen E. Kasza, Amy C. Rowat, Jiayu Liu, Thomas E. Angelini, Clifford P. Brangwynne, Gijsje H. Koenderink, and David A. Weitz. The cell as a material. *Current Opinion in Cell Biology*, 19(1):101–107, feb 2007.

[121] Michael Kazhdan and Hugues Hoppe. Screened poisson surface reconstruction. *ACM Transactions on Graphics*, 32(3):1–13, jun 2013.

[122] Ray Keller. Physical Biology Returns to Morphogenesis. *Science*, 338(6104):201–203, oct 2012.

[123] Daniel Kierzkowski, Adam Runions, Francesco Vuolo, Sören Strauss, Rena Lymbouridou, Anne-Lise Routier-Kierzkowska, David Wilson-Sánchez, Hannah Jenke, Carla Galinha, Gabriella Mosca, and et al. A growth-based framework for leaf shape development and diversity. *Cell*, 177(6):1405–1418.e17, 2019.

[124] Robert Klapper, Christiana Stute, Oliver Schomaker, Thomas Strasser, Wilfried Janning, Renate Renkawitz-Pohl, and Anne Holz. The formation of syncytia within the visceral musculature of the drosophila midgut is dependent on duf, sns and mbc. *Mechanisms of Development*, 110(1):85–96, 2002.

[125] Yael Klein, Efi Efrati, and Eran Sharon. Shaping of Elastic Sheets by Prescription of Non-Euclidean Metrics. *Science*, 315(5815):1116–1120, feb 2007.

[126] J M Kosterlitz and D J Thouless. Ordering, metastability and phase transitions in two-dimensional systems. *Journal of Physics C: Solid State Physics*, 6(7):1181–1203, apr 1973.

[127] Uros Krzic, Stefan Gunther, Timothy E Saunders, Sebastian J Streichan, and Lars Hufnagel. Multiview light-sheet microscope for rapid in toto imaging. *Nature Methods*, 9(7):730–733, jul 2012.

[128] Ivana Y. Kuo and Barbara E. Ehrlich. Signaling in Muscle Contraction. *Cold Spring Harbor Perspectives in Biology*, 7(2):a006023, feb 2015.

[129] Benoit Ladoux and René-Marc Mège. Mechanobiology of collective cell behaviours. *Nature Reviews Molecular Cell Biology*, 18(12):743–757, Dec 2017.

[130] L. D. Landau and E. M. Lifshitz. *Fluid Mechanics, Second Edition: Volume 6.* Course of Theoretical Physics. Butterworth-Heinemann, 2 edition, jan 1987.

[131] Lev. D. Landau. On the theory of phase transitions. *Zh. Eksp. Teor. Fiz.*, 7:19–32, 1937.

[132] Lev D. Landau and Evgeny. M. Lifshitz. *Statistical Physics Part I.* Course of Theoretical Physics. Elsevier, Amsterdam, 3rd edition, 1980. bibtex: landa;b;sp80.

[133] Lev .D. Landau, Evgeny. M. Lifshitz, A.M. Kosevich, J.B. Sykes, L.P. Pitaevskii, and W.H. Reid. *Theory of Elasticity: Volume 7.* Course of theoretical physics. Elsevier Science, 1986.

[134] Michael L Larsen and Raymond A Shaw. A method for computing the three-dimensional radial distribution function of cloud particles from holographic images. *Atmospheric Measurement Techniques*, 11(7):4261–4272, jul 2018.

[135] Ernest Latorre, Sohan Kale, Laura Casares, Manuel Gómez-González, Marina Uroz, Léo Valon, roshna V Nair, Elena Garreta, Nuria Montserrat, Aránzazu del Campo, Benoit Ladoux, Marino Arroyo, and Xavier Trepat. Active superelasticity in three-dimensional epithelia of controlled shape. *Nature*, 563(7730):203–208, 2018.

[136] Peter A Lawrence. Morphogens: how big is the big picture? *Nature Cell Biology*, 3(7):E151–E154, jul 2001.

[137] Huu Le, Tat-Jun Chin, and David Suter. Conformal Surface Alignment with Optimal Möbius Search. In *2016 IEEE Conference on Computer Vision and Pattern Recognition (CVPR)*, volume 2016-Decem, pages 2507–2516. IEEE, jun 2016.

[138] Jean-François Le Garrec, Jorge N Domínguez, Audrey Desgrange, Kenzo D Ivanovitch, Etienne Raphaël, J Andrew Bangham, Miguel Torres, Enrico Coen, Timothy J Mohun, and Sigolène M Meilhac. A predictive model of asymmetric morphogenesis from 3D reconstructions of mouse heart looping dynamics. *eLife*, 6:e28951, nov 2017.

[139] Thomas Lecuit and Pierre-François Lenne. Cell surface mechanics and the control of cell shape, tissue patterns and morphogenesis. *Nature Reviews Molecular Cell Biology*, 8(8):633–644, 2007.

[140] Thomas Lecuit and L Mahadevan. Morphogenesis one century after On Growth and Form. *Development (Cambridge, England)*, 144(23):4197–4198, dec 2017.

[141] Ta-Chih Lee, Rangasami L. Kashyap, and Chong-Nam Chu. Building skeleton models via 3-d medial surface/axis thinning algorithms. *CVGIP: Graph. Models Image Process.*, 56(6):462–478, nov 1994.

[142] Matthew Frederick Lefebvre, Nikolas Heinrich Claussen, Noah Prentice Mitchell, Hannah J Gustafson, and Sebastian J Streichan. Geometric control of Myosin-II orientation during axis elongation. *bioRxiv*, page 2022.01.12.476069, 2022.

[143] Michael Levin, Randy L Johnson, Claudio D Sterna, Michael Kuehn, and Cliff Tabin. A molecular pathway determining left-right asymmetry in chick embryogenesis. *Cell*, 82(5):803–814, 1995.

[144] Michael Levine and Eric H. Davidson. Gene regulatory networks for development. *Proceedings of the National Academy of Sciences*, 102(14):4936–4942, apr 2005.

[145] Bruno Lévy and Hao (Richard) Zhang. Spectral mesh processing. In *ACM SIGGRAPH 2010 Courses*, SIGGRAPH '10, New York, NY, USA, 2010. Association for Computing Machinery.

[146] E. B. Lewis. A gene complex controlling segmentation in Drosophila. *Nature*, 276(5688):565–570, dec 1978.

[147] Ting Li, An Yan, Neha Bhatia, Alphan Altinok, Eldad Afik, Pauline Durand-Smet, Paul T. Tarr, Julian I. Schroeder, Marcus G. Heisler, and Elliot M. Meyerowitz. Calcium signals are necessary to establish auxin transporter polarity in a plant stem cell niche. *Nature Communications*, 10(1):726, feb 2019.

[148] Yan-Wei Li and Massimo Pica Ciamarra. Role of cell deformability in the two-dimensional melting of biological tissues. *Physical Review Materials*, 2(4):045602, apr 2018.

[149] William E Lorensen and Harvey E Cline. Marching cubes: A high resolution 3D surface construction algorithm. In *Proceedings of the 14th annual conference on Computer graphics and interactive techniques - SIGGRAPH '87*, volume 21, pages 163–169, New York, New York, USA, 1987. ACM Press.

[150] Barry Lubarsky and Mark A. Krasnow. Tube morphogenesis. *Cell*, 112(1):19–28, 2003.

[151] Lok Ming Lui, Tsz Wai Wong, Wei Zeng, Xianfeng Gu, Paul M Thompson, Tony F Chan, and Shing-Tung Yau. Optimization of Surface Registrations Using Beltrami Holomorphic Flow. *Journal of Scientific Computing*, 50(3):557–585, mar 2012.

[152] F. C. MacKintosh and A J Levine. Nonequilibrium Mechanics and Dynamics of Motor-Activated Gels. *Physical Review Letters*, 100(1):018104, jan 2008.

[153] Roopa Madhu, Delany Rodriguez, Claudia Guzik, Shambhavi Singh, Anthony W. De Tomaso, Megan T. Valentine, and Dinah Loerke. Characterizing the cellular architecture of dynamically remodeling vascular tissue using 3-D image analysis and virtual reconstruction. *Molecular Biology of the Cell*, 31(16):1714–1725, jul 2020.

[154] Yonit Maroudas-Sacks, Liora Garion, Lital Shani-Zerbib, Anton Livshits, Erez Braun, and Kinneret Keren. Topological defects in the nematic order of actin fibres as organization centres of hydra morphogenesis. *Nature Physics*, 17(2):251–259, 2021.

[155] Yonit Maroudas-Sacks, Liora Garion, Lital Shani-Zerbib, Anton Livshits, Erez Braun, and Kinneret Keren. Topological defects in the nematic order of actin fibres as organization centres of Hydra morphogenesis. *Nature Physics*, 17(2):251–259, feb 2021.

[156] Jerrold E. Marsden and Thomas J. R. Hughes. *Mathematical Foundations of Elasticity*. Dover Publications, New York, revised edition, feb 1994.

[157] Frank J. Massey. The Kolmogorov-Smirnov Test for Goodness of Fit. *Journal of the American Statistical Association*, 46(253):68, mar 1951.

[158] Patricia Mendoza-Garcia, Swaraj Basu, Sanjay Kumar Sukumar, Badrul Arefin, Georg Wolfstetter, Vimala Anthonydhason, Linnea Molander, Ezgi Uçkun, Henrik Lindehell, Cristina Lebrero-Fernandez, Jan Larsson, Erik Larsson, Mats Bemark, and Ruth H. Palmer. DamID transcriptional profiling identifies the Snail/Scratch transcription factor Kahuli as an Alk target in the Drosophila visceral mesoderm. *Development*, 148(23):dev199465, dec 2021.

[159] N. David Mermin. The topological theory of defects in ordered media. *Reviews of Modern Physics*, 51(3):591–648, jul 1979.

[160] Ross J. Metzger, Ophir D. Klein, Gail R. Martin, and Mark A. Krasnow. The branching programme of mouse lung development. *Nature*, 453(7196):745–750, jun 2008.

[161] Fernand Meyer. Topographic distance and watershed lines. *Signal Processing*, 38(1):113–125, jul 1994.

[162] Alexander Mietke, Frank Jülicher, and Ivo F. Sbalzarini. Self-organized shape dynamics of active surfaces. *Proceedings of the National Academy of Sciences*, 116(1):29–34, 2019.

[163] Alessandro Minelli and Giuseppe Fusco. Evo-devo perspectives on segmentation: Model organisms, and beyond. *Trends in Ecology and Evolution*, 19(8):423–429, aug 2004.

[164] Noah P. Mitchell and Dillon J. Cislo. Tubular: Tracking deformations of dynamic tissues and interfaces in 3d. *bioRxiv*, 2022.

[165] Noah P Mitchell, Dillon J Cislo, Suraj Shankar, Yuzheng Lin, Boris I Shraiman, and Sebastian J Streichan. Visceral organ morphogenesis via calcium-patterned muscle constrictions. *eLife*, 11:e77355, may 2022.

[166] Noah P Mitchell, Matthew F Lefebvre, Vishank Jain-Sharma, Nikolas Claussen, Marion K Raich, Hannah J Gustafson, Andreas R Bausch, and Sebastian J Streichan. Morphodynamic atlas for drosophila development. *bioRxiv*, 2022.

[167] Cherry A Murray. *Experimental Studies of Melting and Hexatic Order in Two-Dimensional Colloidal Suspensions*, pages 137–215. Springer New York, New York, NY, 1992.

[168] Pablo Márquez-Neila, Luis Baumela, and Luis Alvarez. A Morphological Approach to Curvature-Based Evolution of Curves and Surfaces. *IEEE Transactions on Pattern Analysis and Machine Intelligence*, 36(1):2–17, jan 2014.

[169] Utpal Nath, Brian C. W. Crawford, Rosemary Carpenter, and Enrico Coen. Genetic Control of Surface Curvature. *Science*, 299(5611):1404–1407, feb 2003.

[170] Joseph Needham. Chemical embryology. *Annual Review of Biochemistry*, 1(1):507–526, 1932.

[171] Tristan Needham. *Visual Complex Analysis*. Clarendon Press, 1998.

[172] Celeste M. Nelson and Jason P. Gleghorn. Sculpting Organs: Mechanical Regulation of Tissue Development. *Annual Review of Biomedical Engineering*, 14(1):129–154, 2012.

[173] D.R. Nelson. *Defects and Geometry in Condensed Matter Physics*. Cambridge University Press, 2002.

[174] Ola Nilsson, Rose Marino, Francesco De Luca, Moshe Phillip, and Jeffrey Baron. Endocrine Regulation of the Growth Plate. *Hormone Research in Paediatrics*, 64(4):157–165, 2005.

[175] Ingo Nitschke, Sebastian Reuther, and Axel Voigt. Discrete Exterior Calculus (DEC) for the Surface Navier-Stokes Equation. pages 177–197. Birkhäuser, Cham, 2017.

[176] J. Nocedal and S. Wright. *Numerical Optimization*. Springer Series in Operations Research and Financial Engineering. Springer New York, 2006.

[177] Nicholas Noll, Madhav Mani, Idse Heemskerk, Sebastian J. Streichan, and Boris I. Shraiman. Active tension network model suggests an exotic mechanical state realized in epithelial tissues. *Nature Physics*, 13(12):1221–1226, dec 2017.

[178] Christiane Nüsslein-Volhard. Maternal effect mutations that alter the spatial coordinates of the embryo in *drosophila melanogaster*. In Stephen Subtelny and Irwin R. Konigsberg, editors, *Determinants of Spatial Organization*, pages 185–211. Academic Press, New York, 1979.

[179] Christiane Nüsslein-Volhard and Eric Wieschaus. Mutations affecting segment number and polarity in Drosophila. *Nature*, 287(5785):795–801, oct 1980.

[180] Andrew C. Oates, Nicole Gorfinkiel, Marcos González-Gaitán, and Carl-Philipp Heisenberg. Quantitative approaches in developmental biology. *Nature Reviews Genetics*, 10(8):517–530, aug 2009.

[181] Andrew C. Oates, Luis G. Morelli, and Saúl Ares. Patterning embryos with oscillations: Structure, function and dynamics of the vertebrate segmentation clock. *Development*, 139(4):625–639, feb 2012.

[182] Stanley J. Osher and Ronald Fedkiw. *Level set methods and dynamic implicit surfaces.*, volume 153 of *Applied mathematical sciences*. Springer, 2003.

[183] Michael A. Palmer, Bryan A. Nerger, Katharine Goodwin, Anvitha Sudhakar, Sandra B. Lemke, Pavithran T. Ravindran, Jared E. Toettcher, Andrej Košmrlj, and Celeste M. Nelson. Stress ball morphogenesis: How the lizard builds its lung. *Science Advances*, dec 2021. Publisher: American Association for the Advancement of Science.

[184] Karl H. Palmquist, Sydney F. Tiemann, Farrah L. Ezzeddine, Sichen Yang, Charlotte R. Pfeifer, Anna Erzberger, Alan R. Rodrigues, and Amy E. Shyer. Reciprocal cell-ECM dynamics generate supracellular fluidity underlying spontaneous follicle patterning. *Cell*, 185(11):1960–1973.e11, may 2022.

[185] Yuanwang Pan, Idse Heemskerk, Consuelo Ibar, Boris I. Shraiman, and Kenneth D. Irvine. Differential growth triggers mechanical feedback that elevates Hippo signaling. *Proceedings of the National Academy of Sciences of the United States of America*, 113(45):E6974–E6983, nov 2016.

[186] G.E. Panganiban, R. Reuter, M.P. Scott, and F.M. Hoffmann. A Drosophila growth factor homolog, decapentaplegic, regulates homeotic gene expression within and across germ layers during midgut morphogenesis. *Development*, 110(4):1041–1050, dec 1990.

[187] J. R. Parker. *Algorithms for Image Processing and Computer Vision*. Wiley Publishing, 2nd edition, 2010.

[188] Anshuman Pasupalak, Yan-Wei Li, Ran Ni, and Massimo Pica Ciamarra. Hexatic phase in a model of active biological tissues. *Soft Matter*, 16(16):3914–3920, apr 2020.

[189] Anastasios Pavlopoulos, Zacharias Kontarakis, Danielle M. Liubicich, Julia M. Serano, Michael Akam, Nipam H. Patel, and Michalis Averof. Probing the evolution of appendage specialization by Hox gene misexpression in an emerging model crustacean. *Proceedings of the National Academy of Sciences of the United States of America*, 106(33):13897–13902, dec 2009.

[190] James B. Pawley, editor. *Handbook of Biological Confocal Microscopy*. Springer New York, New York, third edition, 2006.

[191] D. J. G. Pearce, S. Gat, G. Livne, A. Bernheim-Groswasser, and K. Kruse. Defect-driven shape transitions in elastic active nematic shells. oct 2020.

[192] Esther J Pearl, Jingjing Li, and Jeremy B. A. Green. Cellular systems for epithelial invagination. *Philosophical Transactions of the Royal Society B: Biological Sciences*, 372(1720):20150526, may 2017.

[193] Chris B. Phelps and Andrea H. Brand. Ectopic Gene Expression inDrosophilaUsing GAL4 System. *Methods*, 14(4):367–379, apr 1998.

[194] Ulrich Pinkall and Konrad Polthier. Computing discrete minimal surfaces and their conjugates. *Experimental Mathematics*, 2, 11 1993.

[195] Stephan Preibisch, Fernando Amat, Evangelia Stamataki, Mihail Sarov, Robert H Singer, Eugene Myers, and Pavel Tomancak. Efficient Bayesian-based multiview deconvolution. *Nature Methods*, 11(6):645–648, jun 2014.

[196] Stephan Preibisch, Fernando Amat, Evangelia Stamataki, Mihail Sarov, Robert H. Singer, Eugene Myers, and Pavel Tomancak. Efficient Bayesian-based multiview deconvolution. *Nature Methods*, 11(6):645–648, jun 2014.

[197] J. Prost, F. Jülicher, and J-F. Joanny. Active gel physics. *Nature Physics*, 11(2):111–117, feb 2015.

[198] A. Puliafito, L. Hufnagel, P. Neveu, S. Streichan, A. Sigal, D. K. Fygenson, and B. I. Shraiman. Collective and single cell behavior in epithelial contact inhibition. *Proceedings of the National Academy of Sciences*, 109(3):739–744, jan 2012.

[199] Joshua R Puzey, Sharon J Gerbode, Scott A Hodges, Elena M Kramer, and L Mahadevan. Evolution of spur-length diversity in Aquilegia petals is achieved solely through cell-shape anisotropy. *Proceedings of the Royal Society B: Biological Sciences*, 279(1733):1640–1645, apr 2012.

[200] Carlos Pérez-González, Gerardo Ceada, Francesco Greco, Marija Matejčić, Manuel Gómez-González, Natalia Castro, Anghara Menendez, Sohan Kale, Denis Krndija, Andrew G. Clark, Venkata Ram Gannavarapu, Adrián Álvarez Varela, Pere Roca-Cusachs, Eduard Batlle, Danijela Matic Vignjevic, Marino Arroyo, and Xavier Trepat. Mechanical compartmentalization of the intestinal organoid enables crypt folding and collective cell migration. *Nature Cell Biology*, 23(7):745–757, jul 2021.

[201] Jonas Ranft, Markus Basan, Jens Elgeti, J.-F. Joanny, Jacques Prost, and F. Julicher. Fluidization of tissues by cell division and apoptosis. *Proceedings of the National Academy of Sciences*, 107(49):20863–20868, dec 2010.

[202] Cordelia Rauskolb, Shuguo Sun, Gongping Sun, Yuanwang Pan, and Kenneth D. Irvine. Cytoskeletal Tension Inhibits Hippo Signaling through an Ajuba-Warts Complex. *Cell*, 158(1):143–156, jul 2014.

[203] R. Reuter and M.P. Scott. Expression and function of the homoeotic genes Antennapedia and Sex combs reduced in the embryonic midgut of Drosophila. *Development*, 109(2):289–303, jun 1990.

[204] Emmanuel G Reynaud, Jan Peychl, Jan Huisken, and Pavel Tomancak. Guide to light-sheet microscopy for adventurous biologists. *Nature Methods*, 12(1):30–34, jan 2015.

[205] Nicolas Romeo, Alasdair Hastewell, Alexander Mietke, and Jörn Dunkel. Learning developmental mode dynamics from single-cell trajectories. *eLife*, 10, dec 2021.

[206] Sol I. Rubinow and Joseph B. Keller. Flow of a viscous fluid through an elastic tube with applications to blood flow. *Journal of theoretical biology*, 35 2:299–313, 1972.

[207] David Rudel and Ralf J. Sommer. The evolution of developmental mechanisms. *Developmental Biology*, 264(1):15–37, dec 2003.

[208] Mehdi Saadaoui, Didier Rocancourt, Julian Roussel, Francis Corson, and Jerome Gros. A tensile ring drives tissue flows to shape the gastrulating amniote embryo. *Science*, 367(6476):453–458, jan 2020.

[209] Jun J. Sakurai. *Modern Quantum Mechanics (Revised Edition)*. Addison Wesley, first edition, sep 1993.

[210] Guillaume Salbreux, Linda K. Barthel, Pamela A. Raymond, and David K. Lubensky. Coupling Mechanical Deformations and Planar Cell Polarity to Create Regular Patterns in the Zebrafish Retina. *PLoS Computational Biology*, 8(8):1002618, aug 2012.

[211] Guillaume Salbreux, Guillaume Charras, and Ewa Paluch. Actin cortex mechanics and cellular morphogenesis. *Trends in Cell Biology*, 22(10):536–545, oct 2012.

[212] Guillaume Salbreux and Frank Jülicher. Mechanics of active surfaces. *Phys. Rev. E*, 96(3):32404, sep 2017.

[213] Tim Sanchez, Daniel T. N. Chen, Stephen J. Decamp, Michael Heymann, and Zvonimir Dogic. Spontaneous motion in hierarchically assembled active matter. *Nature*, 491(7424):431–434, 2012.

[214] Siddhartha Sarkar, Matjaž Čebron, Miha Brojan, and Andrej Košmrlj. Elastic multipole method for describing deformation of infinite two-dimensional solids with circular inclusions. *Physical Review E*, 103(5):053003, may 2021.

[215] Thierry Savin, Natasza A. Kurpios, Amy E. Shyer, Patricia Florescu, Haiyi Liang, L. Mahadevan, and Clifford J. Tabin. On the growth and form of the gut. *Nature*, 476(7358):57–62, aug 2011.

[216] Jacob M. Sawyer, Jessica R. Harrell, Gidi Shemer, Jessica Sullivan-Brown, Minna Roh-Johnson, and Bob Goldstein. Apical constriction: A cell shape change that can drive morphogenesis. *Developmental Biology*, 341(1):5–19, may 2010.

[217] Benjamin Schmid, Gopi Shah, Nico Scherf, Michael Weber, Konstantin Thierbach, Citlali Pérez Campos, Ingo Roeder, Pia Aanstad, and Jan Huisken. High-speed panoramic light-sheet microscopy reveals global endodermal cell dynamics. *Nature Communications*, 4(1):2207, oct 2013.

[218] Stephan Schneuwly, Roman Klemenz, and Walter J. Gehring. Redesigning the body plan of Drosophila by ectopic expression of the homoeotic gene Antennapedia. *Nature*, 325(6107):816–818, feb 1987.

[219] Mattia Serra, Sebastian Streichan, Manli Chuai, Cornelis J. Weijer, and L. Mahadevan. Dynamic morphoskeletons in development. *Proceedings of the National Academy of Sciences*, 117(21):11444–11449, 2020.

[220] Friedhelm Serwane, Alessandro Mongera, Payam Rowghanian, David A Kealhofer, Adam A Lucio, Zachary M Hockenbery, and Otger Campàs. In vivo quantification of spatially varying mechanical properties in developing tissues. *Nature Methods*, 14(2):181–186, feb 2017.

[221] R Seshadri and R M Westervelt. Hexatic-to-liquid melting transition in two-dimensional magnetic-bubble lattices. *Physical Review Letters*, 66(21):2774–2777, may 1991.

[222] James P. Sethna. *Statistical Mechanics: Entropy, Order Parameters and Complexity*. Oxford University Press, Great Clarendon Street, Oxford OX2 6DP, first edition, 2006.

[223] Eran Sharon and Efi Efrati. The mechanics of non-Euclidean plates. *Soft Matter*, 6(22):5693–5704, 2010.

[224] James Sharpe. Computer modeling in developmental biology: growing today, essential tomorrow. *Development*, 144(23):4214–4225, dec 2017.

[225] Elijah R. Shelton, Sangwoo Kim, Ben J. Gross, Ray Wu, Marie Pochitaloff, Irene Lim, Ellen M. Sletten, and Otger Campàs. Stress-driven tissue fluidization physically segments vertebrate somites. *bioRxiv*, page 2021.03.27.437325, mar 2021.

[226] Amy E. Shyer, Tuomas Tallinen, Nandan L. Nerurkar, Zhiyan Wei, Eun Seok Gil, David L. Kaplan, Clifford J. Tabin, and L. Mahadevan. Villification: How the Gut Gets Its Villi. *Science*, 342(6155):212–218, oct 2013.

[227] Robin Sibson. A brief description of natural neighbor interpolation. In Vic Barnett, editor, *Interpreting Multivariate Data*, pages 21–36. John Wiley & Sons, New York, 1981.

[228] Pragya Sidhwani and Deborah Yelon. Fluid forces shape the embryonic heart: Insights from zebrafish. In *Current Topics in Developmental Biology*, volume 132, pages 395–416. Academic Press Inc., jan 2019.

[229] J. B. Singer, R. Harbecke, T. Kusch, R. Reuter, and J. A. Lengyel. Drosophila brachyenteron regulates gene activity and morphogenesis in the gut. *Development*, 122(12):3707–3718, dec 1996.

[230] Aravind Sivakumar and Natasza A. Kurpios. Transcriptional regulation of cell shape during organ morphogenesis. *Journal of Cell Biology*, 217(9):2987–3005, jul 2018.

[231] J Maynard Smith, R Burian, S Kauffman, P Alberch, J Campbell, B Goodwin, R Lande, D Raup, and L Wolpert. Developmental Constraints and Evolution: A Perspective from the Mountain Lake Conference on Development and Evolution. *The Quarterly Review of Biology*, 60(3):265–287, sep 1985.

[232] D.Y. Stainier, R.K. Lee, and M.C. Fishman. Cardiovascular development in the zebrafish. I. Myocardial fate map and heart tube formation. *Development*, 119(1):31–40, 09 1993.

[233] Evangelia Stamataki and Anastasios Pavlopoulos. Non-insect crustacean models in developmental genetics including an encomium to Parhyale hawaiensis. *Current Opinion in Genetics & Development*, 39:149–156, 2016.

[234] Oded Stein, Alec Jacobson, Max Wardetzky, and Eitan Grinspun. A Smoothness Energy without Boundary Distortion for Curved Surfaces. *ACM Transactions on Graphics*, 39(3):1–17, jun 2020.

[235] Ernst H K Stelzer. Light-sheet fluorescence microscopy for quantitative biology. *Nature Methods*, 12(1):23–26, jan 2015.

[236] Sebastian J Streichan, Matthew F Lefebvre, Nicholas Noll, Eric F Wieschaus, and Boris I Shraiman. Global morphogenetic flow is accurately predicted by the spatial distribution of myosin motors. *eLife*, 7, feb 2018.

[237] David Strutt. Frizzled signalling and cell polarisation in Drosophila and vertebrates. *Development*, 130(19):4501–4513, oct 2003.

[238] Liyuan Sui, Silvanus Alt, Martin Weigert, Natalie Dye, Suzanne Eaton, Florian Jug, Eugene W Myers, Frank Jülicher, Guillaume Salbreux, and Christian Dahmann. Differential lateral and basal tension drive folding of Drosophila wing discs through two distinct mechanisms. *Nature Communications*, 9(1):4620, dec 2018.

[239] Dennis A. Sun and Nipam H. Patel. The amphipod crustacean Parhyale hawaiensis : An emerging comparative model of arthropod development, evolution, and regeneration. *WIREs Developmental Biology*, 8(5):e355, sep 2019.

[240] Alexandra M. Tayar, Fernando Caballaro, Trevor Anderberg, Omar A. Saleh, M. Cristina Marchetti, and Zvonimir Dogic. Controlling liquid-liquid phase behavior with an active fluid. 2022.

[241] The GIMP Development Team. GIMP, jun 2019.

[242] William Thielicke and René Sonntag. Particle Image Velocimetry for MATLAB: Accuracy and enhanced algorithms in PIVlab. *Journal of Open Research Software*, 9(1):12, may 2021.

[243] William Thielicke and Eize Stamhuis. PIVlab – Towards User-friendly, Affordable and Accurate Digital Particle Image Velocimetry in MATLAB. *Journal of Open Research Software*, 2(1):e30, oct 2014.

[244] Jean Paul Thiery, Hervé Acloque, Ruby Y.J. Huang, and M. Angela Nieto. Epithelial-Mesenchymal Transitions in Development and Disease. *Cell*, 139(5):871–890, nov 2009.

[245] D H Thompson, E Tarleton, S G Roberts, and S P Fitzgerald. Interstitial-mediated dislocation climb and the weakening of particle-reinforced alloys under irradiation. *Physical Review Materials*, 2(8):080601, aug 2018.

[246] D'Arcy Wentworth Thompson. *On Growth and Form*. Cambridge University Press, Cambridge, UK, first edition, 1917.

[247] Melda Tozluoğlu, Maria Duda, Natalie J. Kirkland, Ricardo Barrientos, Jemima J. Burden, José J. Muñoz, and Yanlan Mao. Planar Differential Growth Rates Initiate Precise Fold Positions in Complex Epithelia. *Developmental Cell*, 51(3):299–312.e4, nov 2019.

[248] G Tremml and M Bienz. Homeotic gene expression in the visceral mesoderm of Drosophila embryos. *The EMBO Journal*, 8(9):2677–2685, sep 1989.

[249] Roger Y Tsien. The Green Fluorescent Protein. *Annual Review of Biochemistry*, 67(1):509–544, jun 1998.

[250] Alan Turing. The chemical basis of morphogenesis. *Philosophical Transactions of the Royal Society B*, 237:37–72, 1952.

[251] Farzan Vafa and L. Mahadevan. Active nematic defects and epithelial morphogenesis. 2021.

[252] Wim M. van Rees, Etienne Vouga, and L. Mahadevan. Growth patterns for shape-shifting elastic bilayers. *Proceedings of the National Academy of Sciences*, 114(44):11597–11602, 2017.

[253] Hélène Vignes, Christina Vagena-Pantoula, Mangal Prakash, Hajime Fukui, Caren Norden, Naoki Mochizuki, Florian Jug, and Julien Vermot. Extracellular mechanical forces drive endocardial cell volume decrease during zebrafish cardiac valve morphogenesis. *Developmental Cell*, 57(5):598–609.e5, 2022.

[254] John B. Wallingford, Andrew J. Ewald, Richard M. Harland, and Scott E. Fraser. Calcium signaling during convergent extension in Xenopus. *Current Biology*, 11(9):652–661, may 2001.

[255] He Wang, Lei Dong, Jennifer O'Daniel, Radhe Mohan, Adam S Garden, K Kian Ang, Deborah A Kuban, Mark Bonnen, Joe Y Chang, and Rex Cheung. Validation of an accelerated 'demons' algorithm for deformable image registration in radiation therapy. *Physics in Medicine and Biology*, 50(12):2887–2905, jun 2005.

[256] Ning Wang, Iva Marija Tolić-Nørrelykke, Jianxin Chen, Srboljub M. Mijailovich, James P. Butler, Jeffrey J. Fredberg, and Dimitrije Stamenović. Cell prestress. I. Stiffness and prestress are closely associated in adherent contractile cells. *https://doi.org/10.1152/ajpcell.00269.2001*, 282(3 51-3):606–616, 2002.

[257] Yu-Chiun Wang, Zia Khan, Matthias Kaschube, and Eric F Wieschaus. Differential positioning of adherens junctions is associated with initiation of epithelial folding. *Nature*, 484(7394):390–393, apr 2012.

[258] James. D. Watson and Francis. H. C. Crick. Molecular Structure of Nucleic Acids: A Structure for Deoxyribose Nucleic Acid. *Nature*, 171(4356):737–738, apr 1953.

[259] Michael A. Welte, Steven P. Gross, Marya Postner, Steven M. Block, and Eric F. Wieschaus. Developmental Regulation of Vesicle Transport in Drosophila Embryos: Forces and Kinetics. *Cell*, 92(4):547–557, feb 1998.

[260] Ross T. Whitaker. None. *International Journal of Computer Vision*, 29(3):203–231, 1998.

[261] Eric Wieschaus and Christiane Nüsslein-Volhard. The heidelberg screen for pattern mutants of drosophila: A personal account. *Annual Review of Cell and Developmental Biology*, 32(1):1–46, 2016. PMID: 27501451.

[262] Carsten Wolff and Matthias Gerberding. *"Crustacea": Comparative Aspects of Early Development*, pages 39–61. Springer Vienna, Vienna, 2015.

[263] Carsten Wolff, Jean-Yves Tinevez, Tobias Pietzsch, Evangelia Stamataki, Benjamin Harich, Léo Guignard, Stephan Preibisch, Spencer Shorte, Philipp J Keller, Pavel Tomancak, and Anastasios Pavlopoulos. Multi-view light-sheet imaging and tracking with the MaMuT software reveals the cell lineage of a direct developing arthropod limb. *eLife*, 7:e34410, mar 2018.

[264] Georg Wolfstetter, Kathrin Pfeifer, Jesper R. van Dijk, Fredrik Hugosson, Xiangyi Lu, and Ruth H. Palmer. The scaffolding protein Cnk binds to the receptor tyrosine kinase Alk to promote visceral founder cell specification in Drosophila. *Science Signaling*, 10(502), oct 2017.

[265] Georg Wolfstetter, Margret Shirinian, Christiana Stute, Caroline Grabbe, Thomas Hummel, Stefan Baumgartner, Ruth H. Palmer, and Anne Holz. Fusion of circular and longitudinal muscles in Drosophila is independent of the endoderm but further visceral muscle differentiation requires a close contact between mesoderm and endoderm. *Mechanisms of Development*, 126(8):721–736, aug 2009.

[266] Lewis Wolpert. Positional information and the spatial pattern of cellular differentiation. *Journal of Theoretical Biology*, 25(1):1–47, oct 1969.

[267] Lewis Wolpert. Chapter 6 Positional Information and Pattern Formation. In *Current Topics in Developmental Biology*, volume 6, pages 183–224. Academic Press, jan 1971.

[268] Lewis Wolpert. *Principles of development*. Oxford University Press, Oxford, UK, 2011.

[269] Michele A. Wozniak and Christopher S. Chen. Mechanotransduction in development: a growing role for contractility. *Nature Reviews Molecular Cell Biology*, 10(1):34–43, jan 2009.

[270] Shi-Qing Xin and Guo-Jin Wang. Improving Chen and Han's algorithm on the discrete geodesic problem. *ACM Transactions on Graphics*, 28(4):1–8, aug 2009.

[271] Shigenobu Yonemura. Cadherin-actin interactions at adherens junctions. *Current Opinion in Cell Biology*, 23(5):515–522, oct 2011.

[272] Hiroyuki Yoshida, Simon Warfield, and Michael Vannier. *Abdominal Imaging. Computational and Clinical Applications: 5th International Workshop, Held in Conjunction with MICCAI 2013, Nagoya, Japan, September 22, 2013, Proceedings*. Springer, sep 2013. Google-Books-ID: Ryu6BQAAQBAJ.

[273] A P Young. Melting and the vector Coulomb gas in two dimensions. *Physical Review B*, 19(4):1855–1866, feb 1979.

[274] K Zahn, R Lenke, and G Maret. Two-Stage Melting of Paramagnetic Colloidal Crystals in Two Dimensions. *Physical Review Letters*, 82(13):2721–2724, mar 1999.

[275] J.H. Zar. *Biostatistical Analysis*. Prentice-Hall international editions. Prentice Hall, 1999.

[276] Wei Zeng and Xianfeng David Gu. *Ricci Flow for Shape Analysis and Surface Registration*. SpringerBriefs in Mathematics. Springer New York, New York, NY, 2013.

[277] Zhenru Zhou, Herve Alégot, and Kenneth D. Irvine. Oriented Cell Divisions Are Not Required for Drosophila Wing Shape. *Current Biology*, 29(5):856–864.e3, mar 2019.